Spectroscopic and Microscopic Characterisation of Liquid Phase Exfoliated 2D Materials

***

A thesis presented by
Aideen Griffin

Under the supervision of
Prof. Jonathan N. Coleman

For the degree of
Doctor of Philosophy

in the subject of
Physics

School of Physics
Trinity College Dublin

2021

Declaration

***

I declare that this thesis has not been submitted as an exercise for a degree at this or any other university and it is entirely my own work.

I agree to deposit this thesis in the University's open access institutional repository or allow the library to do so on my behalf, subject to Irish Copyright Legislation and Trinity College Library conditions of use and acknowledgement.

Elements of this work that have been carried out jointly with others or by collaborators have been duly acknowledged in the text wherever included.

_____

Aideen Griffin

Spectroscopic and Microscopic Characterisation of Liquid Phase Exfoliated 2D Materials

***

Abstract

Since the experimental isolation of graphene nearly two decades ago, the research into two-dimensional materials has accelerated at a tremendous rate across a vast range of scientific and engineering fields. Liquid phase exfoliation, a common production method, has progressed in recent years with studies reported on a variety of materials including graphene, transition metal dichalcogenides and layered double hydroxides. While the collection of liquid exfoliated crystals is substantial and growing year on year, the spectroscopy of hexagonal-boron nitride (h-BN) nanosheets, a widely used insulator, and the effect of stabilizers on the exfoliation process have yet to be explored in detail.

Spectroscopy of two dimensional h-BN, unlike many other nanomaterials, contains relatively little information due to the fact that both the absorption and Raman spectra consist of only one feature each. By size-selecting liquid exfoliated h-BN nanosheets the dependence of h-BN optical spectra on nanosheet dimension is analysed. After decoupling the light to separate the absorbance from the scattering, the size-dependence is removed apart from a well-defined variation in the energy of peak absorbance with nanosheet thickness. Furthermore, while the position of the h-BN Raman G band remains constant with nanosheet dimension, the linewidth appears to vary weakly with nanosheet thickness. Through the analysis of solvatochromatic effects in the liquid environment, the behaviour of the h-BN Raman G band width with nanosheet thickness is modelled. The size-dependent spectroscopic properties from both spectroscopic techniques can be used as metrics to estimate nanosheet thickness.

During exfoliation, surfactants are commonly used to stabilize nanosheets against reaggregation. Using WS_2 as a model system, the effect of varying surfactant type and concentration on the yield and dimensions of exfoliated nanosheets is explored. This study shows that for ionic surfactants, the mass of nanosheets decreases sharply past $\sim$10

mM, regardless of surfactant. Very similar dependences were observed for both nanosheet length and thickness. In contrast to previous studies, this data implies that the optimum surfactant concentration is not linked to the critical micelle concentration. In addition, surfactant concentrations as low as 0.07 mM yielded stable nanosheet dispersions with zeta potentials above 40 mV. By decoupling the exfoliation and stabilization effects of the surfactant, it is the (de)stabilization process, rather than the exfoliation process, that is shown to link nanosheet concentration, size and thickness to surfactant concentration.

In addition to frequently used 2D materials such as h-BN and WS_2, novel materials have been predicted in recent databases. The need to improve the performance of lithium ion batteries is ever-increasing due to the current climate crisis and these previously unexplored materials might hold the key. In this work, liquid phase exfoliation was used to produce nanosheets of SnP_3 and SiP, two novel materials with extremely high theoretical capacity of 1670 mAh g^{-1} and 3060 mAh g^{-1} respectively for Li storage. Nanosheet-nanotube composite thin films were formed for use as lithium storing anodes. Active-mass-normalised capacities of 1657 mAh g^{-1} for SnP_3 and 2654 mAh g^{-1} for SiP were measured, close to the theoretical values and state-of-the-art for 2D-based electrodes.

Apart from new materials, scalable techniques are important in the production of nanomaterials for applications. Bubble collapse, the mechanism behind the exfoliation of material in a sonicator, is replicated through boiling graphite and surfactant in an everyday kitchen kettle. Two techniques were demonstrated, the first a standard kitchen kettle producing very low yields of graphene after multiple cycles and the second a modification of the kettle, where a cooling coil maintains a rolling boil for long periods of time, increasing the number of bubbles. The increased heating time in the optimised setup resulted in a 10-fold increase in nanosheet concentration. EDX, XPS and Raman measurements revealed characteristic graphene signatures but also oxidation peaks and a high D band (Raman) indicative of a defective final product. Two regimes were proposed to exist in the kettle exfoliation. In the first regime, only partial exfoliation of graphite occurred resulting in thick graphitic platelets, mostly observed in a standard kettle. In the second regime large, thin nanosheets were exfoliated through the cleavage of neighbouring basal-plane defective sheets as a result of the increased energy input from the optimised set up.

Acknowledgements

***

FIRSTLY, I WOULD LIKE TO THANK Prof. Jonathan Coleman for giving me the chance to complete this work in a fantastic research group. His guidance and support over the last four years, along with the positive working environment that he inspires, has been invaluable. I really appreciate all the opportunities for travel to a range of conferences and meetings, providing plenty of scientific inspiration.

An enormous thank you goes to Claudia Backes for her endless patience, advice and support. From my initial crash course in all things LPE in Heidelberg as a first year and everything since, this work would not have been possible without her knowledge and guidance. Thanks also go to Beata, Kevin and the rest of the group in Heidelberg for welcoming me during my visits.

I have been lucky enough to work with an amazing bunch of people throughout my time in the group. Cian and Dan, we made it to the end, I'll say it was down to our carefully drafted group emails and annual flagship trips. Special thanks also to Andrew for all the training in the beginning and help with various projects over the years. To everyone else during my time in the group: Conor, Seb, Damo, Adam, Dave, Ivan, Sonia, Yash, Domhnall, James, Dominik, Mark, Shixin, Ruiyuan, Harneet, Victor and Kathi, thanks for all the research advice, five-a-side football games, afternoons at the Pav, hikes and Christmas parties (I still think our glühwein was perfectly balanced). Also a special thanks go to Amanda, Enda, Padraic, Jacqueline and Tracy in CRANN for all their help.

To my friends outside of college for all the brunches, drinks, chats and trips around Ireland that have nicely balanced out all the research.

To JB for the infinite support and for putting up with me writing in lockdown, I appreciate it more than I can say.

Finally, an immeasurable thank you to my family; Mum, Dad, Robbie, Orlagh and Johnny, for their constant encouragement and unwavering support over the last eight years, I could not have navigated this path without you.

Publications

***

1. O'Brien, S.A., Harvey, A., Griffin, A., Donnelly, T., Mulcahy, D., Coleman, J.N., Donegan, J.F. and McCloskey, D. Light scattering and random lasing in aqueous suspensions of hexagonal boron nitride nanoflakes. *Nanotechnology*, 28(47), 2017, p.47LT02.

2. Ling, Z., Harvey, A., McAteer, D., Godwin, I.J., Szydłowska, B., Griffin, A., Vega-Mayoral, V., Song, Y., Seral-Ascaso, A., Nicolosi, V. and Coleman, J. Quantifying the role of nanotubes in nano: nano composite supercapacitor electrodes. *Advanced Energy Materials*, 8(8), 2018, p.1702364.

3. Griffin, A., Harvey, A., Cunningham, B., Scullion, D., Tian, T., Shih, C.J., Gruening, M., Donegan, J.F., Santos, E.J., Backes, C. and Coleman, J.N. Spectroscopic size and thickness metrics for liquid-exfoliated h-BN. *Chemistry of Materials*, 30(6), 2018, pp.1998-2005.

4. Harvey, A., Backes, C., Boland, J.B., He, X., Griffin, A., Szydlowska, B., Gabbett, C., Donegan, J.F. and Coleman, J.N. Non-resonant light scattering in dispersions of 2D nanosheets. *Nature Communications*, 9(1), 2018, pp.1-11.

5. Boland, J.B., Harvey, A., Tian, R., Hanlon, D., Vega-Mayoral, V., Szydlowska, B., Griffin, A., Stimpel-Lindner, T., Jaskaniec, S., Nicolosi, V., Duesberg, G. and Coleman, J.N. Liquid phase exfoliation of MoO_2 nanosheets for lithium ion battery applications. *Nanoscale Advances*, 1(4), 2019, pp.1560-1570.

6. Vega-Mayoral, V., Tian, R., Kelly, A.G., Griffin, A., Harvey, A., Borrelli, M., Nisi, K., Backes, C. and Coleman, J.N. Solvent exfoliation stabilizes TiS_2 nanosheets against oxidation, facilitating lithium storage applications. *Nanoscale*, 11(13), 2019, pp.6206-6216.

7. Biccai, S., Boland, C.S., O'Driscoll, D.P., Harvey, A., Gabbett, C., O'Suilleabhain, D.R., Griffin, A., Li, Z., Young, R.J. and Coleman, J.N. Negative gauge factor piezoresistive composites based on polymers filled with MoS2 nanosheets. *ACS nano*, 13(6), 2019, pp.6845-6855.

8. Backes, C., Campi, D., Szydlowska, B.M., Synnatschke, K., Ojala, E., Rashvand, F., Harvey, A., Griffin, A., Sofer, Z., Marzari, N. and Coleman, J.N. Equipartition of Energy Defines the Size–Thickness Relationship in Liquid-Exfoliated Nanosheets. *ACS nano*, 13(6), 2019, pp.7050-7061.

9. Tian, R., Alcala, N., O'Neill, S.J., Horvath, D.V., Coelho, J., Griffin, A.J., Zhang, Y., Nicolosi, V., O'Dwyer, C. and Coleman, J.N. Quantifying the Effect of Electronic Conductivity on the Rate Performance of Nanocomposite Battery Electrodes. *ACS Applied Energy Materials*, 3(3), 2020, pp.2966-2974.

10. Griffin, A., Nisi, K., Pepper, J., Harvey, A., Szydłowska, B.M., Coleman, J.N. and Backes, C. Effect of Surfactant Choice and Concentration on the Dimensions and Yield of Liquid-Phase-Exfoliated Nanosheets. *Chemistry of Materials*, 32(7), 2020, pp.2852-2862.

11. Boland, J.B., Tian, R., Harvey, A., Vega-Mayoral, V., Griffin, A., Horvath, D.V., Gabbett, C., Breshears, M., Pepper, J., Li, Y. and Coleman, J.N. Liquid phase exfoliation of GeS nanosheets in ambient conditions for lithium ion battery applications. *2D Materials*, 7(3), 2020, p.035015.

12. Kaur, H., Tian, R., Roy, A., McCrystall, M., Horvath, D.V., Lozano Onrubia, G., Smith, R., Ruether, M., Griffin, A., Backes, C. and Nicolosi, V., 2020. Production of Quasi-2D Platelets of Nonlayered Iron Pyrite (FeS2) by Liquid-Phase Exfoliation for High Performance Battery Electrodes. *ACS nano*, 14(10), 2020, pp.13418-13432.

13. Nalawade, Y., Pepper, J., Harvey, A., Griffin, A., Caffrey, D., Kelly, A.G. and Coleman, J.N., 2020. All-Printed Dielectric Capacitors from High-Permittivity, Liquid-Exfoliated BiOCl Nanosheets. *ACS Applied Electronic Materials*, 2(10), 2020, pp.3233-3241.

14. Tian, R., Griffin, A., McCrystall, M., Breshears, M., Harvey, A., Gabbett, C., Horváth, D.V., Backes, C., Jing, Y., Heine, T. and Park, S.H., Liquid Exfoliated SnP3 Nanosheets for Very High Areal Capacity Lithium-Ion Batteries. *Advanced Energy Materials*, 2020, p.2002364.

List of Symbols

***

Symbol		Symbol	
A	Absorbance	I	Intensity
α	Absorption coefficient	k	Boltzmann's constant
C	Concentration	λ	Wavelength
Γ	Width of peak	L	Nanosheet length
δ	Hildebrand solubility parameter	ℓ	Path length
ϵ	Intermolecular interaction energy	κ^{-1}	Debye length
ε_0	Permittivity of free space	m	Mass
ε_r	Dielectric constant	N	Number of nanosheet layers
ε	Extinction coefficient	R	Gas constant
E	Energy	S	Sedimentation coefficient
ΔE_c	Cohesive energy density	ΔS	Entropy
E_g	Band Gap	T	Temperature
ζ	Zeta potential	v_0	Solvent molecular volume
η	Viscosity	V	Voltage
G	Gauge factor	σ	scattering coefficient/conductivity
g	gravitational acceleration	ϕ	Volume fraction
δ	Hildebrand solubility parameter	μ_e	Electrophoretic mobility
ΔG	Gibb's Free Energy	ω	Angular velocity
ΔH	Enthalpy	z	Coordination number

Acronym	
AFM	Atomic force microscopy
Abs	Absorbance
BN	Boron nitride
CHP	Cyclohexyl-pyrrolidone
CMC	Critical micelle concentration
CTAB	Cetyltrimethylammonium bromide
CVD	Chemical vapour deposition
2D	2-dimensional
EDL	Electrical double layer
EDX	Energy dispersive x-ray spectroscopy
Ext	Extinction
FLG	Few layer graphene
FWHM	Full width at half maximum
IPA	Isopropyl alcohol
LCC	Liquid Cascade Centrifugation
LDS	Lithium dodecyl sulfate
LIB	Lithium ion battery
LPE	Liquid phase exfoliation
NMP	N-methyl-2-pyrrolidone
PL	Photoluminescence
UV-Vis	Ultraviolet- Visible (spectroscopy)
RCF	Relative centrifugal field
SC	Sodium cholate
SDS	Sodium dodecyl sulfate
SDBS	Sodium dodecylbenzene sulfonate
SEM	Scanning electron microscopy
SOS	Sodium octyl sulfate
STS	Sodium tetradecyl sulfate
Sca	Scattering
TEM	Transmission electron microscopy
TMD	Transition metal dichalcogenide
TTAB	Tetradecyltrimethylammonium bromide

Contents

***

List of Figures

***

To Mum and Dad

1

Introduction

***

Advances in materials over thousands of years have altered human society, where defining discoveries and shifts in thought have paved the path for emerging technologies. In fact, ages in human history have been divided based on the dominant material of that period, from the Stone age to the Silicon age. In the latter half of the 20th century, the acceleration of new technology has been tremendous, the Silicon Chip becoming perhaps the most influential invention of this time. Materials are the fundamental building blocks of any device or application and so while Moore predicted an upward trend in transistors per chip,[1] Feynman proposed the design of materials on the atomic scale,[2] inspiring the emergence of a new field of research, nanoscience.

Nanoscience is a broad term, combining physics, chemistry and engineering and encompassing both materials and technology on the nanoscale. The use of nanomaterials in society is not a new idea. The Lycurgus Cup, a 4th century artefact made of dichroic glass, contains gold-silver alloy nanoparticles ($\sim$ 70 nm) appearing red in transmitted light and green in reflected light[3] while Damascus saber blades forged in the 17th century contained carbon nanotubes and cementite nanowires, together forming an ultrahigh-carbon steel that gave them unparalleled strength and flexibility.[4] The ability to characterise these materials however came hundreds of years later in 1981 when Gerd Binnig and Heinrich

Rohrer invented the Nobel prize winning scanning tunnelling microscope (STM) at IBM's Zürich lab, allowing for the direct imaging of individual atoms for the first time.[5] A few years later Binnig would also invent the atomic force microscope (AFM), another crucial characterisation tool that revealed the topography of a surface on the nanoscale.[6] It was not long after that Buckminsterfullerene[7] (C60, bucky balls) and carbon nanotubes[8] emerged as new forms of carbon materials, propelling nanotechnology to the forefront of scientific research that would continue throughout the 90s and early 2000s. The experimental isolation of single layer of graphite known as graphene in 2004 by Geim and Novoselov,[9] triggered an avalanche of publications on graphene and other novel two-dimensional materials, exhibiting a range of fascinating properties including exceptional strength, thermal and electrical conductivity.

2D materials have been proposed for a range of applications from electronic[10,11] and optoelectronic devices[12] to catalysts,[13,14] supercapacitors[15] and energy storage.[16] The production method of nanomaterials must be scalable if they are to compete with conventional and existing materials. Liquid-phase exfoliation (LPE) is a relatively simple technique, developed over a decade ago, that generates high yields of material at low cost.[17] Since the initial liquid-exfoliation of graphene, a vast number of other 2D materials have been successfully exfoliated and characterised including h-BN,[18] transition metal dichalcogenides,[19–21] layered double hydroxides,,[22,23] transition metal oxides[24,25] and black phosphorous.[26] The aim of this work is to examine in detail the dimension of nanosheets produced by LPE including probing dispersions spectroscopically and studying the effect of altering the stabilisation medium. Furthermore, the LPE process is applied to two novel nanomaterials with potential applications as battery electrodes. The final aim is to take the fundamental mechanism underpinning the technique, cavitation, and investigate whether a similar bubble collapse can be replicated through boiling.

Hexagonal boron nitride is liquid exfoliated and size-selected in Chapter 4. By analysing each sample spectroscopically using both UV-Vis and Raman, nanosheet dimension is linked to systematic spectral changes leading to the establishment of metrics. These metrics allow for h-BN thickness to be estimated through spectroscopy much quicker than statistical analysis of nanosheets with microscopy.

In Chapter 5, surfactants, the stabilisation method of choice for much of this thesis are examined in detail. The effect of surfactant choice and concentration on nanosheet dimension is comprehensively and systematically studied using WS_2 as a model system. The stabilisation of nanosheets produced by LPE is also investigated, related to the ionic conductivity induced by the liquid environment.

Two novel materials SnP_3 and SiP were selected from 2D databases in Chapter 6 based on their high levels of silicon and phosphorous. These elements are predicted to have very high theoretical capacities as electrodes in lithium ion batteries,[27] the development of which are crucial in combating the climate crisis. Both materials are liquid exfoliated and characterised using microscopy and spectroscopy, revealing systematic spectral changes with nanosheet size. SnP_3 and SiP nanosheets are mixed with carbon nanotubes to create nanosheet-nanotube composite electrodes that reach extremely high specific capacities when tested, the highest capacities for 2D materials reported to date.

Ultrasonication, the process that shears crystals during liquid-phase exfoliation, relies on the creation and violent collapse of bubbles. Another scalable and common method of bubble formation is through boiling. In Chapter 7 a novel exfoliation technique is demonstrated in which graphite is exfoliated to few layer graphene in a kitchen kettle. The graphene produced is characterised spectroscopically and microscopically to reveal a large amount of defects.

The main results of this thesis are concluded in the final chapter with some possible avenues for future development suggested. It is hoped that the metrics developed, insights into the exfoliation process reported, and novel materials demonstrated, add value to the field as a whole.

2

The edifice of science not only requires material, but also a plan. Without the material, the plan alone is but a castle in the air-a mere possibility; whilst the material without a plan is but useless matter

–Dmitri Mendeleev

Two-dimensional Materials: Properties and Production

***

TWO DIMENSIONAL MATERIALS HAVE EMERGED AT the forefront of materials science research since the isolation of graphene over a decade ago. Their novel physical properties have inspired an enormous number of publications with proposed applications in scaled-down electronics, energy storage and biological sensing. Understanding the properties of this new class of materials along with the ability to produce and characterise them in a quick, efficient manner will inevitably lead to the faster application realisation. This chapter describes layered materials, the properties and structure of their two-dimensional form and methods of their production. In particular, liquid phase exfoliation and nanosheet stabilisation are examined in detail as the primary production method of nanomaterials in this work.

2.1 Nanomaterials

Layered van der Waals crystals, the parent structure to two-dimensional nanosheets, can be classified as solids that have very strong in-plane bonds between atoms but weak van der Waals bonds between layers. The advantage of this bonding system is that the layers

in these materials can be sheared apart and crystals that were once macroscopic can be reduced to the nanoscale, the basis behind any top-down production method. It is this idea that has inspired a range of multi-layered 2D materials known as van der Waals heterostructures[28]. Nanomaterials can possess enhanced mechanical and electrical properties compared to their bulk counterparts, giving way to many exciting applications from electronic[11,29,30] to biomedical devices.[31,32] The electronics industry has been particularly targeted due to the fact that in the two-dimensional world electrons are confined to a 2D wavefunction, resulting in a change in band structure and sometimes bandgap compared to bulk.

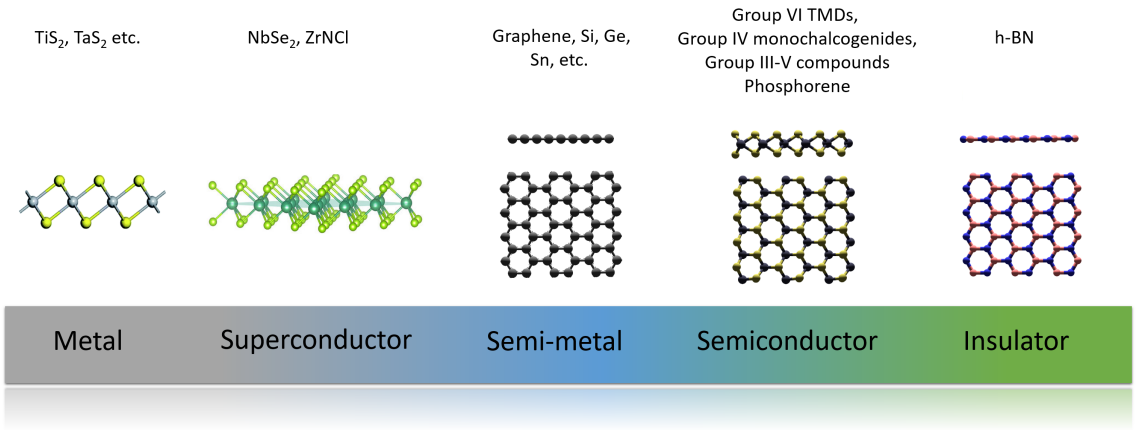

Figure 2.1: An overview of 2D materials grouped in accordance with their bandgap shows the variation and multitude of possibilities.

The research into 2D materials in the last decade or two has grown exponentially from the initial isolation of graphene in 2004.[9] To date, there are a vast number of materials which vary from conducting to insulating to semiconducting and even superconducting (Figure 2.1). A selection of materials used in this thesis are described in more detail below.

2.1.1 Graphene

First conceptualised in 1947 by P.R. Wallace,[33] graphene has risen to become a material of great interest in the world of condensed matter physics and materials science. This two-dimensional sheet of sp^2-hybridised carbon forms a honeycomb lattice, an elementary building block for other allotropes from nanotubes and fullerenes to graphite. While graphene had been used as a theoretical model for quantum electrodynamic studies

throughout the latter half of the twentieth century[34–36] it wasn't until 2004 that graphene was experimentally isolated for the first time by Geim and Novoselov using the scotch tape technique.[9] This discovery sparked the beginnings of a major exploration into the field of stable 2D crystals as the material's extraordinary thermal, mechanical and electrical properties became a topic of interest in the scientific community.

Graphene's atomic structure consists of sp^2 hybridized carbon atoms arranged in a honeycomb, hexagonal lattice (Figure 2.2A). The 2s orbital and two of the 2p (p_x and p_y) orbitals of carbon mix to form hybrid orbitals resulting in three strong, in-plane σ bonds between neighbouring atoms, forming the hexagonal lattice structure.[37,38] The p_z orbital, perpendicular to the plane, binds covalently with neighbouring carbon atoms, leading to the formation of a π band, similar to aromatic benzene. Each p_z orbital contains only 1 electron for binding, leading to a half filled band, underpinning the unusual electronic structure of graphene.[38] However in the 1930s, Peierls[39] and Landau[40] proposed that graphene and other strictly 2D materials could not exist due to thermodynamic instabilities at finite temperatures. However, in recent years it has been reported that graphene is not a completely flat 2D crystal but rather wrinkled with undulations on the order of approximately 10 nm, suppressing thermal vibrations and therefore stabilizing the crystal.[41,42]

In reality, any 2D honeycomb lattice of graphene will contain a number of structural defects,[43–47] imperfections arising naturally from thermodynamics of solids at any finite temperature.[48] The break in symmetry can be as a result of edges, vacancies, substitutional atoms (dopants), grain boundaries or defects from changes in hybridization e.g. sp^2 to sp^3.[44] In terms of exfoliated material, the type and concentration of defects depends both on the starting graphite and method of exfoliation (mechanical, liquid phase etc.) with the properties of the resulting graphene varying significantly. On the one hand, atomic-sized defects so-called resonant scatterers have been shown to greatly limit the carrier mobility of graphene, a hindrance for electronic devices.[49] On the other, defects in graphene layers enable routes for chemical functionalization and can increase chemical reactivity, making defective graphene a potential catalyst.[50] Raman spectroscopy has shown to be a powerful tool in probing the nature of defects in graphene,[44,51,52] with the evolution of new peaks and the intensity ratio of existing D and G peaks giving a measure

of the defect content, used in Chapter 7 of this work and discussed in more detail below.

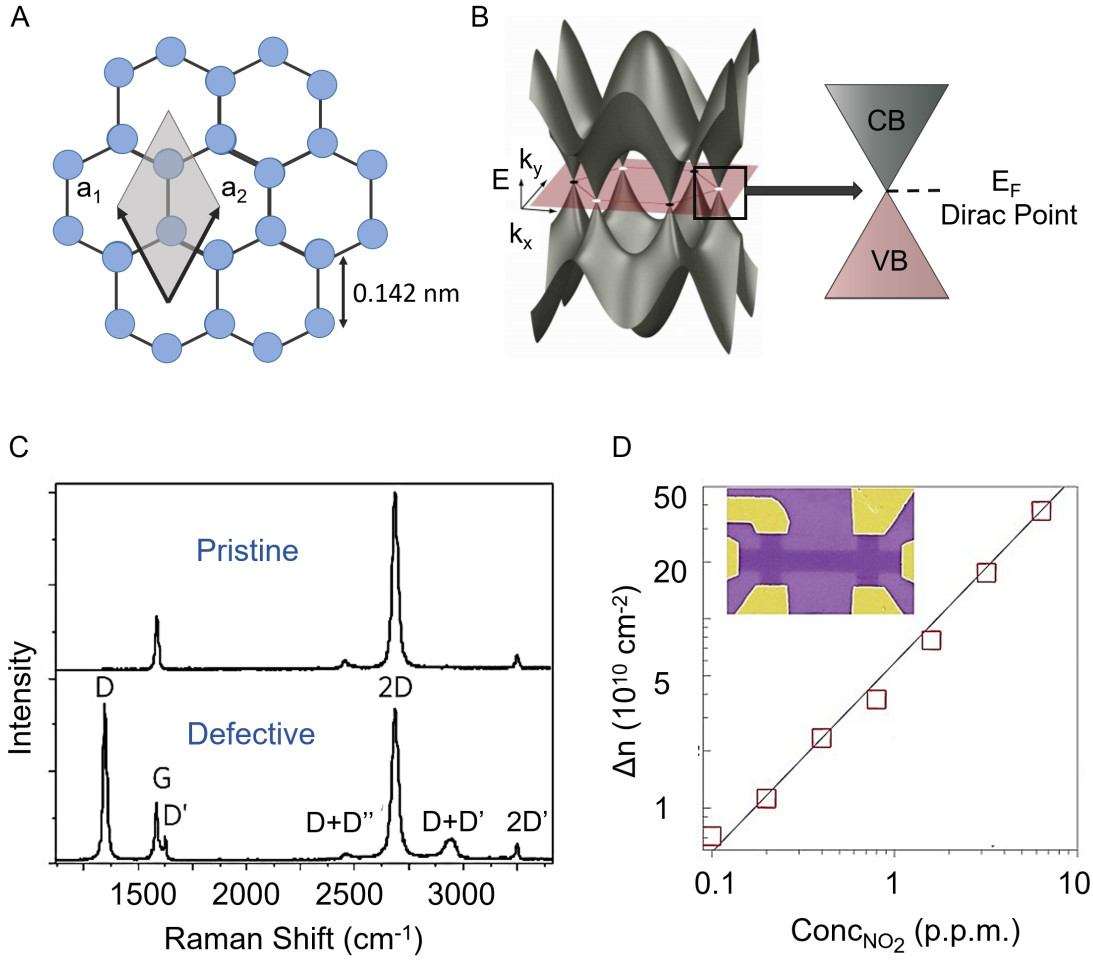

Figure 2.2: (A) Honeycomb lattice structure of a graphene monolayer with a carbon-carbon bond length of 0.142 nm.[42] The unit cell of is composed of 2 carbon atoms with basis vectors $\vec{a}_1$ and $\vec{a}_2$. (B) The electronic band structure of graphene. The conduction band and the valence band form conical shaped valleys that meet at the six corners of the Brillouin zone (indicated by axes). These points are known as Dirac points and in undoped graphene the Fermi level passes through. Image adapted from Beenaker[53] (C) Raman spectra of pristine and defective graphene. Both spectra exhibit large 2D bands compared to G bands, indicative of monolayer graphene. The defective sample shows large D and D' bands used to measure disorder and defects in graphene. A two phonon defect-assisted process leads to the D+D' peak ($\sim$2880 cm^{-1}) measured in the defective spectrum. Adapted from Ferrari et al.[54] (D) A gas sensor fabricated with monolayer graphene, demonstrating one of its many prospective applications. The concentration of chemically-induced charge carriers in the device increases with increasing concentration of NO_2. Image adapted from Schedin et al.[55]

The electronic band structure of graphene is unique, the out-of-plane p_z orbitals creating delocalized π and π^* states and forming the valence and conduction bands. These degen-

erate bands meet at the K and K' points (Dirac points) of the Brillouin zone (Figure 2.2B) and as such graphene can be thought of as a zero-band gap semiconductor but strictly speaking, it is a semi-metal since conduction is only possible with thermally excited electrons at finite temperature.[56] Graphene's remarkable electronic transport properties stem from the unusual nature of its charge carriers which mimic relativistic particles, unlike other materials where carriers are described using the Schrödinger equation as electrons moving in a periodic lattice potential. The motion of electrons in the honeycomb structure of graphene generates new quasiparticles known as massless Dirac fermions. These quasiparticles are best represented by the (2+1) dimensional Dirac equation[34–36] leading to a Fermi velocity $v_F \approx \frac{1}{100}c$. Massless Dirac fermions can be viewed as either electrons that have lost their rest mass or neutrinos that have gained the electron charge, viewing the neutrinos as massless.[57] Electronic transport in monolayer graphene is governed by these particles, giving rise to interesting quantum electrodynamic phenomena including atypical quantum Hall effects.[58] Bilayer graphene, where periodic honeycomb structures stack, contain massive Dirac fermions. This increase in mass leads to the change in the unusual linear dispersion relation ($E = \hbar v_F k$) of single layer graphene to a standard parabolic one. In fact, gating bilayer graphene has been shown to induce a non-zero, tunable bandgap.[56,59,60] In multilayer graphene (3-10 layers) several charge carriers appear and the conduction and valence bands start overlapping at many points.[9,61]

Graphene can be characterised in a fast and non-destructive manner through Raman spectroscopy, a powerful tool used to probe many other 2D materials. An abundance of information can be extracted from a spectrum including the number and orientation of layers, edge type, material quality and the effects from electric and magnetic fields, doping, strain, disorder and functionalization.[54,62,63] There are four main peaks in the Raman spectrum of graphene: D band ($\sim$ 1350 cm^{-1}), G band ($\sim$ 1582 cm^{-1}) D' ($\sim$ 1620 cm^{-1}) and 2D band ($\sim$ 2700 cm^{-1}) related to a number of Raman-active phonons,[63] shown in Figure 2.2C. The D and D' peaks are disorder-activated Raman bands indicating the number of defects, with very low intensity for pristine graphene.[62] The G band is comparable in intensity for both graphite and graphene,[64] a first order signature of the E_{2g} mode at the Γ-point arising from the stretching of the C-C bond.[54] The 2D band (also known as G' like other graphitic materials) is a second order mode involving phonons near the K point. The position blueshifts and the intensity of the 2D band increases for decreasing

number of layers with a very large 2D peak (compared to G band) for monolayer graphene stemming from its linear dispersion relation.[63–66] Meanwhile, Eckmann et al.[44] have reported that the intensity ratios ID/ID' and ID/IG can differentiate between defect types in a sample. Moreover, Backes et al.[67] have shown that LPE graphene exhibits a number of spectroscopic changes with decreasing nanosheet size including an increase in D and D' and 2D bands along with the narrowing of the 2D FWHM.

The abundance of graphite starting materials as well as exciting physical properties make graphene a suitable material for a wide range of applications. Graphene is a low-noise electronic material demonstrated by Schedin et al.[55] who fabricated micron-level gas sensors that can detect adsorption and desorption of individual molecules of NO_2 through changes in resistance based on changes in the chemically induced charge concentration (Figure 2.2D). Other sensors have been shown by Boland et al.[68] by embedding multilayer graphene in a soft polymer matrix to form a material known as G-putty. The mobility of the graphene nanosheets in the low viscosity matrix led to a very sensitive electromechanical sensor with gauge factors (ratio of relative change in electrical resistance to the mechanical strain) of over 500. Graphene, like CNTs have very impressive mechanical properties with a Young's modulus of 1 TPa which can be used to mechanically reinforce plastics.[69,70] Field effect transistors (FETs) using monolayer graphene was perhaps the earliest application, chosen due to the unique band structure supplying electrons and holes that can be continuously tuned by a gated electrical field.[9] Since then, mobilities of over 200,000 $cm^2\ V^{-1}\ s^{-1}$ have been reported to date for a suspended graphene devices.[11] However as a result of the zero bandgap, these devices have low on:off ratios, not ideal for transistors. More work is needed in the field of graphene-based electronics for them to compete with standard materials such as silicon. The high mobility, superlative chemical stability and intrinsic flexibility of graphene has led to its potential as a conductive ink for flexible electronics.[71–73] In a similar vein, graphene materials have shown promise as transparent conducting films for use in optoelectronic devices.[30,74,75] Other applications include graphene-based catalysts,[13,76] supercapacitors,[77,78] hydrogen storage[79,80] and biological sensors and scaffolds.[81–84]

2.1.2 One-dimensional Carbon Nanotubes

Carbon nanotubes (CNTs) can be described as graphene sheets rolled up to form one dimensional cylindrical tubes, first discovered by Iijima and coworkers in 1991 after a high current arc discharge process used to evaporate graphite.[8] The material produced was imaged using high resolution electron microscopy and showed multiple concentric tubes of graphene-like structures with nanoscale diameters which would later become known as multiwalled carbon nanotubes (MWCNTs). A few years later Iijima and colleagues produced 1 nm diameter single walled carbon nanotubes (SWCNTs) utilising the same arc discharge method.[85] Since then, carbon nanotubes have been mainly synthesised using arc discharge[86] and chemical vapour deposition (CVD)[87,88] methods, producing entangled bundles of tubes 10-30 nm in diameter and micrometers in length.[89] Given this large aspect ratio, as high as 10^4-10^5,[90] nanotubes can be considered one dimensional nanostructures.

Depending on the orientation of the hexagonal carbon in the lattice relative to the axis of the nanotube, they can exhibit either metallic or semiconducting behaviour. The chirality of the nanotube, defining the type, is given by a chiral vector $C_h = na_1 + ma_2 = (n, m)$ where a_1 and a_2 are lattice vectors and n and m are integers (Figure 2.3A).[90,91] Based on the angle of chirality ($0 \leq \theta \leq 30$) the nanotubes form in one of three types. Achiral nanotubes, those whose mirror image is identical, are known as zigzag (n,0) and armchair (n,n) where the chiral angle is 0° and 30° respectively. Chiral nanotubes (n,m) have an angle between 0° and 30° (Figure 2.3B). Through calculations of the electronic density of states, using the chiral vector for boundary conditions, all armchair nanotubes are reported to be metallic. In fact Dresselhaus et al.[90] have shown that metallic nanotubes occur when $n-m = 3q$, where n and m are the nanotube specific integers described above and q is an integer. A third of zig zag and chiral tubes are noted to be metallic with others semiconductors. Recent reports however have shown that highly monochiral dispersions (>84%) of (6,5) semiconducting SWCNTs can be produced through shear force mixing with conjugated polymers.[92,93]

Among the interesting properties of CNTs is the remarkable electronic transport. Given the one-dimensional electronic structure, transport in metallic SWNTs and MWNTs occurs

ballistically with essentially no electron scattering over long nanotube lengths and so very large currents can be carried without any heating of the system.[94,95] As a result, nanotube field effect transistors (FETs) have been constructed showing near ballistic levels of transport when nanotubes are contacted across palladium or gold contacts.[96–98] Logic gates[99,100] have also been constructed with CNTs, demonstrating their promise for a range of nanoelectronic devices.

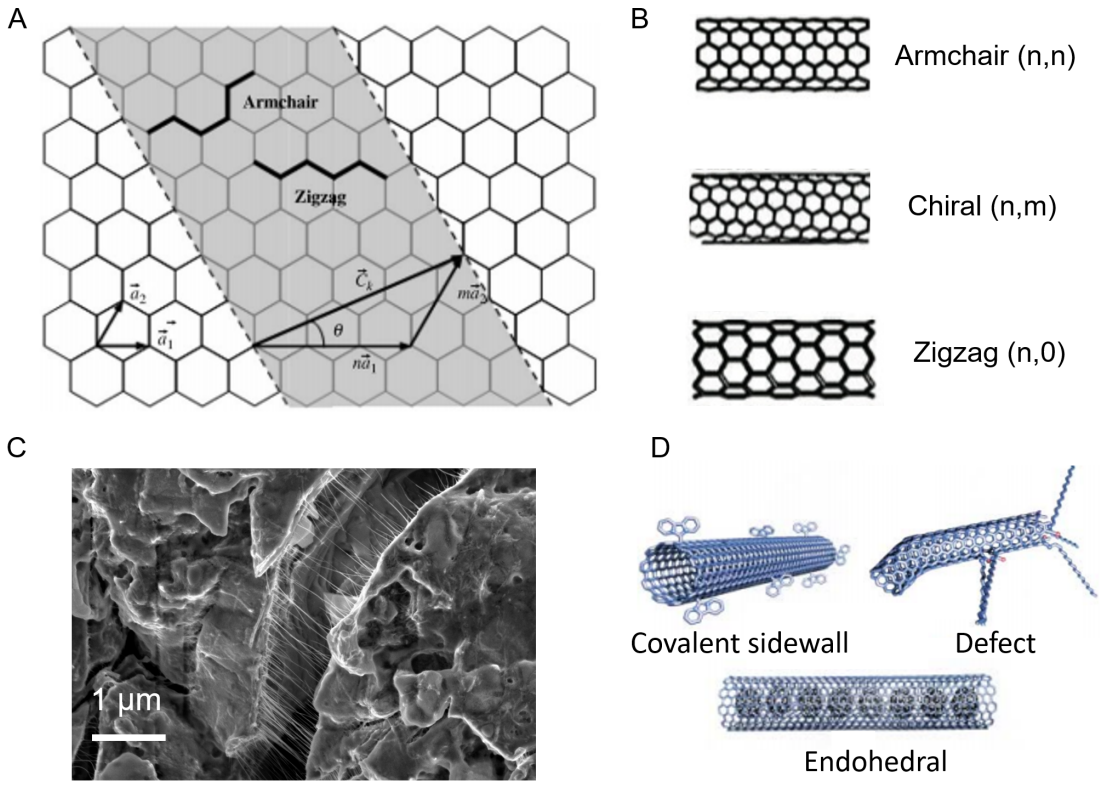

Figure 2.3: (A) An unrolled honeycomb lattice of a nanotube showing the chiral vector, C_h, a sum of multiples of the unit cell lattice vectors $\vec{a}_1$ and $\vec{a}_2$, defining the type of nanotube formed. Image from Wu et al.[101] (B) Three types of nanotubes with their chiral vectors (n,m): Armchair, chiral and zig zag from top to bottom, adapted from Tserpes et al.[102] (C) Silicon phosphide-CNT composite used in a lithium ion battery application, Chapter 6. The addition of CNTs increases the conductivity and mechanically strengthens the electrode. (D) Examples of nanotube functionalization used in a range of optoelectronic and biological applications, adapted from Hirsch et al.[89]

Moreover, CNTs have extremely high tensile strengths (up to 63 GPa[103]) and Young's moduli ($\sim$ 1 TPa[104]) and so have great potential for integration in polymer matrices as mechanical reinforcement. In Chapter 6 CNTs are mixed with novel 2D materials SnP_3 and SiP to improve the conductivity and mechanically reinforce electrodes (Figure 2.3C). High elec-

trical and thermal conductivities of nanotubes along with an extremely large surface area enhance the electrochemical capabilities of both cathode and anode nanomaterials. CNTs with their small diameters and increased lengths offer a much larger degree of accessibility for Li insertion than other conventional additives such as carbon black.[105] Furthermore, highly conductive networks of CNTs are flexible, an important property for reversible Li cycling and controlling volume expansion of electrodes. CNTs can also be functionalized to varying degrees with a wide range of chemical compounds (Figure 2.3D). Nanotubes are often difficult to disperse and dissolve in many organic media but functionalization can help solubility and processing, increasing the material's compatibility with a chosen biological molecule, polymer or solvent.[89] Functionalization may also change the mechanical and electrical properties of the nanotubes which can be tuned for specific applications.

2.1.3 Transition Metal Dichalcogenides

Transition metal dichalcogenides (TMDs) are a subclass of layered 2D materials that increased in popularity after Geim and Novoselov isolated graphene in 2004.[106] The history of TMDs dates much further back however, with studies of MoS_2 crystals from 1923[107] that inspired further explorations in the area. In 1965, MoS_2 was micromechanically cleaved down to the nanoscale with thicknesses as low as 10 nm reported.[108] By 1970 there were about 60 TMD compounds reported with various elemental compositions and properties.[109] The production of a single layer of suspended MoS_2 was shown by Joensen et al.[110] in 1986 through lithium intercalation of the bulk crystal followed by a reaction with water. Depending on the metal, chalcogen and thickness of the material, the properties of each TMD vary, making this category of nanomaterials used in a range of applications from electronics to catalysis.

A TMD has a stoichiometry of MX_2, where M is a transition metal of groups 4-10 and X is chalcogen atom, such as sulfur, selenium or tellurium (Figure 2.4A). TMDs from groups 4-7 are generally layered crystals while groups 8-10 tend to be non-layered.[111] The transition metal layer is sandwiched between two chalcogen layers and like graphene is characterized by weak interlayer van der Waals bonding between chalcogen (sandwich) layers and strong M-X covalent bonding making TMDs readily cleavable.[111,112] Each metal atom provides four electrons for bonding with the chalcogen layers resulting in oxidation

states of +4 for the metal and -2 for the chalcogen atoms. Furthermore every chalcogen atom has a lone-pair of electrons that terminates the surfaces of the layers, making them free of any dangling bonds and therefore stable against any chemical reactions with the environment.[111]

Depending on the coordination of the transition metal, TMDs can be one of three common polymorphs: 1T tetragonal (D_{3d} group), 2H hexagonal (D_{3h} group) or 3R rhombohedral (C^5_{3V} group) symmetry. Both the 2H and 3R polymorphs have trigonal prismatic coordination of the metal atoms whereas the 1T polymorph has an octahedral coordination.[113] The 3R phase is mainly found in bulk crystal and relaxes to the 2H phase after mild heating,[114] however 3R-WS2 and WSE2 phases have also been reported.[115] The integer indicates the number of layers X-M-X in the unit cell of each polymorph.[116] A variation in stacking sequence between layers produces different polytypes. For example, MoS_2 is naturally found in the 2H phase where the stacking sequence is AbA-BaB (capital and lower case letters stand for chalcogen and metal atoms respectively). Monolayer TMDs, on the other hand, only have a stacking sequence between metal and chalcogen sublayers within the monolayer structure itself, shown in Figure 2.4B. The 2H phase has a stacking sequence of ABA while the 1T phase stacks in ABC. Depending on the transition metal, one of the two phases will be more thermodynamically stable, the other phase being described as metastable. The most studied TMDs, MoS_2 and WS_2, are found in the 2H phase but the 1T phase can be obtained through lithium intercalation and exfoliation.[117,118]

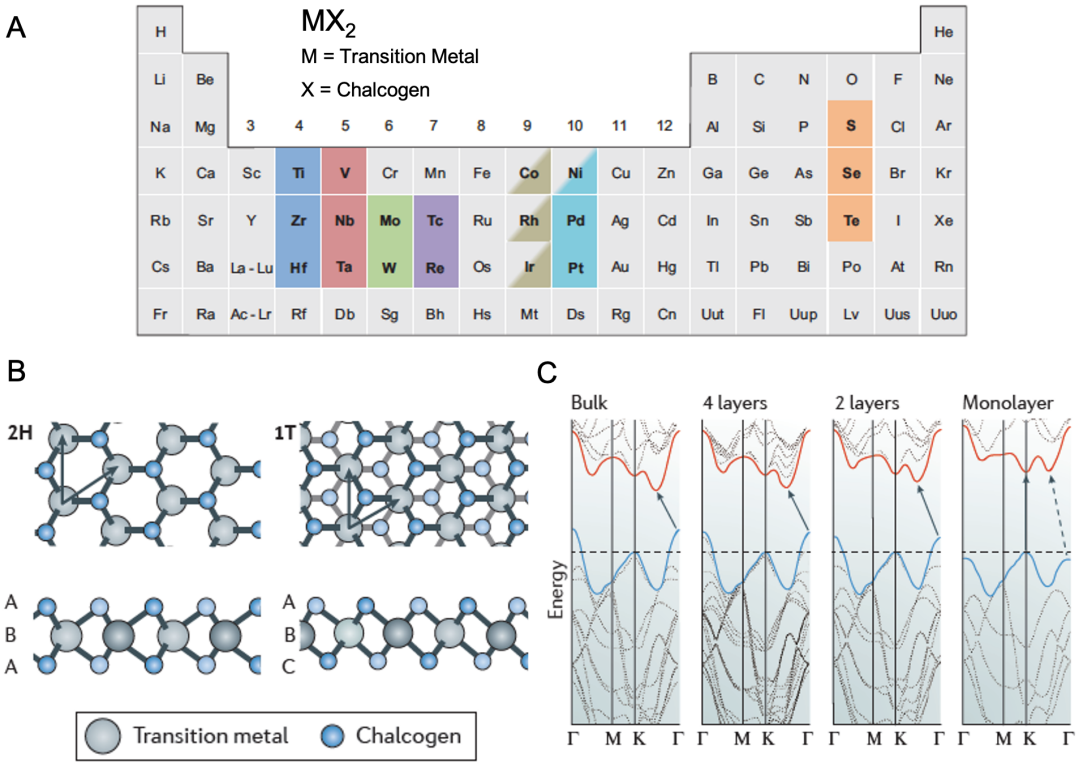

Figure 2.4: (A) Periodic table highlighting metallic and chalcogen elements that make up transition metal dichalcogenide crystals, adapted from Chhowalla et al.[111] (B) Atomic structure of a monolayer TMD in trigonal prismatic (2H) and octahedral (1T) phases from left to right with lattice vectors shown (C) Band structures of 2H-MoS_2 calculated for decreasing number of layers of from left to right showing the transition from indirect to direct band gap from few layer to monolayer. (B,C) Images adapted from Manzeli et al.[119]

TMDs with different phases will exhibit different electronic properties, MoS_2 in the 2H phase is semiconducting while the 1T phase is metallic. The transition metal coordination along with number of valence electrons in the d orbitals determine the electronic structure of each TMD. If the d-band is partially filled, for example in 2H-$NbSe_2$ or 2H-TaS_2, the Fermi level is within the band and the compound is metallic.[111,120] In contrast, completely filled orbitals, such as those in 2H-MoS_2, 2H-WS_2 and 1T-PtS_2, give a Fermi level in the bandgap between bonding (σ) and antibonding (σ^*) states leading these TMDs to exhibit semiconducting characteristics. The bulk bandgap decreases slightly with increasing atomic number of the chalcogen atom for semiconducting TMDs from 1.3 eV for 2H-MoS_2 to 1 eV for 2H-$MoTe_2$.[109,111]

The bandgap for multilayer TMDs like MoS_2 and WS_2 is indirect at the Γ point of the

Brillouin zone with the conduction band minimum at a different point to the valence band maximum. MoS_2 is used as a model system in many studies of the Group VI TMDs but the behaviour of each other compounds is similar, differing only in bandgap. When exfoliated down to the monolayer, the bandgap transitions from indirect to direct with the valence band maximum and conduction band minimum at the K point of the Brillouin zone, shown for 2H-MoS_2 in Figure 2.4C. This change in band structure with decreasing layer number is a result of quantum confinement leading to a change in hybridization between p_z orbitals on S atoms and d orbitals on Mo atoms.[121–123] The direct transition manifests in a greatly enhanced photoluminescence (PL) signature from monolayer MoX_2 and WX_2 type TMDs. Heinz et al.[121] demonstrated this behaviour with mechanically exfoliated MoS_2 layers (from monolayer to 6L) reporting that monolayers exhibit PL around 1.84 eV. The PL was quenched for bilayer and multilayer (bulk) samples.

In fact, spectroscopic techniques such as UV-Visible, photoluminescence, Raman spectroscopy and optical second harmonic generation (SHG) measurements can help identify the number of layers in TMD nanosheets based on photoluminescence and exciton fingerprints, unique to their electronic band structures.[19,124–127] WS_2 monolayers have been reported to generate a second-order Raman resonance involving the longitudinal acoustic mode (LA(M)) using 514 nm laser excitation.[124] Strong PL peaks from PL spectroscopy have been shown for mechanically exfoliated monolayer MoS_2[128] and CVD grown monolayer WS_2.[129] Raman spectroscopy can also be used to detect photoluminescence in liquid exfoliated WS_2 and MoS_2 samples, the peak intensity indicative of the monolayer volume fraction in a liquid dispersion.[19,20] Li et al.[130] reported strong second harmonic generation for odd numbers of MoS_2 layers where the material's structure is noncentrosymmetric compared to a negligible response from even layers of the same material.

The dimensionality of Group VI TMDs are noted to have an effect on excitonic transitions.[131,132] The A exciton, in common TMDs MoS_2 and WS_2, is the lowest excitation energy exciton, a strongly bound electron-hole pair formed upon optical excitation.[133,134] The exciton binding energies of monolayer TMDs are very large, on the order of 0.5 eV[135,136] meaning that these excitons are in fact more stable at room temperature than those in conventional bulk semiconductors and quasi-2D quantum well systems like GaAs.[137,138] As stated previously, decreasing the number of layers causes an increase in

bandgap as a result of quantum confinement effects that occur from the hybridization of electron orbitals when excitons are confined to a size smaller than the exciton Bohr radius.[121,123,133] Furthermore, both the quantum confinement and weak dielectric screening effects results in an increase in the effective Coulomb interaction.[134] The changes in Coulomb interaction are reflected in the renormalization of both the exciton binding energy effects and free particle band gap which manifests itself experimentally in shifts of the A-exciton position in optical absorbance spectra.[133,139,140] This phenomenon has been reported by Backes et al.[19,20] for both MoS_2 and WS_2 liquid exfoliated nanosheets. Similarly, Castellanos-Gomez et al.[141] found a blueshift in A-exciton position with decreasing number of MoS_2 layers through differential reflectance measurements of mechanically exfoliated nanosheets. Many group VI-TMDs have been reported to show excitonic spectral shifts including WSe_2,[142] $MoSe_2$[143] and $MoTe_2$[144] among others.

TMDs range from being semiconducting (MoS_2 and WS_2) to semi metallic (WTe_2 and $TiSe_2$) and metallic (NbS_2 and VSe_2) so there are an abundance of possible applications. Semiconducting MoS_2 has been used for transistors with effective mobilities reported as high as 700 $cm^2\ V^{-1}\ s^{-1}$ for a backgated device.[10] The true mobility is likely much lower due to the higher effective mass of its charge carriers. To put this in perspective, graphene has mobilities on the order of 200,000 $cm^2\ V^{-1}\ s^{-1}$ [11] but lacks a bandgap and therefore does not have the on/off ratios of a semiconducting material. In contrast, single layer MoS_2 has shown to exhibit on/off ratios of $\sim 10^8$.[145] Improvement in the field is still needed but TMDs show promise as electronic device materials. MoS_2 has been reported to exhibit impressive hydrogen evolution reaction (HER) activity[146] from high surface area MoS_2 mesoporous networks as a low-cost replacement for traditional catalytic elements such as Pt and Ir.[14] In the optoelectronics world, thin films of MoS_2 and WS_2 exhibit photosensitivity[147] and phototransistors constructed with monolayer MoS_2 have shown potential for photodetectors.[12] Other examples include flexible photovoltaic devices[148] made by sandwiching WS_2 between other 2D layers to form heterostructures.[149,150] The electrical conductivity of semiconducting TMDs alone is too low to be used as electrodes in Li ion battery applications, however when mixed with a carbonaceous material such as graphene, 2D MoS_2-graphene composite electrodes have shown relatively high specific capacities of 1,200-1,300 mAh g^{-1} along with good cycling stability and high-rate capability.[151–153]

Other materials used in this thesis include hexagonal boron nitride (h-BN), SnP_3 and SiP. h-BN is a widely used 2D insulator while SnP_3 and SiP show potential for energy storage applications. Detailed literature reviews on these materials can be found in their respective experimental chapters: Chapter 4 for h-BN and Chapter 6 for SnP_3 and SiP.

2.2 Production of 2D Materials

Micromechanical Cleavage

MoS_2 was the first material to be synthesised by micromechanical cleavage using the scotch-tape method in 1965,[108] a technique that gives high quality, low defect nanosheets. It was also used by Geim and Novoselov to isolate graphene in recent years, catapulting it back into the limelight as a means of producing 2D materials. By exerting a normal force to the crystal via peeling the tape, the van der Waals interlayer bonds are broken. Repeating this process multiple times leads to thinner and thinner pieces and eventually single layer material is produced. This method is labour-intensive and time-consuming with very low yields compared to others on the exfoliation side of production. However, due to the high quality of the nanosheets produced coupled with easy transferability, mechanical exfoliation is ideal for studying more fundamental physics such as quantum Hall effect,[154] thermal conductivity,[155] electron-hole transport,[156] spin-orbit coupling[157] and photovoltaic effects.[156]

Chemical Vapour Deposition

Chemical vapour deposition (CVD) is a technique in which thin solid films are deposited on a substrate from chemical precursors in the vapour phase. Precursors are evaporated and transported in the gas flow region in the high temperature furnace. In the reaction zone, gas phase reactions of precursors produce reactants which are mass transported to the substrate surface and adsorbed. Once adsorbed on the surface, the precursors diffuse to growth sites, initiating nucleation and chemical reactions, leading to the formation of a thin film.[158] The film growth rate depends on the substrate temperature, reactor pressure and the composition and chemistry of the gas-phase. Graphene can be produced by CVD methods[159–161] using a heated (1035°C[162]) metal substrate, usually copper. The elevated temperature of the substrate increases the domain size[162] of both the metal and thin film.

The methane precursor decomposes at high temperatures and carbon is deposited on the substrate. Similar methods are used to grow TMDs such as MoS_2 and WS_2 where a metal oxide precursor is heated to produce the atomic metal and then treated with the gaseous chalcogen (S) precursor.[163] In recent years, large scale growth of monolayer graphene,[164] MoS_2[165] and WS_2[166] has become common in the field with films grown transferred to other substrates using mechanical or chemical treatments after the furnace.[167] Furthermore, the technique is more easily integrable to current industrial processes than many other production methods, making it the method of choice for numerous giants in the world of micro-electronics. Large scale-up of the CVD process is difficult however with expensive equipment and low production rate hindering its use for certain industrial applications.

Ball milling

Ball milling is a type of mechanical cleavage that has been used to reduce the size of graphite particles since the 1950s.[168,169] A partially filled chamber of steel or ceramic balls, the grinding medium, along with the chosen material is rotated around a fixed axis. Impact and attrition of the rapidly moving balls with the powder material causes a size reduction in the particles down to the nanoscale. The rate of grinding depends on the particle size such that there is a decreasing rate for decreasing particle size, eventually it becomes very difficult to achieve smaller sized particles.[170] Wet ball milling using a dispersing agent can help produce a higher volume of small particles. The shape and size of the mill along with the density of both balls and powder as well as milling rate will all affect the material produced. Usually, longer milling times with a larger ball to powder ratio will produce better results.[171] This method generally does not use any toxic chemicals, is cost effective and scalable and has been used to create a wide range of 2D materials including BN,[172] graphene nanocomposites[173] and TMDs.[174,175] On the other hand, the balls can introduce defects and impurities to the nanomaterial produced and it can take days to create small nanosheets.

Chemical Exfoliation

Chemical exfoliation is a scalable, top-down approach that is achieved by intercalation of a chemical species followed by a chemical reaction or exchange of ions already present

in the layered material.[176] Intercalants ranging from acids/bases and oxidizing agents to inorganic salts and reactive functional molecules can be used for exfoliation. The role of the intercalant is to decrease the van der Waals bonding between layers by increasing the interlayer spacing, thus making the cleavage of single or few layers more accessible while preventing reaggregation and in some cases functionalizing for applications. A common intercalant that lowers the energy barrier for exfoliation of MoS_2 is n-butyllithium[110,111,177,178] which transfers electrons from the guest (Li) to the unoccupied energy levels of the host (MoS_2).[179] The intercalated crystal is then exfoliated via ultrasonication or thermal shock with nanosheets stabilized using surfactants, functional groups or intercalant charges that were transferred. An example of this process is shown in Figure 2.5 by Knirsch et al.[178] where bulk MoS_2 crystal is intercalated with n-butyllithium, sonicated to exfoliate and then functionalised with a diazonium salt that quenches the negative charges present post-lithiation, forming C-S bonds on the basal plane. Similar chemical exfoliation and functionalisation has been reported for graphite using a sodium/potassium alloy for intercalation followed by organic diazonium salt functionalisation.[180]

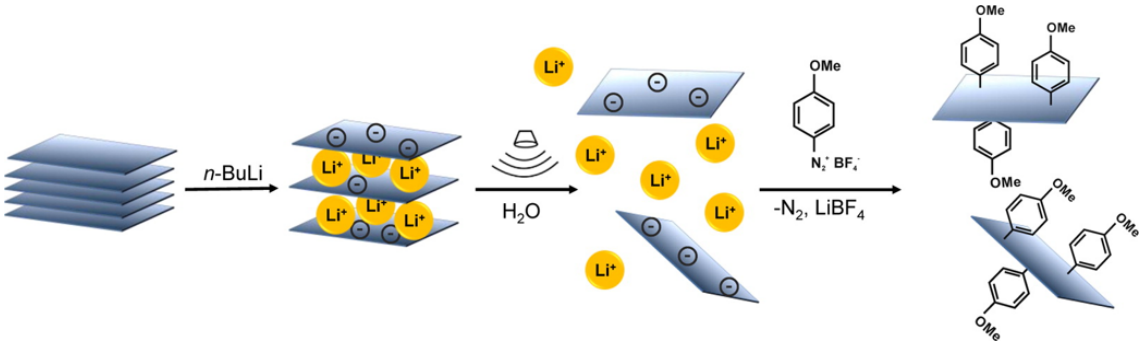

Figure 2.5: Schematic representation of the chemical exfoliation and intercalation of MoS_2 using n-butyllithium and diazonium salts to produce basal-plane functionalized MoS_2 nanosheets, image from Knirsch et al.[178]

In general, residual impurities from intercalants and oxidizing/reducing agents can adsorb chemically or physically to the exfoliated nanosheets leading to structural defects and changes in phase.[111] As an example, the Li charge transfer to MoS_2 induces a phase transition from semiconducting 2H to metallic 1T polytype. However, the 2H to 1T phase change in MoS_2 can be stopped or reversed through modified intercalation protocols[178] or IR-laser induced reversal respectively.[181] Other 2D materials exfoliated after intercalation

include MXenes,[182] TMDs,[183] LDHs,[184] black phosphorous[185] and metal chalcogens.[186] The intercalated lithium, potassium or sodium ions and subsequent exfoliation can result in promising electrode materials for energy storage applications.[187] Layered double hydroxides, metal oxides and clays possess an exchangeable interlayer of cationic counterions that can be used in ion exchange exfoliation.[188] Mixing layered materials with acids for example leads to protons being exchanged for bulky organic ions, resulting in swelling. Once the ions have been exchanged, the material can be easily exfoliated through ultrasonication or shear mixing, producing negatively charged nanosheets.[189]

2.3 Liquid Phase Exfoliation

Layered crystals can be exfoliated down to mono and few layer nanosheets through the versatile method of liquid phase exfoliation (LPE). First demonstrated by Hernandez et al.[17] a few years after Geim and Novoselov's scotch tape technique,[9] this method involves the dispersion of a layered crystal in a stabilizing solution with the application of ultrasonic energy to separate layers into nanosheets. LPE has proven successful for many different 2D materials in a variety of solvent and surfactant environments,[17–20,24,26,67,190–193] while being relatively cheap and scalable compared to other methods such as chemical vapour deposition (CVD), mechanical exfoliation and thermally assisted conversion. LPE produces a polydisperse dispersion with lateral sizes that vary from material to material but are typically 40-1000 nm with thicknesses of 1-30 monolayers. The resulting dispersion can then be processed to narrow the range of sizes required through centrifugation.

Liquid phase exfoliation involves the application of either shear forces or ultrasound to a layered crystal in a chosen solvent or surfactant dispersion. The basic idea is that is that ultrasonic energy imparts a high frequency vibration ($>$ 15 kHz) to the layered crystal material. Micro cavities are formed which collapse and emit a high energy micro-jet,[194,195] the force of which shears the material into nanosheets (Section 3.1.1). Interactions between the surfactant/solvent and nanosheets in the liquid medium (Section 2.4) account for their stability and prevent reaggregation of the material.[196]

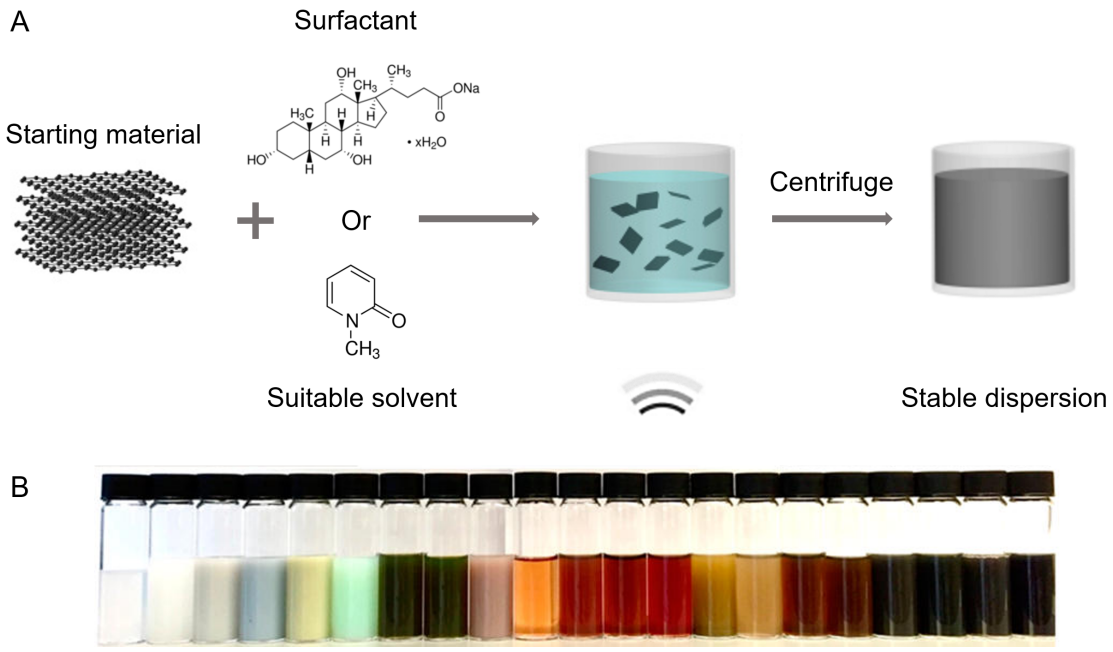

Figure 2.6: (A) Schematic representation of the liquid phase exfoliation method. Starting material is mixed with aqueous surfactant solution or a suitable solvent and sonicated using an ultrasonic processor. The product is then centrifuged to remove any unexfoliated material, resulting a stable colloidal dispersion of nanosheets stabilised with surfactant or solvent. Image adapted from Bonaccorso and Sun.[197] (B) Range of 2D materials exfoliated to date. Image from Backes et al.[198]

The mechanism for exfoliation of graphite has recently been reported in detail by Li et al.[199] LPE consists of two simultaneous processes: exfoliation and fragmentation, that happen in three stages (Figure 2.7A). Exfoliation reduces the crystallites in the z plane i.e. thickness while fragmentation reduces the lateral dimensions in the xy plane (L and W).[18,200–203] Li et al. noted that the preference for exfoliation over fragmentation or vice versa was related to the ratio of the surface energy of edges and basal planes of the graphite along with the ratio of the out-of-plane and in-plane mechanical properties. The parent graphite was reported to initially be fragmented by ultrasound induced cavitation along naturally existing basal plane defects, as suggested previously by Coleman et al.[18] to be topological rather than vacancies or impurities. Other statistical models have suggested that larger flakes are fragmented first followed by an "erosion" process in which smaller flakes are separated from the edges of larger flakes as result of peeling.[204–208] The fragmentation of the parent crystallites leads to the formation of kink bands that peel off in the second stage of exfoliation to form graphite strips. This hypothesis is consistent with increased surface roughness in the form of partial terraces/ridges which can be

viewed microscopically in any liquid exfoliated sample.[199] The graphite strips are fragmented further in a third stage to produce thin nanosheets. Crucially, the defect density of the starting material governs the degree of exfoliation and fragmentation. Higher defect density graphite will result in a quicker drop in thickness and lateral dimension of exfoliated flakes. The choice of solvent is reported to the effect the exfoliation rate while an increased sonication time narrows the lateral size distribution.[199]

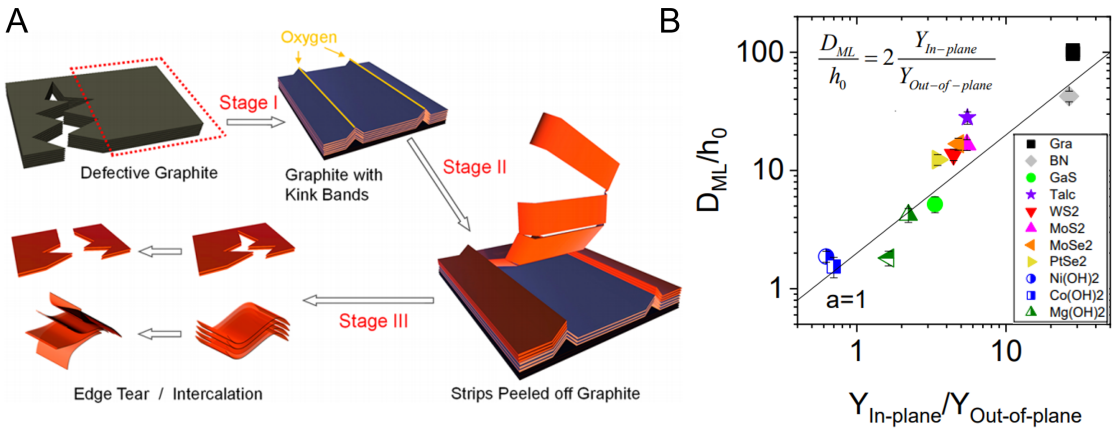

Figure 2.7: (A) Stages of fragmentation and exfoliation during LPE. The parent graphite is fragmented by ultrasound induced cavitation along existing defects in Stage 1. In stage 2, graphite with kink bands are peeled into graphitic strips which are then further exfoliated by tearing and peeling into graphene nanosheets in Stage 3. Image from Li et al.[199] (B) D_{ML}/h_0, the characteristic monolayer length divided by the theoretical monolayer height versus ratio of the in-plane to out-of-plane Young's moduli shows that all 2D materials providing evidence for the equipartition of energy of tearing and peeling. This plot gives a measure of the exfoliation efficiency of a number of materials. Image adapted from Backes et al.[202]

The physics of exfoliation was also examined by Ji et al.[201] and Backes et al.,[202] both authors reporting that nanosheet dimension depends on the ratio of the in-plane and out-of-plane Young's moduli of the layered material. Backes et al.[202] provided strong evidence for the equipartition of energy between the tearing and peeling during exfoliation. The interlayer binding energy, unique and intrinsic to each material, was found to play an important role in the exfoliation efficiency. A characteristic monolayer length (as a fraction of theoretical monolayer height) was plotted versus the ratio of its Young's moduli (Figure 2.7B), giving a measure of the exfoliation efficiency and importantly following a slope of $a \approx 1$ showing that there is in fact a balance between the tearing and peeling energies during exfoliation. Each material showed different size distributions linked to the interlayer

binding energy, for example, WS_2 nanosheets were found to be significantly smaller than graphene but had a comparable thickness. However, it was noted that in general, larger nanosheets tend to be thicker than smaller ones due to the fact it costs more energy to exfoliate a larger area nanosheet of a given thickness. As such the authors suggest there may be a fundamental limitation of the aspect ratio of an exfoliated nanosheet that is determined by the starting material itself rather than the exfoliation conditions, a possible limitation for certain applications. The exfoliation efficiency for two novel 2D materials is calculated in Chapter 6 based on this study. Moreover, the exfoliation yields were attributed to solvent-nanosheet interactions which in fact govern stabilization rather than exfoliation, in agreement with other studies,[17,199,209] and also examined in Chapter 5 for surfactant-based dispersions.

One of the main advantages of LPE is the ease at which nanosheets can be solution processed and analysed. The liquid environment of a sample can be readily changed through redispersal of the sediment produced after centrifugation (Section 3.1.2). Centrifuging also allows nanosheets to be selected by lateral size and thickness, depending on the application required. Spectroscopic techniques like Raman and UV-Visible spectroscopy probe the ensemble in solution and so millions of nanosheets can be statistically characterized at once.[19,20,67] LPE disperions are therefore ideal for solution-based processing techniques such as freeze drying,[210] ink-jet printing,[211,212] spray coating[73,213] and spin coating.[214] The method can be scaled-up through shear force mixing, a branch of liquid exfoliation that produces industrial scale quantities of nanomaterial.[215] LPE nanosheets have been utilised in a range of structures and devices including transistors,[72] supercapacitors,[25,216] optoelectronics,[217,218] catalysts,[23] gas barrier composites,[219,220] strain sensors[68,221] and battery components.[222]

2.4 Dispersion Stabilisation

Nanosheets can be stabilized thermodynamically with appropriate solvents or by using surfactants which prevent reaggregation electrostatically or by steric hindrance, each method described in more detail below. The choice between surfactant and solvent stabilisation generally tends to be made based on the prospective application. However it is sometimes the case that the material may be chemically unstable in an aqueous environment,

e.g. black phosphorous.[26] For any nanosheets that are being further processed for electronics a low boiling point solvent is ideal. Printing and spraying, common techniques utilised in fabricating nanosheet networks for transistors as an example,[72,73] require solvents that don't clog nozzles and evaporate easily post-deposition. Surfactants are not easily removed once deposited and can inhibit transport in nanosheet networks. On the other hand, aqueous surfactant solutions are a less toxic and cheaper alternative. Moreover, surfactant dispersions tend to contain more small/thin nanosheets along with a nearly 4-fold increase in yield (5% for solvent, 19.5% for surfactant[202]) compared to solvent-stabilised dispersions using the same centrifugation parameters. Smaller, thinner nanosheets are reported to be as a result of differences in interfacial stress transfer at surfactant nanosheet versus solvent-nanosheet interfaces.[202] Therefore aqueous surfactant stabilisation is utilised for more fundamental scientific investigations where a larger range of nanosheets is probed and solvent stabilisation for applications-based studies, as is indeed the case in this thesis. Nanosheets are stabilised with surfactants in Chapters 4, 5 and 7 where fundamental aspects of liquid exfoliation are examined in detail while solvents are used for nanosheet-composite batteries in Chapter 6.

2.4.1 Solvent stabilisation

Depending on the liquid environment exfoliated nanosheets may either be drawn towards each other or the liquid molecules, leading to reaggregation or stabilisation respectively. For nanosheets exfoliated in organic solvents, stabilisation can be understood through solubility theory. The mixing interaction between the solvent and material must be taken into account, defined thermodynamically by the Gibb's free energy of mixing, ΔG_{mix}

$$\Delta G_{mix} = \Delta H_{mix} - T\Delta S_{mix} \tag{2.1}$$

where ΔH_{mix} is the enthalpy of mixing, T is temperature and ΔS_{mix} is entropy of mixing. The mixture must have a negative Gibb's energy to be energetically favourable, otherwise nanosheets will aggregate.[37,223] Mixtures with small molecules may have very large entropies but 2D nanosheets are considered as relatively large and rigid meaning entropy is small. Cao et al.[224] report that entropic effects may in fact be non-negligible in stabilising LPE nanosheets but that changes in entropy change depending on material rigidity and

solvent. In general however, minimising the enthalpy of mixing leads to a stable solvent dispersion. A rough approximation in the early years of LPE development related the enthalpy of mixing to solvent and graphene surface energies

$$\frac{\Delta H_{mix}}{V} \approx \frac{2}{T_{NS}}\left(\sqrt{E_{S,S}} - \sqrt{E_{S,G}}\right)^2 \phi_G \tag{2.2}$$

where $E_{S,S}$ and $E_{S,G}$ are the solvent and graphene surface energy respectively, T_{NS} is nanosheet thickness, and ϕ_G is the graphene volume fraction dispersed in solvent. This behaviour is demonstrated graphically in Figure 2.8 where the nanosheet concentration peaks for solvent energies close to that of the material.

For a more thorough approach however, the enthalpy of mixing can be broken down into several interactions: solute-solvent, solute-solute and solvent-solvent, encompassed by what is known as the Flory-Huggins parameter χ[225–227]

$$\chi = -\frac{z}{2}\frac{(2\epsilon_{AB} - \epsilon_{AA} - \epsilon_{BB})}{kT} \tag{2.3}$$

where k is the Boltzmann constant, z is the coordination number of solute and solvent and ϵ represents the strength of the inter-molecular pairwise interaction energies of solute, A, and solvent, B. From equation 2.3 above, it is clear the strength of the solvent-solute interaction, ϵ_{AB} compared to the other interactions energies is critical in the value of this parameter. If nanosheets are more attracted to each other than the solvent, χ becomes large indicating that the nanosheets will reaggregate and sediment.

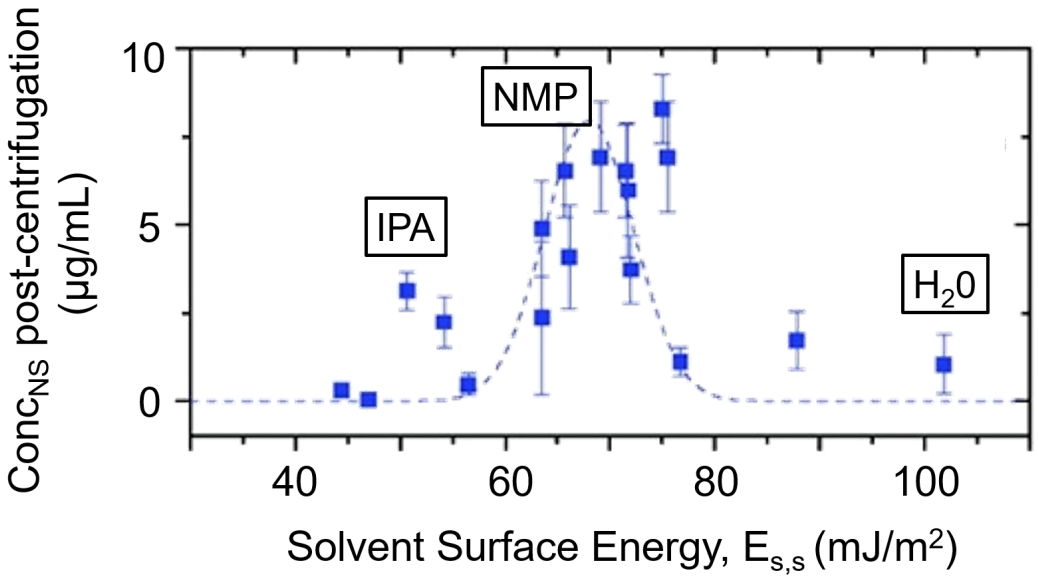

Figure 2.8: Nanosheet concentration as a function of solvent surface energy for a range of solvents adapted from Coleman et al.[196] When the solvent energy is closely matched to the nanosheet surface energy (graphene $\approx$ 68 mJ/m^2[196]), the concentration is maximised indicating more efficient exfoliation.

The stronger the solvent-solute interaction energy, the smaller the value of χ leading to a more stable dispersion. Indeed the enthalpy of mixing can be related to the Flory-Huggins parameter by[227]

$$\frac{\Delta H_{mix}}{V_{mix}} = \chi\phi\left(1-\phi\right)\frac{kT}{v_0} \tag{2.4}$$

where ϕ is the solvent volume fraction and v_0 is the solvent molecular volume. The interaction energies between solute and solvent can be described by Hildebrand solubility parameters,[228] indicative of the relative solvency of a solvent. The parameter is derived from the cohesive energy density, ΔE_c

$$\Delta E_C = \Delta H_V - RT = \frac{-z}{2}\frac{\varepsilon}{v_0} \tag{2.5}$$

The cohesive energy density reflects the degree of van der Waals forces between the molecules in a solvent and is derived from the heat of vaporisation ΔH_v.[229,230] The Hildebrand solubility parameter , δ, is related to the cohesive energy density by $\delta = \sqrt{\Delta E_c/V}$. The Flory-Huggins parameter can then be written, converting the interaction energies to

Hildebrand solubility parameters

$$\chi = \frac{v_0}{kT}(\delta_A - \delta_B)^2 \tag{2.6}$$

Similar to the surface energies in Equation 2.2, equating the Hildebrand solubility parameters leads to a minimisation of the enthalpy of mixing, giving stable dispersions. The energy cost per unit volume of mixing as a function of nanosheet thickness was modelled and approximated, taking into account the energy required to separate individual layers in a van der Waals crystal and the solvent molecules in a dispersion.[223] This equation is approximated as

$$\frac{\Delta H_{mix}}{V_{mix}} \approx \frac{2}{T_{NS}}(\delta_{nanosheet} - \delta_{solvent})^2\phi \tag{2.7}$$

This expression is rather generalised and does not differentiate between polar and non-polar contributions, a fact which was corrected by Hansen[229] who defines the Hildebrand solubility parameter to be a combination of Hansen solubility parameters representing dispersion (δ_D), polar (δ_P) and hydrogen bonding (δ_H) interactions.

$$\delta^2 = {\delta_D}^2 + {\delta_P}^2 + {\delta_H}^2 \tag{2.8}$$

The Hansen solubility parameters are based on the 'like dissolves like' term. The more similar one molecule is to another, the more likely it is to bond and dissolve. It should be noted however that nanosheets do not dissolve in liquid and are not solutions. Rather they are stabilised colloidal dispersions that are not at thermodynamic equilibrium but stable for long periods if the right solvent is chosen. The dispersion parameter δ_D is a measure of the atomic London dispersion forces between molecules correlating to the polarizability and van der Waals forces. The polar term defines the permanent dipole-dipole interactions, from polar solvents. For example methanol and acetone will have a large polar Hansen solubility because of their polar -OH and -C=O groups respectively. The hydrogen parameter accounts for hydrogen bonding which at first glance one would assume would be zero for all aprotic solvents. However recent reports[231] have suggested many of these solvents, like formaldehyde for example, can accept protons and form hydrogen bonds when mixed resulting in non-zero δ_H values. Both solvent and solute can therefore be thought of as a point in three-dimensional Hansen solubility space with XYZ coordinates corresponding to δ_D, δ_P and δ_H terms respectively.[229] The closer the distance between

solvent and solute, the more miscible the system will be. The Flory-Huggins parameter can be re-written in terms of Hansen solubility parameters as

$$\chi = -\frac{v_0}{kT}\left[(\delta_{D,A}-\delta_{D,B})^2+(\delta_{P,A}-\delta_{P,B})^2+(\delta_{H,A}-\delta_{H,B})^2\right] \tag{2.9}$$

Ideally, each Hansen solubility parameter would be matched between solute and solvent to minimise the enthalpy of mixing and optimise nanosheet concentration. N-methyl-2-pyrrolidone (NMP) was the main solvent used for exfoliation in Chapter 6, a low boiling point solvent whose energy tends to match the surface energy of many 2D materials leading to efficient exfoliation (Figure 2.8).

2.4.2 Surfactant stabilisation

For the majority of this work (Chapters 4, 5 and 7) nanosheets are stabilised in surfactant solutions of various types and concentrations. Surfactants (surface-active agents) are stabilising molecules that usually consist of a long hydrophobic alkyl chain known as the tail with a hydrophilic ionic head group at one end, known as an amphiphatic structure.[232] In aqueous dispersions, the surfactant molecules are adsorbed to the surface of the nanosheet via London dispersion interactions with the non-polar tail group. There is a subsequent electrostatic interaction of the polar head group, oriented outwards, with surrounding water molecules. Due to the amphiphilic nature of the surfactant, they allow for the solubility of non-polar compounds that may not otherwise be soluble in water.

Surfactants can be classified into three types based on their ionicity; anionic, cationic and non-ionic. Anionic surfactants have a positively charged head group (e.g. Na^+) while cationic surfactants have a negatively charged headgroup (e.g. Br^-). Non-ionic surfactants don't have a charged group but stabilise nanosheets physically through steric hindrance. Each surfactant type will self-assemble on a hydrophobic surface in individual monomers at low concentration. At a certain point, known as the critical micelle concentration (CMC), any additional molecules form micelles (aggregates), leaving the monomer concentration more or less unchanged at this point.[233] The formation of micelles is energetically favourable, minimising the interaction between the hydrophobic tail and solvent.[232] As the concentration increases beyond the CMC, both the average size and number of micelles increases.[234] Each surfactant has a different critical micelle concentra-

tion that changes with temperature and pH.

A representative nanosheet coated by surfactant molecules adsorbed via tail group is displayed in Figure 2.9. At room temperature, the surfactant is assumed to be dissociated/ionised. The positive head groups are repelled from the negative tail groups, bound to the nanosheet surface, via Brownian motion. These head group ions (e.g. Na^+) are so called mobile counterions that diffuse through solution. However they remain close to the nanosheet because of the attractive force pulling them back to the oppositely charged tail groups. As stated above, the sign of the counterions depends on the head group of the surfactant, anionic surfactants such as sodium cholate have a positive Na^+ counterion while cationic surfactants such as cetyltrimethylammonium bromide (CTAB) have a negative Br^- counterion. An environment is maintained around the nanosheet called the electrical double layer (EDL). First modelled by Helmholtz[235] and then superseded by Gouy,[236,237] Chapman[238] and Stern,[239] the EDL consists of a layer of strongly held counterions adsorbed close to the oppositiely charged surface followed by a diffuse layer of mobile counterions, analogous to a parallel plate capacitor model.[232,233] The thickness of this potential layer is known as the Debye length (Equation 2.13), κ^{-1} as seen in Figure 2.9. More commonly used and measured is the zeta potential ζ, a value for the electric potential at the edge of the bound ions. The theory and instrumentation of zeta potential is discussed in more detail in Section 3.2.7. Each nanosheet in a dispersion will be electrostatically repelled from each other as a result of charged surfactants adsorption.

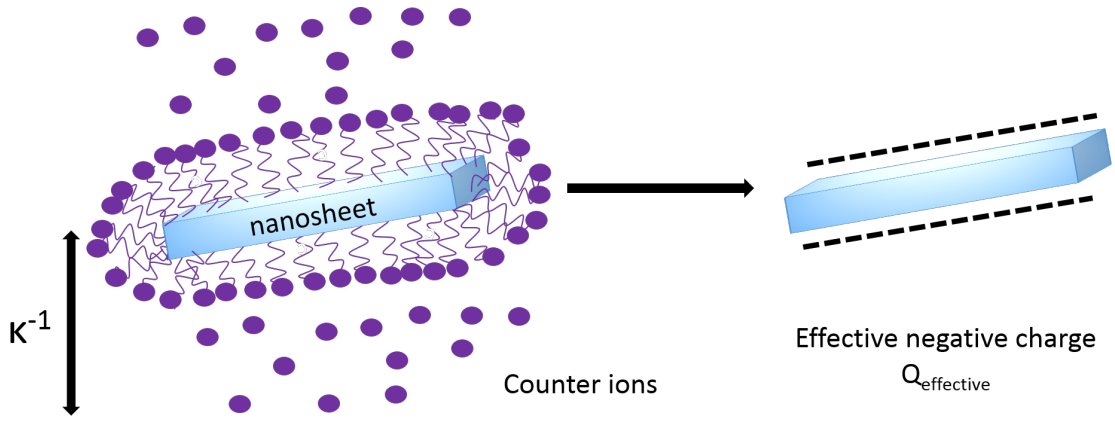

Figure 2.9: A surfactant coated nanosheet forms a diffuse double layer: bound negative effective charge with a diffuse double layer of positive counterions. The Debye length κ^{-1} is a measure of the thickness of mobile counterions from the charged surface.

The physics behind the electrostatic behaviour of particles in solution can be described by DLVO theory. Pioneered by Derjaguin and Landau (1941),[240] and Verwey and Overbeek (1948)[241] it combines both the attractive van der Waals and repulsive double layer interactions. For nanosheets to be dispersed evenly in solution and not reaggregate, the repulsive force must be greater than the attractive force. The total potential energy will be a sum of the attractive and repulsive interaction energies[232]

$$V_T = V_{rep} + V_{vdW} \tag{2.10}$$

All particles are attracted to each other via van der Waals forces. These forces are a result of fluctuating dipoles in atoms or molecules. The attractive interaction potential of two surfactant coated nanosheets can be derived[190] similar to that of Hamaker[242] for two spheres. The total attractive interaction energy, V_{vdW} is given by

$$V_{vdW}(D) = -\frac{A\pi\rho^2 C}{2D^4} \tag{2.11}$$

where A is the sheet area, ρ is the number of atoms per unit area in a sheet, D is the separation distance and C is a constant from the van der Waals potential V= -C/r^6. It can be shown[190] that $\rho^2 C$ can be related to the van der Waals minimum separation distance between two sheets (d_0) and the surface energy (γ) of the material such that

$$\rho^2 C = -\frac{2d_0^4\gamma}{\pi} \tag{2.12}$$

Using BN as a model material (Chapter 4), d_0 is approximately 0.33 nm[243] and $\gamma \approx 50$ mJ/m^2,[244] $\rho^2 C$ is estimated to be 3.77 $\times 10^{-40}$ J m^2. This is a rough estimation due to the fact that the surface energy of BN is the value for vacuum rather than liquid where van der Waals interactions may be screened.

The repulsive component of the total potential, from DLVO theory, takes into account the potential of the bound ions at the nanosheet surface as well as the Debye length κ^{-1}. Firstly, the Debye length κ^{-1} needs to be defined as a measure of the thickness of mobile counterions from the charged surface, largely dependent on the properties of the liquid and given by[233,245]

$$\kappa^{-1} = \left(\frac{\varepsilon_r \varepsilon_0 kT}{2e^2 n_0}\right)^{1/2} \tag{2.13}$$

where ε_r is the dielectric constant of dispersing liquid, ε_0 is the vacuum permittivity, k is Boltzmann's constant, T is temperature, e is electron charge and n_0 is the number of surfactant molecules per volume. Sodium cholate (SC) is taken as a model surfactant, used in Chapters 4, 5 and 7. Estimating the number of SC surfactant molecules per m^3, n_0 (using C_{SC}= 2 g L^{-1}), to be 2.8 $\times 10^{24}$ molecules m^{-3} and ε_r = 80, at room temperature the Debye length is calculated to be 4.52 nm. The Debye length will clearly change with each surfactant and concentration used for exfoliation.

The repulsive potential V_{rep} accounts for the electrostatic repulsion between charged nanosheets, multiplied by 2 for two nanosheets charged on both sides, given by[233,246]

$$2V_{rep}(D) \approx 4A\varepsilon_r\varepsilon_0\kappa\zeta^2 e^{-\kappa D} \tag{2.14}$$

This expression is strictly valid for low zeta potential values of $|\zeta| < 25$ mV.[233] However it gives a good approximation for the general behaviour of colloidal dispersions and as with the attractive potential is a rough, numerical estimation. The addition of both the attractive (Equation 2.11) and repulsive (Equation 2.14) potentials gives the overall potential interaction energy per unit area of two parallel nanosheets $V_T(D)$ as

$$\frac{V_T(D)}{A} \approx 4\varepsilon_r\varepsilon_0\kappa\zeta^2 e^{-\kappa D} - \frac{\pi\rho^2 C}{2D^4} \tag{2.15}$$

A graphical representation of this expression is displayed for a BN-sodium cholate model system in Figure 2.10 below for increasing zeta potential. The estimations calculated above are used to add function plots (with the interaction energy, V_T/A, as a function of separation distance, D) on the graph where parameters are as follows: $\rho^2 C$ = 3.77 $\times 10^{-40}$ J m^2, n_0 = 2.8 $\times 10^{24}$ molecules m^{-3}, ε_r = 80 at room temperature, the Debye length κ = 4.52 nm.

As the nanosheets come closer together they are repelled from each other due to the rising potential barrier $V_{T,max}$. If they have enough energy to overcome the barrier they will fall into a deep potential well and never separate, a term known as coagulation. As seen in the graph for lower zeta potentials, the barrier is lowered. At $|\zeta| < 20$ mV, the barrier falls so low that there is a net attraction between particles rather than a repulsion and so the nanosheets stick together.

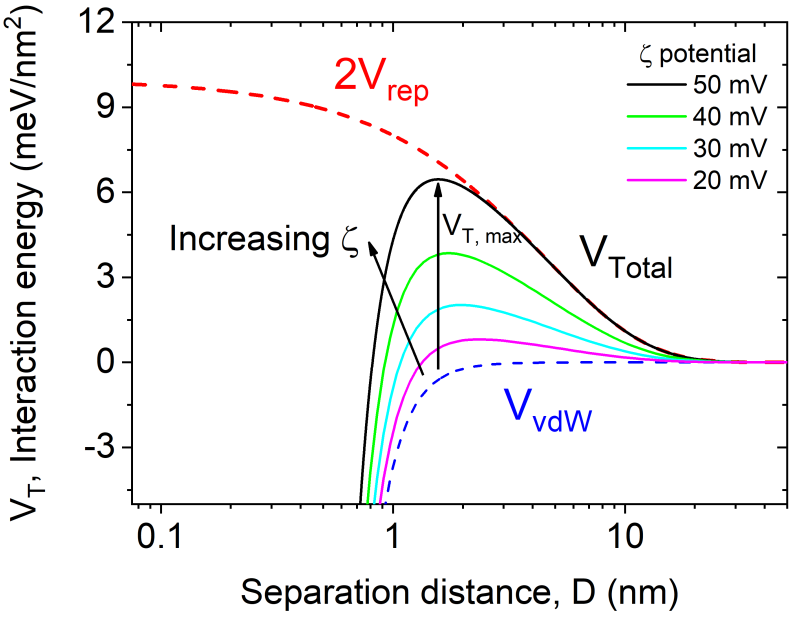

Figure 2.10: DLVO theory model of liquid phase exfoliated BN nanosheets in sodium cholate surfactant solution. A plot of total interaction energy per unit area for two nanosheets as a function of their separation distance with increasing zeta potential ζ. The repulsive double layer potential (dashed red line, equation 2.14) and attractive van der Waals potential (dashed blue line, equation 2.11 are also plotted separately. Equation 2.15, a combination of the attractive and repulsive potentials, was plotted using the estimations of parameters for BN-SC system described above for a number of zeta potential values. Based on previous work by Lotya et al.[190]

The ideal system is one in which this barrier height is large so the nanosheets remain stable in a dispersion. A zeta potential of $|\zeta| > 30$ mV is considered to be a stable dispersion.[190] This is achieved by changing the surfactant type and concentration which will alter the values for n_0 and ζ. Since the Debye length is a function of n_0, a lower κ^{-1} will result in lower barrier height as counter ions are closer to the bound ions adsorbed to the nanosheet, negating the repulsion they experience. DLVO theory only holds for electrostatic interactions present when using ionic surfactants. Non-ionic surfactants will also stabilise nanosheets by producing steric barriers to aggregation.

In this chapter layered materials were reviewed including an analysis of their properties and structure. An overview of various production methods of 2D materials was given, describing both bottom-up and top-down approaches. In particular, liquid phase exfoliation and nanosheet stabilisation were explained in further detail as the primary production method of nanomaterials in this work.

3

Machines take me by surprise with great frequency.

–Alan Turing

Methods and Characterisation

***

THIS CHAPTER OUTLINES THE PRODUCTION AND characterisation methods used in this thesis to exfoliate the layered materials described previously. The main production method of nanomaterials in this work is liquid phase exfoliation via ultrasonication and centrifugation of layered crystals. The resulting dispersions are then characterised using a variety of material characterisation tools including UV-Visible and Raman spectroscopy, atomic force, transmission electron and scanning electron microscopies and electrophoresis. The combination of multiple characterisation techniques aims to give a comprehensive picture of the material's physical and electronic structure, nanosheet size, defect content, stability and level of oxidation. Each technique utilised in this work, from production to characterisation, is examined in more detail below. Photographs of the experimental setups and equipment used can be found in Appendix A.1.

3.1 Production of 2D Materials

3.1.1 Sonication

Ultrasonic energy is used to exfoliate bulk crystals and form two-dimensional nanosheets that are stabilized through solvent or surfactant interactions. Conventional power ultra-

sound has a frequency range of 20-100 kHz, above human hearing which is between 16 Hz and 18kHz.[247,248] In LPE, an ultrasonicator probe is immersed in a liquid mixture containing the bulk crystal and stabilizer. As the ultrasound wave propagates through the liquid medium bubbles are created, a phenomenon known as acoustic cavitation. Cavitation occurs when periodic expansion and contraction cycles caused by the wave produces a negative pressure, pulling the molecules apart and creating voids commonly known as bubbles.[247–249] A schematic of bubble formation and collapse is shown in Figure 3.1. After formation, the bubble undergoes volume oscillations due to time varying local sound pressure.[250] The bubble increases in size until it reaches a point where it can no longer absorb the energy and it violently collapses, with enough energy to exfoliate crystals into nanosheets. The localised temperature at the point of collapse has been reported to reach 5000 °C along with an extremely high pressure of 2000 atm.[251] The bubbles are small compared to the total volume of liquid so this heat is quickly dissipated and does not affect the overall environment significantly. Cavitation is sometimes known as cold boiling due to this very fact. The rate of localised cooling is estimated to be around 10^{10} °C s^{-1}.[251]

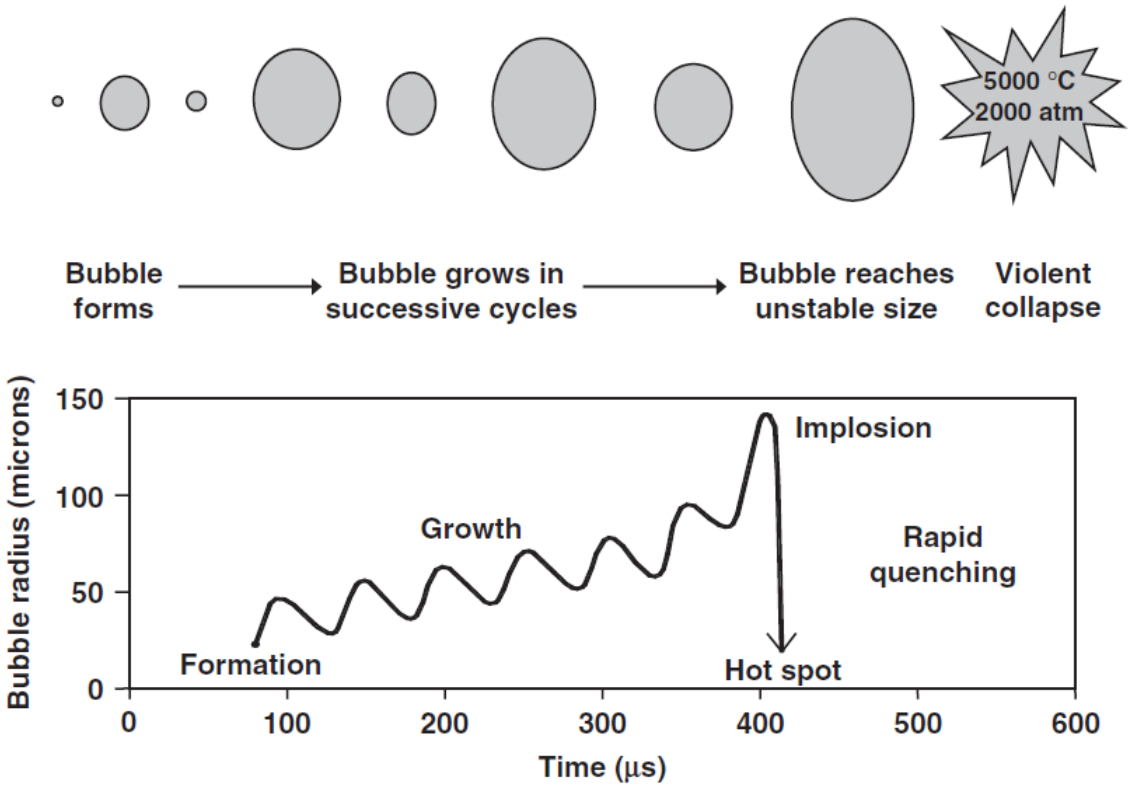

Figure 3.1: Cavitation bubble formation and collapse pictured schematically as a function of time. Image from Luque de Castro and Capote[247]

There are many factors that influence cavitation including the solvent viscosity, temperature, applied frequency and intensity. An increase in viscosity means the cohesive forces binding the liquid are stronger, raising the threshold for cavitation.[247,252] In contrast, the cavitation threshold has been reported to decrease with increasing temperature as a result of the rise in vapour pressure from heating a liquid.[247] The sonication intensity is proportional to the source vibration amplitude squared so in general increasing the intensity will increase sonication effects. However this is limited by the amount of energy the system can take. The cavitation bubble size is dependent on the pressure amplitude and so intensity cannot be increased indefinitely.[247] Moreover, at high frequencies (>20 MHz) cavitation becomes increasingly difficult because the intensity must be increased to ensure the voids (bubbles) are formed.[249] At very high frequencies the compression and expansion cycle becomes so short that the molecules of the liquid can no longer create these voids and no cavitation occurs.

Figure 3.2: Image of a Sonics® VibraCell VCX 750 ultrasonic processor used for liquid exfoliation.[253]

A Sonics® VibraCell VCX 750 ultrasonic processor was used for exfoliation in this thesis, pictured in Figure 3.2 above. The mains voltage is converted to high frequency electrical energy (20 kHz) through a generator. A piezoelectric ultrasonic converter then transforms the electrical energy into mechanical vibrations at a fixed amplitude. A standard horn

probe attached to a booster horn transmits the ultrasonic energy to the sample at magnified power intensity.[249] The intensity is dependent on the shape of the probe. A tapered probe was also used in this thesis for small volume samples (<30 mL). An ultrasonic probe applied at a high power and frequency to a liquid will increase its temperature. As discussed above, cavitation is most effective at low temperature. Furthermore, increasing the temperature of nanosheets may cause degradation effects depending on the material. Photoluminescence may be quenched at high temperatures,[20] problematic for many future applications. To combat these potential effects, the sample is placed in an ice bath or chilled jacketed beaker while sonicating to ensure the rapid dissipation of heat. In addition to cooling techniques, the ultrasonic processor is set to pulse mode where the amplifier switches the power on and off repeatedly to avoid increasing temperatures.[249] A standard sonication time (t) is 5 hours with a pulse of 6 seconds on and 2 seconds off. The concentration of nanosheets produced has been founded to scale with $t^{1/2}$,[24,196] while there is no considerable change in mean nanosheet dimension (Appendix A.6). A trade-off is made between the power and time costs versus the concentration produced.

3.1.2 Centrifugation

Centrifugation, although most widely used in biological sciences, is a method employed in this work to separate nanosheets in a liquid dispersion based on size. The principles underlining the technique are based on sedimentation theory, describing the movement of particles in a viscous medium in a gravitational field.[254,255] Sedimentation theory assumes a spherical structure and so should not strictly hold for 2D nanosheets. As a first approximation however, it should roughly describe the behaviour, given that, to date, there is a lack of studies completed on the sedimentation of 2D systems. A particle in solution experiences three forces; gravitational (F_g), buoyancy (F_B) and frictional drag (F_D) as shown with their respective equations in Figure 3.3 where d=particle diameter, ρ_p= particle density, ρ_l=liquid density,μ= liquid viscosity, v= sedimentation velocity and g=gravitational force.[255]

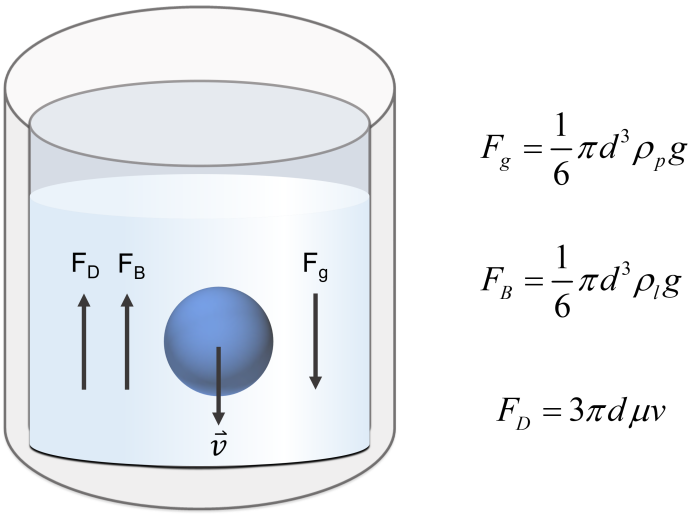

Figure 3.3: Forces acting on a particle suspended in a fluid, used in sedimentation theory, the basis of centrifugation.

The net force on the particle is equal to the force resisting its motion through the liquid if the particle reaches a constant terminal velocity (v_T) and so

$$\frac{1}{6}\pi d^3(\rho_p - \rho_l)g = 3\pi d\mu v_T \tag{3.1}$$

Rearranging equation 3.1, gives the terminal velocity v_T as a function of all other parameters, one of the most common in sedimentation studies

$$v_T = \frac{d^2(\rho_p - \rho_l)g}{18\mu} \tag{3.2}$$

It is clear that sedimentation depends on the difference in densities between the particle and liquid but also the particle diameter and liquid viscosity. A particle will sediment if $\rho_p > \rho_l$ and will float if $\rho_p < \rho_l$, since v_T becomes negative. In general, there is not much of a difference between liquid and particle densities and so the particle diameter is the most important factor in sedimentation.[255]

Centrifugation increases the magnitude of the gravitational field by spinning a tube containing a dispersion about a fixed axis at very high speeds (Figure 3.4). This greatly accelerates any natural sedimentation process that may occur or forces one that might not otherwise under Earth's gravitational field. The particles experience a radial centrifugal

force of magnitude F such that

$$F = m\omega^2 r \tag{3.3}$$

where m is the effective particle mass, ω is the angular velocity and r is the distance of the particle from the axis of rotation. This force is usually expressed relative to Earth's gravitational force called the relative centrifugal field (RCF), given in terms of *g* units. RCF can be interchanged with the instrumentation standard RPM (revolutions per minute) through

$$RCF = 1.18r\left(\frac{RPM}{1000}\right)^2 \tag{3.4}$$

where r is the rotor radius in cm. The sedimentation rate of a particle per unit of centrifugal force is known as the sedimentation coefficient, S, with units of seconds given by[256,257]

$$S = \frac{v_T}{a} = \frac{v_T}{\omega^2 r} = \frac{2d(\rho_p - \rho_l)}{18\mu\omega^2} \tag{3.5}$$

where a is the acceleration provided by the centrifuge. Normally a sedimentation coefficient is expressed in Svedberg units (S) where 1S=1×10^{-13} s.[255] Equation 3.5 is used for spherical particles but this equation can be modified to account for arbitrary shapes[256] by applying a frictional coefficient term, f/f_0

$$S = \frac{2d_{equiv}(\rho_p - \rho_l)}{18\mu\omega^2}\left(\frac{f}{f_0}\right)^{-1} \tag{3.6}$$

where the diameter, d_{equiv} is the diameter of a sphere of equivalent volume. The frictional coefficient term, f/f_0, for an arbitrary shape is estimated numerically and describes the translational hydrodynamic friction on rigid Brownian particles, first described by Hubbard and Douglas.[258] f is the frictional coefficient of the arbitrary shape while f_0 is the frictional coefficient of a sphere of equivalent volume. The authors note that the frictional contribution increases as particles are distorted further from symmetric shapes.

When LPE nanosheets are centrifuged, large and thick nanosheets will sediment out at a faster rate and a lower centrifugal forces while small, thin nanosheets will remain in the liquid dispersion in line with equation 3.5. The pellet or mass formed at the bottom of the vial after centrifugation is known as the sediment while the remaining liquid containing smaller nanosheets is the supernatant (Figure 3.4). The liquid viscosity also has an effect on the sedimentation rate and therefore depending on the solvent or aqueous sur-

factant solution used, the size distribution of nanosheets in sediment may change slightly. Typically nanosheets in this work were centrifuged between 25 and 32,000 *g* in standard bench-top centrifuges however, an ultracentrifuge was also used with an RCF of 270,000 *g*.

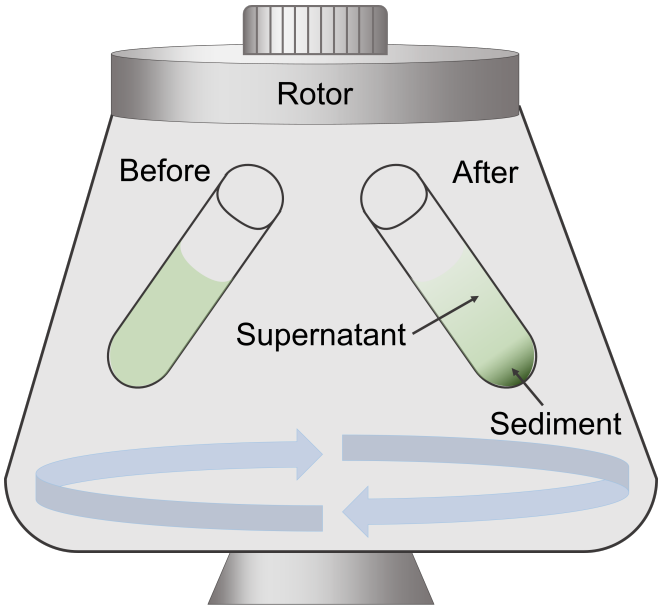

Figure 3.4: Schematic of a standard centrifuge, vials are spun about a fixed axis in a rotor at high speeds. The sediment will contain large particles while small particles remain in the supernatant.

Ordinarily, an LPE dispersion will be centrifuged at least twice after sonication to produce what is known as a standard sample. Large unexfoliated material is removed in the first step by centrifuging at low speed (26 *g*) and discarding the sediment. The supernatant is subject to further centrifugation at a high speed (2600 *g*). The sediment after the high speed step contains nanosheets with the unwanted bulk material removed. The supernatant generally consists of very small nanosheets ($<$ 50 nm) and ionic impurities. The sediment is known as a trapping and labelled by the lower and upper bounds of centrifugation, for example 0.026-2.6k *g* for the scenario described above. Relative centrifugal force, expressed in terms of earth's gravitational field, *g*, is an important parameter used to express the centrifuge speed of a trapped sample. It is taken to be the midpoint between the lower and upper bounds of the sample, for example the RCF of the 0.026-2.6k *g* sample would be 1.313 k *g*.

Liquid cascade centrifugation[20] is a variation in which an LPE dispersion is subject to

increasing centrifugation speeds to select narrow fractions decreasing in both lateral size and thickness as shown schematically in Figure 3.5 above. The smaller the step in centrifugation speed, the narrower the resultant size distribution will be. Typically samples are selected in 1000 rpm increments. In general, multiple sizes are selected by performing an 8-10 step cascade of increasing centrifugation speed however the user has an option to produce a specific size distribution by trapping the desired nanosheets between just two fixed speeds. Various secondary cascades can also be performed to increase the monolayer population in a dispersion[20] or to decouple the lateral size and thickness relationship as discussed in Chapter 4.

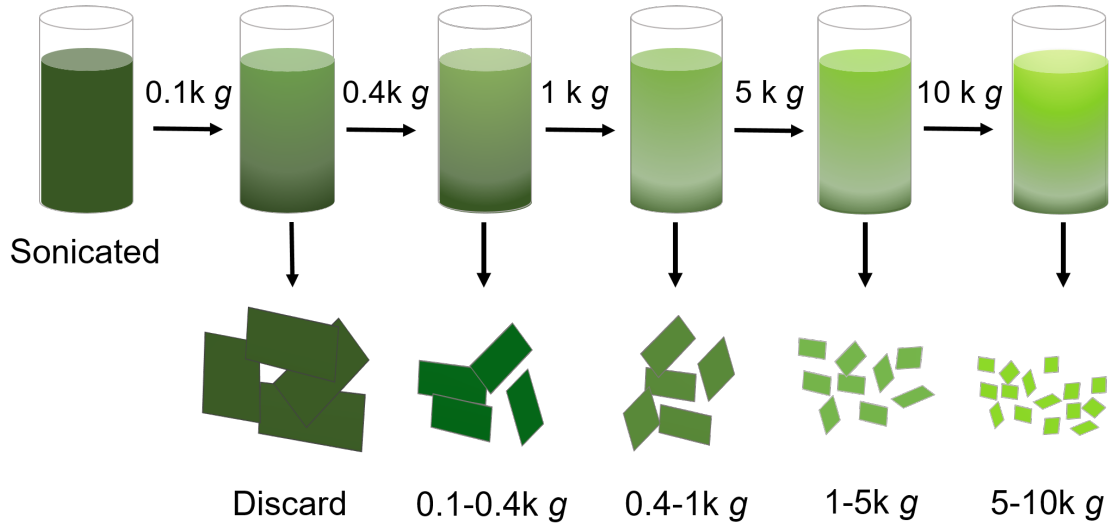

Figure 3.5: Schematic of of Liquid Cascade Centrifugation (LCC). A dispersion is subject to iteratively higher centrifugation speeds so that narrow distributions can be selected with decreasing size nanosheets.

There are a number of advantages to this technique, and to centrifugation in general. Firstly, the sediment can be redispersed in a range of liquid environments, not just its sonication medium, offering flexibility in further processing. Moreover, the volume of liquid for redispersing is entirely user dependent and so the concentration of nanosheets can be easily altered. Finally there is very little material wasted in cascade centrifugation and so relatively large masses of size-selected nanosheets can be obtained. An example of the range of mean lateral sizes and layer numbers of nanosheets obtained in a standard cascade can be seen in Figure 3.6A and B respectively below. The mean lateral size and thickness measured by statistical microscopy is plotted as a function of the relative cen-

trifugal force, the midpoint between the lower and upper bounds of each trapping in the cascade.

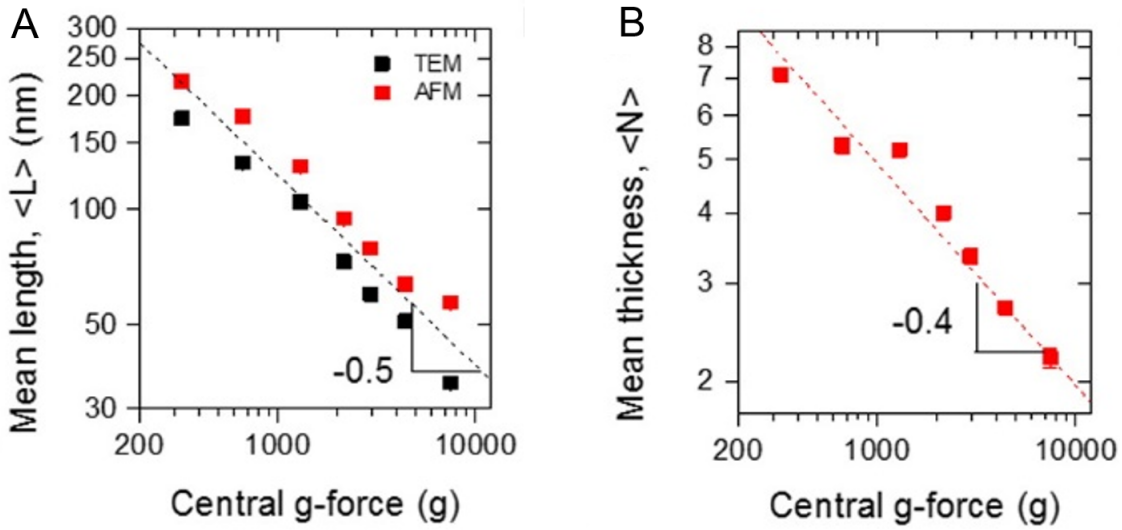

Figure 3.6: Examples of the range of (A) lateral size and (B) nanosheet thickness plotted for relative centrifugal force (RCF, in *g*) obtained from a standard LCC cascade of WS_2 nanosheets in sodium cholate. Image adapted from Backes et al.[20]

3.2 Characterisation of 2D Materials

3.2.1 Optical spectroscopy

The interaction of light with matter is one of the most fundamental characterisation techniques and especially useful for probing colloidal samples such as LPE nanosheet dispersions. As a beam of light travels through a medium, the intensity can change as a result of absorption and scattering processes that are characteristic of the material under examination. The energy input by the incident light can supply a molecule with enough energy to be excited from its ground state to a higher energy state. One would therefore expect any transition to appear as a very narrow spectral line. However, if molecules are sufficiently close together (high concentration), they can impact each other's energy levels in such a way there is a loss of fine structure that blurs any sharp spectral lines into bands (peak broadening).[259] Moreover, solute-solvent interactions can also increase the broadening of absorption bands.[260] Characteristic electronic transitions at specific wavelengths give important insights into the chemical makeup of a material and are studied throughout this

thesis.

A dual spectrophotometer was used for work carried out, a schematic of which is represented in Figure 3.7 below. Two light sources are used to cover the entire UV-Visible range, a deuterium lamp for low wavelengths 200-400 nm and tungsten lamp for the visible and near-IR wavelengths (400-1500 nm). The emitted light travels through a filter and monochromator to select a narrow waveband from the continuous source. The monochromator is series of slits, diffraction gratings and curved mirrors, producing a parallel beam through a single exit slit. Ideally, a monochromator would select a single wavelength i.e. monochromatic light, however instrumental limitations mean that a narrow range of wavelengths is output, defining the spectral resolution of the spectrometer. The narrower the slit, the higher the spectral resolution but at a cost of increased measurement time. The beam then passes through a beam splitter (chopper) that switches the beam between reference and sample cuvettes several times per second, correcting for changes in lamp intensity. The absorbance of the sample is measured by comparing its intensity output to that of the reference output.[260] This absorbance is detected using an InGaAs photodiode. When the light strikes the semiconducting material, the charge in embedded capacitor(s) is depleted. The amount of charge required to recharge the capacitor(s) is proportional to the light intensity and this variation in intensity is recorded as absorbance.[260]

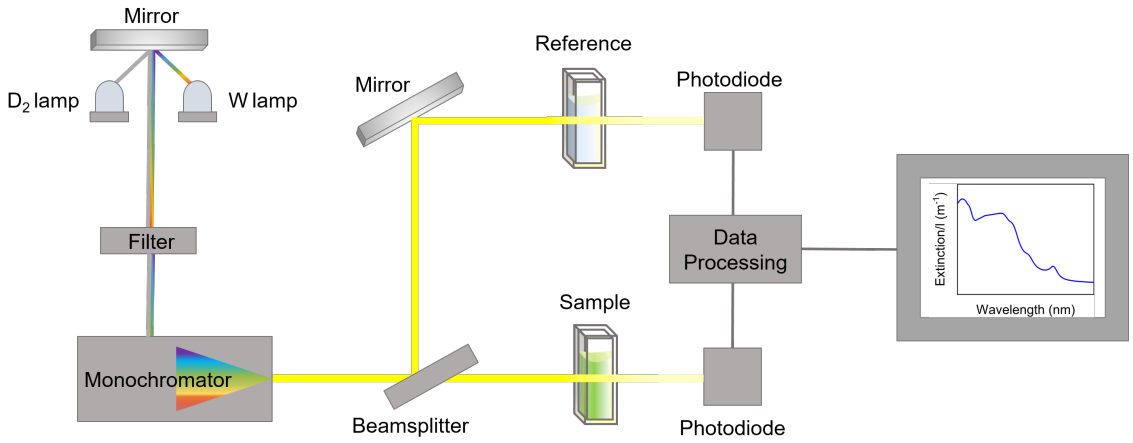

Figure 3.7: A schematic of a standard dual-beam spectrophotometer used.

The transmittance T (the light that has passed through the sample without being absorbed or scattered) can be related to the extinction via $T=10^{-Ext}=I/I_0$, where I is the output

intensity and I_0 is the initial intensity of the beam. As a beam of light travels through the sample, its intensity decreases due to absorption and scattering. This increase in absorption is detected by the spectrometer. The Beer-Lambert law[37,261] is used to relate the absorbance to the concentration of a sample. The change in intensity when light, dI passes a given thickness of a material, dl is proportional to the concentration of the absorbing species, C, the input light intensity, I, and the thickness of the layer such that

$$\mathrm{d}I = -\kappa C I \mathrm{d}l \tag{3.7}$$

where κ is a material-dependent constant. Rearranging equation 3.7 and integrating over the thickness of the sample, the output intensity that emerges from a sample of thickness l, can be estimated as

$$\int_{I_0}^{I} \frac{\mathrm{d}I}{I} = -\kappa \int_{0}^{l} C \mathrm{d}l \tag{3.8}$$

Assuming the concentration is uniform across the sample, C is independent of length and so the expression becomes

$$\ln \frac{I}{I_0} = -\kappa C l \tag{3.9}$$

By converting this expression to log base 10 and letting the constant, κ=εln10, the Beer-Lambert law is given as

$$Ext = -\log_{10}(T) = -\log_{10}\left(\frac{I}{I_0}\right) = \varepsilon C l \tag{3.10}$$

where ε is the extinction coefficient, l is the path length of the cuvette and C is the concentration. Once the extinction coefficient is known, a simple extinction spectrum can be used to calculate the concentration of a given dispersion.

In practice two measurements are run in succession in the same quartz cuvette rather than using the dual beam feature to acquire both the solvent and sample at the same time. Firstly, the baseline (solvent or surfactant solution) is measured followed by a second measurement containing the sample using the same experimental conditions. The cuvette sides are wiped down after handling, between samples, to ensure that any reflectance differences from the cuvette interface are kept to a minimum. Moreover, the baseline spectrum is subtracted post measurement from the sample. It is assumed that the

reflectivities of the cuvette are similar in both measurements (air-cell wall-liquid interfaces in both cases) and therefore a subtraction of the baseline spectrum would ideally negate most of these effects, though some discrepancies cannot be ruled out.

Theoretically speaking, the extinction (ε) is a sum of the absorbance (α) and scattering (σ) of light through a sample:

$$\varepsilon(\lambda) = \alpha(\lambda) + \sigma(\lambda) \tag{3.11}$$

In general, most small molecules in liquid do not scatter light and so the extinction can be approximated as the absorbance and used interchangeably (Equation 3.11). However, this is not the case with nanosheets when the particle size is generally greater than 50 nm. An integrating sphere allows for measurement of the absorbed part of the extinction. Scattering of nanosheets can vary greatly depending on particle size, so it is vital that the scattering contribution is separated from measurements. The walls of the integrating sphere, represented in Figure 3.8 below, are fabricated with a white reflective coating. This coating reflects incident light throughout the sphere until the intensity is at a steady state i.e. the reflectance is uniform inside the sphere.[262,263] Measuring the absorbance in this way means that excitonic spectral changes with nanosheet size can be observed that would otherwise be masked by broad scattering backgrounds.

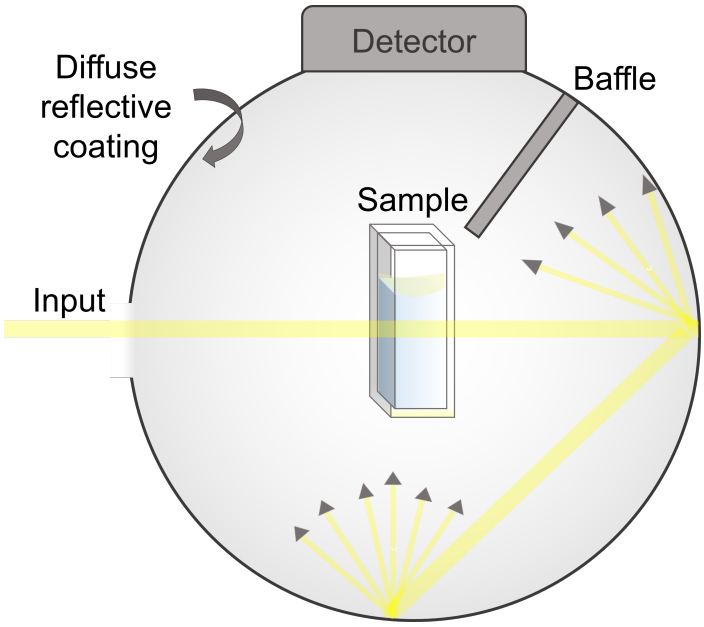

Figure 3.8: Representation of the integrating sphere, used to separate the scattering component from transmitted light.

Once the absorbance is separated from the extinction with the integrating sphere, the scattering component can then be subtracted as the difference between the extinction and absorbance spectra. Scattering effects can vary depending on particle size and until recently[264] were not well understood for LPE nanosheets. Scattering in general can be described by two regimes; Rayleigh[265] and Mie[266] scattering, represented in Figure 3.9 below. Rayleigh scattering occurs when particle size is much smaller than the wavelength of incident light ($< \lambda/10$) and light is scattered uniformly in forward and backward directions with a decrease in intensity perpendicular to the incident light (Figure 3.9A).[267] As the particle size increases, light is scattered more intensely in the forward direction, with the forward bias even further emphasized for large particles (Figure 3.9B,C).[266,267] The particles at this point are at a size comparable with the wavelength of incident light. When the particle size is much larger than the wavelength, the majority of the incident light is reflected and follows geometrical optics.[267]

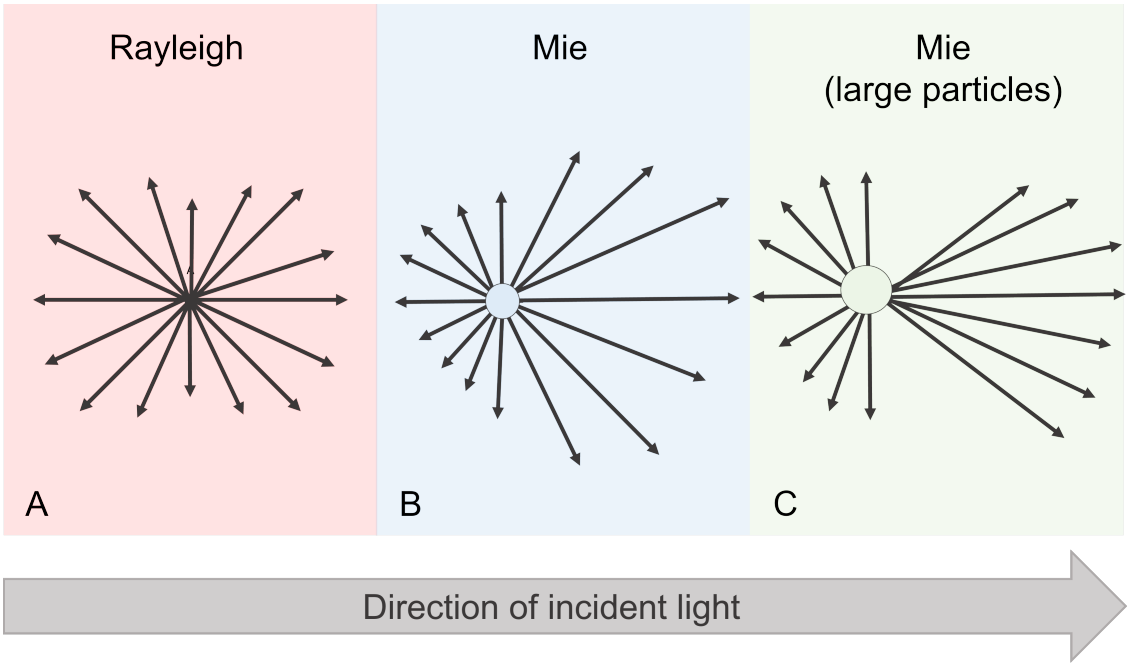

Figure 3.9: Light scattering of particles, increasing in particle size from left to right, described by (A) Rayleigh[265] and (B,C) Mie[266] theory.

LPE nanosheets generally have a broad size distribution in the range 50-1500 nm and the type of scattering measured by a spectrometer will depend both on nanosheet size and the spectral wavelength. Experimentally, scattering has been found to increase with increasing nanosheet size,[264] <L>, with the scattering coefficient, $\sigma \propto (\lambda / < L >)^{-m}$

where λ is the wavelength of light and m is what as known as the scattering exponent. As nanosheet size increases the scattering exponent transitions from m=4 to m=2 indicative of a change from Rayleigh to van de Hulst scattering, where the latter is an approximation of Mie theory for small particles described by van de Hulst.[268]

Furthermore, as a general note on the optical spectra of 2D materials, UV-Vis transmission spectroscopy is a powerful tool that gives insights to a material's structure as electrons are excited upon exposure to ultra-violet and visible wavelength light. Many layered inorganic materials have characteristic excitonic transitions[109] that can be seen in UV-Vis extinction spectra. When a layered crystal is exfoliated it undergoes a change in band structure as electrons are confined to a 2D wavefunction. Edge and confinement effects resulting from this change are visible in optical extinction spectra through the position and magnitude of excitons in layered materials.[19]

3.2.2 Raman spectroscopy

Raman spectroscopy is a technique used to examine inelastic light scattering due to molecular vibrations in a material. While UV-Vis spectroscopy measures elastic Rayleigh scattering, Raman scattering is an inelastic process i.e. the scattered radiation is at a different frequency than was originally input, an overview of which is represented in Figure 3.10. About 1 in 10^7 incident photons are scattered inelastically,[37] an inherently weak effect compared to optical spectroscopy. An incident photon induces polarization in the molecule in the form of an oscillating dipole moment as a result of its oscillating EM (electromagnetic) field.[269,270] These polarized electrons relax and radiate photons at three oscillating frequencies. The first frequency is the same frequency as the incident light (monochromatic laser),[269] an elastic process known as Rayleigh scattering. This occurs when a scattered photon transitions from a virtual state back to the ground state with no change in energy. If the collision between the incident photon and the molecule is inelastic, the scattered photon has a different energy and frequency giving rise to two types of Raman scattering.

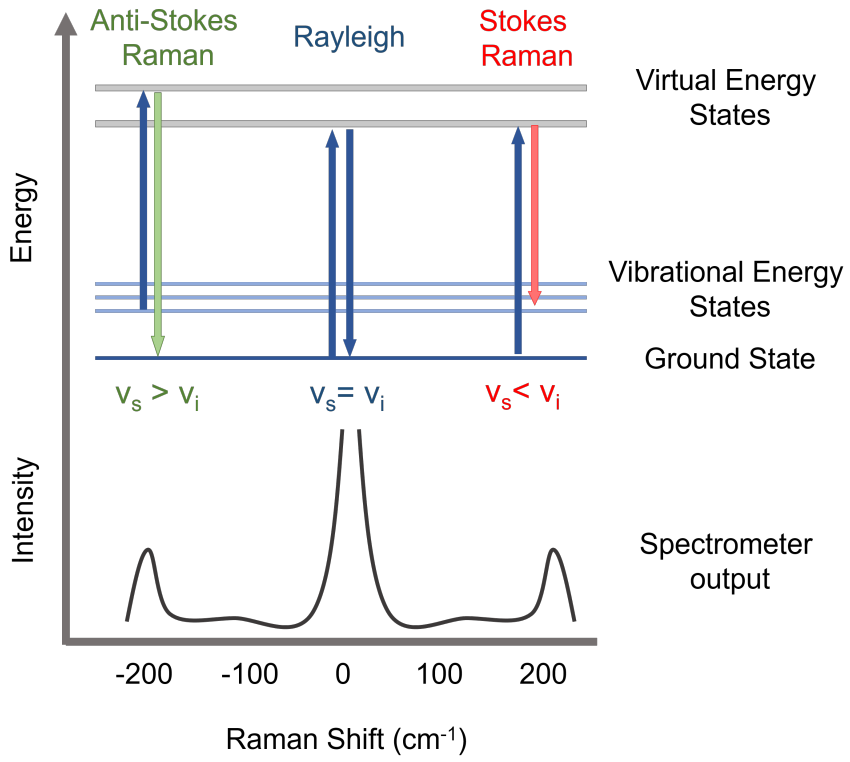

Figure 3.10: Schematic representation of Rayleigh scattering (blue) as well as Stokes (red) and Anti-Stokes (green) Raman scattering.

The Raman shift ($\bar{\nu}$) can be expressed in terms of wavenumber (inverse wavelength) as

$$\bar{\nu} = \bar{\nu}_i - \bar{\nu}_s = \frac{1}{\lambda_i} - \frac{1}{\lambda_s} \tag{3.12}$$

where λ is the photon wavelength with subscripts i and s denoting incident and scattered photons respectively. As shown in Figure 3.10, Stokes Raman scattering occurs with a transition from the ground state and terminates in the molecule in an excited vibrational state while Anti-Stokes is the opposite. In this case, the molecule is initially in an excited vibrational state and transitions to its ground state. The Stokes and Anti-Stokes peaks are symmetric about the Rayleigh peak at 0 cm^{-1} however their intensities are generally not the same with the Anti-Stokes appearing much weaker.[269] This is due to the fact that very few molecules are initially in an excited vibrational state at room temperature.[37,270] Sometimes a molecular vibration induced by a photon will not change a molecule's polarizability. When this is the case, the molecule is said to be Raman inactive and other techniques such as infrared (IR) spectroscopy may be required for characterisation. Molecular

symmetry in liquids or point group symmetry in solids determines which vibrations are Raman and IR active.[270,271]

The vibrational energy levels are unique to each molecule and so each transition is associated with a particular molecular lattice vibration, making this characterisation method invaluable for analysing 2D materials. As well as a "fingerprint" indication of chemical composition, Raman spectroscopy can be used to assess defect content, doping level, stress and sample degradation in nanomaterials.

In terms of instrumentation, a Raman spectrometer is a combination of an optical microscope, laser and series of optical mirrors, lenses and gratings. A schematic representation is shown in Figure 3.11 below. Monochromatic light is produced by a laser most commonly at 532 and 614 nm wavelengths. The laser beam is deflected by a series of mirrors to a sample placed on the optical microscope stage. In this thesis, Raman measurements were performed both on solid state samples and in liquid. For the measurement of liquid samples, the beam was focused approximately 5 μm above the surface of the droplet to minimize reabsorption and inner-filter effects.[19,198] Laser power can be adjusted depending on the sample. While high laser power leads to an increase in signal, the higher power density hitting the sample can cause thermal damage and so a balance between the two needs to be found.[269] The scattered light passes through a series of lenses, a Rayleigh filter (to eliminate dominant elastic scattering) and diffraction grating and subsequently detected. The integration time and number of spectral acquisitions can be increased to increase the quality of spectra but this both increases measurement time.

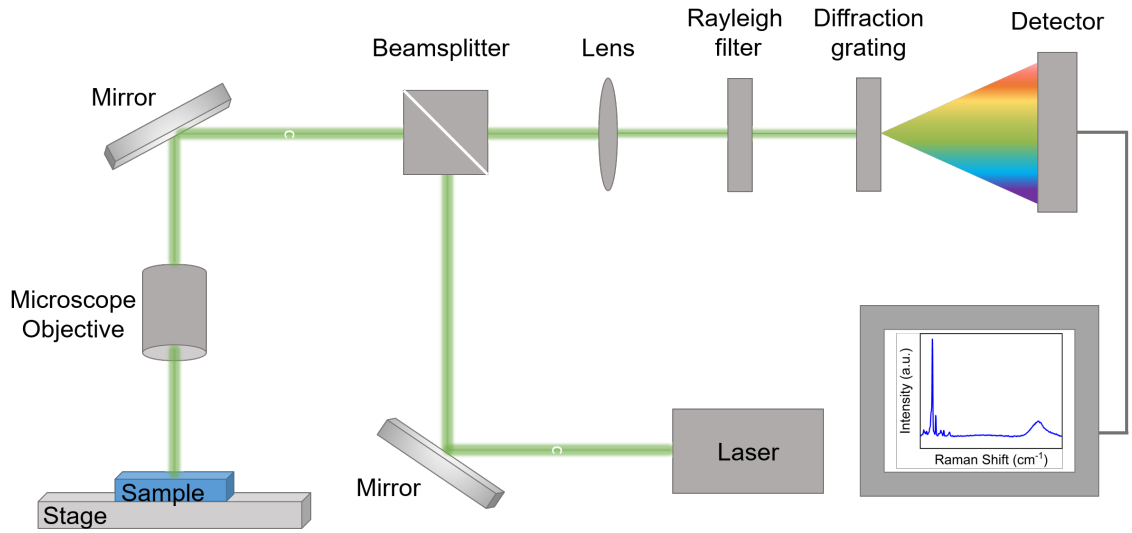

Figure 3.11: Schematic representation of a Raman spectrometer, similar to that used in this work.

3.2.3 Atomic force microscopy

First invented by Binnig, Quate and Gerber[6] in 1986, atomic force microscopy (AFM) has since become an essential characterisation tool for materials research. The technique is unique in that it probes the topography of sample, giving a three dimensional representation down to the nanoscale. Interaction forces between a sharp probe (tip) rastered across the sample surface are used to create a 3D model of the surface. AFM can be called a 'blind microscopy technique' since the surface height is measured at each point of a 2D array to create an image of the surface topography, each 'image' essentially a long list of XYZ data points.

In a standard AFM, represented schematically in Figure 3.12, a sharp tip is connected to a flexible cantilever that can bend subject to forces.[272] The behaviour of the tip and cantilever in tandem interacting with a surface is akin to a classical spring system (cantilever acting as the spring) described by Hooke's Law as

$$F = -kz \tag{3.13}$$

where F is the spring force, k is the cantilever spring constant and z is tip displacement from its equilibrium position (undeflected cantilever).[272,273] A laser beam is focused on the cantilever and reflected in a photodetector such that any deflections of the cantilever

arising from objects on the surface are recorded. In static (contact) mode this feedback is sent to the software and the piezoelectric scanner adjusts the height of the cantilever so that it remains at a constant height from the sample. The voltage required by the piezo to keep the tip-sample distance constant is converted to the sample height.[274]

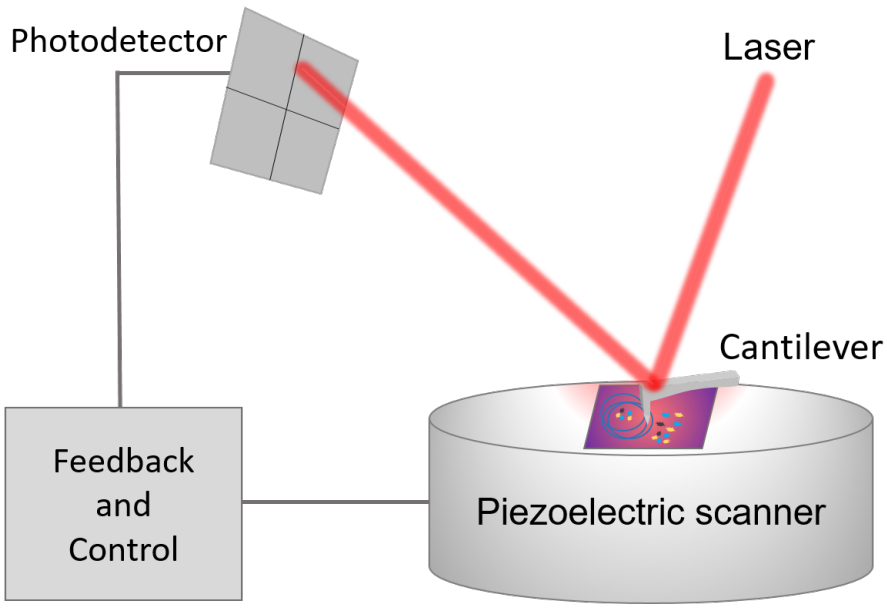

Figure 3.12: Schematic representation of an atomic force microscope, similar to that used in this work.

There are three standard operation modes in total; contact (described above), non-contact and tapping mode. All three modes are best represented on a force-distance curve that follows a Lennard-Jones potential (Figure 3.13); over short distances the forces are repulsive due to overlapping electron orbits in the form of Pauli repulsion whereas at longer distances, attractive van der Waals and dispersion forces dominate. Contact mode was the original mode in the first development of AFM and perhaps the simplest. The force-distance curve shows that contact mode is in the repulsive regime where tip-sample separation is roughly kept constant. Contact mode is best used for hard samples, not prone to distortion or degradation since the tip and sample risk being damaged by the scanning process.[272,274] However it does have the advantage in that the close contact leads to very high resolution imaging. Non-contact mode is a type of oscillating mode used for mainly for delicate biological samples. In this case, the cantilever is set to oscillate with a small amplitude at its resonant frequency. As the oscillating cantilever comes close to the sample surface, the frequency changes due to the interaction between the tip and the

surface. The feedback set up detects reductions in oscillation amplitude and frequency and sends signals to the piezo to maintain the tip at a fixed distance from the surface.[274] Tapping (intermittent contact) mode is similar to non-contact in that it is also a dynamic, oscillating mode. A large oscillation amplitude is applied to the cantilever compared with non-contact, moving back and forth between repulsive and attractive regimes with every cycle (Figure 3.13).[274] The piezo scanner reactively changes the tip to sample distance so that the amplitude of the oscillation is kept constant.[272] Due to the large oscillation amplitude the tip passes through any surface contamination (water, solvent) layer as well eliminating lateral friction forces making tapping mode perhaps the most utilised mode.[274]

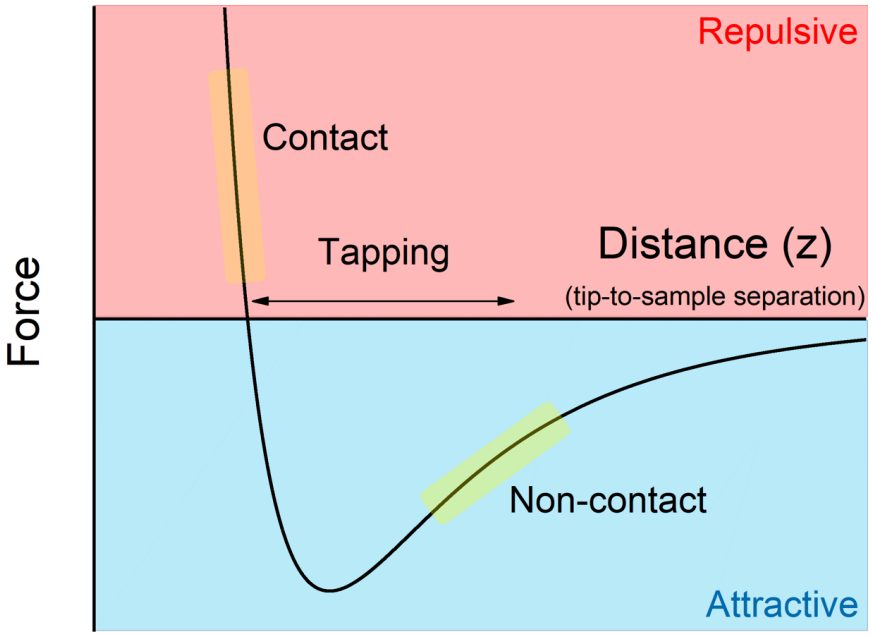

Figure 3.13: The force-distance curve can be described Lennard-Jones potential with different z ranges defining three standard AFM modes.

ScanAsyst^{TM}mode was used for the majority of the AFM imaging in this thesis, although standard tapping mode was also used. Designed by Bruker, an intelligent feedback algorithm quickly measures a force-distance curve at each pixel and adjusts the scan parameters to optimise the image in real-time. There is less user input, without the need to tune the cantilever, however parameters may still need to be monitored or changed to enhance image quality from time to time.

To measure the dimensions of liquid exfoliated nanosheets, diluted dispersions are dropcast on pre-heated Si/SiO_2 wafers ($\sim$ 15 μL). Wafers with a 200-300 nm oxide layer

are used enabling nano-sized material to be seen with an optical microscope as blue areas.[106,198] By heating the wafer to 190-210 °C (∼ 50-70 °C above the boiling point of the solvent), it immediately evaporates resulting in more uniform deposition and preventing reaggregation. During image acquisition, the field of view must be adjusted depending on nanosheet size. Ideally, the area measured should be small enough that there is minimal pixilation of nanosheets but also large enough to accumulate a sufficient number of counts. If the sample is polydisperse, both low and high magnification images are required to avoid biasing the statistics towards larger, more apparent nanosheets in wide view images.

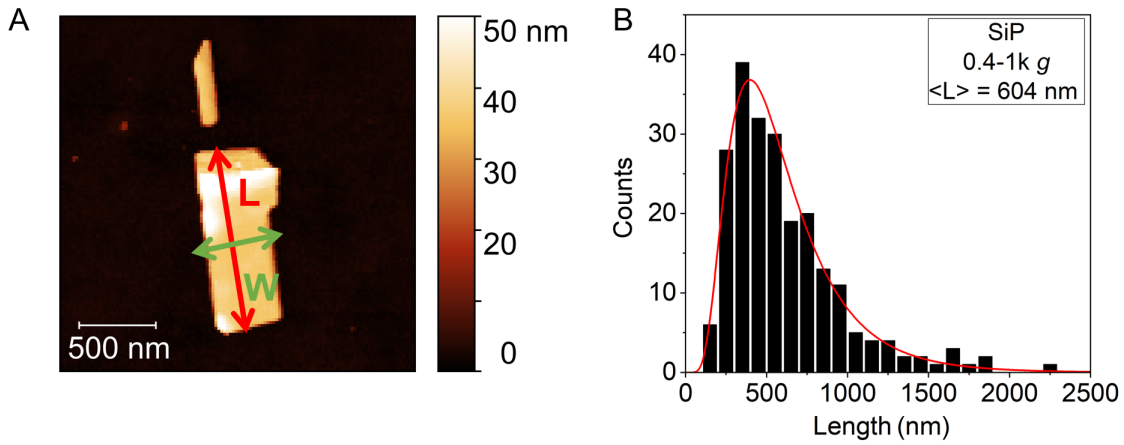

Figure 3.14: (A) AFM image of a liquid exfoliated SiP nanosheet showing the length and width measured for statistical analysis. (B) Example of a typical log-normal histogram of nanosheet length. If the histogram does not follow log-normal distribution the counting and/or imaging may be biased.

For statistical analysis of AFM images, three dimensions of each individual nanosheet are recorded: the length (taken as the longest dimension), the width (perpendicular to the length) and the thickness (Figure 3.14A). If the thickness is not homogenous, the mean value is taken. Every nanosheet in an image should be counted to avoid bias. Typically a minimum of 100 nanosheets are counted for size selected samples and a minimum of 200 for polydisperse samples to obtain a relatively accurate mean value. Once the nanosheets are counted, population distributions are represented through histograms. These histograms typically follow a log-normal shape[203] as shown in Figure 3.14B. If reaggregated nanosheets or impurities are counted or if there is biased counting by the user, a deviation from the log-normal distribution appears. Mean arithmetic values can then be

extracted from the counted data. The standard error of the mean (the standard deviation divided by the number of counts) is the error used for the mean values discussed in the thesis. The full width at half maximum of the log-normal distribution (FWHM) is also displayed for each population distribution. For a further discussion about the use of standard deviation, error and FWHM see Appendix A.3. After counting, the nanosheet thickness can be converted to number of layers through step height analysis, discussed below.

Step Height Analysis

The apparent monolayer step height is larger than the theoretical monolayer height of liquid exfoliated nanosheets due to residual surfactant and/or solvent. Through the step height analysis method, explained in detail in Chapter 4, the step height of an LPE monolayer is calculated and then used to convert the counted thickness data in terms of layer number.

Nanosheet thicknesses with terraces of partially exfoliated material are recorded and are displayed in increasing step height, an example of which is shown in Figure 3.15 for LPE MoS_2. Adsorbates, residual surfactant and water make the first layer appear thicker than the theoretical height at 1.9 nm. To confirm that this thickness correlates to a single layer, Raman/PL spectroscopy was performed on the same flakes, exhibiting characteristic photoluminescence signature of a semiconducting monolayer. It is assumed that there residual surfactant/solvent both underneath and on top of each nanosheet but it remains unclear whether adsorbates are trapped between layers.

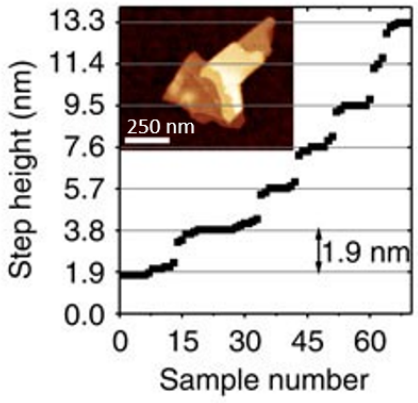

Figure 3.15: Heights of steps observed for LPE MoS_2. Inset: Example of a terraced nanosheet used. Image adapted from Backes et al.[19] The authors suggest that the step height is found to be a multiple of 1.9 nm.

Smaller steps of approximately 0.3-0.5 nm can also been seen in Figure 3.15. These may be due to user errors in counting heights or inaccuracies in the instrument while measuring. Nanosheets partially covered in adsorbates can be difficult to measure using AFM tapping mode as capillary and adhesion forces are dependent on both the scanning parameters and the material itself.[275] Image feedback settings and surface chemistry and tip-sample interactions will all play a role in the measured height. A possible alternative for future experiments would be to measure in contact mode AFM. In fact, Nemes-Incze et al.[275] have shown that the step height of graphene shows less variation using contact mode than tapping mode but a 0.2 nm change in lateral forces when scanning left to right as opposed to right to left, not present in tapping mode (Figure 3.16).

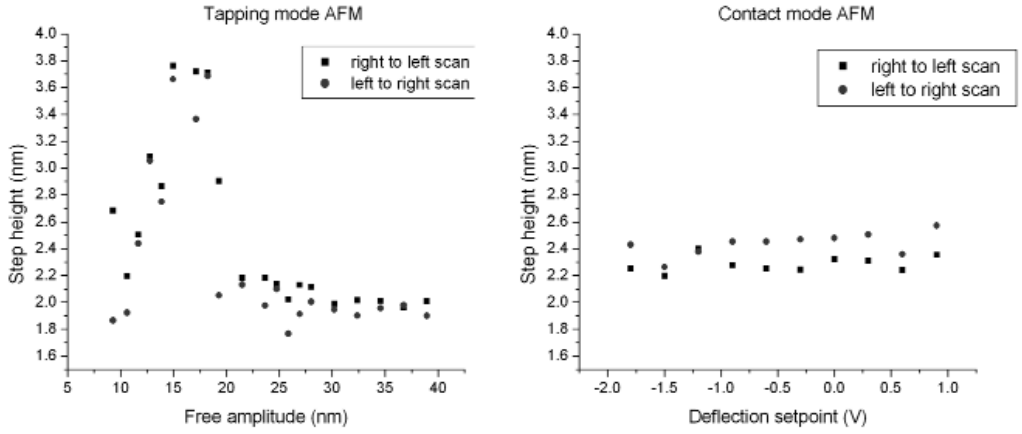

Figure 3.16: Tapping and contact modes for step height determination. Image from Nemes-Incze et al.[275] (A) Tapping mode AFM of few layer graphene gives varied step heights at different amplitudes (B) Contact mode AFM of few layer graphene shows that the step height does not depend on the contact force but lateral forces in scans from left to right and right to left differ by approximately 0.2 nm.

Another possibility for the small steps may be that while there is a thick adsorbate layer under the nanosheet (between the substrate surface and nanosheet), a near-theoretical monolayer height may be measured for any subsequent layers. If this is the case, the LPE method could in fact be preferentially exfoliating nanosheets in certain multilayers. This behaviour could be related to the intrinsic crystallographic structure of a material where different stacking sequences are predicted. For sample an energetically favourable ABC type stacking may be more stable in liquids leading to nanosheets that are multiples of trilayers.

It may however be the case that each layer in a measured nanosheet is many times thicker than the theoretical height as suggested by the authors in Figure 3.15 where the apparent height of a single layer is predicted to be 1.9 nm in height. In this scenario, trapped solvent and residues between the layers may widen the interlayer distance, making each layer appear thicker than the theoretical height by a fixed factor. This has been reported for many liquid-exfoliated 2D materials to date.[20,26,67,191,191] The step height roughly scales with the crystallographic height of these materials. Materials with a larger theoretical height have been found to have thicker step heights than those with a relatively smaller theoretical height and corresponding step height. For example, LPE GaS has a step height of 1.5 nm[191] and theoretical height of 0.75 nm[276] compared to graphene with a step height of 0.9 nm[67] and theoretical height of 0.34 nm.[277] Unfortunately, it remains unclear as to why this trend exists. Annealing samples and comparing AFM step heights may provide insights into the behaviour of adsorbates with LPE nanosheets, a possible avenue for further investigations.

3.2.4 Transmission electron microscopy

Transmission electron microscopy (TEM) is a powerful characterisation tool with the ability to generate nanoscale resolution of materials through a sample's interaction with an electron beam. Similar in operation to an optical microscope, a TEM operates using an electron beam instead of light. The resolution (d) of an optical microscope is limited by the wavelength (λ) of light and in a system is described by Rayleigh's criterion[278]

$$d = \frac{1.22\lambda}{2NA} \tag{3.14}$$

where NA is the numerical aperture, a measure of the amount of light captured by the objective. In practice, the resolution of an optical microscope is about half the wavelength of visible light , typically 250 nm.[279] In an electron microscope, the resolution is governed by the wavelength of an electron related to its momentum (p) through De Broglie's wave-particle equation

$$\lambda = \frac{h}{p} \tag{3.15}$$

where h is Planck's constant. Momentum is imparted to the electron by accelerating through a potential difference, V, resulting in a kinetic energy of eV which must equal

the potential energy[280] such that

$$eV = \frac{m_0 v^2}{2} \tag{3.16}$$

The momentum can then be equated to the electron mass times velocity and substituting v from equation 3.16

$$p = m_0 v = (2 m_0 e V)^{1/2} \tag{3.17}$$

Finally, replacing p in the De Broglie wavelength equation (3.15), the relationship between the electron wavelength and the acceleration voltage of the microscope V can be defined as

$$\lambda = \frac{h}{(2 m_0 e V)^{1/2}} \tag{3.18}$$

There is an inverse relationship between the electron wavelength and the acceleration voltage up until relativistic effects become non-negligible ($> \sim$100 keV). An acceleration voltage of 100 kV gives an electron wavelength of 4 pm,[280] extremely small compared to the light microscope. In reality, this resolution is typically 0.3 nm due to limitations of the lens system in correcting abberations. After being accelerated through an electromagnetic lens system, the electrons pass through a very thin sample. Samples need to be transparent so that they can transmit enough electrons to be detectable on the imaging screen. The electrons interact with the sample in a number of ways. Some are completely transmitted straight through to the detector while others are scattered both elastically and inelastically to produce Auger, backscattered and secondary electrons as well as characteristic X-rays of the material.[280] In addition to an image of the sample, TEM also constructs a diffraction pattern containing information on the crystal structure, dislocations and defects.

In a typical microscope (Figure 3.17) electrons are produced by an electron gun source that can be either field emission or thermionic depending on the resolution required. Higher resolution microscopes generally use field emission guns, Schottky and cold FEG are the most common. Lower resolution electron gun sources are made with thermionic materials, either tungsten or LaB_6 filament. A set of condenser lenses and apertures then focus the beam on the sample. The lenses in the system create spherical and chromatic aberrations that decrease the resolution[280,281] but can be corrected to a certain extent with multipole aberration correctors giving resolutions of around 0.1 nm.[282]

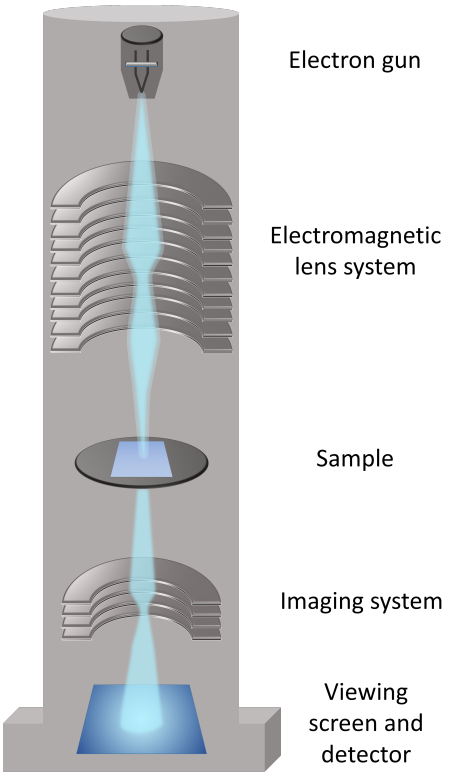

Figure 3.17: Schematic representation of a standard TEM column.

Upon striking the sample, some electrons are transmitted depending on its thickness and transparency. The transmitted beam then passes through a set of projection lenses that magnify and focus the image on a fluorescent viewing screen or detector. In standard bright-field imaging, the darker regions of the image represent areas of the corresponding sample where fewer electrons are transmitted through while the lighter regions represent sample spots where more electrons were transmitted through.[280,281]

3.2.5 Energy Dispersive X-Ray Spectroscopy

Energy dispersive x-ray spectroscopy (EDX) was performed alongside TEM for work in this thesis and was used to quantify the elemental composition of nanosheets viewed in the TEM. EDX uses the characteristic x-rays scattered when the electron beam interacts with the sample. The high-energy beam excites an inner shell electron in an atom of the specimen to a higher level, leaving a positively charged hole behind.[283] An electron from an outer shell is attracted by the hole to fill the vacancy and moves from its outer higher-energy shell to the inner lower energy shell. This transition emits energy in the form of x-rays. This energy is relative to the number of shells the electron has moved.[284] The

x-rays are converted into a voltage by a silicon drift detector. Characteristic X-rays, as the name suggests, have specific energy corresponding to each element thus the element can be identified from the peak energy measured. The amount of a certain element present in a material can be quantified through integrating the peak intensity. The emission probability of characteristic x-rays is noted to increase with increasing atomic number.[283]

3.2.6 Scanning electron microscopy

Similar to the TEM, a scanning electron microscope (SEM) utilises an electron beam to form a high resolution image. The beam energy is generally lower than TEM, operating between 2 and 5 kV and rastered across the sample surface systematically. Interactions between the electron beam and specimen are detected and used to create an image. There are two primary interactions when the electron beam scans the surface leading to two products; backscattered electrons and secondary electrons.[285] Backscattered electrons are elastically scattered electrons, experiencing negligible energy loss after being scattering and deflected by the electric fields of a sample atom. Secondary electrons meanwhile are electrons that have been ejected from the specimen atom after excitation from the electron beam. This inelastic scattering process produces electrons with very low kinetic energy, typically below 5 eV.[285] Other signals produced include Auger electrons, characteristic x-rays, and cathodoluminescence. Insulating samples develop surface electrical charge on impact with the electron beam in the vacuum of the SEM column. These samples therefore require a conductive coating so that any surface charges are dissipated through grounding.[285]

Mirroring the TEM, a thermionic electron gun with a tungsten or LaB_6 filament emits electrons in the form of a small beam that is accelerated through a magnetic field and focused by a condenser lens system. In order to form an image from a series of XY spots, the beam is rastered across the specimen surface. Scanning coils deflect the electron beam so it can scan along the x or y axis.[286] Backscattered and secondary electrons are then detected for each point scanned by their respective detectors. The signal is digitized and an image is formed. The number of backscattered electrons increases with increasing atomic number allowing for the elemental composition of a sample to be analysed through the relative intensity of signal detected.[286]

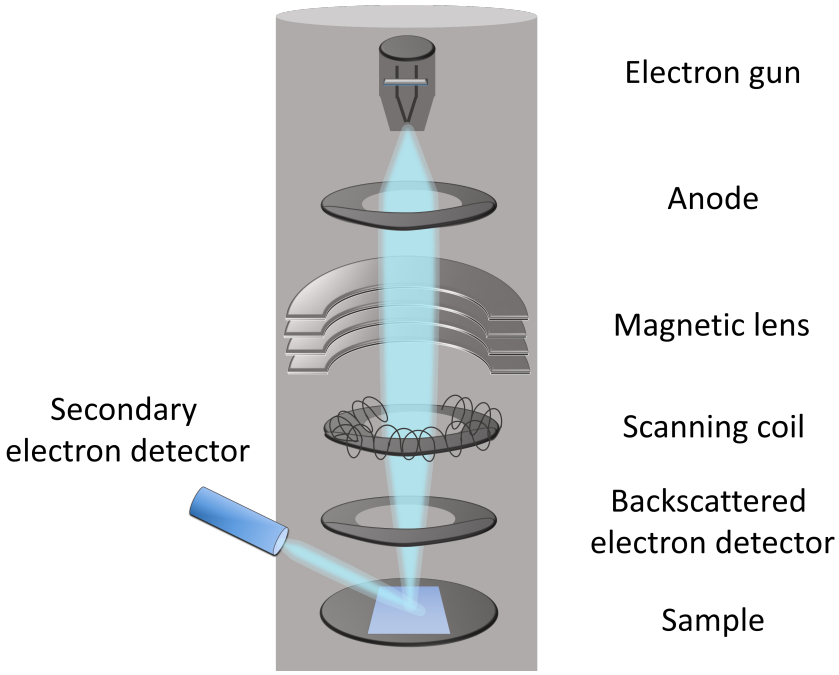

Figure 3.18: Schematic representation of a standard SEM column.

3.2.7 Electrophoresis: Zeta Potential

The zeta potential is a fundamental parameter describing electrostatic interactions in a system and gives important information of the stability of colloidal dispersions such as surfactant-stabilized LPE nanosheets. Although nanosheets themselves are neutrally charged, they gain a charge on the adsorption of ionic surfactants in dispersions in the form of an electrical double layer, as represented in Figure 3.19 below. The double layer is made up of two parts; a Stern layer and a slipping plane. The Stern layer is a layer of oppositely charged ions compared to the particle surface, bound by electrostatic forces. Beyond this is a diffuse layer of balanced ions and counterions the composition of which depends on the pH, concentration and ionic strength of the liquid.[287] Upon movement of the charged particle in an electric field, the ions within the slipping plane (outer layer) boundary move with the particle. The potential at this particle-liquid interface is known as the zeta potential (ζ),[288] represented schematically in Figure 3.19 . Nanosheets with absolute values of $>$30 mV are noted to be stable against aggregation.[289]

A Malvern Zetasizer instrument was used for the work in this thesis which measures laser Doppler electrophoresis. The zeta potential, while not measured directly, is then

estimated using a mathematical approximation. A voltage is applied across a pair of electrodes at either end of a capillary cell containing a nanosheet dispersion. A folded capillary cell is shown in Figure A.5, containing contacts to apply the voltage across the cell, and is compatible with the Malvern Zetasizer system and equipment. The sample concentration must be similar to that used for UV-Vis spectroscopy. If the concentration is too high, no scattered light is detected.[287] The movement of these charged particles in an electric field causes an incident laser beam to shift in frequency (Δf) proportional to the particle speed, scattering light at an angle θ[290]

$$\Delta f = 2v\frac{\sin(\theta/2)}{\lambda} \tag{3.19}$$

where v is the particle velocity and λ is the laser wavelength.

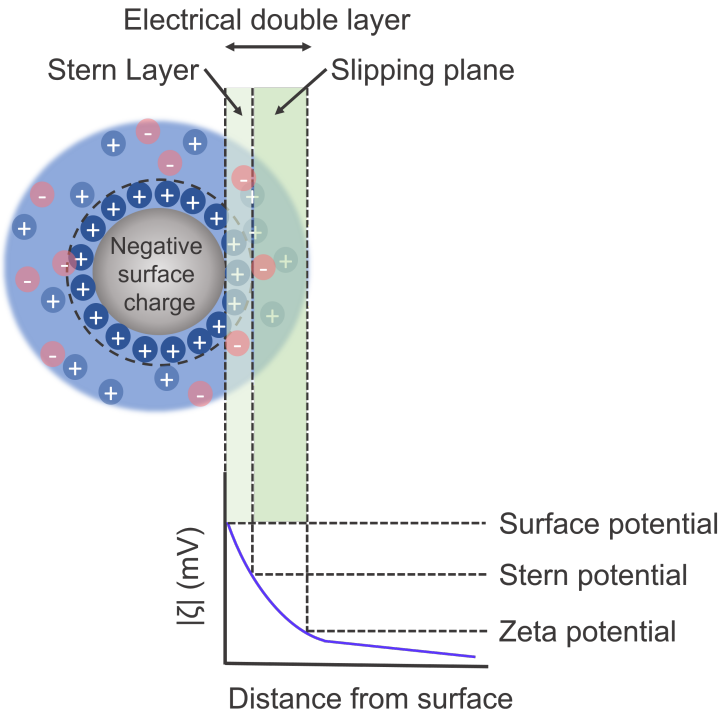

Figure 3.19: Schematic representation of the electrostatic interactions of a charged particle in a colloidal dispersion. The zeta potential is a measurement of the electric potential of a charged particle at the electrical double layer boundary.

The electrophoretic mobility μ_e is then expressed as a ratio of the particle velocity to the applied electric field E

$$\mu_e = \frac{v}{E} \tag{3.20}$$

The zeta potential is related to the electrophoretic mobility by Henry's equation[291]

$$\mu_e = \frac{2\varepsilon\zeta f(\kappa a)}{3\eta} \tag{3.21}$$

where ε is the dielectric constant, f(κa) is Henry's constant (ratio of particle radius to electrical double layer thickness) and η is viscosity. If the particle is large with a thin double layer, Henry's equation can be approximated to Smoluchowski's equation[292] for electrophoretic mobility by letting f(κa)=1.5,[287,288] giving

$$\mu_e = \frac{\varepsilon\zeta}{\eta} \tag{3.22}$$

The Smoluchowski approximation was used for all zeta potential measurements in this thesis.

In this chapter, the methods of both production and characterisation of liquid phase exfoliated nanosheets were described in detail. A discussion of ultrasonication and centrifugation showed how nanosheets are synthesised and size-selected while a variety of material characterisation tools including UV-Visible and Raman spectroscopy, atomic force, transmission electron and scanning electron microscopies and electrophoresis were described including theory, instrument operation and the specific treatment of LPE samples.

4

Basic research is like shooting an arrow into the air and,
where it lands, painting a target

–Homer Burton Adkins

Spectroscopic Metrics for hexagonal Boron Nitride

***

LPE PRODUCES NANOMATERIALS FROM A WIDE RANGE of van der Waals crystals.[18] Nanosheets can be dispersed in a range of liquid environments and can easily be transferred from one solvent or aqueous surfactant solution to another via centrifugation at high speed. Moreover, LPE samples show promise in terms of scalability and yield compared to other top-down methods. However, optical characterisation of nanosheets in dispersion through UV-Vis spectroscopy can be problematic due to a large scattering background that very sensitively depends on nanosheet size. The scattering is linked to the intrinsic extinction coefficient and so even measuring nanosheet concentration becomes difficult. In addition, LPE produces polydisperse samples with a wide range of nanosheet lengths and thicknesses. Samples can be size selected by centrifugation at iteratively higher speeds to roughly divide the original polydisperse sample into distinct size fractions. However, measuring these size fractions through statistical atomic force microscopy (AFM) is tedious and time-consuming. While optical or transmission electron microscopy will give an estimation of mean lateral size, it cannot probe nanosheet thickness. Each sample needs to be deposited on silicon substrates and statistically analysed via AFM with information on over 200 nanosheets required for an accurate representation.

By relating the optical and Raman spectroscopy to statistical microscopy information we can establish metrics as completed successfully for other 2D materials. Metrics provide a quick and facile way of estimating nanosheet dimension without the need for repeated, time-consuming microscopy.

Hexagonal boron nitride (h-BN), the material in question, has yielded much less information than other materials when using optical spectroscopy. For example, TMDs including WS_2 and MoS_2 have information-rich absorption spectra that allow for the estimation of nanosheet dimension. In contrast, the absorption spectrum of h-BN appears, on first look, to be information-poor, displaying a single peak relating to the band edge at approximately 6 eV. Similarly with Raman spectroscopy, the spectra of MoS_2 and graphene give information about defect content[54] and nanosheet dimensions.[67,293] The h-BN Raman spectrum contains a single feature (the G-band mode).[294] There have not been any connections made between this feature and any physical dimension or properties to h-BN. Cathodoluminescence is a technique that can give information about nanosheet thickness and defectiveness[295] however it isn't widely used. Furthermore, this method is highly specialised, making measurement challenging while also involving costly equipment. In this chapter, it is shown that there is significant information in both the absorption and Raman spectra. By measuring size selected h-BN samples it is found that the extinction spectra are dependent on nanosheet lateral size and that metrics can be established for the nanosheet thickness from both absorption and Raman spectra.

Hexagonal boron nitride is isostructural to graphene, alternating boron and nitrogen atoms form a hexagonal (honeycomb) lattice in the 2D plane with unit cell lattice parameter $\vec{a_1} = \vec{a_2} \approx 2.5$Å as seen in Figure 4.1 below. In-plane consists of sp^2 hybridised boron and nitrogen atoms that form strong σ bonds in contrast to the out of plane interactions consisting of weak van der Waals forces.[296,297] Although the carbon-carbon bonds in graphene are isoelectronic to the boron-nitrogen bonds in h-BN, there is a localisation of charge at the more electronegative nitrogen site leading to a more ionic type of hybridised bonds.[298]

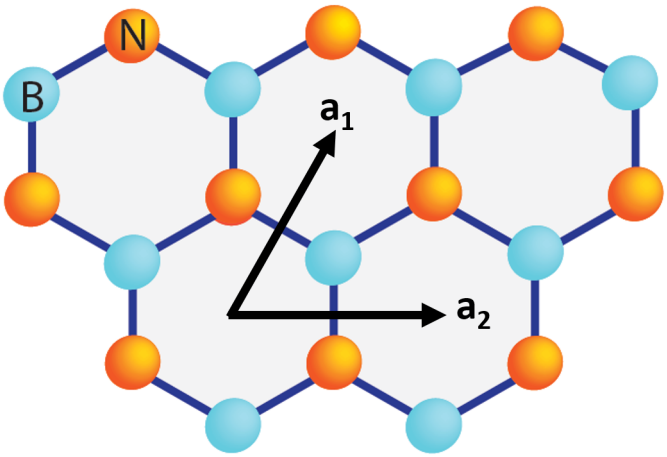

Figure 4.1: Atomic structure of hexagonal-Boron Nitride with unit cell vectors $\vec{a_1}$ and $\vec{a_2}$

Like any other van der Waals crystal, exfoliation is possible due to the relative weakness of the out of plane bonds compared to the ionic in plane bonds. Electron delocalisation is reduced in h-BN compared to graphene producing a large band gap (5.97 eV[299]). Strong in-plane covalent bonding between boron and nitrogen in the hexagonal lattice makes for a relatively inert material with very few charged surface states. Therefore, BN is a good candidate for use as an encapsulating layer or substrate in a 2D electronic device.[72,300–303] Other applications include reinforcing[304] and gas-barrier[219] fillers in polymer-based composites as well as thermally conductive inclusions[305] in oils.

4.1 Experimental Methods

4.1.1 Sample Preparation

Liquid Phase Exfoliation

Boron nitride powder (Sigma Aldrich ~1 um, 98%) was probe sonicated (VibraCell CVX, 750W) at a concentration of 30 g L^{-1} powder dispersed in a 6 g L^{-1} aqueous sodium cholate solution (Sigma Aldrich BioXtra, $\geq 99\%$) for 1 h with 60% amplitude. The dispersion was then centrifuged in a Hettich Mikro 220R centrifuge at 2260 *g* for 2 h using a fixed angle rotor (model no. 1016). After centrifugation the supernatant was separated and discarded, allowing for the removal of impurities. The sediment was redispersed in

fresh aqueous surfactant solution (SC, 2 g L^{-1}) and sonicated again for 6 h at 60% amplitude and a pulse of 6 seconds on and 2 off. The resulting dispersion was centrifuged at 27 *g* for 2 h, sediment discarded and the supernatant kept for subsequent size selection.

Size Selection

A centrifugation cascade[20] (Section 3.1.2) was used to separate the sample into a range of sizes. At each iteration the supernatant was decanted from the sediment and subjected to an increased speed. Meanwhile, the sediment was collected and redispersed in fresh surfactant solution (SC, 2 g L^{-1}). The centrifugal speeds used were 0.1k *g*, 0.4k *g*, 1k *g*, 5k *g*, 10k *g*, 22k *g*. The time for each centrifugation step was 2 h at 15°C. For low speed (<3k *g*) a fixed-angle 1016 rotor was used in a Hettich Mikro 220R centrifuge (4x 50 mL vials filled with 20 mL dispersion). For speeds over 3k g, a Beckman Coulter Avanti XP centrifuge was used with a JA25.15 rotor (8x 14 mL vials filled with 10 mL dispersion each). Samples were labelled according to the lower and upper centrifugation limits used to produce each size. For example, a supernatant was produced after centrifuging at RCF=1,000 × g-force (1k-g) and the resultant supernatant was centrifuged at 5,000 *g*. The sediment collected after the 5k-g step was referred to as the 1-5k *g* fraction. Further to the standard centrifugation cascade, two additional samples were prepared by taking the samples 0.1-0.4k *g* and 0.4-1k *g* and centrifuging for 16 h at 50 *g* (Hettich Mikro 220R centrifuge, fixed angle rotor 1195-A, 1.5 mL vials). The aim of this extra centrifugation was to decouple the quantitative relationship between layer number and lateral size.

The concentration of BN nanosheets in each size fraction was determined by filtration and weighing using alumina membranes with pore size of 0.02 μm. Alumina membranes were weighed before the addition of any nanomaterial. Each membrane was then placed on a vacuum filter setup. 10 mL of each size fraction was added to an individual membrane and the liquid allowed to filter through. Each membrane was then washed with 600 mL of deionised water. Once the water was completely filtered through, the membranes were removed and placed in a vacuum oven at 70°C overnight to dry completely. Finally each membrane's final mass was measured. The concentration of each size fraction was obtained by dividing the change in mass of the membrane (post filtration - pre filtration) by the 10 mL of each nanosheet volume added.

4.1.2 Characterisation of Nanosheets

Atomic force microscopy was completed using a Bruker Icon Dimension Atomic Force microscope in ScanAsyst mode with Bruker OLTESPA-R3 cantilevers. Each liquid sample was diluted until the sample was transparent (optical density of approximately 0.2). 10 μL of each sample was drop cast onto a pre-heated (180 °C) Si/SiO_2 (300 nm oxide layer) wafer. The wafer was then washed with water to remove excess surfactant on the surface. Individually deposited nanosheets were analysed through measurement with the AFM. Previously established length corrections[20] were applied to correct nanosheet length from tip broadening effects.

A Cary 6000i spectrometer along with quartz cuvettes (path length 4mm) were used for optical extinction and absorbance measurements. Each size selected dispersion was diluted by an appropriate factor for the spectrometer (optical density approx. 1). Samples that are too concentrated can cause saturation of the detector. Each spectra was measured at 0.5 nm increments with a 1 nm bandwidth for higher resolution at lower energy. For absorbance measurements, an integrating sphere was fitted to the spectrometer, allowing all scattered light to be transmitted (for more details see Section 3.2.1). For these measurements, the cuvette was placed in the centre of the sphere and the absorbance was measured with a bandwidth of 2 nm and increment of 10 cm^{-1}. For absorbance, the optical density of the BN was adjusted to 0.3-0.4 at the peak by dilution. By measuring both the extinction and absorbance it was possible to calculate the scattering through Ext - Abs = Sca.

A Renishaw InVia-Reflex Confocal Raman microscope was used with a 532 nm excitation laser in air under ambient conditions. The Raman emission was collected by a 50 $\times$ objective lens in streamline mode and dispersed by a 2400 l/mm grating with 10% laser power ($<$1.4 mW). Liquid dispersions ($\sim$ 20 μL) were dropped onto Si/SiO_2 wafers (300 nm oxide layer) and left to dry in air before measuring. A minimum of 5 spectra at different positions were recorded and averaged for final values. In streamline mode, where a larger sample area is sampled we did not observe spot to spot variations except for absolute intensities.

4.2 Results and Discussion

4.2.1 Size Selection of Boron Nitride

Liquid phase exfoliation yields polydisperse samples with a broad distribution of nanosheet thickness and lateral size. In order to observe any spectral changes in nanosheet dimension it is necessary to separate the polydisperse sample into size fractions. Liquid cascade centrifugation (Section 3.1.2) is a coarse size control method yielding fractions of decreasing size and thickness with increasing centrifugation speed and used in this study. After each iteration, the supernatant was subjected to higher centrifugation speed and the sediment was collected and redispersed in fresh aqueous surfactant solution.

To determine the mean lateral size and thickness of nanosheets in each fraction, statistical analysis of AFM topographic images was used with 200-350 nanosheets measured for each fraction. The length (longest lateral dimension), width (dimension perpendicular to length) and thickness of each flake were recorded using Gwyddion,[306] data visualisation and analysis software for scanning probe microscopy. Pixelation and tip broadening effects result in an overestimation of nanosheet length and width. To adjust for these effects, a correction formula was applied in line with previous work for LPE nanosheets.[19,20,67]

Due to intercalated/adsorbed water and surfactant, the apparent height of a single BN layer appears thicker than the theoretical value of 0.34 nm.[307,308] Step height analysis is used to determine the apparent thickness of a single monolayer, in line with previous studies.[19,20,26,67] Nanosheet thicknesses with terraces of partially exfoliated material were recorded (Figure 4.2A) and are displayed in increasing step height in Figure 4.2B. Terraces of similar heights were grouped and averaged to give a mean step height for a group. The slope of a plot of mean step height versus step height group gave the apparent monolayer height of 0.99 nm +/- 0.01 nm as seen in Figure 4.2C. This value is similar to the 0.9 nm observed for LPE graphene[215] which is believed to be reasonable given the similar hexagonal atomic structure of these 2D materials.

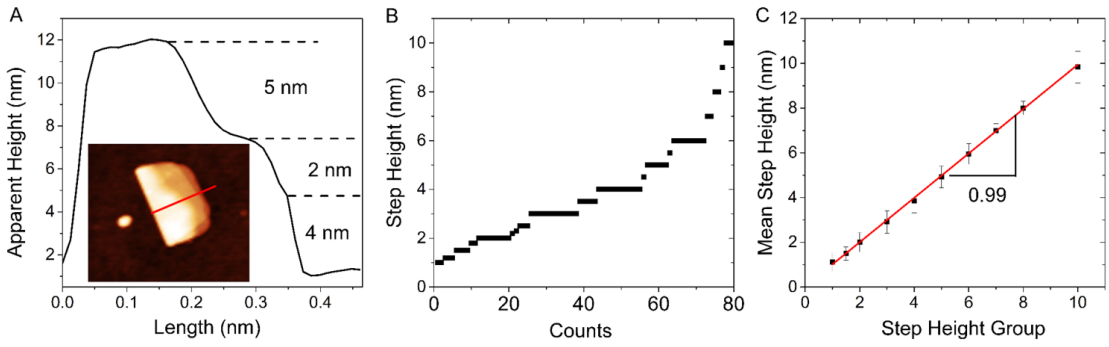

Figure 4.2: (A) Height profile along the line of the nanosheet (inset) showing clear, resolvable steps each consisting of multiple monolayers. (B) Step heights of $>$ 70 BN nanosheets in ascending order. The step height clustered in groups and is always found to be a multiple of $\sim$1 nm, which is the apparent height of one monolayer. (C) The mean height for each group (the error is the sum of the mean step height error and the standard deviation in step height within a given group) is plotted in ascending order with the slope giving a mean monolayer step height of 0.99 $\pm$ 0.01 nm.

These values are thicker than those seen with mechanical or CVD exfoliated graphene/BN because of the exfoliation medium. A hotplate was used to evaporate water after dropcasting the sample. In addition, the wafer was washed with both water and IPA to dislodge underlying surfactant present, however it is clear some still remains between layers. This is evident in both the step height (larger than predicted) and in Raman spectroscopy measurements where we see a consistent surfactant peak in dried films of LPE BN in sodium cholate solution (Section 4.2.3 for more quantitative details on the surfactant Raman peak). A large apparent monolayer height is not material-dependent but rather method dependent. Although it is difficult to judge the difference between mono and bi-layer BN, in WS_2 for example, the step height analysis is validated from the presence of a monolayer photoluminescence peak in Raman spectroscopy. Based across a number of LPE 2D materials[19,20,67,191,196] the dropcasting method for AFM gives apparent monolayer heights of approximately 2-3 times predicted theoretical heights. Using this information the number of layers, N, of the nanosheets can be determined and in turn, the mean number of layers <N> for each size selected sample. Histograms can then be constructed for nanosheet N and L for each size fraction, a selection of which is displayed in Figure 4.3 below. For all other sizes see Appendix B.1. The histograms show a narrowing in the log-normal distributions of both N and L with increasing centrifugation speed. As larger, thicker nanosheets remain in the sediment with each step at higher centrifugal force, there is an increase in monolayer and few layer BN.

AFM probes both the lateral dimensions and thickness of the nanosheets, therefore the volume can be estimated as length $\times$width$\times$thickness. Using the volume of each nanosheet, the volume fraction weighted mean nanosheet thickness $<N>_{Vf} = \Sigma N^2 LW / \Sigma NLW$ can be calculated. This takes into account the fact that the majority of the mass in each fraction is concentrated on thicker nanosheets. The volume fraction weighted mean nanosheet thickness is analogous to the weight-average-molecular-weight in polymer physics[309] as opposed to arithmetic $<N>$ comparable to the number-average-molecular-weight. $<N>_{Vf}$ is directly proportional to $<N>$ in a 1.5:1 ratio as seen in Appendix B.2.

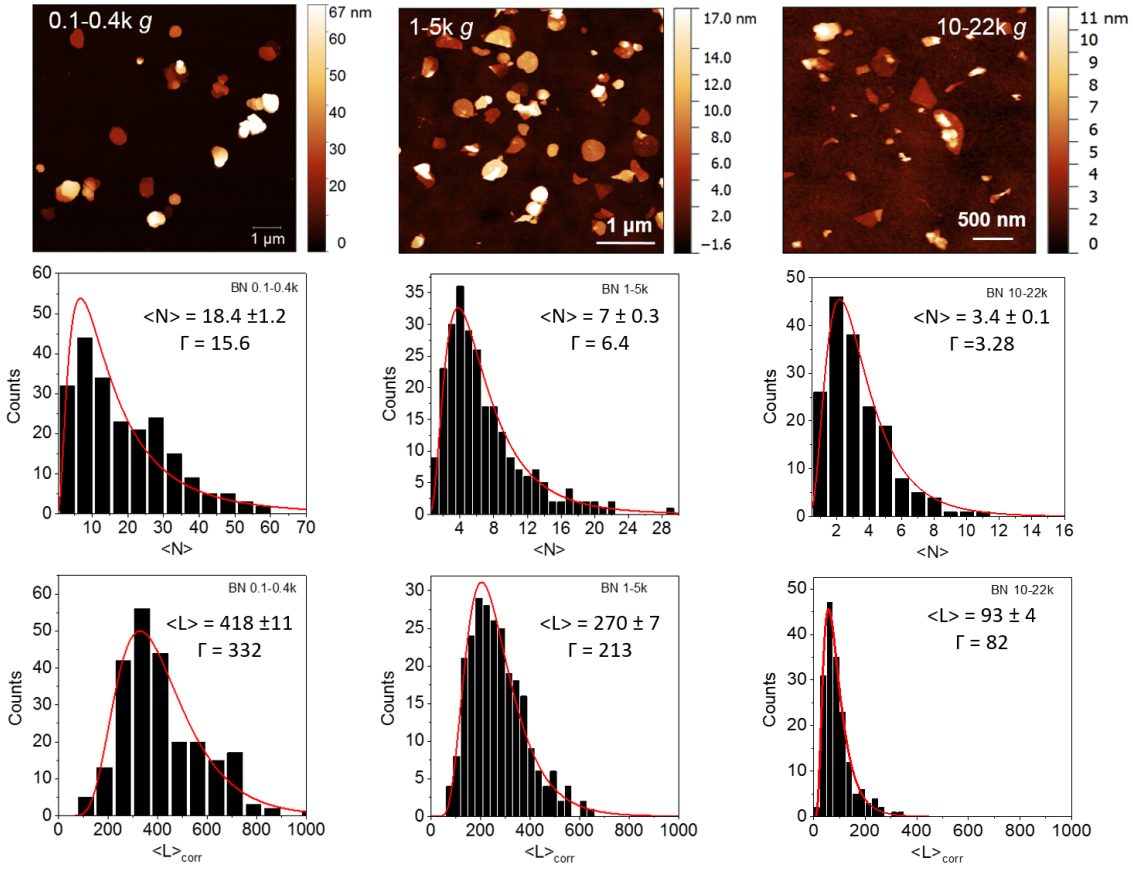

Figure 4.3: Representative AFM images (top row), layer number (middle row) and length (bottom row) distribution histograms on three trappings produced from the standard size selection cascade. Γ is the width of each lognormal distribution. From left to right: 0.1-0.4k *g*, 1-5k *g*, 10-22k *g*.

Arithmetic and volume-fraction weighted mean values of nanosheet layers $<N>$ and $<N>_{Vf}$ for each fraction are plotted as a function of relative centrifugal force (in units of earth's gravitational field, $10^3 g$) in Figure 4.4 below. The midpoint of the pair of centrifugal accelerations of the cascade is used. The volume fraction weighted mean layer results in large layer number for the same central g-force, as predicted by the ratio. A power law

decay that scales as $g^{-0.4}$ can be observed in Figure 4.4A.

Similarly, the mean nanosheet length <L> is plotted versus central g force. Experimental values found for other 2D materials[20,202,310] predict a scaling of $g^{-0.5}$. The dashed line is a guide to expected behaviour in Figure 4.4B rather than a fit to the actual data. Peukert et. al[311] define a 'cut size' as the maximum particle diameter remaining in the supernatant after centrifugation. The cut size is inversely proportional to the rotation rate and so we would expect that smaller nanosheets for increasing centrifugation speed as shown. It is clear the data presented here does not scale clearly with $g^{-0.5}$. However, a fit of all data points except the first gives a scaling of -0.39 $\pm$0.09. Conversely fitting the last three data points gives a scaling of -0.60 $\pm$0.07. Meanwhile, fitting the last 4 data points gives a scaling of -0.44 $\pm$0.08. These values come in close agreement to the $g^{-0.5}$ within standard error. It should also be noted that the standard error is reduced when taking into account the last three data points only. The error bars in Figure 4.4 are the standard error of each sample i.e. the standard deviation divided by the square root of the number of counts. Due to the large number of counts (200-300) for each sample, the error appears rather small, however the lowest g-force data point (0.1-0.4 k g) deviates from -0.5 scaling, possibly due to an underestimation in <L>.

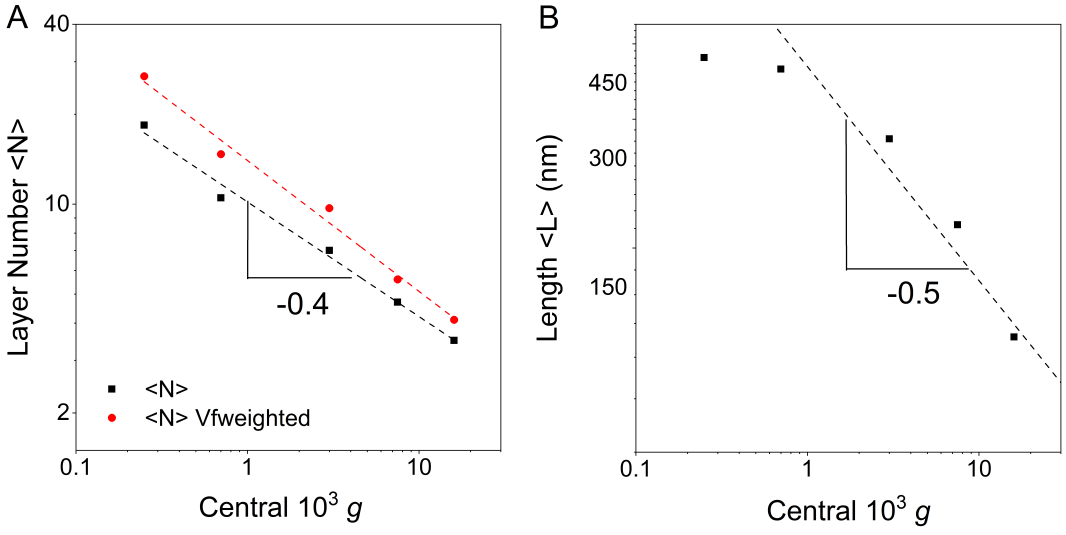

Figure 4.4: (A) Mean layer number <N> and volume-fraction-weighted mean layer number $< N >_{Vfweighted}$, both plotted versus central centrifugal force, 10^3 g. (B) Mean nanosheet length, <L> as a function of central centrifugal force, 10^3 g. The dashed line is a guideline of the expected behaviour of nanosheet length with central g force as seen with previously studied 2D materials[19,20,67] and is the line $10^{2.6}x^{-0.5}$. It fits the last 4 data points within standard error.

4.2.2 Dependence of Optical Spectra on Nanosheet Dimension

Optical extinction and absorbance spectra have been shown to change systematically with nanosheet dimensions for many other 2D materials from TMDs to graphene.[19,26,67,191,264,312] Here, UV-vis spectroscopy is used to measure the dependence of extinction and absorbance spectra on LPE BN nanosheet dimensions. Standard transmission mode was used for the extinction spectra while an integrating sphere was used for the absorbance.[19,313] The extinction is a combination of both the absorbance and scattering such that Ext(λ) = Abs(λ) + Sca(λ). By measuring both the absorbance and extinction of each sample, the scattering component can be extracted.

Length metric from Extinction spectra

Extinction spectra were measured in a UV-Visible spectrometer in standard transmission mode. The transmittance T is related to the extinction by T=10^{-Ext}. The spectra for each size fraction are plotted in Figure 4.5A below showing a distinct peak at approximately 6.1 eV (205 nm). Other than this peak, the spectra are dominated by a powerlaw scattering background that increases prominently with size.[18,19,264,314] Larger nanosheet scatter light more strongly than smaller nanosheets as described by Harvey et al.[264] due to an increase in their scattering coefficient. This is associated with a transition from Rayleigh to van de Hulst scattering as described by the authors.

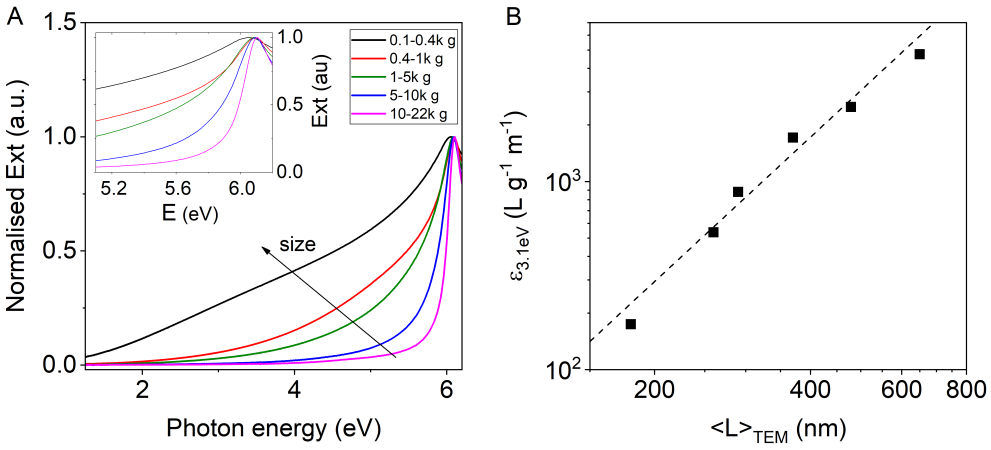

Figure 4.5: Optical extinction spectra normalized to each peak's maximum showing the intensity dependence increasing for increasing nanosheet size at energies below 6 eV. Inset: magnified view of peak region (B) Extinction coefficient at 3.1 eV, $\varepsilon_{3.1eV}$, plotted versus nanosheet mean length <L> as measured by TEM. Dashed line: fit of eqn 4.1

The scattering is size-dependent and therefore the extinction coefficient, usually an intrinsic property, is also size-dependent. We can relate the extinction coefficient, ε, to the Extinction, Ext, via the Beer-Lambert law where Ext=εCℓ with C as the nanosheet concentration and ℓ is the path length. To calculate the size dependent extinction coefficient we first needed to find the concentration of each sized sample. Samples of a known volume were filtered and weighed with the concentration being estimated through the change in nanosheet mass. Using these concentrations along with <L> estimated from TEM measurements, we can convert from extinction to extinction coefficient at a given photon energy or wavelength. Figure 4.5B shows the extinction coefficient at a selected photon energy versus the mean nanosheet length <L> measured with TEM (TEM and filtration completed by Dr. Andrew Harvey prior to these experiments). The relationship between $\varepsilon_{3.1eV}$ and <L> is fit to get the following empirical formula:

$$\varepsilon_{3.1eV} = 4 \times 10^{-4} < L >^{2.55} \tag{4.1}$$

where $\varepsilon_{3.1eV}$ is in L g^{-1} m^{-1} and <L> is in nm. Knowing the extinction coefficient at 3.1 eV, the average length <L> can be calculated. Conversely, if <L> is measured through statistical microscopy, the concentration can be estimated through $\varepsilon_{3.1eV}$ and Ext$_{3.1eV}$ as in Equation 4.2 below.

$$C = \frac{Ext_{3.1eV}}{\ell \varepsilon_{3.1eV}} \tag{4.2}$$

Thickness metric from Extinction spectra

Measurement with an integrating sphere allows for the separation of the extinction into absorbance and scattering components. We obtain a true value for the absorbance by using the sphere which can then be subtracted from the extinction to give the scattering in the sample, Sca = Ext - Abs. From the extinction spectra we expect most of the signal to come from the scattering shown in the inset of Figure 4.6A. The scattering spectra follows a power-law decay in the non resonant regime, as observed for other 2D materials.[19,20] The absorbance of all sizes is plotted in Figure 4.6A. There is a well-defined peak at 6.02-6.13 eV and an absorption edge at approximately 5.8 eV (213 nm). The absorbance goes to zero for energies below 3.5 eV consistent with wide bandgap semiconductors. Moreover, this confirms the fact the majority of the signal detected in the extinction spectra was in

fact due to scattering (for plots of all three components for each fraction see Appendix B.4).

A 2nd derivative plot of the absorbance with respect to energy allows for a more accurate evaluation of peak positions in Figure 4.6B. Each spectra was smoothed with Lowess smoothing parameter using OriginLab® software. The main absorbance peak can be attributed to the free exciton transitions.[315–317] In previous studies the BN in question was grown using CVD technique and free excitons were observed through photoluminescence measurements at a position of $\sim$ 5.7 eV with bound excitons resulting from impurities at $\sim$ 5.5 eV. The excitonic peak of this LPE BN is shifted upwards of 0.4 eV in comparison to literature[315–317] which can be attributed to the difference in sample environments. Aqueous surfactant solution affects the dielectric constant which may cause different excitonic binding energies. The excitonic energy changes due to a combination of dielectric screening affecting the binding energy and confinement effects,[318] therefore a shift in the exciton peak position is expected with nanosheet thickness. Figure 4.6C shows the excitonic peak absorbance versus the mean weighted nanosheet thickness from statistical AFM analysis. The peak absorbance energy is red-shifted gradually from 6.153 eV for a mean weighted thickness of 3.4 layers to 6.118 eV for a mean weighted thickness of 27 layers.

This thickness dependence has been corroborated by theoretical calculations in the published version of this work.[192] The variation of absorption spectra with number of layers was calculated using many-body Quasi-Particle Self consistent (QSGW) and Bethe-Salpeter (BSE) approximations as well as hybrid functional HSE06 methods. There was excellent agreement between calculated and experimental absorption spectra with a slight energy-overestimation in the former. Different levels of theory all showed similar variations of the peak shift with layer thickness as found experimentally.

The relationship between peak absorbance energy and mean weighted thickness can be empirically fit and is given by the dashed line in Figure 4.6C as:

$$\langle N \rangle_{Vf} = 10^{43.5(6.152 - E_{Abs})} \tag{4.3}$$

where $<N>_{Vf weighted}$ is the mean weighted thickness, and E_{Abs} is the absorbance peak position in eV. A simple absorbance measurement therefore allows for the estimation of

the mean weighted nanosheet thickness in a given dispersion.

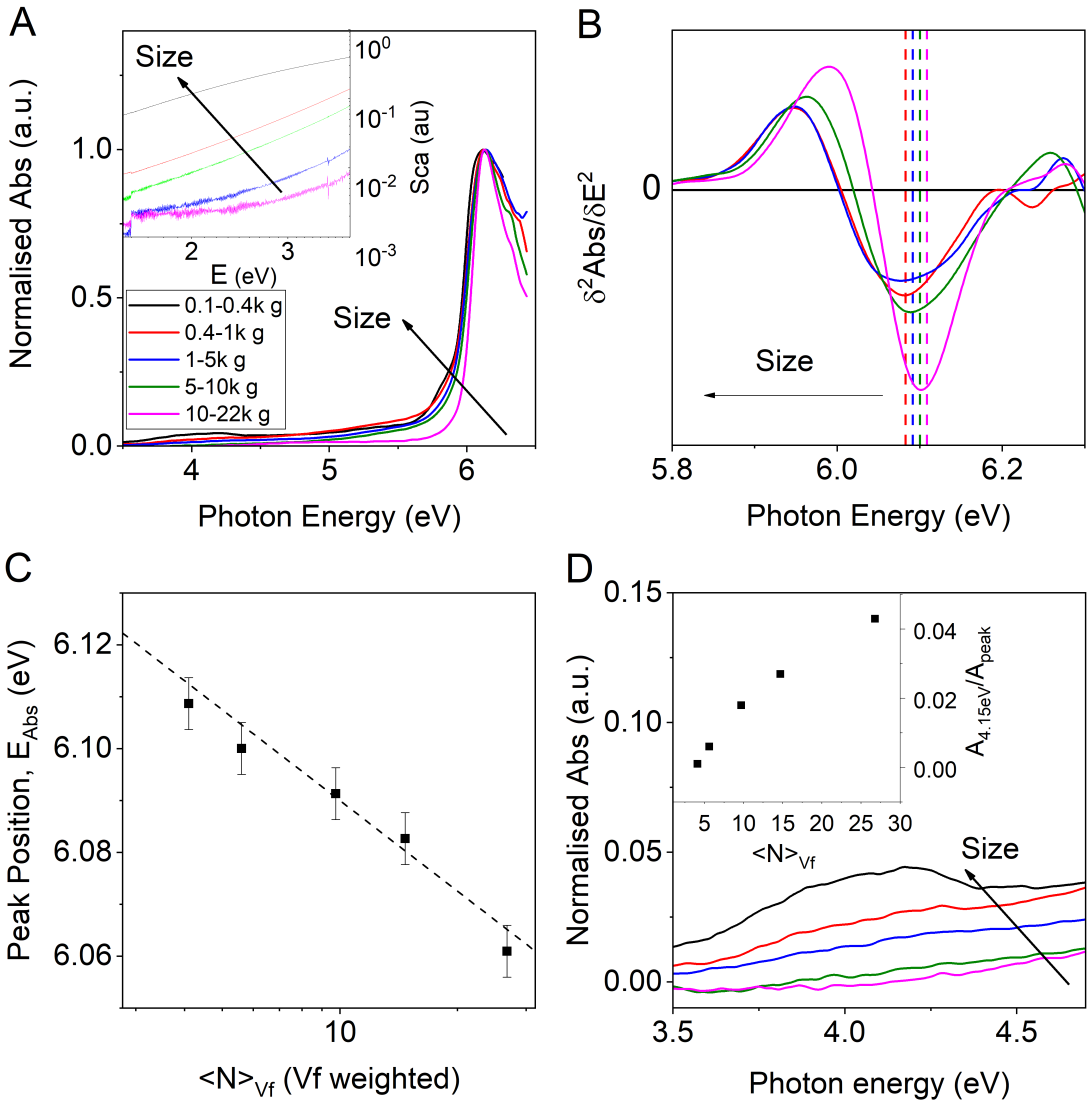

Figure 4.6: (A) Optical absorption spectra normalised to each peak's maximum ($\sim$ 6.12-6.14 eV) for different nanosheet sizes to show that the absorbance peak is weakly dependent on thickness, more clearly demonstrated in (B). Inset: Scattering spectra in the non-resonant regime. (B) Second derivative of the peak region of the absorption spectra. (C) Peak position of the absorbance spectra plotted versus the volume fraction weighted average layer number $<N>_{Vfweighted}$ as measured by AFM with normalized absorbance as a function of energy (inset). (D) Magnified view of normalised absorption spectra in the energy range close to 4 eV. Each spectra was normalised to the peak maximum to show the intensity dependence of the features with size at approximately 4 eV. Inset: Absorbance at 4.15 eV normalized to peak absorbance plotted versus mean nanosheet thickness.

In addition to the absorption peak, magnified views of the spectra focusing on the region near 4 eV are shown in Figure 4.6D. Some small features are noted that increase in relative intensity with increasing nanosheet size as seen in Figure 4.6D inset. Previous reports have

attributed these features to impurity related donor-acceptor pair transitions involving a nitrogen vacancy donor and a deep level acceptor for example carbon atoms occupying the nitrogen vacancy site.[317,319,320] Given the fact that these impurities are credited to substitutional defects, a more extensive study with a range of BN starting materials would be needed to investigate this effect fully. It is proposed that absorbance spectroscopy not only allows for a quick method of investigating nanosheet thickness but also sample purity. Another possible explanation could be that there is a zero-phonon transition at 4.15 eV with phonon replicas at higher energies.[321]

4.2.3 Dependence of Raman Spectra on Nanosheet Dimension

Raman spectroscopy is a powerful characterisation tool for many 2D materials giving insights into doping, strain, nanosheet thickness and defect content.[18,54,67,313,322] The BN Raman spectra however contains relatively little information compared to other 2D materials with the exception of a single phonon mode at approximately 1366 cm^{-1}, denoted as the G-band.[323–326] BN is non-resonantly excited and gives a weak Raman signal. In addition, low frequency modes are not easily accessible.[327] Gorbachev et al.[325] recorded minor blue shifts in peak position when transitioning from monolayer to bulk BN. These shifts were reported to be both sample-dependent with a magnitude dependent on strain in the material. In this work, size fractions were dropcasted onto Si/SiO_2 wafers and then measured through Raman spectroscopy with the aim of extracting some information. The laser power ($\sim$1.4 mW) was chosen as a compromise between heat-induced broadening at high power and poor signal to noise ratios at low power. Laser power tests can be seen in Appendix B.5. The normalised Raman spectra are shown in Figure 4.7.

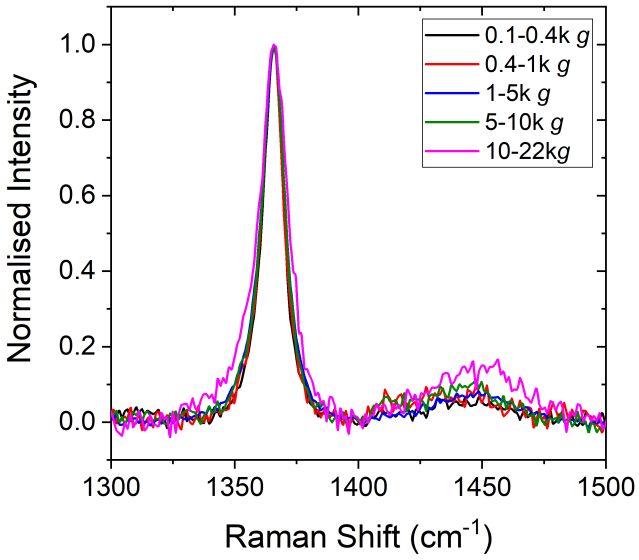

Figure 4.7: Raman spectra of size-selected BN nanosheet dispersions normalized to the peak maxima at the G band frequency ($\sim$ 1366 cm^{-1}). shows that the peak positions appear to be independent of Raman shift. Secondary, smaller broad peaks are noted at higher Raman shifts (1400-1470 cm^{-1}) attributed to sodium cholate surfactant.

The G band is clearly visible at approximately 1366 cm^{-1} but secondary, smaller broad peaks are also noted at higher Raman shifts (1400-1470 cm^{-1}). Upon further inspection of these modes, they can be attributed to the sodium cholate surfactant used. Sodium cholate also has a Raman mode at 1365.2 cm^{-1}, very close to the BN G-band mode. In order to account for the surfactant present on the wafers, a Raman spectrum of surfactant powder was measured as seen in Figure 4.8A. Indeed, the fact that the SC peak is present at all reaffirms the idea that residual surfactant may be trapped between layers, a justification for step height analysis in section 4.2.1.

There are slight differences in the sample preparation of Raman and AFM. For Raman, a high concentration 0.5-1.5 g L^{-1} of BN is required in order to observe the active modes. The BN to surfactant ratio is higher than AFM where samples are diluted to avoid aggregation on the surface. However, the wafer is not washed to remove excess surfactant before Raman measurements (unlike AFM) so the amount of surfactant in solution will most likely remain on the wafer. Estimating the intensity of the SC peak in each Raman measurement, it appears surfactant accounts for 2-10 % of the measured peak.

Focusing on the region between 1330 and 1400 cm^{-1} the 1365.2 cm^{-1} SC peak width

and intensity can effectively be subtracted from the measured BN spectrum as shown with the example 5-10 k *g* size in Figure 4.8B. A double Lorentzian is fit, constraining one Lorentzian using the known SC peak position and width. By doing this for each size fraction the true peak position and width of the BN is obtained. As seen in Figure 4.8C, the peak position is invariant with nanosheet thickness found from AFM. This is in agreement with literature[325] and indicated by a dashed line centred at 1366 cm^{-1}.

However, the G-band width does show a systematic change with nanosheet thickness across size fractions. The full width at half maximum (Γ_{G-band}) was extracted from each fit and plotted versus the nanosheet thickness for each size in Figure 4.8D. The result is a near-linear scaling of G band width with $1/<N>V_f$. The inverse scaling with thickness implies peak broadening is related to the nanosheet surface, that is the basal planes of the nanosheets as opposed to edges. Standard liquid phase exfoliated samples produce a relationship between N and L i.e. as nanosheets become laterally smaller they are also thinner.

To isolate the source of the linewidth dependence, two samples were prepared using a secondary cascade to give a different N-L relationship compared to standard samples. Two samples were re-centrifuged overnight (16h) at low speed (50 *g*). The lateral size distribution remained similar but the nanosheets appeared significantly thinner after this centrifugation step (see Appendix B.3). A plot of Γ_{G-band} versus $1/<L>$ (Appendix B.6) does not scale smoothly with $1/1/<L>$. Interestingly, the overnight centrifugation samples agree with the same G-band width vs. $1/<N>$ relationship but different $1/<L>$ even though they have a different $<N>$-$<L>$ dependence than the standard size-selected samples as shown in Figure 4.8D (red stars). This supports the idea that peak broadening is in fact due to increasing nanosheet thickness not lateral size.

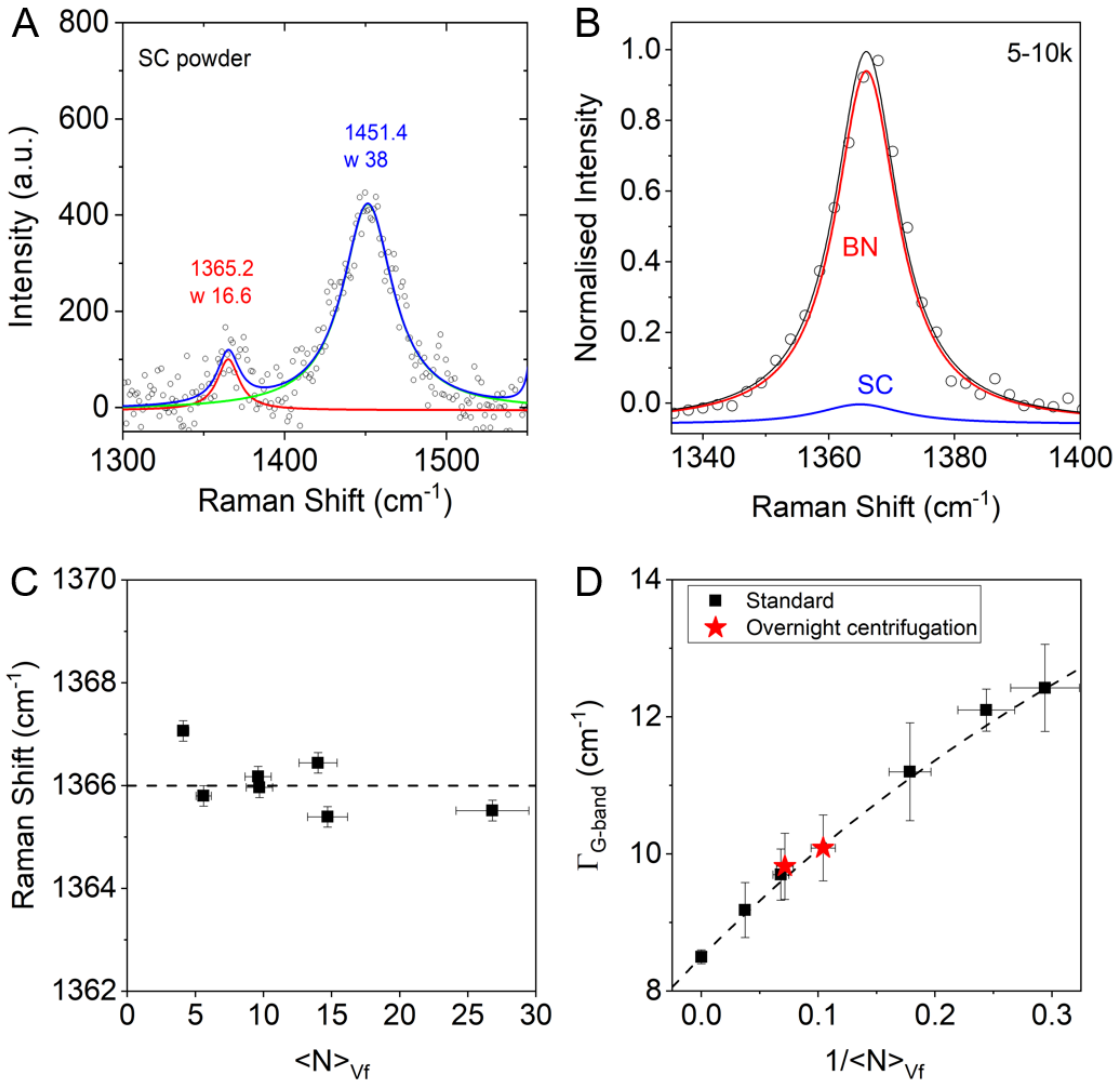

Figure 4.8: (A) Raman spectrum in the region 1300-1550 cm^{-1} of sodium cholate powder. The spectrum was fit to a double Lorentzian function with peaks at 1365.2 cm^{-1} and 1451 cm^{-1}. This fitting was subtracted from the BN spectra to obtain accurate peak widths and positions. (B) Fitted Raman spectrum of the fraction 5-10k *g* (black), normalized to the maximum intensity and fitted to two lines, one representing h-BN (red) and the other representing sodium cholate (blue). The h-BN spectrum (red) is extracted and the position and width estimated. (C) Plot of the h-BN G-band position as function of mean layer number. The G-band is centred at 1366 cm^{-1} (dashed line). (D) h-BN G-band peak width (full width and half maximum, FWHM from fit) as function of the inverse nanosheet thickness. The dashed line is a fit to Equation 4.4 suggesting that broadening is due to solvatochromic effects.

An investigation into the effects of the dielectric environment on peak broadening with nanosheet thickness was carried out. The idea behind these experiments was that residual surfactant and water would surround thinner nanosheets more thoroughly and so would

experience different solvatochromatic effects. A drop of N-cyclohexyl-2-pyrrolidone (CHP) was placed on top of the deposited BN. Raman spectra were measured before and after the treatment with CHP. Figure 4.9 below shows that the G band width increases from $\sim$ 9 (Figure 4.9A) to $\sim$ 12 cm^{-1} (Figure 4.9C). This results confirms that the nature of the peak broadening is from solvatochromism at the outer-monolayer-liquid/air interface.

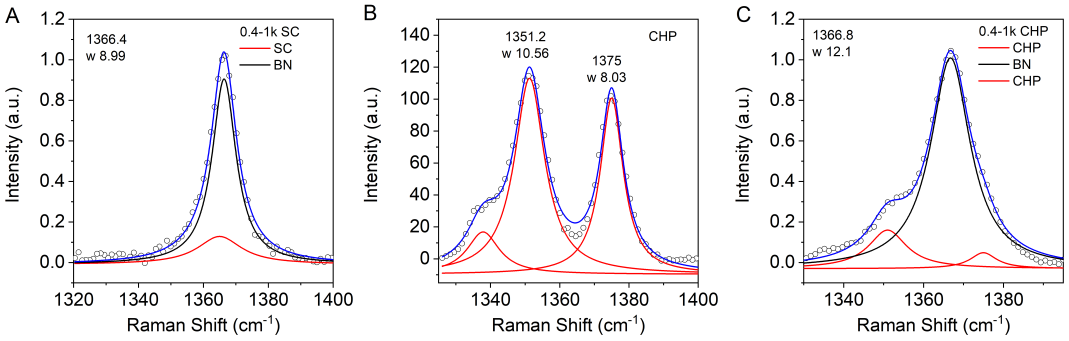

Figure 4.9: Solvatochromic effects on the Raman spectra of LPE BN. (A) Fitted Raman spectra of the as deposited BN-SC. (B) Raman spectrum of N-cyclohexypyrrolidone (CHP) in the same spectra region. The data can be fit well to three Lorentzians with the component at 1335 cm^{-1} being significantly lower in intensity and this is negligible in a BN-CHP spectrum. (C) Raman spectrum of the LPE BN sample shown in (A) after deposition of a drop of CHP. In addition to the BN signal, the contribution from CHP is clearly discernible. To extract the FWHM of the BN, the CHP signals were fixed in position and width according to the CHP reference spectrum. The BN G-mode increased in width from 9 cm^{-1} to 12 cm^{-1} in the presence of CHP suggesting significant solvatochromism.

There is also the question of whether the liquid environment during the actual exfoliation had an effect on the G band width. To address this, BN exfoliated in SC was transferred via centrifugation to a range of liquid environments (aqueous sodium dodecyl benzene-sulfonate, poly(vinyl alcohol), H2O, isopropanol, CHP) and deposited on Si/SiO_2 wafers for Raman measurements. Figure 4.10 shows that the G band width does not vary greatly with each liquid and the range is within the error of the fit suggesting that the BN-air interface is the primary factor for the change in linewidth.

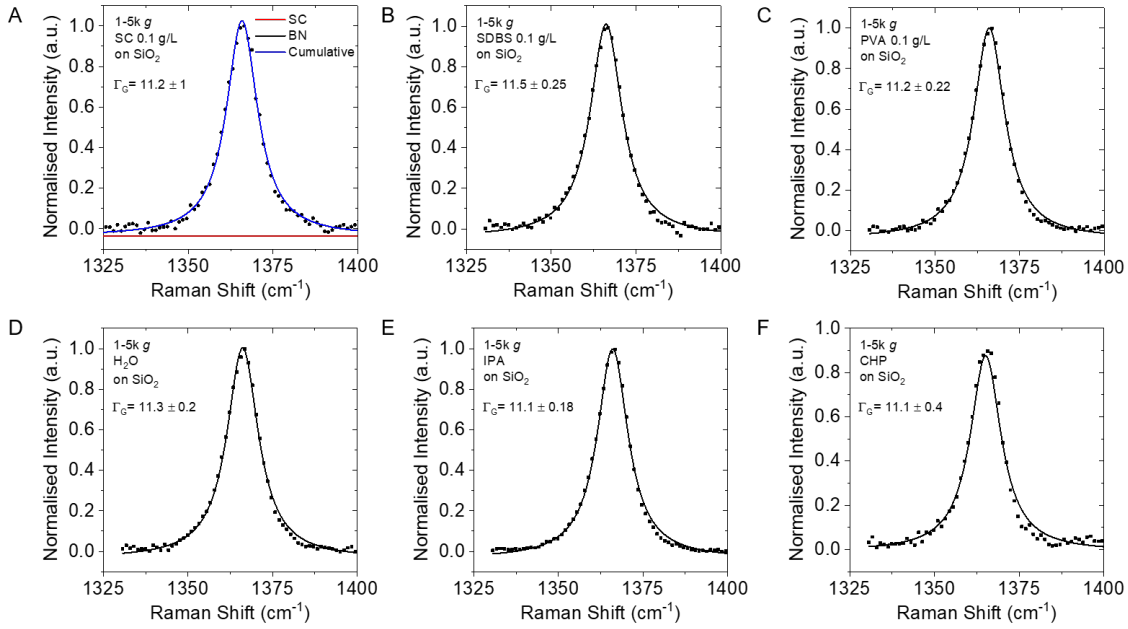

Figure 4.10: Fitted Raman spectra of LPE BN deposited from different liquid environments. The sample 1-5k *g* (A) was transferred to a range of liquid environments. To achieve this, the sample was centrifuged at 10k *g* for 1 h, the supernatant decanted and discarded, water added to the sediment, followed by another centrifugation of 10k *g* for 1 h. Again the supernatant was decanted and the sediment redispersed in B) sodium dodecyl benzene sulfonate in water (SDBS, 0.1 g L^{-1}), C) polyvinyl alcohol (PVA, 0.1 g L^{-1}), D) H_2O, E) Isopropanol (IPA), F) N-cyclohexyl-2-pyrrolidone (CHP) prior to deposition on Si/SiO_2 wafers. No changes of the Raman G-band are observed. This suggests that the main factor influencing the linewidth is the BN-air interface if samples are measured in a dried state.

Finally the bottom interface i.e. substrate-BN interface was tested as to whether it had an effect on the G-band width. The sample was deposited onto two other substrates, aluminium and copper foil and measured as normal. Again, the G band did not change within the standard error of the fit (Figure 4.11). This result confirms the proposal that the nanosheet-air interface is dominant when measuring dried films with Raman spectroscopy.

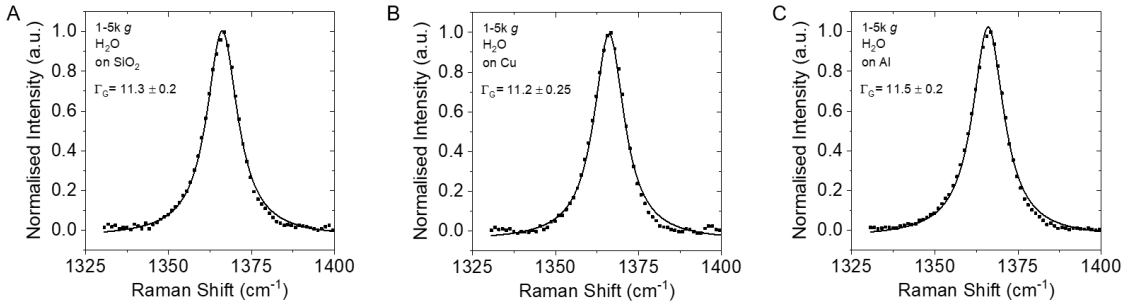

Figure 4.11: Fitted Raman spectra of LPE BN deposited on different substrates. The sample 1-5k *g* was redispersed in water (after centrifugation) to avoid the (minor) contribution from the SC and improve the accuracy of the fits. A) Si/SiO_2 substrate used as the standard substrate in the study, B) copper foil, C) alumina foil. No changes of the Raman G-band are observed suggesting that the dominant factor influencing the linewidth is the BN-air interface, when porous networks of randomly restacked LPE BN are measured. Although the sample was dispersed in water to avoid the contribution from the surfactant, it is possible that small amounts of surfactant remain at higher Raman shifts (1400-1470 cm^{-1}) and appears the spectra deviates from the Lorentzian fit at approximately 1380 cm^{-1}.

Using the relationship between the Raman G-band width and nanosheet thickness (Figure 4.8D) a model can be designed. The fraction of monolayer surfaces exposed to the environment scales with the solvatochromic increase in linewidth compared to bulk. This gives a scaling of ∼2/(N+1). From this scaling, a width-thickness relationship is suggested as:

$$\Gamma_{G-band} = \Gamma^{Bulk}_{G-band} + \frac{2\Delta\Gamma_{M-B}}{\langle N \rangle_{Vf} + 1} \tag{4.4}$$

where $\Delta\Gamma_{M-B}$ is the width change from monolayer to bulk. This function is applied to the data in Figure 4.8D represented by the dashed line fit. The function fits well to the data with better allowance for deviations from the simple $1/<N>_{Vf}$ scaling as seen in Figure 4.12 below.

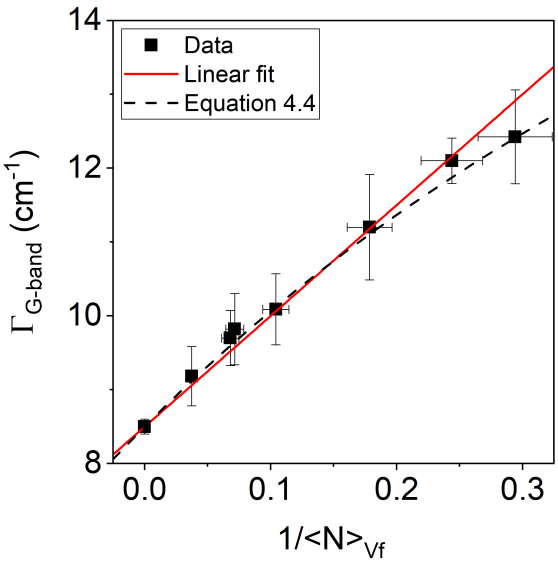

Figure 4.12: A comparison between simple $1/<N>_{Vf}$ scaling and a fitting using Equation 4.4 shows the function fits well to the data with better allowance for deviations than the simple scaling.

A consistent value of $\Delta\Gamma_{M-B}$ = 8.7 cm^{-1} is extrapolated from the data, 3-4 cm^{-1} higher than values reported by Gorbachev et. al[325] for BN nanosheets on SiO_2 wafer. This may be due to the environment surrounding the nanosheets. Nanosheets exfoliated via LPE are most probably surrounded on all sides by the environment compared to the air-liquid-substrate interface used (BN dropcast as a film on SiO_2 wafer). A value for Γ^{Bulk}_{G-band} = 8.5 cm^{-1} is extracted. This indicates that the BN produced is of high quality with low basal plane defect content similar to the FWHM of high quality BN crystals of approximately 8 cm^{-1}.[327] Rearranging equation 4.4 above the nanosheet thickness from the G band width can be estimated as:

$$\langle N\rangle_{Vf} = \frac{2\Delta\Gamma_{M-B}}{\left(\Gamma_{G-band} - \Gamma^{Bulk}_{G-band}\right)} - 1 = \frac{17.2}{\Gamma_{G-band} - 8.5} - 1 \tag{4.5}$$

where Γ_{G-band} is in cm^{-1}. The solvatochromatic effects will make the value of Γ_{M-B} system dependent i.e. this is specifically for LPE BN dropcast on a wafer. However, the liquid environment experiments above show that the exact liquid is not dependent on the G-band width (Figure 4.9 and 4.10). In addition, the equations are only valid for the measurements made at the same laser power (1.4 mW). An approximate power-dependent expression has been proposed and further data discussed in Appendix B.5. With knowledge of both the top and bottom environments of a sample, the thickness dependence

of the Raman linewidth can be exploited. Therefore, this metric can be altered slightly depending on the environment to suit other work such as CVD grown h-BN.

4.3 Conclusions

In this work nanosheet thickness metrics have been successfully established for liquid phase exfoliated h-BN through UV-Vis and Raman spectroscopy. Using atomic force microscopy the nanosheets in each size fraction were statistically analyzed. Applying step height analysis, the apparent height of a monolayer of BN exfoliated in surfactant was found to be 0.99 ± 0.01 nm. The mean nanosheet length and volume fraction weighted mean layer numbers were calculated for each sample.

UV-Visible extinction measurements showed a relationship between the extinction coefficient and the mean nanosheet length (length taken as the longest dimension of the nanosheet). If the extinction coefficient is known at a given wavelength it can be used in conjunction with the extinction value at the same wavelength to obtain a value for sample concentration. Alternatively the extinction coefficient can be used to estimate mean nanosheet length. A well-defined peak was observed at approximately 6 eV for absorbance measurements, with a zero absorbance at energies of less than 3.5 eV as predicted for a wide bandgap semiconductor. The nanosheet thickness can be found from the position of the maximum in the absorbance spectrum due to thickness-dependent excitonic confinement. The excitonic peak for LPE BN is Stokes-shifted upwards by 0.4 eV in comparison to previously reported values[315–317] which can be attributed to the different environments of the samples. A large scattering background was noted that is more prominent for larger sized samples in line with scattering theory of LPE samples.[264] Small features were observed at $\sim$4 eV which can be attributed to impurities in the sample. It cannot be said for certain what these impurities are but it is suggested that they may be substitutional defects from donor-acceptor pair transitions involving a nitrogen vacancy donor and a deep level acceptor for example carbon atoms occupying the nitrogen vacancy site. These features decrease in intensity with decreasing nanosheet thickness. It was proposed that the magnitude of this peak can be used as an estimation of nanosheet quality and defect content.

Raman spectroscopy measurements showed the G band mode of h-BN at approximately 1366 cm^{-1}. Upon measurement and analysis of the surfactant sodium cholate, a peak was observed in the same region as the BN G-band mode. The SC peaks were estimated and double Lorentzian fitting was used to accurately determine the position and width of the h-BN G band. A linear fit of peak width as a function of inverse nanosheet thickness suggested that broadening is due to solvatochromic effects. It was proposed that residual surfactant and water will surround nanosheets differently and so a solvatochromatic study was carried out. A broadening due to solvatochromism was observed at the outer monolayer-liquid interface when CHP was placed on top of the BN film. The G-band width did not change when the dispersion was transferred to different liquid environments or when the bottom interface (substrate) was changed. This lead to the design of a model based on the thinking that the BN-air interface was the dominant factor in the G-band linewidth. The model obtained can be utilised as a metric for an estimation of nanosheet thickness from the width of the G band. It is proposed this metric could be altered for other systems where the air-substrate interface is well-defined such as CVD grown BN.

5

I'm on the verge of a major breakthrough, but I'm also at the point where physics ends and chemistry begins, so I'll have to drop the whole thing

–Sidney Harris

Effect of Surfactant Choice and Concentration on Nanosheet Dimension

***

Liquid phase exfoliation is a versatile and scalable production method for 2D materials. A broad range of 2D materials have been exfoliated in this manner to date including graphene,[17,328,329] BN,[192,304] GaS,[191] phosphorene,[26] MXenes,[330] transition metal dichalcogenides (TMDs)[19,20] and layered double hydroxides (LDHs).[22] Nanosheets can either be stabilized thermodynamically in appropriate solvents or electrostatically with surfactants (see Section 2.4.2). Surfactant exfoliation is environmentally friendly and relatively low cost with many processing techniques compatible with aqueous environments. While various surfactants have been used as stabilizers during liquid phase exfoliation, the effect of surfactant choice and concentration on nanosheet yield and dimensions has yet to be explored comprehensively.

Binding of common surfactants such as sodium dodecyl sulfate to 3D graphite has been reported in detail,[331] however studies of surfactant-stabilized 2D nanosheets are limited with graphene being the primary material of focus.[332–335] Ionic surfactants are the most common type in previous reports with sodium cholate (SC), sodium dodecyl sulfate (SDS) and other long alkyl chain surfactants foremost used.[335–339] To recap, nanosheet

stabilization (and colloids generally) using ionic surfactants is relatively simple. The non-polar part of the surfactant molecule, usually the tail group, adsorbs to the nanosheet surface. This results in a layer of bound ions (creating a charge) on the surface which is balanced by a diffuse layer of counterions from the surfactant head group. A combination of the these two layers (bound and diffuse counterion layers) leads to what is known as an electric double layer akin to a parallel plate capacitor model. There is an effective negative (or positive) charge surrounding each nanosheet and therefore adjacent surfactant-coated nanosheets experience an electrostatic repulsion, preventing aggregation,[233] (Section 2.4.2) On a more in-depth level, various binding orientations and mechanisms have been suggested for surfactant coated nanosheets, requiring further study in the field.[333,337–341]

Surfactants can by classified into three main types based on their ionicity namely; anionic, cationic and non-ionic. Many ionic surfactants have a common structure consisting of a long, hydrophobic alkyl chain and a hydrophilic charged head group. Anionic surfactants have a positively charged mobile counterions (e.g. Na^+) while cationic surfactants have a negatively charged mobile counterions (e.g. Br^-). Other than the chain-like structure, surfactants can also exist as facial amphiphiles with the hydrophilic and hydrophobic groups located on two opposite faces i.e. a structure with planar polarity. Facial amphiphiles tend to form smaller micelles at higher critical micelle concentrations than standard surfactants.[342]

An example of such a facial amphiphile is sodium cholate (SC). This surfactant is very commonly used for the liquid phase exfoliation of many 2D materials,[19,20,22,192] including being the surfactant of choice in Chapter 4. Sodium cholate has been noted to lie flat on the surface of graphene with its hydroxyl and carboxyl groups facing towards the aqueous solution.[343] Because of the geometric similarity of its rigid, hydrophobic surface and hexagonal lattice type structures, it yields stable graphene dispersions.[332] SC exhibits great steric repulsion from its bulky set of aliphatic rings.[332] The hydrophobicity of the tail group can be further increased with the removal of the oxygen atom in the centre of the aromatic ring forming the sodium deoxycholate (SDC) molecule. The resulting increase in hydrophobic interactions has been reported to yield higher concentrations in graphene dispersions.[334]

On the contrary, alkyl chain type amphiphiles such as sodium dodecyl sulfate absorb to graphene in a head-to-tail or tails-on configuration depending on the surfactant concentration.[341] Theoretical studies[333] on the alkyl chain group have shown that the surface coverage increases with increasing chain length. van der Waal forces in the form of chain-nanosheet and chain-chain interactions increase up to a carbon chain length of 16 (the range used in this work). The stability of graphene dispersions is noted to be largely due to mean field electrostatics from the ionic surfactants and their effective surface charge densities, rather than steric repulsion. Sodium dodecylbenzenesulfonate (SDBS), a long chain ionic surfactant, has a hydrated sulfonate group attached to a benzene ring. Benzene rings such those as seen in the non-ionic TX-100 enable strong π- π interactions with graphene's aromatic structure reportedly producing high graphene concentrations.[332] However, contrasting studies note the surfactant is hindered by its hydrated sulfonated group preventing the π system fully interacting with the graphene surface.[343]

Given the discussion above, one would expect that the efficiency of the stabilization of LPE nanosheets depends primarily on surfactant concentration and chemical structure. There have not been studies, where not only nanosheet concentration, but also lateral size and thickness were examined for a range of surfactant concentrations. TMDs are ideal model systems for a study like this due to the availability of established spectroscopic metrics. Metrics allow for the fast and reliable determination of nanosheet concentration and dimension through relatively simple UV-Vis spectroscopy.

Gupta et al., have reported studies on surfactant-stabilized TMDs (mainly MoS_2) using both the anionic SDS and cationic CTAB surfactants.[337,339] Zeta potential measurements and molecular dynamic simulations were the primary techniques used to explore the relationship between the surfactant double layer coating the nanosheet and the zeta potential. In MoS_2-CTAB and MoS_2-SDS dispersions the bound and free surfactant chains are said to undergo rapid exchange with the surfactant chains arranged flat on the nanosheet in a random fashion. More recent studies from the same authors,[339] focusing on MoS_2 in CTAB, note that at equilibrium, just under half of the surfactant chains in the MD simulation had adsorbed to nanosheet balanced on either side. It was suggested that the ions in solution cannot access the MoS_2 surface because of hydrophobic CTAB cation chains. Zeta potential was found to depend on both the surface charge and on the ionic strength

of the media. MoS_2- SDS dispersions produced a similar magnitude and effective surface charge distribution with only the sign of the zeta potential differing. Therefore, one would expect that the absolute value of the zeta potential for TMDs would not vary significantly between cationic and anionic surfactants on the same concentration.

One-dimensional carbon nanotube (CNT)-surfactant systems have been studied more extensively than 2D nanosheet systems.[344–355] Although surfactant concentrations below the critical micelle concentration (CMC) can be used to disperse CNTs,[349] CNT dispersion efficiency is greatly increased at higher concentrations than those typically used in nanosheet LPE dispersions.[344–346,348] At very high surfactant concentration ($> 10\times$ CMC[353]), there has been a reported reduction in CNT concentration due to attractive depletion interactions.[346,353,354,356,357] CNT concentrations are dependent on the nature of the surfactant molecule. Ionic surfactants stabilize nanotubes through electrostatic interactions as hydrophobic tails are thought to adsorb to the nanotube surface.[355] Meanwhile aromatic molecules, such as sodium dodecylbenzene sulphonate, adsorb strongly to the nanotube surface through π-stacking interactions of the benzene ring.[348,353] Furthermore, increasing the alkyl chain length of a surfactant results in greater hydrophobicity, increasing the nanotube dispersibility.[353] Overall, anionic surfactants have been shown to be more effective than cationics in dispersing CNTs as found experimentally by Blanch et al.[346] and Fernandes et al.[353] and investigated theoretically by Xu et al.[347] In fact White et al.[344] determined that SDS preferentially binds to nanotubes over CTAB in dispersions. The Na^+ counterion in anionic surfactants is suggested to play an important role in dispersion stabilization, balancing the electrostatic forces.[347] Overall, the CNT information available strongly indicates that dispersed concentration and dispersion quality is dependent on both surfactant concentration and type.

Due to the limited reports on TMD-surfactant systems, this chapter aims to investigate if there is an effect on the properties of nanosheets produced by liquid exfoliation as a result of surfactant type and concentration. Simple alkyl sulfates and bile salts were used in this work, where one would not expect any specific chemical interactions to occur. Aromatic interactions are the primary basis of other types of stabilizers such as pyrene-based derivatives[358–360] used in LPE where strong adsorption occurs through π-π interactions of the planar pyrene based surfaces and graphene for example. This work was carried out us-

ing a broad range of commercially available standard surfactants to investigate the role of surfactant type and its respective concentration on the resulting nanosheet concentration and dimensions. WS_2 is used as a model system because of the availability of published metrics for concentration, lateral size and layer number. Dispersions are stabilized with twelve different surfactants of varying ionicity and molecular weight (i.e. chain length) (Figure 5.1). Through both UV-Vis and Raman spectroscopy as well as zeta potential measurements, the effect of each surfactant on the concentration, lateral size and thickness of nanosheets is investigated.

5.1 Experimental Methods

5.1.1 Sample Preparation

A two-step sonication procedure was carried out to prepare LPE dispersions. The first sonication step was done in water with the aim of removing impurities present in the starting material. For a detailed discussion on experimental design see Appendix C.1. WS_2, MoS_2 and graphene dispersions were prepared by sonicating (tapered tip, VibraCell CVX, 750W) powder (WS_2 Sigma Aldrich $\sim$ 2 μm, 99%, MoS_2 Sigma Aldrich $\sim$ 2 μm, 99%, Asbury Graphite grade 3763) at a concentration of 20 g L^{-1} as standard, in 20 mL of deionised water for 0.5 h at 25% amplitude. The dispersion was subsequently centrifuged in a Hettich Mikro 220R centrifuge equipped with a fixed-angle rotor 1016 at 3,660 *g* for 2 h. The supernatant was discarded and the sediment was redispersed in an aqueous solution of chosen surfactant and concentration (Figure 5.1). It was then sonicated for 2 h at 25% amplitude with a pulse of 6 seconds on and 2 off in an ice bath to ensure cooling. The resultant dispersion was centrifuged at 27 *g* for 0.5 h to remove unexfoliated material. The sediment was discarded and the supernatant was trapped between 106 g and 21,130 *g*. For the low speed centrifugation (106 *g*), a Hettich Mikro 220R centrifuge equipped with a fixed-angle rotor 1016 was used. Once again, the sediment was discarded and the supernatant was centrifuged at 21,130 *g* in a high speed, fixed-angle 1195-A rotor. Each centrifugation step was performed at 2 h at 10 °C. The supernatant from the high speed step was discarded and the sediment was redispersed in 3 mL of chosen surfactant and concentration. The final volume of each sample varied slightly due to the variation in the amount of sediment produced. The exact volume was recorded and used for the calcula-

tion of nanosheet mass (Equations 5.7, 5.8). The high speed centrifugation also allowed for the concentration of nanosheet mass in a smaller volume. Higher concentration samples allow for easier PL/Raman analysis. Furthermore, two additional dispersions were made with SC SC 0.1 g L^{-1} and 40 g L^{-1} that were analysed by UV-Vis spectroscopy prior to high speed centrifugation where the sediment pellets out. This data (Figure 5.4) is in agreement with the data obtained using the trapping procedure.

For the stabilization test (Figure 5.11), a standard sample was prepared using 2 g L^{-1} SC. WS_2 powder was sonicated at a concentration of 20 g L^{-1} as standard, in 20 mL of deionised water for 0.5 h at 25% amplitude. The dispersion was then centrifuged at 3,660 *g* for 2 h. The supernatant was discarded and the sediment was redispersed in an aqueous solution of 2 g L^{-1} SC. This was subsequently sonicated for 2 h at 25% amplitude with a pulse of 6 seconds on and 2 off. The resultant dispersion was centrifuged at 27 *g* for 0.5 h to remove large, unexfoliated material. The sediment was discarded and the supernatant subjected to a trapping between 106 *g* and 21,130 *g*. After the 21,130 *g* ($\sim$ 21k *g*) step, the sample was divided in two with half the sediment redispersed in 2 mL each of low (0.1 g L^{-1} SC) and high (40 g L^{-1} SC) surfactant concentration respectively. The low and high concentration samples were centrifuged at 106 *g* for 2 h to remove aggregated material and the supernatant of each was analyzed with UV-Vis spectroscopy as described below.

5.1.2 Characterisation of Nanosheets

A Cary 50 spectrometer with quartz cuvettes was used for UV-Vis spectroscopy measurements, performed in 0.3 nm increments. A Veeco Nanoscope III-a (Digital Instruments) Atomic Force microscope in tapping mode with HA_HR NT-MDT cantilevers was used for AFM measurements. To prepare samples for AFM, samples were diluted until transparent. 15 μL of each sample was then dropcast onto preheated (180 °C) Si/SiO_2 (300 nm oxide layer) wafers. Bright-field TEM imaging was performed using a JEOL 2100 LaB microscope, operated at 200 kV. To prepare samples for TEM, samples were diluted until optically transparent. The samples were then manually dropcast onto a copper TEM grid with the aim of dropping approximately 0.1 mg of material. This procedure was done slowly, one drop at a time as close to the grid as possible to avoid displacing any material. The grids were left to dry in ambient conditions and then placed overnight in a vacuum at

70 °C to dry completely before measurement.

Raman spectroscopy was using an Horiba Jobin Yvon LabRAM HR800 with a 532 nm excitation laser in air under ambient conditions. The Raman emission was collected by a 100×, long working distance objective lens with 10 % of the laser power (∼ 1.4 mW). Liquid dispersions were dropped (∼ 100 μL) onto glass microscope slides and spectra were measured while the material remained in liquid form. A minimum of 8 spectra at different positions on the liquid drop were recorded and averaged.

Zeta potential and ionic conductivity measurements were carried out on a Malvern Zetasizer Nano system using a 633 nm He-Ne laser. The electrophoretic mobility (μ) was measured using laser Doppler velocimetry. The electrophoretic mobility is related to the drift velocity of a colloid (ν) via the applied electric field (E); ν=μE. The zeta potential ζ is related to the measured electrophoretic mobility μ using the Smoluchowski approximation for plate-like particles (details in Section 3.2.7). Measurements were conducted using folded capillary cells at 20 °C. 10 measurements were recorded for each sample and averaged to give a mean zeta potential value and standard error for each sample.

5.2 Results and Discussion

5.2.1 Experimental Design

The aim of this study was to identify the effect of surfactant choice and concentration on both yield and nanosheet dimension of LPE samples. WS_2 was exfoliated in a wide range of surfactants while also differing the surfactant concentration of each chosen surfactant. The exfoliation and centrifugation procedure was kept constant for each sample (see Methods 5.1 for details). The surfactants used for this work were sodium cholate (SC), sodium deoxycholate (SDC), sodium dodecyl sulfate (SDS), sodium tetradecyl sulfate (STS), sodium octyl sulfate (SOS), lithium dodecyl sulfate (LDS), sodium dodecylbenzene sulphonate (SDBS), cetyltrimethylammonium bromide (CTAB), tetradecyltrimethylammonium bromide (TTAB) as seen in Table 5.1.

Surfactant	CMC (mmol L^{-1})	Carbon chain length	Charge	Structure
Sodium Cholate (SC)	15	-----	Anionic	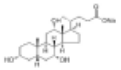
Sodium dodecyl sulfate (SDS)	8.2	12	Anionic	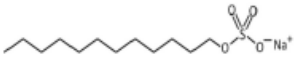
Sodium tetradecyl sulfate (STS)	2	14	Anionic	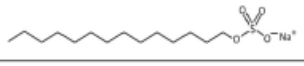
Sodium octyl sulfate (SOS)	130	8	Anionic	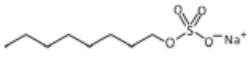
Lithium dodecyl sulfate (LDS)	10	12	Anionic	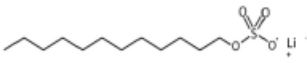
Sodium dodecylbenzenesulfonate (SDBS)	1.6	12	Anionic	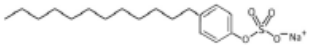
Cetyltrimethylammonium bromide (CTAB)	0.91	16	Cationic	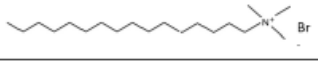
Tetradecyltrimethylammonium bromide (TTAB)	3.7	13	Cationic	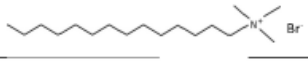
Brij® 35	0.9	-------	Non-ionic	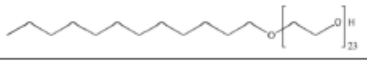
TWEEN® 20	0.06	-------	Non-ionic	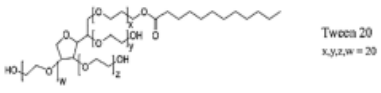
TWEEN® 80	0.012	-------	Non-ionic	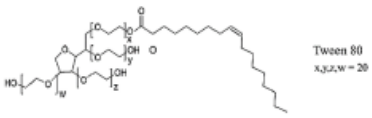
Sodium Deoxycholate (SDC)	4	-------	Anionic	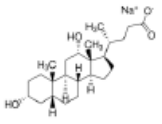

Figure 5.1: List of surfactants used in this work each with given critical micelle concentration (CMC), carbon chain length (where applicable), ionicity and structure.

After a purification step, each sample was sonicated for 2 h with a tapered tip and then centrifuged in two steps to remove the largest and smallest material (i.e. centrifuged at 106 *g* to remove large material and 21,130 *g* to remove small material, each for 2 h). For details on experimental design, see Appendix C.1. For each surfactant, nanosheets were exfoliated in surfactant solutions using 4-16 different surfactant concentrations within the global range of 0.05-40 g L^{-1}. In addition, graphene and MoS_2 were exfoliated in SC for a comparison of different materials. The starting WS_2 concentration was also varied for comparison. Examples of dispersions of WS_2 nanosheets exfoliated in solutions of SC at

varying concentrations are displayed in Figure 5.2A, showing the typical dark green colour expected for WS_2 nanosheets. It should be noted that each sample was diluted by a factor of 10 to better show the colour change which will be discussed in more detail in Section 5.2.3.

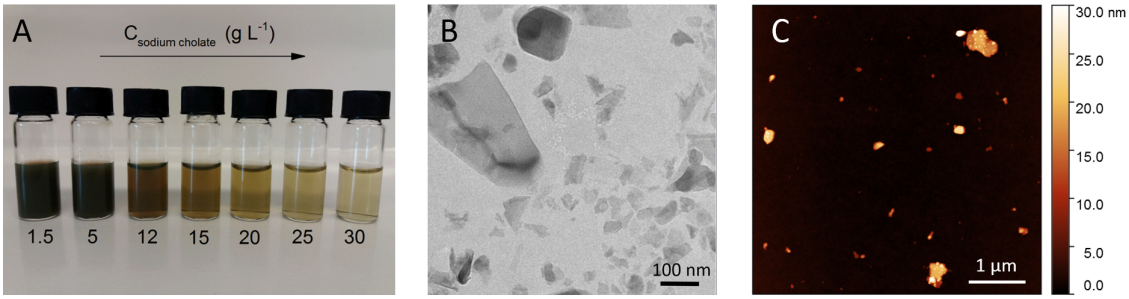

Figure 5.2: (A) Images of LPE dispersions of WS_2 nanosheets with sodium cholate surfactant showing a decrease in nanosheet content with increasing surfactant concentration. Each sample was diluted by a factor of 10 to better show the colour change. (B) Representative TEM image of WS_2 nanosheets prepared by exfoliation in sodium cholate surfactant solution (2 g L^{-1}). (C) Representative AFM image of WS_2 nanosheets exfoliated in sodium cholate (2 g L^{-1}). Each image shows a broad range of nanosheet sizes and thicknesses.

Liquid phase exfoliation yields polydisperse samples with a very broad distribution of nanosheet length and thickness. This study focused on the effects of different surfactants and so samples were not size-selected through liquid cascade centrifugation as shown in previous work[20,192] (Chapter 4). A selection of samples were characterized microscopically and are shown in Figure 5.2B and 5.2C as TEM and AFM images respectively. These images were used to confirm that the WS_2 nanosheets were in agreement in terms of lateral size and thickness to previous reports.[19,20] A sample TEM image of WS_2 nanosheets produced in sodium cholate surfactant (2 g L^{-1}) is represented in Figure 5.2B showing nanosheets with lateral sizes in the range 50 to 400 nm and demonstrating the polydispersity of the nanosheets produced by LPE. AFM images such as that displayed in Figure 5.2C show a broad nanosheet thickness variation with nanosheets varying from monolayers to 30-40 layers, in line with previous reports for WS_2 in sodium cholate surfactant (2 g L^{-1}).[20]

Although AFM images, like those in Figure 5.2C give information on the distribution of nanosheet sizes and allow for statistical analysis, measuring each sample is time-consuming. With over 90 different samples produced in this study, this technique was not

a feasible way of estimating mean nanosheet length and thickness. WS_2 was chosen as the model system for this study specifically because material nanosheet size and thickness, as well as concentration, can be extracted quickly and easily from optical spectra.[20,67]

Optical extinction spectra were measured for each sample (extinction, Ext, is related to the transmission, T, via $T = 10^{-Ext}$ and $Ext = \varepsilon C \ell$ where ε is the extinction coefficient, C the concentration and ℓ the path length) in 0.3 nm increments. The nominal surfactant and concentration was measured and subtracted as a baseline from the corresponding sample spectrum. Using previously established metrics,[20,361] the nanosheet concentration as well as mean nanosheet length and thickness can be estimated from these extinction spectra.

The extinction spectra do indeed vary with surfactant concentration as seen in a plot of extinction spectra for WS_2 exfoliated in sodium cholate at a range of SC concentrations in Figure 5.3A. The absolute magnitude of the extinction changes with surfactant concentration, indicating the concentration of WS_2 nanosheets changes as the surfactant concentration is varied. Spectral changes can be seen with more clarity in Figure 5.3B where the spectra have been normalized to the extinction at 294 nm. Significant changes in shape can be seen with varying surfactant concentration. These changes are a reflection of flake edge to basal plane ratio in each dispersion as reported previously.[19,20] The nanosheet edge ratio effects the size-dependent extinction coefficient. The extinction coefficient is also influenced by light scattering contributions.[264] This demonstrates that the mean nanosheet lateral size is dependent on the surfactant concentration, demonstrated through spectroscopic changes. The inset of Figure 5.3B zooms in on the A-exciton peak at around 650 nm. This peak appears to shift subtly with surfactant concentration as observed previously for WS_2 nanosheets.[20] The A-exciton shift can be attributed to confinement effects in the nanosheets.[19,362] As a result of the spectral changes outlined above, the extinction spectra can be used to quantitatively estimate the nanosheet concentration, length and thickness.

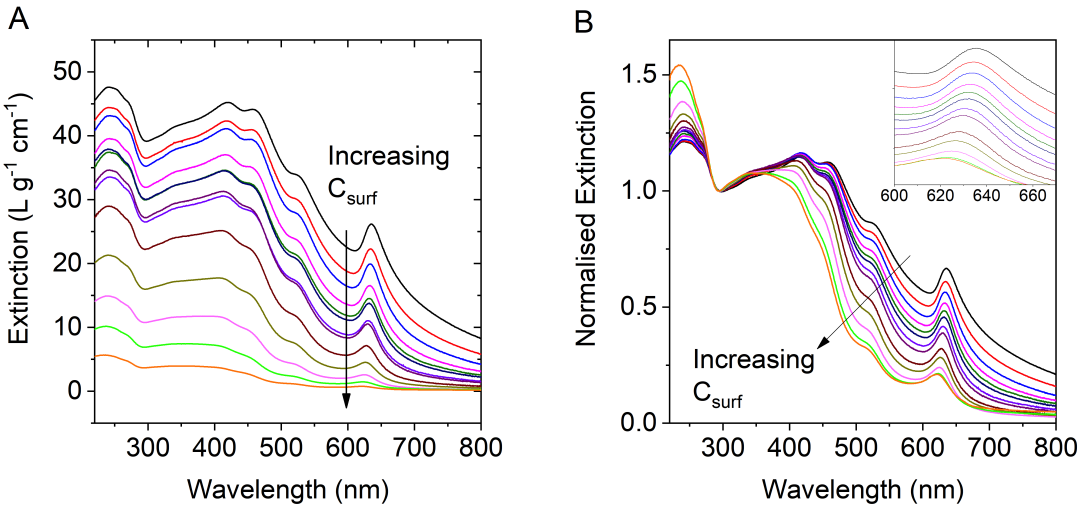

Figure 5.3: (A) Optical extinction spectra of dispersions of WS_2 nanosheets exfoliated in aqueous sodium cholate surfactant solutions with a range of surfactant concentrations from 0.2 to 25 g L^{-1} (0.46 to 58 mM). (B) The same spectra as in A, normalized to the extinction value at 294 nm. Inset: magnified view of A-exciton region.

The following metrics were used to estimate mean nanosheet thickness, length and concentration throughout this study:

Nanosheet Thickness

The mean number of layers in a dispersion was estimated using the metric described in Backes et al.[20] for WS_2 where the A-exciton was found to shift with nanosheet thickness:

$$< N >= 6.35 \times 10^{-32} e^{\lambda_A(nm)/8.51} \tag{5.1}$$

where λ_A is the position of the A-exciton. Two other 2D materials were compared in this study, each with previously reported metrics. The mean number of layers in a MoS_2 dispersion was estimated using the metric described in Backes et al.:[19]

$$< N >= 2.3 \times 10^{36} e^{-54{,}888/\lambda_{A(nm)}} \tag{5.2}$$

The mean number of layers in a graphene dispersion was estimated using the metric described in Backes et al.:[67]

$$< N >= 35.7 \times \varepsilon_{550nm}/\varepsilon_{325nm} - 14.8 \tag{5.3}$$

where ε_{550nm} and ε_{325nm} are the extinction values at 550nm and 325 nm respectively.

Nanosheet Length

As mentioned above, nanosheet edges are electronically different to the basal plane and so they have a different absorbance spectral profile. Peak intensity ratios are used to construct quantitative metrics for mean nanosheet length <L>. Early reports of WS_2 metrics for nanosheet metrics used a peak ratio in the UV region of the extinction spectra. Here, the metric used for nanosheet length was taken from extinction values in the visible region. The UV region can be problematic for high surfactant concentration due to absorbance from the surfactant itself. Furthermore the UV region of TMD spectra is highly sensitive to any oxidation. Although efforts were made to prevent oxidation, it was though that the visible range would be most accurate in the broad centrifugation range used (0.1-21k *g*). The length metric used for WS_2 from Biccai et al.:[361]

$$< \mathrm{L} >= \frac{3.698238Ext_{465nm} - Ext_{365nm}}{0.01164Ext_{365nm} + 0.00111Ext_{465nm}} \tag{5.4}$$

Similarly, the length metric used for MoS_2 from Djamil et al.:[363]

$$< \mathrm{L} >= \frac{0.48182Ext_{400nm} - Ext_{443nm}}{0.01774Ext_{443nm} - 0.02125Ext_{400nm}} \tag{5.5}$$

There is currently no length metric from optical spectroscopy reported for LPE graphene. Raman spectroscopy intensities can be used to estimate length however graphene produces much larger mean lengths for the same centrifugation conditions and so is not comparable for this study. For further information of the metrics applied to optical spectra see Appendix C.2.

Nanosheet Concentration

Nanosheet concentration was estimated through the Beer-Lambert law (Ext=εCℓ). The standard extinction coefficient at 235 nm as used in previous work[20] was deemed not suitable for this study because of the absorbance of higher surfactant concentrations in this region. Therefore, the scaling of the extinction coefficient at the A-exciton with L[20,133] was used to determine the extinction coefficient (ε_A) as follows:

$$\varepsilon_{A-exciton} = 1.82 + 3.506e^{0.0076L} \tag{5.6}$$

where L is in nm. Then the nanosheet concentration ($Conc_{NS}$) was calculated using the Beer-Lambert law as

$$Conc_{NS} = \frac{Ext_{A-exciton}}{\varepsilon_{A-exciton}\ell} \tag{5.7}$$

where $Ext_{A-exciton}$ is the extinction value at the A-exciton and ℓ is the path length. The nanosheet mass can then be estimated as:

$$Mass_{NS} = Conc_{NS} \times Vol_{Liquid} \tag{5.8}$$

5.2.2 Dependence of nanosheet concentration and dimensions on the SC concentration

Before extending the study to a wide range of surfactants, it was first important test the suitability of sample preparation and data analysis by focusing on WS_2 exfoliated in sodium cholate. Samples were exfoliated using a two-step procedure (Methods 5.1). Firstly, the starting material was exfoliated in water as a pre-cleaning step to remove impurities. Not only do impurities have an impact on the accuracy of UV Vis spectra but due to their ionic nature they also have an impact on the colloidal stability when using ionic surfactants. Figure 5.4A shows a plot of ionic conductivity as a function of SC concentration with a dashed line fit through the origin representing a linear scaling above a SC concentration of 0.5 g L^{-1}. This strongly suggests that the surfactant concentration (above 0.5 g L^{-1}) controls the electrostatic interactions in the dispersion. At very low concentrations, traces of ionic impurities left from the cleaning step have an effect on the data.

Along with UV-Vis, Raman/PL spectroscopy gives information about the monolayer population.[20] This is facilitated in high concentration dispersions with a higher signal to noise ratio. To address this requirement, the second exfoliation step was followed by the trapping of samples through centrifugation. Centrifuging at high speed allowed for the sediment to be pelleted out and redispersed in a smaller volume of surfactant solution, considerably increasing the concentration of the dispersion. The same surfactant concentration used in exfoliation was used to redisperse the nanosheets. However, it is possible that the sedimentation might have a higher local concentration of surfactant trapped be-

tween the nanosheets in the precipitate than the nominal surfactant concentration used on redispersion. To test whether there is a significant effect on the data, two samples (low and high surfactant concentration) were analysed in which the high speed centrifugation step was omitted. The non-trapped samples are plotted in Figure 5.4 below as red stars and compared to the standard SC dataset. The concentration data points were adjusted to represent as if they were redispersed in the same volume as the standard data samples. The 0.1 k *g* supernatant points appear to fall in line with the standard data, confirming that the trapped surfactant has a negligible impact. A plot of ionic conductivity as a function of surfactant concentration shows all points collapse on the same curve (Figure 5.4A). This confirms that the amount of trapped surfactant is in fact quite low and also that the pre-cleaning step removes most of the ionic impurities. If the pre-cleaning step wasn't effective, there would be an increase in ionic conductivity of the 0.1 k *g* supernatant samples (due to impurities) compared to the standard data.

Using UV Vis spectroscopy we can estimate the nanosheet concentration as well as the mean lateral size <L> in nm and mean layer number <N> from the extinction. The data displayed for these parameters as a function of sodium cholate surfactant concentration is represented in Figure 5.4B-D. For a discussion on error bars seen in Figure 5.4 and used throughout this chapter, see Appendix C.3. In Figure 5.4B, there is an initial increase in nanosheet concentration with increasing surfactant below C_{SC} 2 g L^{-1} (4.6 mM). This increase can be attributed to an increase in surfactant coverage until a maximum is reached at which point the nanosheet concentration is also at a maximum. Above this surfactant concentration however, there is a sharp decrease in the concentration of dispersed nanosheets. While <N> (Figure 5.4C) and <L> (Figure 5.4D) are invariant with surfactant concentration below C_{SC} 2 g L^{-1}, they show the same marked decrease at the same surfactant threshold. The rest of this chapter is dedicated to the decreases in nanosheet concentration and dimension and how they can be rationalized in terms of surfactant concentration and stabilization.

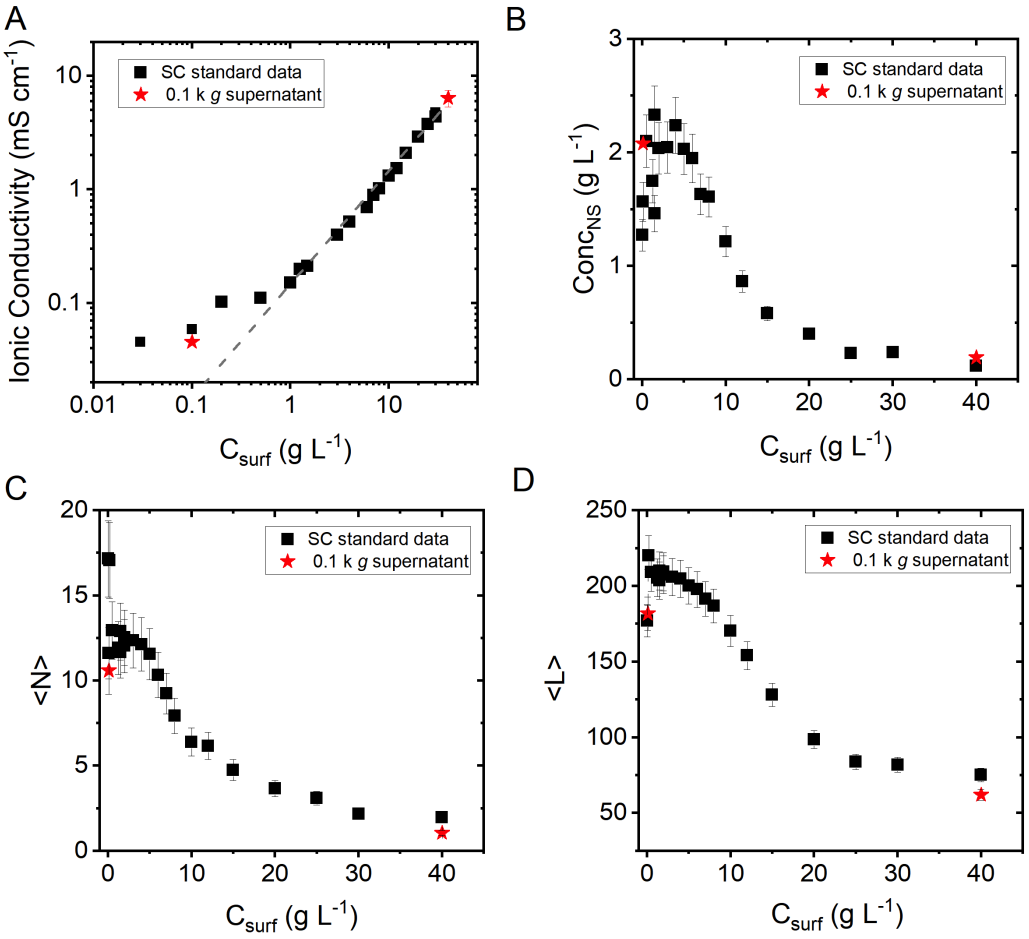

Figure 5.4: (A) Ionic conductivities of WS_2-SC dispersions as function of SC concentration. The dashed line it a linear fit (going through the origin when converted to linear-linear scale) illustrating that ionic impurities will only affect data at low surfactant concentration. (B) Concentration of WS_2 nanosheets as a function of SC concentration expressed in g L^{-1} on a linear scale. (C-D) Mean layer number <N> (C) and mean nanosheet length <L> in nm (D) versus SC concentration. The red stars are samples where the centrifugation step at high speeds (required for further PL/Raman measurements) was omitted.

5.2.3 Dependence of nanosheet concentration on surfactant concentration for various stabilizers

As mentioned above, nanosheet concentration can be extracted through the extinction spectra. Nanosheet concentration was calculated for each sample and plotted versus surfactant concentration in Figure 5.5. The surfactant concentration C_{surf} can be expressed in g L^{-1} (5.5A) and mM (5.5B) across the range used. The range of surfactant molecular weights in this study was relatively small (232-430 g/mol) and so both graphs look very

similar. Unlike Figure 5.4, the data has been plotted in log-log scale to see changes at high C_{surf} more clearly. Data includes WS_2 exfoliated in 9 ionic surfactants as well as two other 2D materials, MoS_2 and graphene exfoliated in SC. Each of these samples were prepared using a standard starting material concentration of 20 g L^{-1}. WS_2 was also exfoliated in SDS using 10 and 40 g L^{-1} WS_2 starting concentrations as a comparison. For these two samples, the nanosheet concentration in Figure 5.5A,B was corrected to account for the different starting concentration to allow for better comparison with the rest of the dataset. This was done by multiplying the estimated nanosheet concentrations by 2 for 10 g L^{-1} and 0.5 for 40 g L^{-1} starting material concentrations. For actual values see Appendix C.5. This study focused primarily on ionic surfactants and so the data and discussions presented below are for these surfactants only. The non-ionic surfactant data are represented separately in Appendix C.6 .

All the data seems to fall roughly on the same curve in Figure 5.5. At low surfactant concentration, the nanosheet concentration is roughly constant at 1-2 g L^{-1}. This agrees with previous reports showing the concentration of surfactant-stabilized graphene to vary weakly with surfactant choice.[246] However, a sharp decrease in nanosheet concentration can be seen for surfactant concentrations above a critical value of $\sim$ 5 g L^{-1} (10 mM). Nanosheet concentration decreases to as low as 0.05 g L^{-1} for surfactant concentrations of 30 g L^{-1} ($\sim$ 70 mM). Above this critical concentration (10 mM), depletion interactions[364,365] may possibly lead to the preferential flocculation of larger nanosheets leading to a decrease in nanosheet concentration. The large number of micelles at high surfactant concentration can create short-ranged depletion attractions between large nanosheets. This may in turn result in aggregation of large nanosheets which then sediment out in centrifugation, leading to a decrease in nanosheet concentration.[365]

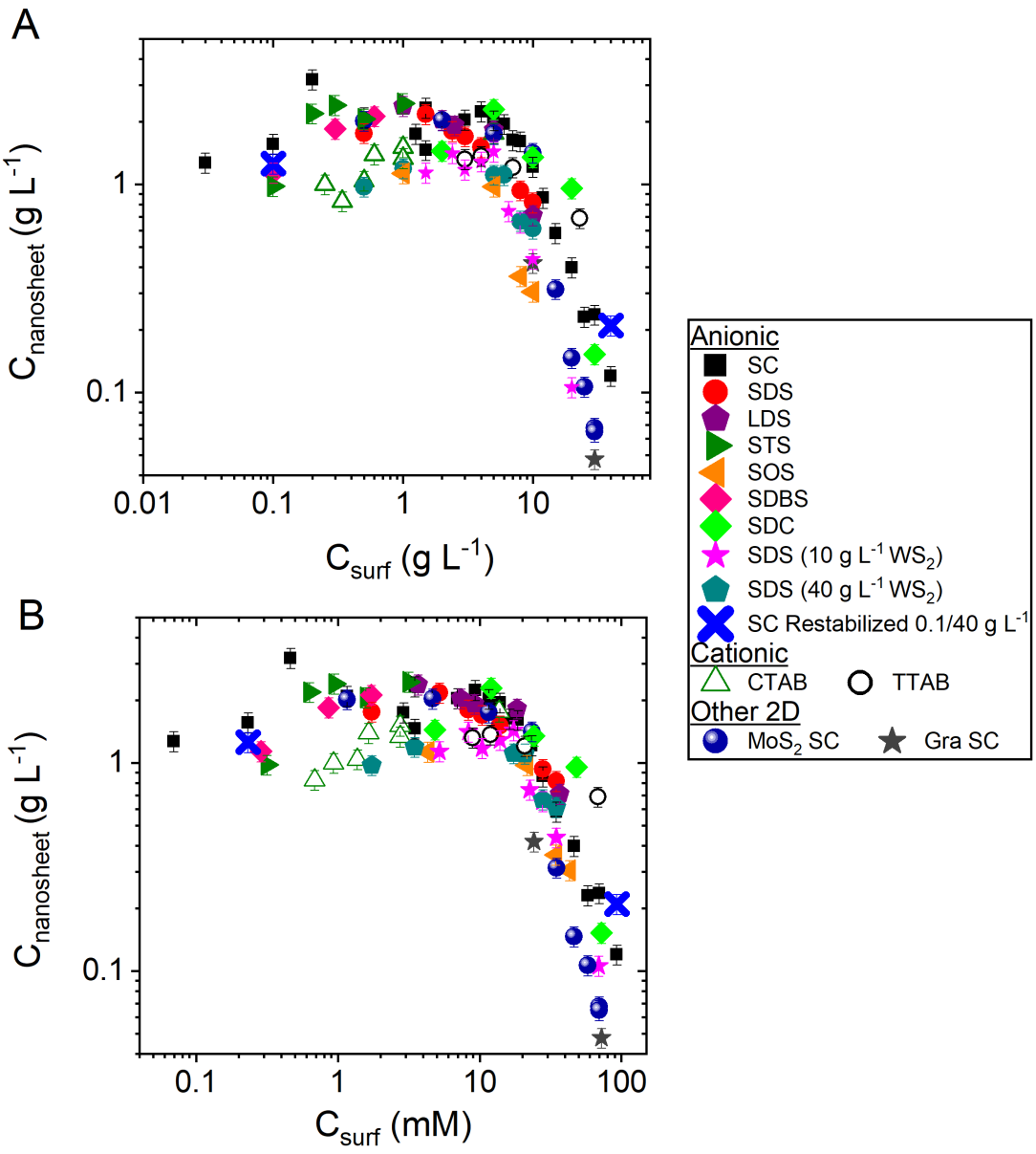

Figure 5.5: (A) Concentration of WS_2 nanosheets as a function of surfactant concentration expressed in g L^{-1} for a range of ionic surfactants. (B) The same data as A with surfactant concentration expressed in mM. Right: Symbol legend for each surfactant.

Previously, it was thought that the optimal surfactant concentration i.e. the surfactant concentration that would yield the highest nanosheet concentration was governed by the critical micelle concentration (CMC) of each surfactant.[336] More recent reports however have suggested that the CMC might not be the primary factor in determining the optimal surfactant concentration.[335] The bar chart displayed in Figure 5.6 below shows the CMC for anionics (grey), cationics (red) and non-ionic (blue) surfactants used in the

study. It should be noted that it varies broadly from ~1 to 130 mM. Generally, the alkyl chain type surfactants (both cationic and anionic) decrease in CMC with increasing chain length.[366,367] The nanosheet concentration versus surfactant concentration data shown in Figure 5.5A,B appears independent of the CMC with all data falling on a curve. Nanosheet concentration decreasing with C_{surf} irrespective of CMC is in line with data reported by Wang et al.[335]

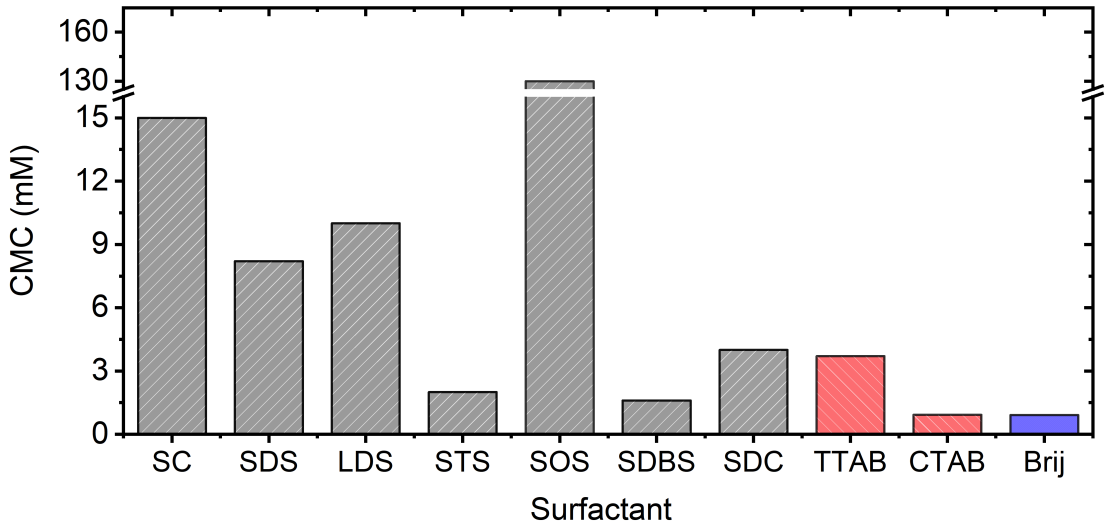

Figure 5.6: Bar chart of the critical micelle concentration (CMC) (mM) of each surfactant with anionics (grey), cationics (red) and non-ionic (blue).

This behaviour, unlike nanoparticles, suggests that the nanosheets are not encapsulated surfactant micelles. It is more likely that individual surfactant molecules adsorb on the surface irrespective of surfactant type and concentration. Interestingly, the sharp decrease in nanosheet concentration is not above the CMC of all surfactants. For example, SOS has a CMC of 130 mM while the threshold concentration at which nanosheet concentration decreases is 10 mM. This does not seem to agree with the depletion theory suggested above where micelles flocculate around larger nanosheets.[364,365] However, the local concentration of surfactant around the nanosheet may be higher than the concentration of free surfactant in solution, skewing the result. Unfortunately, there is no clear method of estimating this accurately.

5.2.4 Dependence of nanosheet dimensions on surfactant concentration for various stabilizers

In addition to nanosheet concentration, nanosheet dimensions can also be extracted from extinction spectra, one of the primary reasons in choosing WS_2 as a model system. As stated in Section 5.2.1 above, the positions and intensity of features in the extinction spectrum allow for the determination of nanosheet thickness and length. For each sample the mean nanosheet thickness, <N>, for both WS_2 and MoS_2 was calculated using the position of the A-exciton peak in previously reported metrics.[19,20] For graphene dispersions mean nanosheet thickness was calculated from the ratio of extinction values at 550 nm versus 325 nm (Ext_{550}/Ext_{325}) as reported previously.[67] Nanosheet thickness, represented as the number of monolayers per nanosheet (mean layer number <N>) is plotted versus surfactant concentration in Figure 5.7A. <N> is roughly constant at 10-15 layers for low surfactant concentrations, below 10 mM. At this point <N> decreases with increasing surfactant concentration becoming as thin as <N> $\sim$ 2 layers for very high surfactant concentrations (70 mM).

Furthermore, mean nanosheet length, <L>, for each dispersion was calculated from extinction spectra. For WS_2 the ratio of extinction at two wavelengths (465 nm and 345 nm), Ext_{465}/Ext_{365} and MoS_2 Ext_{440}/Ext_{400} , again these are taken from published metrics.[133,361,363] <L> was calculated using extinction values in the visible region to avoid any effects of oxidation in the UV region. The robustness of both <L> and <N> spectroscopic metrics were validated by performing statistical microscopy on a selection of dispersions. More details on the comparison of UV-Vis spectroscopic values to statistical microscopy values can be found in Appendix C.4. Similar to <N>, nanosheet length remains roughly constant at approximately 200 nm for low surfactant concentrations until a surfactant concentration of around 10 mM. At this point, <L> decreases sharply and reaches about 80 nm for very high surfactant concentration. It should be noted that the MoS_2 nanosheets appear smaller than the WS_2 for the same surfactant and concentration at approximately 50 nm. This may be down to a difference in the two metrics rather than a true dimensional variation. The breakdown of metrics for very small or large nanosheets depends on the material, discussed in more detail below. A comparison between cationic, anionic and non-ionic surfactants can be seen in Appendix C.7.

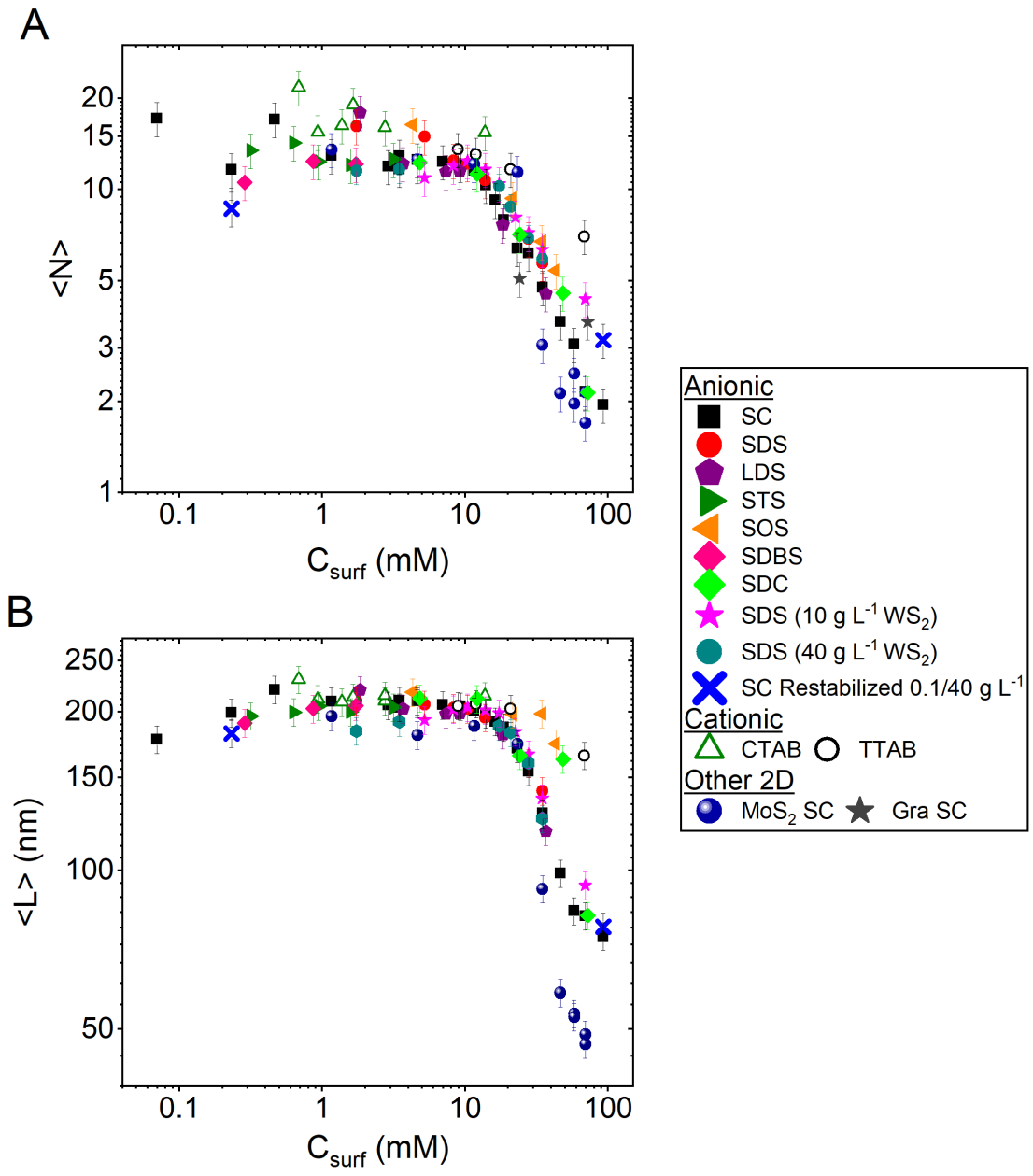

Figure 5.7: (A) Mean layer number <N> and (B) mean nanosheet length <L> versus surfactant concentration. Right: Symbol legend for each surfactant.

While the metrics discussed above can give good estimations of nanosheet dimension, care must be taken when using them. The metrics only give reliable values over certain ranges of <N> and <L>. This is particularly true for the <N> metric which does not work well for <N> > 10 layers at which point nanosheets become bulk-like. Theoretically, one would not expect a shift in A-exciton when this occurs. However due to the coupled nature of <N> and <L>, nanosheets that are thicker are also laterally larger and therefore

have increased contributions from light scattering. Artificial peak shifts of the A-exciton in extinction spectra not due to confinement and dielectric screening effects can occur as a result of scattering spectra being red-shifted to the absorbance spectra in the resonant regime. To test the reliability of the metrics $<L>^2$ versus $<N>$ is plotted in Figure 5.8A below. A recent report has shown that exfoliated nanosheet area scales roughly with a power law as $<N>^2$ due to the equipartition of energy.[202] Nanosheet area is estimated here as L^2 and this scaling is represented by the dashed line fit in Figure 5.8A. While the data below $<N> = 10$ scales well, there are clear deviations for $<N> > 10$. This may indicate that the values of $<N> > 10$ estimated in Figure 5.7A are overestimated and could be closer to 10 layers. If changes were made to reflect this thinking however, the overall trend (little variation and then a sharp decrease at 10 mM) would not change considerably. Low C_{Surf} data would just become less scattered. The similarity in $<N>$ v C_{Surf} and $<L>$ v C_{Surf} curves may be due to this general relationship. However, it remains unclear as to why both nanosheet dimension and concentration fall off about $C_{Surf} \sim 10$ mM. Moreover, the nanosheet concentration, $<N>$ and $<L>$ trends do not appear to be material dependent as shown in Appendix C.5 with MoS_2 and graphene in SC falling on the same mastercurve.

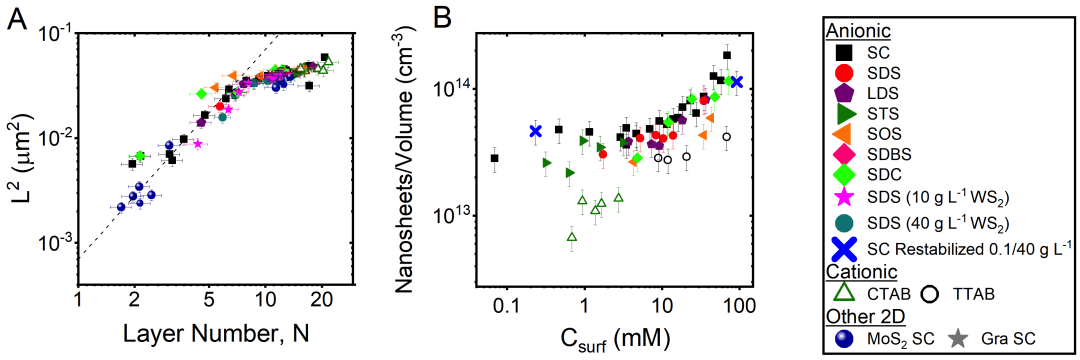

Figure 5.8: (A) Square of mean nanosheet length plotted versus layer number. As expected, $<L>^2$ vs $<N>$ follows a power law up to $<N> \sim 10$ (dashed line). The deviation above this indicates the metrics are no longer fully reliable in the range. (B) Total number of nanosheets per volume of initial exfoliated dispersion ($\sim$ 20 mL) versus surfactant concentration. Right: Symbol legend for each surfactant

The total number of nanosheets per volume in the initial dispersion ($\sim$ 20 mL) can be estimated through known nanosheet concentration and dimension. Nanosheets per volume is plotted versus surfactant concentration in Figure 5.8B and shows that the number

of nanosheets in solution varies weakly with surfactant concentration. This indicates that there may only be a certain number of nanosheets available for stabilization in a given liquid volume. The effect of surfactant stabilization is investigated in more detail in section 5.2.7 below.

Multiple comparisons can be made between different surfactants. Previous reports have shown that the hydrophobicity of the tail group can be further increased with the removal of one (of three) oxygen atoms in the molecule resulting in the surfactant sodium deoxycholate (SDC). The authors found a higher nanosheet yield resulting from an increase in the hydrophobic interactions between surfaces using SDC for graphene dispersions.[334,340] Contrary to those reports however, an appreciable difference in concentration or nanosheet dimension was not observed when comparing WS_2 dispersions stabilised with sodium cholate and sodium deoxycholate (Appendix C.5 for detailed comparison).

Focusing on cationic surfactants (shown clearly in Appendix C.7), this surfactant type does not produce WS_2 nanosheets which are quite as small or as thin as those exfoliated with anionic surfactant. It is possible that the positively charged sodium ion in the anionic surfactant plays an important role in dispersion of WS_2 nanosheets. This idea has been suggested theoretically by Xu et al.[347] for carbon nanotubes dispersed in SDS and by Poorsargol et al for graphene.[368] The higher affinity of adsorption of smaller sodium ions to the adsorbed surfactants, compared to bulkier bromine ions from cationic surfactants, may alter the inter-nanosheet attraction, leading to smaller, thinner nanosheets. However, due to the relatively high Krafft temperature of CTAB[369] (close to room temperature) it is difficult to say with certainty whether this is the case or not. The Krafft temperature is the temperature point at which the solubility of a given surfactant is equal to the critical micelle concentration. Therefore, the CTAB data might generally be obscured slightly due to the formation of crystallites instead of the intended individual molecules or micelles.

5.2.5 Dependence of monolayer population on surfactant concentration for various stabilizers

Mean nanosheet thickness falls with increasing surfactant concentration as seen in Figure 5.9A. UV-Vis spectroscopy probes the liquid dispersion as an ensemble and is related to mean nanosheet thickness through the mean found with statistical microscopy. If <N> is

small, it can be implied that the fraction of monolayers (single layer nanosheets) is large, occurring when C_{Surf} is high. Information on the monolayer population can be extracted from analysis of Raman spectra. When an LPE WS_2 sample is excited with a 532 nm laser, the measured Raman spectrum contains both material characteristic Raman modes at low shifts < 400 cm^{-1} and also a peak attributed to direct bandgap photoluminescence (PL) from monolayers (~ 2500 cm^{-1}). The ratio of PL to Raman intensities (I_{PL}/I_R) is proportional to the monolayer volume fraction due to the fact that only monolayers contribute to PL but all nanosheets exhibit the characteristic Raman modes.[20] Raman measurements were performed on liquid droplets (~ 100 μL) of each dispersion. The laser was focused approximately 3-5 μm above the surface to minimize reabsorption and inner-filter effects. Normalized Raman spectra for a subset of surfactant concentrations of sodium cholate are shown in Figure 5.9A. The characteristic WS_2 2LA(M) and E^1_2g (Γ) modes can be seen at approximately 356 cm^{-1}.[124] The spectra were normalized to this mode. In addition to these modes, a peak attributed to photoluminescence (PL) is observed at approximately 2460 cm^{-1}. A final peak at 3400-3500 cm^{-1} can be assigned to water since measurements were carried out in dispersion.

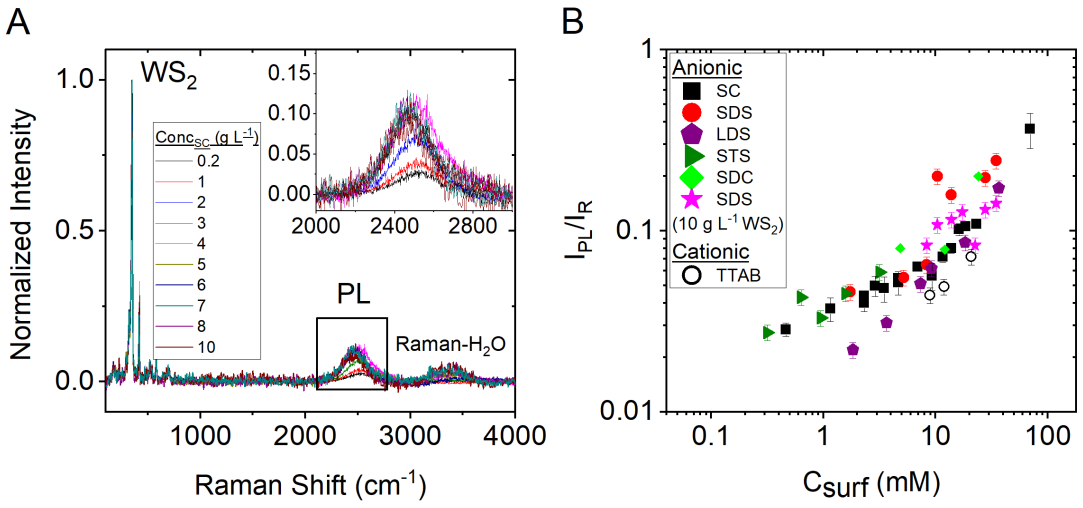

Figure 5.9: (A) Examples of Raman spectra (λ_{ex}=532 nm) for WS_2 nanosheets in sodium cholate surfactant at a range of concentrations normalized to the WS_2 Raman mode at $\sim$350 cm^{-1}. The peak at $\sim$2500 cm^{-1} is photoluminescence from WS_2 which increases with increasing surfactant concentration (inset). (B) Ratio of the intensities of PL peak and WS_2 Raman peak ($\sim$350 cm^{-1}) versus surfactant concentration.

A plot of I_{PL}/I_R versus surfactant concentration can be seen in Figure 5.9B. The peak

intensity is plotted as opposed to peak area. In agreement with previous reports for LPE WS_2,[370] the intensity and area were found to scale linearly with each other (Appendix C.8), confirming the trend still holds. The data points with the largest areas are slighlty lower in intensity than expected, most probably due to a much lower signal to noise ration from these low concentration samples, hindering the Lorentzian fit. This graph, Figure 5.9B, clearly indicates that the monolayer volume fraction increases with increasing surfactant concentration. Previous studies have shown that the monolayer volume fraction scales with layer number <N>.[202] The I_{PL}/I_R trend above confirms what was observed in UV-Vis analysis, decreasing <N> with increasing surfactant concentration. <N> varies weakly below 10mM (Figure 5.7B) which is reflected in Figure 5.9B where the I_{PL}/I_R ratio also levels off below 10 mM. This trend is more gradual than what was shown in the optical spectroscopy data which can be attributed to a limited accuracy of the PL/Raman ratio to predict the monolayer content for dispersions containing mainly few-layered sheets. Similar to nanosheet concentration and dimension, the PL intensity data falls roughly on a mastercurve just with slightly more scatter. This suggests that the monolayer population does not change considerably with surfactant type. Moreover, the fact that the trend is largely independent of surfactant type (for those under study at least), implies that this scaling is robust and valid for a broad range of stabilisers. This is contrary to what one might expect i.e. that the surfactant surrounding nanosheets would have an impact on the A-exciton photoluminescence response. It should be noted the PL position and widths varied for the different surfactants. However, the fact that all surfactants studied fall roughly on the mastercurve suggests that the monolayer PL quantum yield is similar across different surfactants resulting in an I_{PL}/I_R ratio governed by the monolayer content.

5.2.6 Dependence of Zeta potential on surfactant concentration

Surfactant-coated nanosheets are mainly stabilized by electrostatic repulsion due to the electrical double layer associated with the bound surfactant molecules (see Sections 2.4.2 and 3.2.7). A common measure of the strength of this repulsion is the Zeta potential. The zeta potential is a value for the electric potential at the edge of the bound ions to nanosheet surface. For nanosheets to be considered stable against aggregation in a colloidal system, zeta potentials need to be greater than +/-30 mV with higher zeta potentials leading to greater stability.[190] The zeta potential was measured for both cationic and anionic samples (Non-ionics C.6). Cationic and ionic surfactants gave positive and negative zeta potential respectively but for ease of comparison the zeta potential is displayed as its absolute value. The absolute zeta potential is plotted versus surfactant concentration in Figure 5.10A. All surfactant concentrations, even as low as 0.07 mM gave zeta potential values above 30 mV. Similar to both Raman and UV-Vis plots versus surfactant concentration, the zeta potential values appear to fall close to a trendline. The zeta potential appears to be roughly constant at ∼40 mV for low surfactant concentrations up to approximately 10 mM. However, it begins to increase above C_{Surf} ∼10 mM, reaching ∼70 mV for the highest surfactant concentrations. There is a difference in the trend between facial amphiphiles like SC and linear amphiphiles, alkyl chain type surfactants like SDS. There appears to be sharper increase in zeta potential with increasing surfactant concentration for the linear kind indicative of a difference in adsorption mechanism between the two.

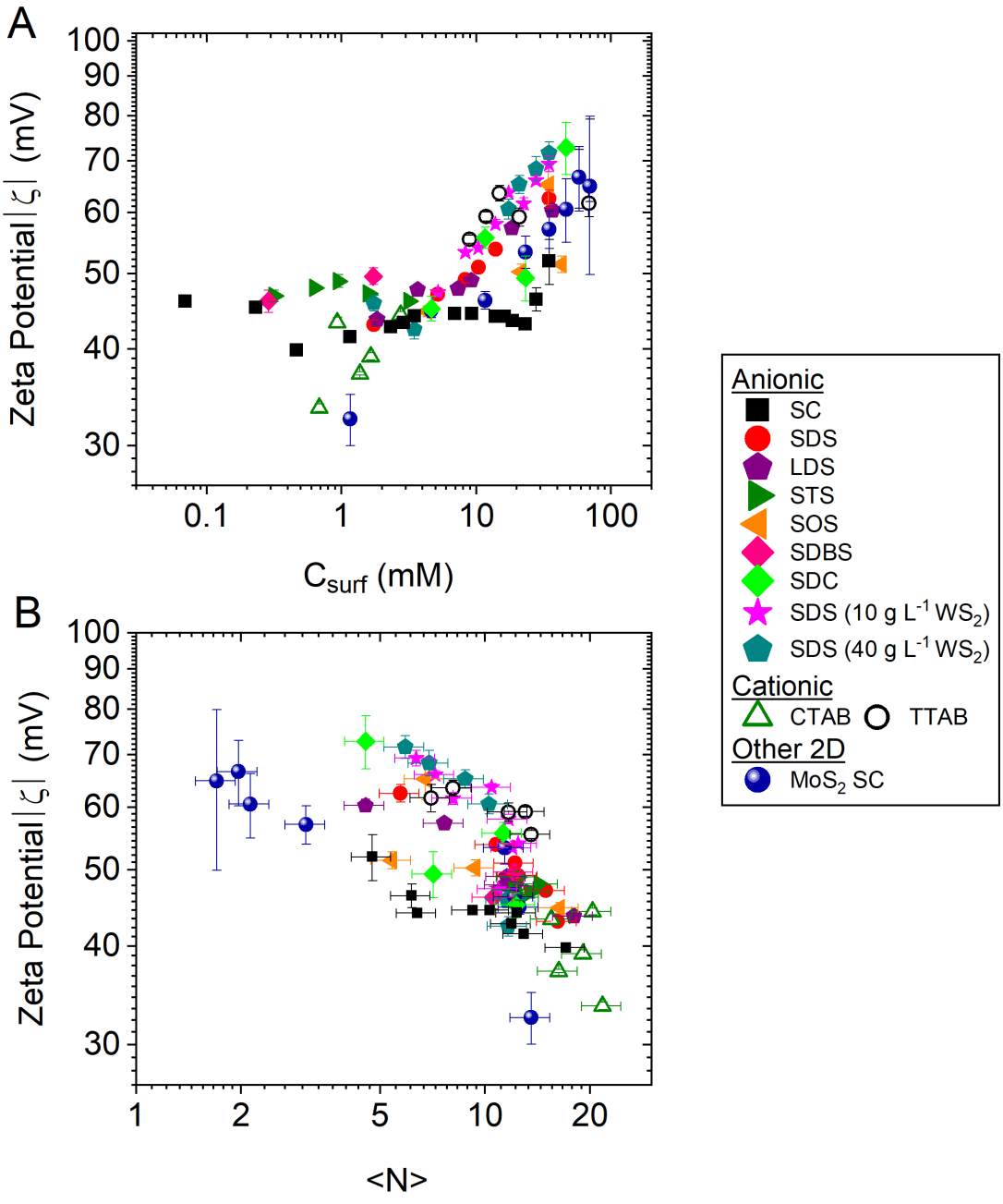

Figure 5.10: (A) A plot of the absolute value of zeta potential measurements versus surfactant concentration. (B) A plot of the absolute value of zeta potential measurements versus mean layer number <N>.

A couple of comparisons can be made at this point with all methods of material characterisation employed. Other than an increase/decrease in concentration of nanosheets produced, changing the initial concentration of WS_2 starting material does not change nanosheet dimensions, Raman or zeta potential results (Appendix C.5). In addition, changing the head group in the alkyl chain type anionic surfactants does not change con-

centration, nanosheet dimensions, Raman or zeta potential results considerably as illustrated by a comparison of lithium dodecyl sulfate (LDS) and sodium dodecyl sulfate (SDS) in Figure C.12.

Finally, returning to the Zeta potential measurements, the zeta potential as a function of nanosheet thickness <N> is plotted in Figure 5.10B showing an increase in zeta potential with decreasing <N>. As nanosheets become thinner, they also become laterally smaller resulting in an increase in the ratio between nanosheet edges to basal plane. The increased zeta potential suggests that the adsorbed surfactant density may be higher at nanosheet edges compared to the basal plane. This would result in a greater number of surfactant molecules per unit area for smaller, thinner nanosheets and in turn a higher zeta potential. Another possibility is that the edges, a source of defects in LPE WS_2, are charged in the aqueous surfactant environment. Grieger et al.[371] have recently shown that facial SC preferentially adsorbs to the basal plane of WS_2 nanosheets in comparison with linear SDS resulting in a less optimal surfactant coverage for decreasing lateral size and lowering the Zeta potential magnitude. This can also be seen in the data presented above in Figure 5.10A. Interestingly, contrary to reports by Gupta et al.[339] and Varrla et al.,[289] a drop in the zeta potential for very high surfactant concentrations was not observed due to charge screening effects from the larger pool of counterions.

5.2.7 Destabilization of nanosheets in low and high surfactant concentration

The trends represented above demonstrate a decrease in both nanosheet dimension and concentration with increasing surfactant concentration. Zeta potential measurements showed that even low surfactant concentrations resulted in stable dispersions. However, the results are for nanosheets that were coated in surfactant during exfoliation and remained in the same liquid environment after centrifugation and redispersing. In order to decouple the effect of stabilization/destabilization (i.e. redispersion of sediment after centrifugation) from the exfoliation process a sample was exfoliated using a standard surfactant concentration (2 g L^{-1} SC), trapped between 0.1k *g* and 21k *g* via centrifugation, with the sediment of 21k *g* redispersed in low (0.1 g L^{-1} SC) and high (40 g L^{-1} SC) surfactant concentrations as shown in Figure 5.11 below.

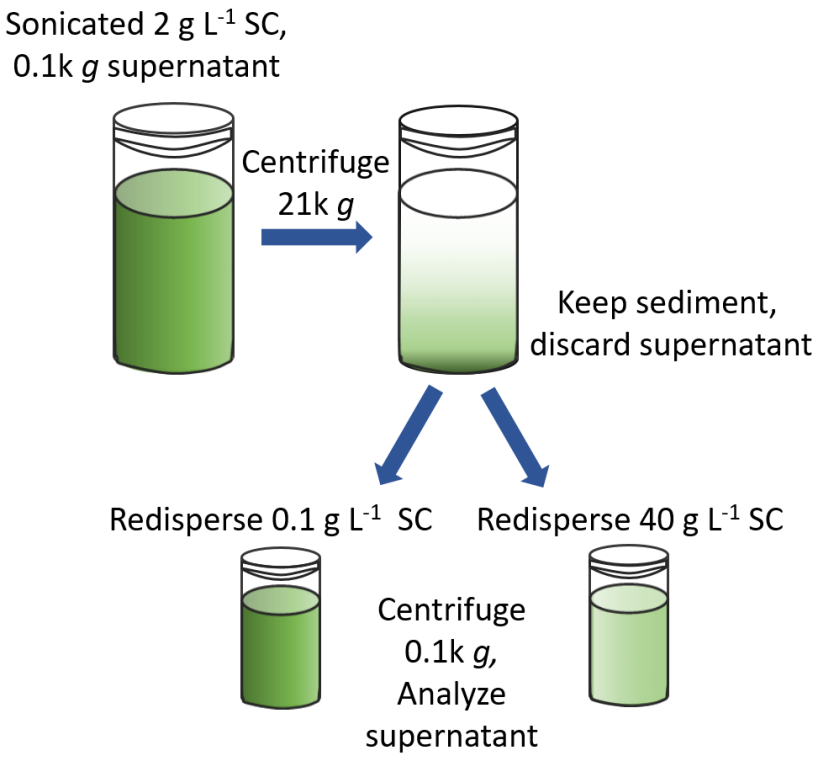

Figure 5.11: Schematic of the experiment to test the stabilization of nanosheets. An exfoliated WS_2 sample in 2 g L^{-1} SC was prepared, trapped 0.1-21k *g* with the 21k *g* sediment redispersed in low (0.1 g L^{-1}) and high (40 g L^{-1}) surfactant concentration. The samples were re-centrifuged at 0.1k *g* to remove aggregated material.

The samples were measured with UV-Vis spectroscopy, extracting nanosheet concentration, <N> and <L> from the extinction spectra. The restabilized samples were compared to a standard 2 g L^{-1} SC exfoliated and trapped sample, the 'exfoliation' surfactant concentration used. The mass of nanosheets, <N> and <L> in redispersed samples are lower compared to the original exfoliated sample as seen in Figure 5.12A-C below. Nanosheet mass was multiplied by a factor of 2 to account for the sample being divided in two after initial centrifugation.

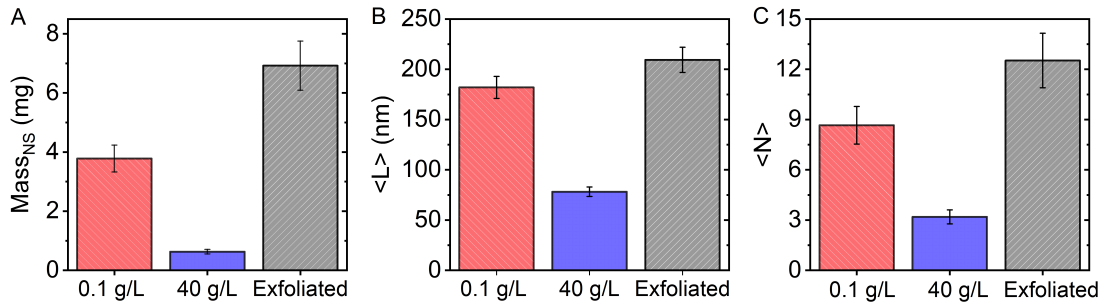

Figure 5.12: (A) Bar chart of nanosheet mass for each surfactant concentration i.e. the low (0.1 g L^{-1} SC) and high (40 g L^{-1} SC) used in the stabilization test and the original exfoliated sample (2 g L^{-1}). The calculated mass was multiplied by a factor of 2 to take into account that the original dispersion was divided in half for redispersing. (B) Bar chart of mean layer number <N> for each surfactant concentration (C) Bar chart of mean nanosheet <L> for each surfactant concentration.

This data is compared with the rest of the data sets in Figures 5.5 and 5.7, represented as blue crosses. The low and high surfactant points appear to fall on the standard mastercurves i.e. where expected for exfoliated samples, rather than only (de)stabilized, in their given surfactant concentrations. The high surfactant concentration point may appear slightly larger in <N> and <L> than the standard exfoliated data point of the same surfactant concentration. However, this is not an appreciable difference and the overall trend remains valid. This is an interesting result, suggesting that surfactant choice does not necessarily effect the exfoliation of nanosheets during sonication, but has a great impact on their stabilization. This agrees with previous work showing graphene can exfoliated in water with brute force but will only stabilize in suitable liquids.[209]

Moreover, similar results were demonstrated by Fernandes et al.[353] for 1D carbon nanotube systems. They suggested that the dispersion effectiveness is related to surfactant binding and availability in stabilization rather than exfoliation. As shown in Figure 5.8B, the number of stabilized nanosheets does not vary considerably with surfactant concentration. However, the nanosheet dimensions do change roughly from 200 nm to 50 nm and 10+ layers to 2 layers. It is clear that the nanosheets are destabilized at high surfactant concentration causing a drop in nanosheet concentration, <N> and <L>, occurring at a surfactant concentration threshold of 10 mM.

It is still unclear as to why the sharp decrease is seen at this surfactant concentration in particular but the overall destabilization effect is proposed to be as a result of electrostatic

screening. Ionic conductivities were measured for each sample in situ with Zeta potential. Intuitively, the ionic conductivity increases with increased ionic strength from the addition of more ionic surfactant as seen in a plot of ionic conductivity versus surfactant concentration for the 3 types of surfactant in Figure 5.13. The non-ionic surfactant data has been added at this point as a comparison.

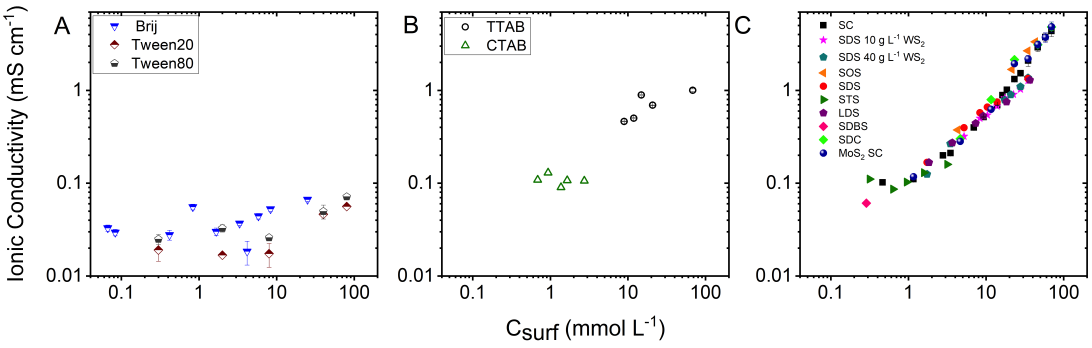

Figure 5.13: Ionic conductivity plotted versus surfactant concentration for (A) Nonionic (B) Cationic and (C) Anionic surfactants. The fact that the ionic conductivity in the CTAB samples does not increase with increasing surfactant concentration might be a manifestation of the relatively high Krafft temperature of 25 °C.[369] The linear scaling of the ionic conductivity with the nominal surfactant concentration above 0.5 mM strongly suggests that potentially trapped surfactant in the pelleted out nanosheets has a negligible effect.

The non-ionic surfactants display small (and non zero) ionic conductivities due to remaining impurities in dispersions. The destabilization effect is reflected in plots of nanosheet concentration, <L> and <N> as function of ionic conductivity (Figure 5.14). The concentration data is a bit scattered however it is clear that all <L> and <N> data falls on a mastercurve including the non-ionic surfactants. This relates to Figure 5.14 only, concentration and nanosheet dimensions of non-ionic surfactant samples deviated from trends above 10 mM when analysed versus surfactant concentration in the previous Section 5.2.4. It is worth emphasising however that the non-ionic surfactants only display this ionic conductivity due to the presence of impurities. The drop in <N> and <L> occurs at an ionic conductivity of $\sim$0.5 mS cm^{-1} indicating that the threshold conductivity for electrostatic screening (resulting in destabilization) is at this value.

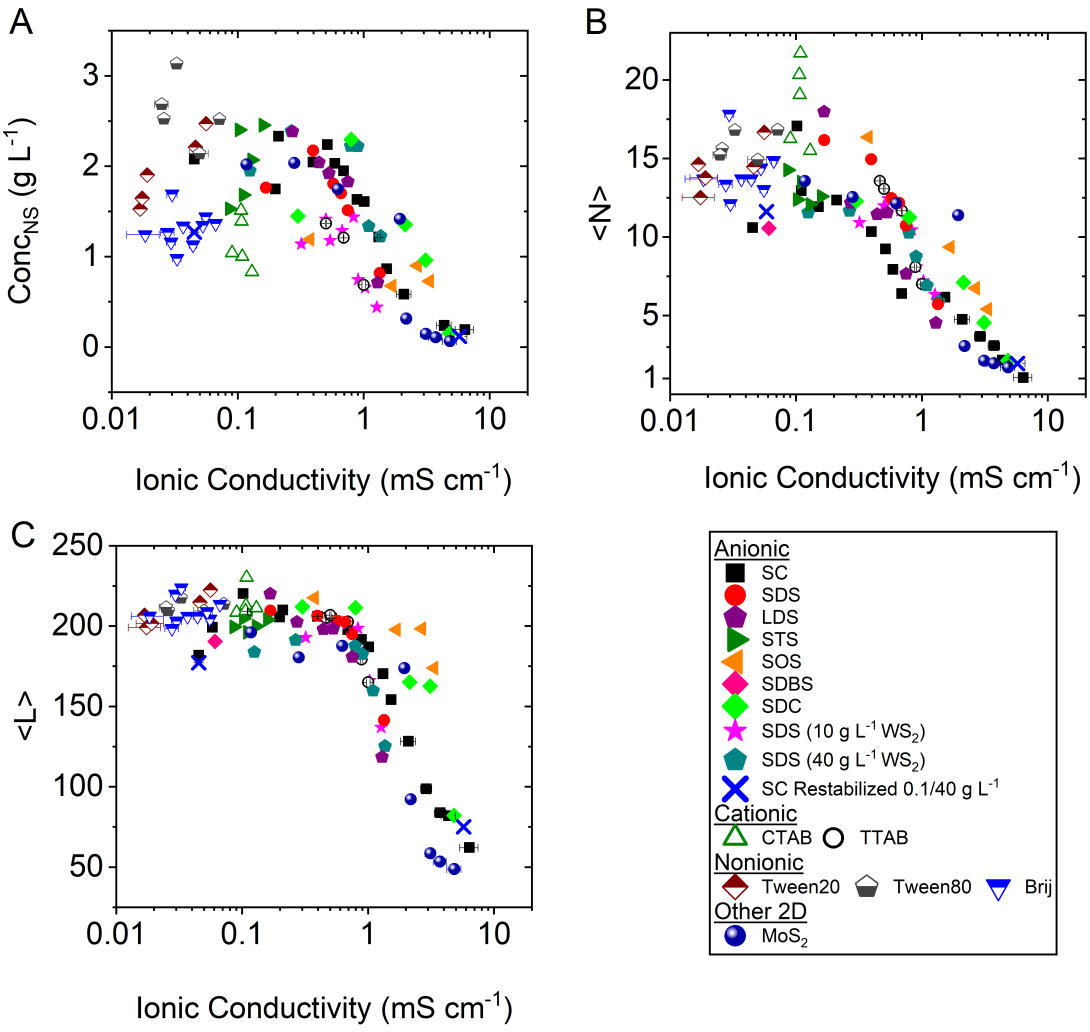

Figure 5.14: (A) Nanosheet concentration (B) Mean layer number <N> plotted versus ionic conductivity (C) Mean nanosheet length <L>. Bottom right: legend. While the concentration data is scattered, it is clear that the nanosheet dimensions are governed by the ionic conductivity with all data, including non-ionic surfactants collapsing on a curve. The exception is <N> for the CTAB samples. This could be due to the fact that some surfactant has already crystallized in this case which results in an increased scattering background which has an impact on the determination of <N> from the A-exciton peak position.

5.3 Conclusions

Laterally smaller and thinner nanosheets on average were detected at surfactant concentrations above ∼10 mM. The average number of layers falls as low as 2 with lengths as low as 50 nm for very high surfactant concentration (70 mM). Nanosheet concentration also decreases at the same surfactant concentration threshold of 10 mM. Raman spectroscopy confirms that the monolayer population increases with increasing surfactant concentra-

tion, in agreement with optical spectroscopy. The zeta potential increases with decreasing nanosheet size most likely as a result of increased edge effects for smaller nanosheets. Even very small concentrations of surfactant ($\sim$0.07 mM) give stable dispersions. In general, all ionic surfactants studied behave in a similar manner with respect to nanosheet exfoliation. There was no appreciable difference when varying chain length, head group ion or with the removal of the oxygen atom in the case of sodium deoxycholate. Therefore, surfactant choice is less important than might be expected. Other factors such as cost and environmental effects could prove more important when choosing a suitable surfactant for liquid phase exfoliation. Upon measurement of ionic conductivity, all surfactants including non-ionics (due to the presence of adsorbed impurities) fall on the same curve for nanosheet dimensions. A threshold ionic conductivity value of 0.5 mS cm^{-1} was noted to be the point at which electrostatic screening takes effect resulting in destabilization of nanosheets in dispersion.

6

I often say that research is a way of finding out what you are going to do when you can't keep on doing what you are doing now

–Charles F. Kettering

Novel 2D materials for battery applications: SnP_3 and SiP

***

THERE HAS BEEN A RAPID INCREASE in energy generation and storage research in recent years in response to the ongoing climate-change crisis. The improvement of lithium ion batteries (LIBs) resulting in higher energy densities would help the development of electric vehicles and bulk energy storage. Enhancing the performance of electrodes is vital in the overall improvement of LIBs. Layered 2D materials have both high surface areas compared to bulk and the potential to store large amounts of lithium via intercalation between the layers or via conversion reactions.[372] Furthermore, they are predicted to perform at high rates as a result of the high diffusivity of ions between the layers.[373,374] High capacities and greater stabilities have been shown for electrodes fabricated from liquid-processed and exfoliated nanosheets in comparison to those produced with unexfoliated layered particles.[375,376] To date, specific capacities (measure of discharge current over time, normalised to the total electrode mass) have been reported for a number of 2D electrodes including graphene (700 mAh g^{-1})[377] and MoS_2 (1200 mAh g^{-1}).[378]

In recent years, multiple 2D databases have been published,[379–382] predicting hun-

dreds of stable 2D crystals with a wide range of electric and magnetic properties. Among these lists are unexplored electrode materials with the potential for effective Li storage. Yushin et al.[27] have reported the gravimetric and volumetric capacities for a range of elements in a version of a periodic table shown in Figure 6.1. Elements in group 14 and 15 such as silicon, germanium and phosphorous are predicted to have the highest capacities for Type B conversion anodes (yLi + X $\leftrightarrow$ Li$_y$X). It was a combination of the 2D databases and the elemental capacity predictions that two new materials were chosen, namely SnP_3 and SiP. The databases were scanned for compounds with the following criteria. Firstly, that they were commercially available or could be synthesised in a research laboratory and secondly that they contained silicon and/or phosphorous. SnP_3 has a theoretical storage capacity of 1670 mAh g^{-1} for both lithium and sodium while SiP, containing two high capacity elements has an even higher theoretical capacity of 3060 mAh g^{-1} for lithium. Layered SnP_3 was tested by Park et al.[383] as an anode material but capacities were far below theoretical values at 700 mAh g^{-1} and space for improvement. To date, SiP has not been tested as an electrode material.

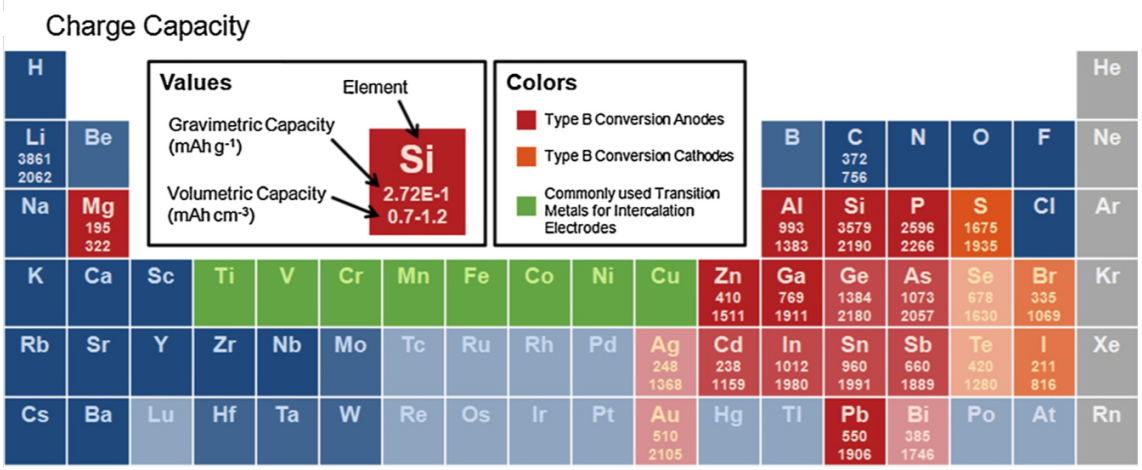

Figure 6.1: Periodic table of elemental capacities for lithium ion batteries, image from Nitta et al.[27] The elements silicon and phosphorous are predicted to have the highest gravimetric and volumetric capacities for Type B Conversion Anodes.

In this chapter synthesised SnP_3 and SiP, by collaborators at Universität Leipzig, are liquid exfoliated and characterised with spectroscopy and microscopy. Both materials display size-dependent spectral changes in UV-Vis and Raman spectroscopy. SnP_3 produces relatively thicker nanosheets compared to SiP with the exfoliation efficiency calculated for each. Both materials are fabricated into nanotube-enhanced composite anodes and reach

near theoretical specific capacities. Full-cells based on SnP_3-CNT electrodes are shown to display extremely high areal capacities.

SnP_3

The structure and synthesis of bulk SnP_3 can be traced back to the 1970s by Gullman et al.[384] SnP_3 crystallizes in the A7, α-arsenic type structure, each layer consisting of puckered phosphorous rings connected by tin atoms as shown in Figure 6.2A. The bulk form belongs to the trigonal R3m space group,[384] analogous to GeP_3, in which monolayers are stacked in ABC pattern such that every third layer is repeated.[385,386] The bond angles between bulk and monolayer SnP_3 differ quite considerably (10-15%),[385,387] with larger bond angles for monolayer SnP_3. Therefore single layer SnP_3 puckers to a greater extent with a shrinkage of the lattice parameters, a key force in the band structure transition described in more detail below. Gong et al.[387] calculated that the vertical interlayer distance of bulk SnP_3 is 1.94 Å, much shorter than other van der Waals crystals such as graphite and h-BN (d=3.36 Å[388]), MoS_2 (6.2 Å).[389]

The larger interlayer distance may play a role in the calculated cleavage energies of SnP_3, a measure of how easily the material can be exfoliated from bulk. The values reported vary from model to model but are in the range 0.71 -1.36 J/m^2 for monolayer SnP_3 and 0.45-0.78 J/m^2 for bilayer.[385,390,391] GeP_3, a similar structure has a predicted value of 0.91 J/m^2.[392] Ramzan et al.,[390] note that the cleavage energy should be equal to or below 1 J/m^2 for possible exfoliation of a material through micromechanical or liquid phase methods. They therefore suggest that exfoliation of monolayer SnP_3 may in fact be impossible due to instability. However, contradicting reports[385,386] calculate cleavage energies below 1 with monolayer exfoliation stated as feasible.

The electronic band structure of bulk SnP_3 shows multiple bands crossing the Fermi level and is noted to be metallic in nature.[386,387] Interestingly, both monolayer and bilayer SnP_3 are indirect semiconductors of 0.72 and 1.02 eV[386] respectively. The more puckered monolayer structure leads to a decreased strength in the π bonding between the Sn and P atoms while at the same time increasing the overlap between the σ and π orbitals. This results in the weakened electrical conductivity of monolayer SnP_3, a semiconducting material.[393] The valence band maximum is located at the K point while the conduction band minimum appears at the G point, leading to the indirect gap.[386] The

increase in band gap from mono to bilayer is contrary to GeP_3[392] (decreasing bandgap) but in line with arsenene and antimonene.[394] The semiconductor to metal transition occurs when N reaches 3 layers.[385,386,390,391] Sun et al.[386] suggest that trilayer metallic transition could be due to the interlayer interactions given that the structure stacks in an ABC type sequence. Other authors[391,393] propose that the transition is a result of quantum confinement effects, however it may in fact be a combination of both of these theories.

Theoretical absorption studies reveal that both monolayer and bilayer SnP_3 give absorption coefficients on the order of 10^5-10^6 cm^{-1}.[385,386] The monolayer mainly absorbs in the IR range between 1 and 2 eV while bilayer can absorb in IR, visible and near UV-range.[386] The values are comparable with organic perovskite solar cells,[395,396] currently at the forefront of research in the optoelectronic field. Therefore, it is no surprise that future applications for 2D SnP_3 include LEDs, photovoltaic solar cells.[385,387,391] As well as excellent optical properties, SnP_3 is predicted to be 4-10 times less stiff than MoS_2 or graphene,[385] indicating that the material may be suited for flexible electronics. Gas sensing[397] and thermoelectrics[398] are other areas of note for future exploration. The layered structure of SnP_3 in addition to its phosphorous rich elemental composition make the material a very promising candidate for energy storage applications as anodes in both lithium and sodium ion batteries.[383,393] This application is explored in more detail in Section 6.2.3, where LPE SnP_3 is demonstrated to have a very high storage capacity in lithium ion batteries.

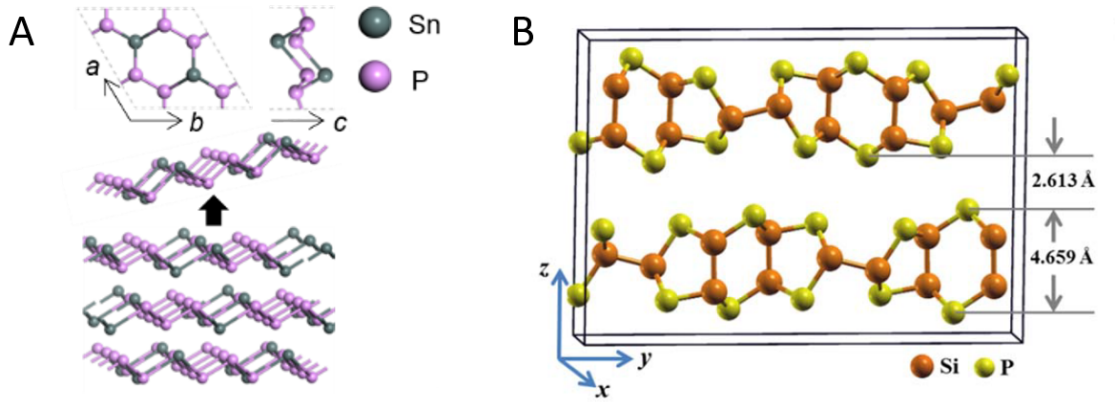

Figure 6.2: (A) Atomic structure of SnP_3 crystallises as an α-arsenic type (B) Atomic structure of orthorhombic SiP, image adapted from Shu et al.[399]

SiP

A group IV-V compound, SiP was first found on the surface of silicon that had been heavily doped with phosphorous.[400] A few years later, in 1966, Beck et al.[401] studied bulk SiP grown by vapour growth on silicon substrate. In the 1970's further investigations into P-doped silicon substrates led to microscopic examinations of silicon phosphide precipitates.[402–404] More recently synthesis methods have included high pressure melt and chemical transport techniques.[405,406] The explosion of interest in 2D materials since graphene was experimentally isolated in 2004[9] has led to the exploration of a range of van der Waals type crystals and the general desire to create materials on the nanoscale. SiP is no different in this respect with reports of CVD grown nanostructures published in recent years[407,408] as well as a large number of theoretical predictions for both monolayer and 2D SiP.[399,399,409–418]

Silicon phosphide crystals have an orthorhombic layered structure, possessing Cmc21 symmetry as shown in Figure 6.2B.[399,405,407,408,413,418,419] Each Si atom is covalently bonded to a further Si atom and 3 phosphorous atoms, creating a rectangular unit cell. Singles layers are stacked with a large interlayer spacing, (6.803 Å[413]) and weak interaction force between each layer. Other 2D materials with similar interlayer spacing include MoS_2 (6.015 Å[420]), a very commonly studied semiconductor, indicating that SiP is a prime candidate for ion intercalation and exfoliation.[408,413] These strong in-plane bonds and weak interlayer bonds, characteristic of van der Waals materials, having led to the calculation of the possible exfoliation of SiP. Ashton et al.[409] predicted the formation energy of SiP to be approximately 70 meV/atom, the same as graphene, suggesting that exfoliation should be relatively facile. The structure is noted to orientate in the [0,0,1] direction with cleavage favourable in this plane.[408,410] The exfoliation energy has been theoretically calculated to be between 0.235[399]and 0.26[410] J/m^2. To put this in perspective, graphite has a predicted exfoliation energy of 0.37 J/m^2,[421] similar to the SiP exfoliation energy, a suggestion of comparatively easy exfoliation.

Bulk SiP is semiconducting in nature with an indirect bandgap, reported values ranging from 1.23 eV[413] to 1.7 eV.[406,418] The band gap increases when the number of layers is reduced, analogous with the one-dimensional infinite well model where the bandgap Eg and layer number N are akin to the energy eigenvalue and width of the well respectively.[399]

Similar behaviour can be seen in TMDs[121] and black phosphorous.[422] An indirect-to-direct bandgap transition is observed when the number of layers reaches 1, i.e. for SiP monolayers.[399,412,418] At this point both the valence band maximum and conduction band minimum are located at the gamma point, with a calculated band gap reported in the range 1.82-2.64 eV,[399,410,412,415,418] depending on models.

Semiconducting SiP is predicted to exhibit significant excitonic effects in optical absorption spectra. Strong absorption in the visible and near UV range is reported from 2 to 4.5 eV for SiP monolayers.[399,410] Moreover, monolayers are noted to show strong UV absorption with an absorbance peak at 5 eV.[410] Zhang et al.[418] demonstrated that as bulk SiP is reduced to just a few layers, the absorption features are blue shifted with increasing bandgap to the range of visible light. Both the tunable bandgap and high carrier mobility makes 2D SiP a potential candidate for novel electronic and optoelectronic devices.[399,408,410,413,418] In its bulk form, SiP has been shown to have fast laser responses, an indicator that it may be used as a sensitive photodetector.[406] Furthermore, SiP's elemental composition containing both Si and P, the highest elemental charge capacity materials (3579 and 2569 mAh g^{-1} respectively[27]), propel it to the forefront of promising materials for energy storage applications.

6.1 Experimental Methods

6.1.1 SnP_3

Starting materials and synthesis method was performed by collaborators at Universität Leipzig, Germany. Details can be found in Appendix D.1. The powder was sonicated (tapered tip, VibraCell CVX, 750W) in 30 mL of 1-methyl-2-pyrridone (NMP, Sigma Aldrich HLPC grade $\geq$ 99%) for 5 h at pulse of 6 s on and 2 s off and an amplitude of 25%. The dispersion was then centrifuged in a Hettich Mikro 220R centrifuge equipped with a fixed-angle rotor 1016 at 26 *g* and the supernatant retained. The sediment was redispersed in 30 mL fresh NMP and exfoliated again for 16 h (overnight). The dispersion was centrifuged at 26 *g* and supernatant retained. The exfoliation procedure above was then repeated such that 4 $\times$ 26 *g* supernatant samples were produced. These samples were centrifuged at 2.6 k *g* and the sediment of each was redispersed in 5 mL IPA and

combined to give a 20 mL standard sample trapped between 0.026-2.6 k *g*.

For size selected samples SnP_3 powder was exfoliated as above and the 26 *g* supernatant was subject to increasing iterative centrifugation steps termed Liquid Cascade centrifugation as described in previous work.[20] The sediment of each centrifugation speed was collected and redispersed in IPA and the supernatant was moved to a higher speed. The speeds used for centrifugation were 0.026, 0.1, 0.4, 1, 1.6 and 2.6 k *g*. Samples were labelled according to the lower and upper centrifugation limits used to produce each fraction. For example, a supernatant was produced after centrifuging at RCF = 400 $\times$ *g*-force (0.4 k *g*) and the resultant supernatant was centrifuged at 1000 *g*. The sediment collected after the 1 k *g* step was referred to as the 0.4-1k *g* fraction.

Optical spectra were measured using a Perkin Elmer Lambda 1050 UV-Visible spectrometer with a quartz cuvette (path length 4 mm). The spectrometer was equipped with an integrating sphere for measuring the absorption where scattering effects are removed. To determine the extinction coefficients, nanosheet concentrations of size selected samples were determined gravimetrically by Dr Andrew Harvey. Samples were filtered through alumina membranes, washed with 500 mL of water and once dried were weighed.

A Horiba Jobin-Yvon LabRAM HR800 was used to acquire the Raman spectra with a 633 nm excitation laser in air under ambient conditions. Raman spectroscopy was performed by Dr Victor Vega-Mayoral. Laser spot on the sample was focused in 2 μm with 0.2 mW power. Scattered light was collected by a long working distance objective with a magnification of 100$\times$. A diffraction grating of 600 grooves was chosen, obtaining $\sim$1.5 cm^{-1} spectral resolution. Each spectrum is the average of 16 different spectra, each of them integrated for 30 seconds. Measurements were performed on both drop-cast and filtered SnP_3 thin films. Liquid dispersions (15 μL) of size selected samples were diluted until transparent and drop cast onto preheated (180 °C) Si/SiO_2 (300 nm oxide layer) wafers. AFM was subsequently carried out on a Bruker Multimode 8 microscope in ScanAsyst mode with Oltespa R3 cantilevers.

In preparation for TEM imaging, each dispersion was diluted to optical transparency and manually drop-cast one drop at a time onto a holey carbon TEM grid with the aim of dropping approximately 0.1 mg of material. The grids were left to dry in air and then

placed overnight in a vacuum oven at 70 °C to dry completely before measuring. Bright field TEM imaging was performed using a JEOL 2100 microscope. Energy-dispersive X-ray (EDX) spectroscopy was performed in situ with TEM imaging using an 80 mm^2 XMAX EDX detector. 36 nanosheets were selected at random and elemental analysis was performed with Cliff Lorimer thin ratio section quantitation method. The TEM and EDX measurements were performed by Dr Andrew Harvey.

SEM images of the SnP_3 powder, the prepared SnP_3 and SnP_3:SWCNT composite films were obtained using a Zeiss Ultra Plus scanning electron microscope by Cian Gabbett. Accelerating voltages of 2 - 5 kV, with a 30 μm aperture at a working distance of 3-6 mm were used. The pure SnP_3 and the SnP_3:SWNT composite films were imaged on the polymer filtration membrane and the Al current collector, respectively. In order to minimise charging, the sides of the samples were coated with silver paint. Furthermore, the SnP_3:SWNT composite films were snapped at room temperature and the fractured sides were looked at for the cross-sectional images.

6.1.2 SiP

Starting materials and synthesis method was performed by collaborators at Universität Leipzig, Germany. Details can be found in Appendix D.1. The powder was sonicated (tapered tip, VibraCell CVX, 750W) in 30 mL of 1-methyl-2-pyrridone (NMP, Sigma Aldrich HLPC grade $\geq$ 99%) for 5 h at pulse of 6 s on and 2 s off and an amplitude of 25%. The dispersion was then centrifuged in a Hettich Mikro 220R centrifuge equipped with a fixed-angle rotor 1016 at 26 *g* and the supernatant retained. The sediment was redispersed in 30 mL fresh NMP and exfoliated again for 16 h (overnight). The dispersion was centrifuged at 26 *g* and supernatant retained. The exfoliation procedure above was then repeated such that 4 $\times$ 26 *g* supernatant samples were produced. These samples were centrifuged at 2.6 k *g* and the sediment of each was redispersed in 5 mL IPA and combined to give a 20 mL standard sample trapped between 0.026-2.6 k *g*.

Size selection characterisation was carried out a Heidelberg University, Germany. A 'stock' sample was made in Dublin as described above but the high speed 2.6 k *g* step was omitted. The 26 *g* supernatant samples were brought to Germany and size selection/characterisation was performed there. A centrifugation cascade was used to separate

the sample into a range of sizes. At each iteration the supernatant was decanted from the sediment and subjected to an increased speed. Meanwhile, the sediment was collected and redispersed in IPA. The centrifugal speeds used were 0.1, 0.4, 1, 3, 6 and 35 k *g*. The time for each centrifugation step was 2 h at 15 °C. For low speed ($<$ 3k *g*) a fixed-angle 1016 rotor was used in a Hettich Mikro 220R centrifuge (4 $\times$ 50 mL vials filled with 20 mL dispersion). For speeds over 3k *g*, a Beckman Coulter Avanti XP centrifuge was used with a JA25.15 rotor (8 $\times$ 14 mL vials filled with 10 mL dispersion each). Samples were labelled according to the lower and upper centrifugation limits used to produce each size. For example, a supernatant was produced after centrifuging at RCF=1,000 $\times$ *g*-force (1k *g*) and the resultant supernatant was centrifuged at 3,000 *g*. The sediment collected after the 3k-*g* step was referred to as the 1-3k *g* fraction.

Atomic force microscopy was completed using a Bruker Icon Dimension Atomic Force microscope in ScanAsyst mode with Bruker OLTESPA-R3 cantilevers. Each liquid sample was diluted until the sample was transparent (optical density of approx. 0.2). 10 μL of each sample was drop cast onto a pre-heated (180 °C) Si/SiO_2 (300 nm oxide layer) wafer. Individually deposited nanosheets were analysed through measurement with the AFM. Previously established length corrections[423] were applied to correct nanosheet length from tip broadening effects.

A Cary 6000i spectrometer along with quartz cuvettes (path length 4mm) were used for optical extinction and absorbance measurements. Each size selected dispersion was diluted by an appropriate factor for the spectrometer (optical density approx. 1). Each spectra was measured at 0.5 nm increments for higher resolution. For absorbance measurements, an integrating sphere was fitted to the spectrometer, allowing all scattered light to be transmitted. For these measurements, the cuvette was placed in the centre of the sphere and the absorbance was measured. By measuring both the extinction and absorbance it was possible to calculate the scattering through Ext-Abs = Sca. A Renishaw InVia-Reflex Confocal Raman microscope was used with both 532 nm and 785 nm excitation lasers in air under ambient conditions. The Raman emission was collected by a 50 $\times$ objective lens in streamline mode and dispersed by a 2400 l/mm grating with 10% laser power ($<$ 1.4 mW). Liquid dispersions ($\sim$ 20 μL) were dropped onto Si/SiO_2 wafers (300 nm oxide layer) and left to dry in air before measuring. A minimum of 5 spectra

at different positions were recorded and averaged for final values. TEM, EDX and SEM were performed by the same colleagues and using the same method as described above for SnP_3 nanosheets.

6.2 Results and Discussion

6.2.1 Liquid exfoliation of SnP_3

The bulk starting SnP_3 material was synthesized by mixing tin and red phosphorous and heating under vacuum, carried out by collaborators at Universität Leipzig, Germany. The starting material (pictured in Figure 6.3A) was then liquid exfoliated via sonication in 1-methyl-2-pyrridone (NMP). The dispersion was subsequently trapped between 0.026 and 2.6k *g* i.e. low and high speed limits to remove large, unexfoliated material and small impurities resulting in the typical black standard sample as displayed in Figure 6.3B. TEM microscopy in Figure 6.3C shows that nanosheets were in fact produced, with lengths varying from 200 to 2000 nm. Furthermore, energy dispersive X-ray spectroscopy (EDX) in the TEM confirmed the elemental composition remained unchanged during exfoliation and the Sn:P ratio was still approximately 1:3 (Figure 6.3D). The presence of oxygen is to be expected from both transport and the exfoliation process but the peak remains relatively low compared to both Sn and P.

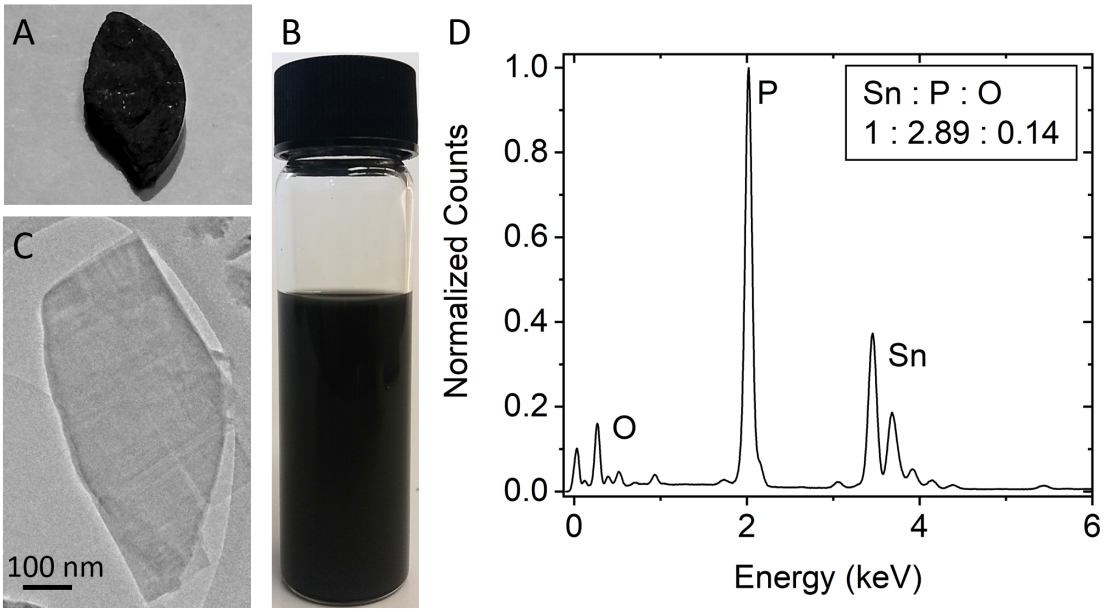

Figure 6.3: (A) Starting material as synthesised by collaborators at Universität Leipzig, Germany. (B) Image of a standard sample (0.03-2.6k g) of SnP_3 nanosheets dispersed in NMP. (C) Representative TEM image of liquid exfoliated SnP_3 nanosheets (standard sample). (D) Example of an EDX spectrum measured from a single SnP_3 nanosheet.

Further material characterisation was done using Raman spectroscopy. The starting material and film made via filtration of the liquid exfoliated dispersion are compared in Figure 6.4 below. There is very little difference in the starting material to exfoliated film, indicating that the exfoliation itself was a relatively non-destructive process. The A_g^1 mode predicted at 323 cm^{-1} for monolayer SnP_3 is upshifted for bilayer and multilayer SnP_3. The nanosheet film spectrum confirms that multi-layered nanosheets are present in the dispersion. Other modes present in both the starting material and nanosheet film spectra are suggested to be signatures of tin oxide species as a result of sample degradation and oxidation.[424]

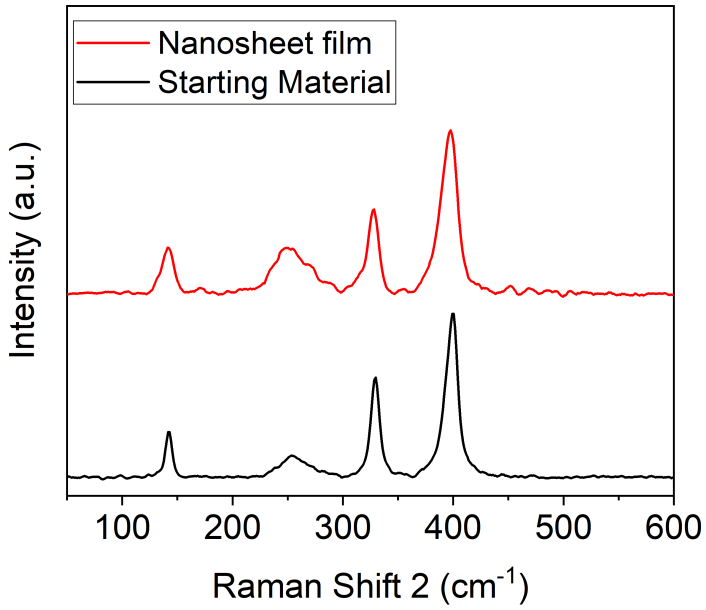

Figure 6.4: Raman spectra measured for Bulk SnP_3 powder and a film of liquid exfoliated SnP_3 nanosheets.

Optical spectroscopy (Figure 6.5) on the standard sample reveals a flat extinction coefficient spectrum with no clear features apparent, as expected from the visual appearance of the black dispersion, in agreement with the metallic nature of SnP_3 with layer numbers >3. By measuring with an integrating sphere[264] (Section 3.2.1), the absorption can be extracted without scattering effects. The absorption coefficient indicates that the extinction coefficient is mainly dominated by scattering effects. The absorption remains flat and relatively low until approximately 270 nm at which point it increases, probably due to NMP as the solvent. The scattering coefficient (Sca(λ)=Ext(λ)-Abs(λ)) increases with decreasing wavelength (increasing energy). There is no band edge observed for photon energies between 1.55 and 4.1 eV with the absorption coefficient flat over this range.

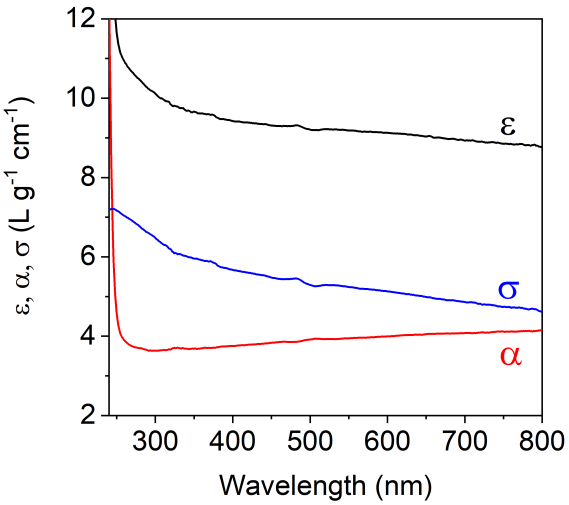

Figure 6.5: Optical extinction, ε, absorption, α, and scattering, σ, coefficient spectra of an SnP_3 standard sample.

As a way of measuring dispersion stability, an important processing parameter, the same standard sample was spectroscopically measured periodically for over 500 hours. Figure 6.6A shows the extinction spectra for the standard sample measured 10 times over 500 hours. There is clearly a decrease in extinction intensity as time increases. This suggest a degradation of the material over time but with just the UV-Vis spectra to analyse, the type of degradation cannot be estimated. It is possible that the solvent doesn't stabilise the nanosheets indefinitely, resulting in material to sediment at the bottom of the vial over time, leading to an apparent decrease in nanosheet concentration and therefore a drop in intensity. Another possibility is that the nanosheets are oxidised in the solvent over time. This oxidised product may in fact be soluble in the liquid resulting in nanosheets that do not contribute to the absorption of light in the same manner as when fresh and a subsequent drop in extinction intensity. Other techniques such as FTIR (Fourier Transform Infrared Spectrscopy), EDX and XPS over time would give further insights into the sources and mechanisms of degradation. This decrease is demonstrated in Figure 6.6B where the extinction values are normalized to the extinction at 0 hours (fresh sample). The intensity appears to drop to approximately 65% of its initial value over a course of 500 hours, indicating that the dispersions should be processed into films relatively quickly to avoid sample degradation.

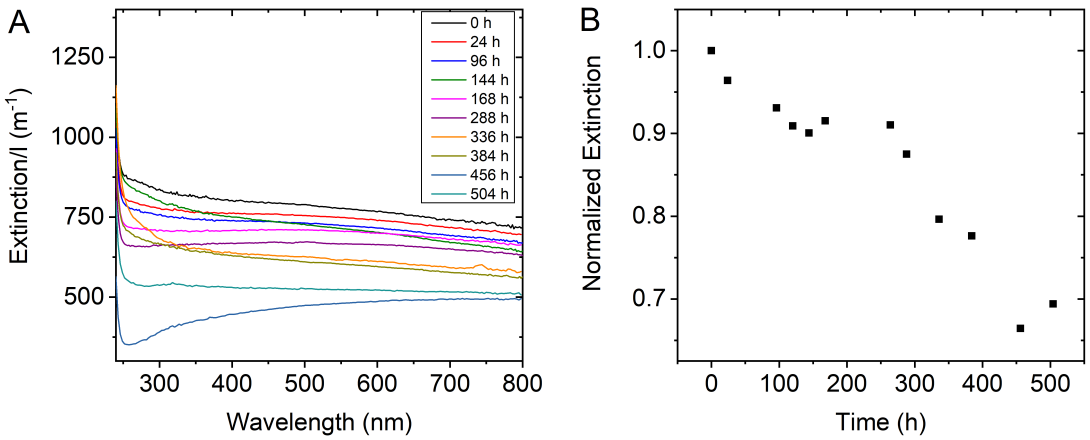

Figure 6.6: (A) Optical extinction spectra of an SnP_3 standard sample measured over 500 hours to investigate dispersion stability. (B) Extinction value at 700 nm normalized to the Ext_{700nm} at 0 h (fresh sample) shows a decrease in intensity over time to approximately 65% of the initial value.

6.2.2 Size Selection of SnP_3

In addition to a standard sample, SnP_3 nanosheet dispersions were also size-selected through liquid cascade centrifugation[20] (Section 3.1.2) to narrow what initially is a very broad size distribution after exfoliation. Five size fractions were produced by centrifuging at increasing speeds; 0.03, 0.1, 0.4, 1, 1.6 and 2.6 k *g*. The sediment of each centrifugation speed was collected and redispersed in IPA and the supernatant was moved to a higher speed. A selection of the size fractions were characterized microscopically with both TEM and AFM. The latter allows for not only statistical analysis of nanosheet lengths but also importantly nanosheet thickness. As with previous work[19,20,26] (Chapter 4), the apparent height of an LPE monolayer measured with AFM is thicker than its theoretical value due to intercalated water and solvent unavoidably present as a result of the exfoliation process. To convert nanosheet thickness to number of layers, step height analysis was performed on a range of nanosheets across 3 size fractions. Nanosheets with terraced steps were counted and plotted in order of step height in Figure 6.7A, indicating that the steps are a multiple of approximately 2 nm. When step heights of similar values are grouped together and the mean of each group is plotted versus step group, the slope gives an apparent monolayer height of 1.95 $\pm$ 0.03 nm (Figure 6.7B).

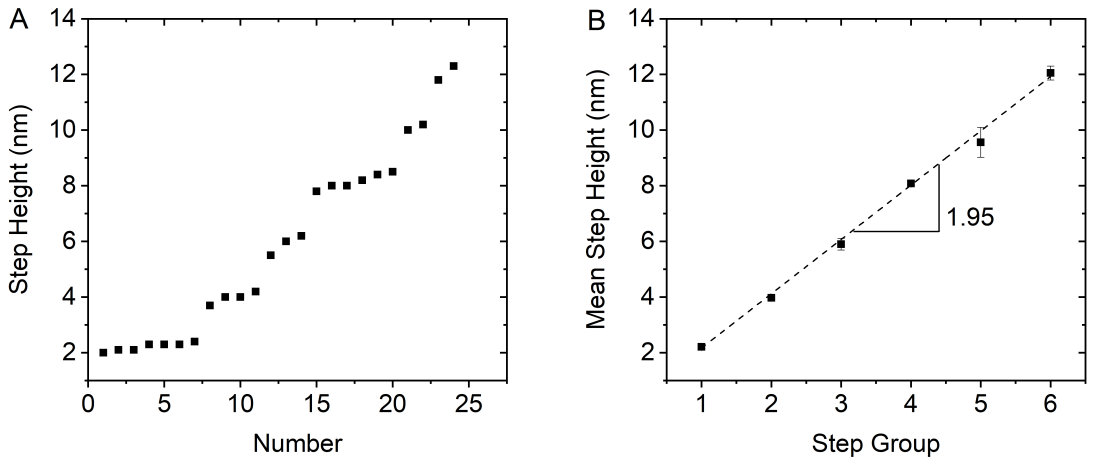

Figure 6.7: Step heights of $>$ 20 SnP_3 nanosheets in ascending order. The step height clustered in groups and is found to be a multiple of $\sim$2 nm, which is the apparent height of one monolayer. (C) The mean height for each group (the error is the sum of the mean step height error and the standard deviation in step height within a given group) is plotted in ascending order with the slope giving a mean monolayer step height of 1.95 $\pm$ 0.03 nm. This step height is on the thicker side in comparison with previous reports, unlike BN (Chapter 4), and more in line with values observed for layered double hydroxides[22,23] and TMDs.[19,20] The theoretical monolayer thickness of SnP_3 is reported to be 0.35 nm.[387]

Converting nanosheet thickness to multiples of the apparent monolayer height allows for histograms of mean nanosheet layer number and nanosheet length represented alongside representative AFM images for each size in Figure 6.8 below. A decrease in both nanosheet size and thickness is evident with increasing centrifugal force from left to right, however the log-normal distributions are relatively broad with the largest size 0.03-0.1k *g* containing nanosheets of hundreds of layers thick. On the contrary, the smallest size contains bilayer nanosheets, indicating that LPE as a technique can produce few layer SnP_3. The number of layers for SnP_3 nanosheets exfoliated in NMP are clearly much larger than other materials exfoliated in surfactants in Chapters 4 and 5. Although there has been no clear reason for this phenomenon reported to date, a previous study has suggested there might be a difference in the interfacial stress transfer at the solvent-nanosheet interface compared to the surfactant-nanosheet interface.[202]

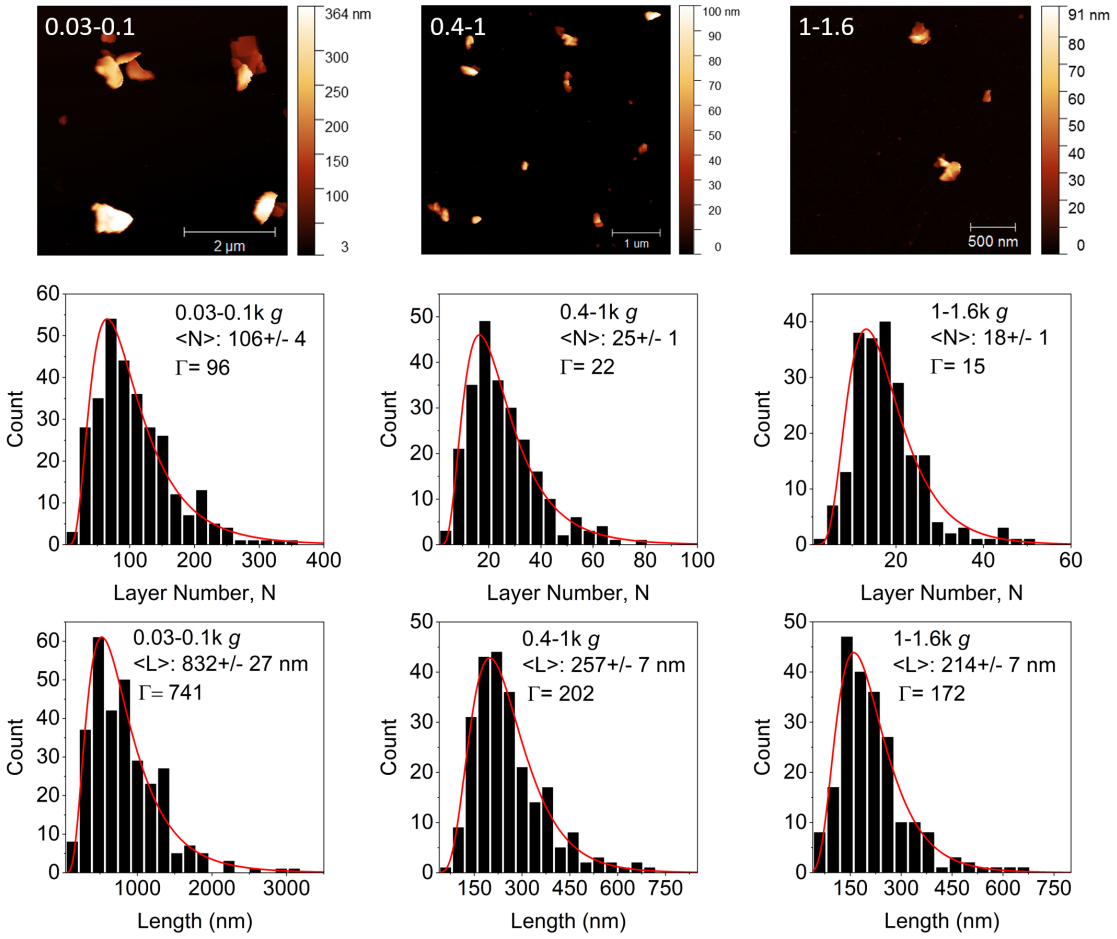

Figure 6.8: Representative AFM images (top row), layer number (middle row) and length (bottom row) distribution histograms on three trappings produced from the standard size selection cascade. From left to right: 0.03-0.1k *g*, 0.4-1k *g*, 1-1.6k *g*.

Moreover, it should be noted that the centrifugal accelerations used to size select SnP_3 were significantly lower than for example BN in Chapter 4. This is because large masses were required for film formation and electrochemical testing and so the characterisation was also focused on the portion of large/thick nanosheets isolated at low centrifugation speeds.

The mean nanosheet length and layer number are plotted as a function of central relative centrifugal force (RCF) in Figure 6.9A and B respectively. In both graphs, the mean values scale approximately as $(\text{RCF})^{-1/2}$, in agreement with previous reports for other LPE materials,[20,202,264,310] and confirming that increasing centrifugation speed decreases nanosheet dimensions. In addition, nanosheet area (approximated as length $\times$ width) is plotted versus layer number, N, for each nanosheet measured (Figure 6.9C). The

nanosheet area increases with layer number with roughly quadratic scaling as represented by the dashed line fit. Extrapolating this line to N=1 gives the characteristic monolayer area for SnP_3 of 60 nm^2. Taking the square root of this area, the characteristic monolayer size D_{ML} is estimated to be 7.75 nm. Previous work has shown that intrinsic nanosheet mechanics can be related to nanosheet dimensions of LPE nanosheets,[202] details in Section 2.3. The characteristic monolayer lateral size D_{ML} has been shown to be related to the ratio of in-plane and out-of-plane Young's modulus of the nanosheet by:

$$D_{ML} \approx 2h_0 \frac{Y_{In-plane}}{Y_{Out-of-plane}} \tag{6.1}$$

where h_0 = 0.35 nm is the SnP_3 monolayer thickness.[387] The Young's modulus ratio was previously proposed by Ji et al.[201] in terms of exfoliation of 2D materials. They proposed that the larger the in-plane modulus compared to out-out-plane, the more easily a 2D material could theoretically be exfoliated. The in-plane bonding strengths of various van der Waals crystals will have an effect on this ratio. Materials such as graphite were estimated to have extremely high ratios of 28.39 while black phosphorous was relatively low at 4.11.[201] The ratio for SnP_3 can be estimated with the above D_{ML} and h_0 values to give an in-plane to out-of-plane ratio of approximately 11. This value is close to those for MoS_2, $MoSe_2$, WS_2 and WSe_2 of 4-7 and higher than values for LDHs (approx. 1) reported by Backes et al.[202] However, it is considerably smaller than the 30 ratio for graphite reported by both Backes et al.[202] and Ji et al.[201]

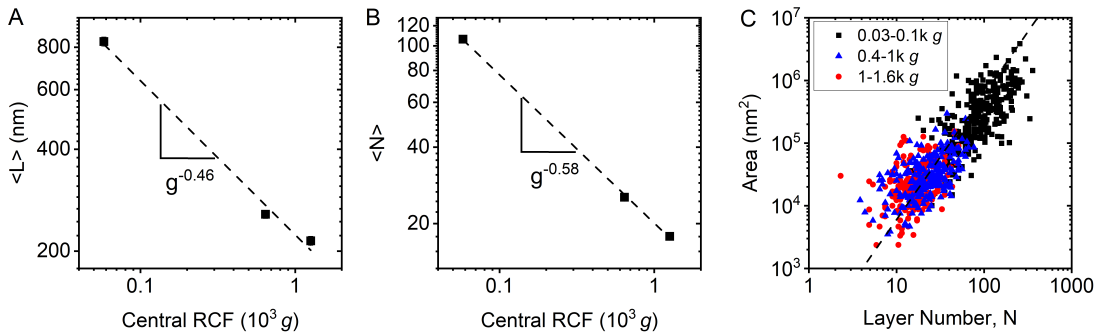

Figure 6.9: (A) Mean nanosheet length, <L> as a function of central centrifugal force g. The dashed line is a linear fit to the data with $g^{-0.46}$ scaling. (B) Mean layer number <N> as a function of central centrifugal force g. The dashed line is a linear fit to the data with $g^{-0.58}$ scaling. (C) Nanosheet area (approximated as length × width) plotted versus layer number for three different sizes. Each point represents an individual nanosheet measured by AFM. The dashed line shows a quadratic fit (i.e. Area = $60N^2$) to the mean values of the data clouds for each size fraction.

Another parameter worth extracting from the AFM data is the aspect ratio. For many applications of 2D materials, a high aspect ratio is desirable. The aspect ratio, k, is the ratio of nanosheet area to its thickness given by:[202]

$$k = \frac{\sqrt{\langle LW \rangle}}{\langle N \rangle h_0} \tag{6.2}$$

Nanosheets with high aspect ratios are large in lateral dimensions (length and width) but also thin. For example, BN nanosheets in Chapter 4, the mean aspect ratio across all sizes was 118. The aspect ratio for SnP_3 ranges between 10-30, considerably smaller than BN and graphene. However, the low aspect ratio may in fact play in the favour of SnP_3 given that ratios such as these are suggested to give better performance in battery electrodes.[373] High aspect ratios can lead to longer diffusions times, a major disadvantage in the operation of Li-ion batteries. The author of this thesis exfoliated the material, performed UV-Vis spectroscopy and AFM measurements and analysed the resulting data in the work above.

6.2.3 Lithium storage of SnP_3

The electrochemical studies were carried out by Dr Ruiyuan Tian and Mark McCrystall. To produce electrodes for batteries, SnP_3 dispersions were mixed with single-walled carbon nanotube (SWCNT) dispersions to both aid electrical conductivity and mechanical stability.[24,373] Mixed dispersions were vacuum filtrated and the resulting film was transferred from cellulose filter membranes to copper foil for electrochemical testing. Thick electrodes increase the energy density and lead to better overall energy storage.[425,426] Representative scanning electron microscopy (SEM) images of the SnP_3/SWCNT composites taken by Cian Gabbett can be seen in Figure 6.10A,B. The films are mostly uniform with nanotubes dispersed evenly throughout. Particulates of 300-400 nm thick can be seen, suggesting that there is a large amount of nanosheet reaggregation during thick film formation.

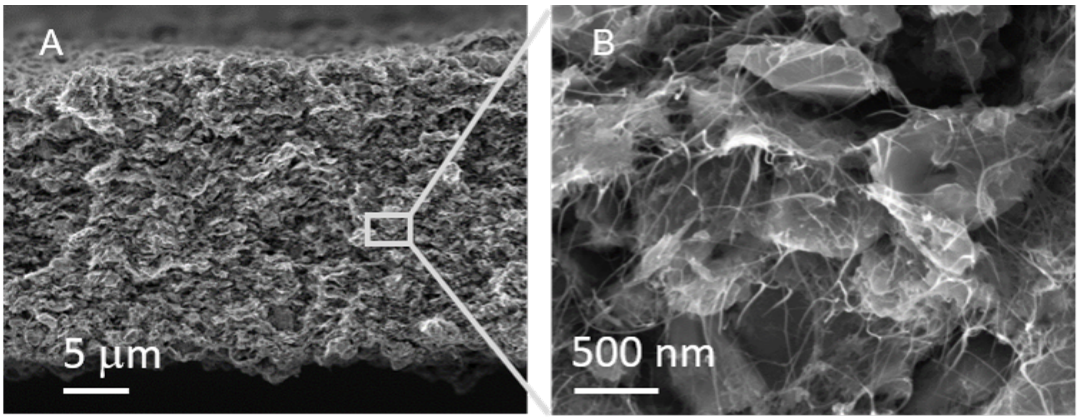

Figure 6.10: (A,B) SEM images at two magnifications of SnP_3/nanotube composite films used for battery tests (mass fraction of nanotubes M_f = 25%, electrode mass per area M_T/A = 2.3 mg cm^{-2}).

Although a detailed electrochemical study is beyond the scope of this thesis, a selection of some of the results of the published work[427] can be seen in Figure 6.11 below. Cyclic voltammetry measurements show the measured current as a function of input potential at the SnP_3 based electrode (Figure 6.11A). There are relatively narrow reduction peaks at 0.2, 0.5 and 0.8 V and oxidation peaks at 0.6, 0.8 and 1.3 V. These peaks are very similar to those observed previously for unexfoliated SnP_3.[383] Relatively symmetric oxidation and reduction peaks indicate good cyclability across the potential range. The first peak appears less symmetric than the other curves due to the inital cell activation and the solid electrolyte interface being formed.

Through the analysis of the CV data in combination with the intercalation and conversion reactions, one can calculate that 13.25 charges can be stored per formula unit of SnP_3. The equivalent capacity can then be calculated as:

$$\frac{Q}{M} = \frac{nF}{M} = \frac{13.25F}{M_{SnP_3}} \tag{6.3}$$

where F is Faraday's constant and M_{SnP_3} is the molecular weight of SnP_3. The theoretical capacity is calculated to be 1670 mAh g^{-1} and represented by the dashed line in Figure 6.11B. The figure also shows the specific charging capacity plotted versus nanotube loading for composite anodes, normalised to both the active mass and the total electrode mass. Normalised to the active mass (SnP_3), at 25% nanotube mass fraction the capacity

is maximised and remains at this value for any higher loadings. More importantly it is nearly identical to the theoretical value. When normalised to the electrode mass, the capacity is still maximised at 25% mass loading but the capacity drops for higher nanotube mass fractions due to increased effect of the nanotubes. Figure 6.11 therefore indicates the 25% nanotube mass loading is optimal for high capacity electrodes with a $Q/M_{total} \approx$ 1250 mAh g^{-1}.

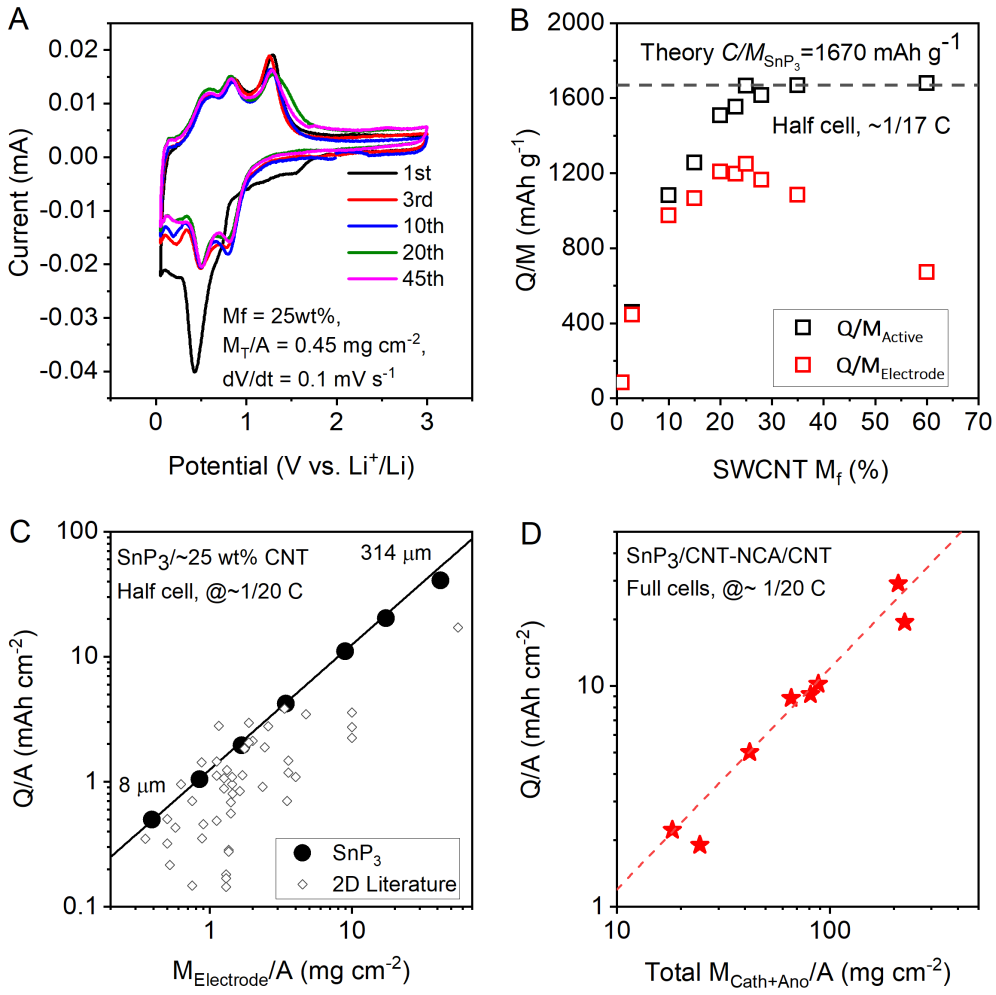

Figure 6.11: : (A) Cyclic voltammetry of a similar films used as a lithium battery anode (M_f = 25wt%, MT/A = 0.45 mg cm^{-2}, dV/dt = 0.1 mV s^{-1}) (B) Specific charging capacity plotted versus nanotube loading for composite anodes. Data is shown for capacity normalised to both the active mass and the total electrode mass. The dashed line represents the theoretical capacity of SnP_3. (C) Areal capacity plotted as a function of total electrode mass loading, M_T/A. The solid line represents a specific capacity of Q/M_T = 1250 mAh g^{-1} (C-rate ≈ 1/20C, M_f = 25%). The thicknesses of the thickest and thinnest electrodes are indicated in the panel. Empty diamond data points represent literature values for 2D-based electrodes extracted from Tian et al.[373] (D) Full cell areal capacity plotted as a function of total anode plus cathode mass loading, M_{A+C}/A (C-rate ≈ C/20).

Using the 25% mass fraction, the areal capacity (capacity per unit area) as a function of areal mass loading (total mass of electrode per unit area) can be plotted as shown in Figure 6.11C for a range of electrode thicknesses (8-314 μm). As previously mentioned, thicker electrodes are more favourable for increased energy storage. The slope of the linear fit gives the specific capacity of the overall electrode Q/M_T to be 1250 mAh g^{-1}, in agreement with the data extracted in Figure 6.11C. Moreover, this data can be compared to other 2D materials in literature[373] (empty diamonds, Figure 6.11C) demonstrating the advantage of producing very thick electrodes. It is believed that this SnP_3/CNT system is the highest areal capacity 2D lithium-storing electrode reported to date. The author of this thesis prepared and characterised the nanomaterial that were integrated into these electrodes. Full cells were produced using anodes consisting of SnP_3 with 25wt% SWCNT and cathodes fabricated from lithium nickel cobalt aluminium oxide (NCA) mixed with 0.5wt% SWCNT. The total electrode mass per unit area, M_{A+C}/A is plotted versus the cell areal capacity Q/A in Figure 6.11D, showing a linear increase in areal capacity with electrode mass with a slope of 120 mAh g^{-1}, a very high value compared to literature.[428,429]

6.2.4 Liquid exfoliation of SiP

Bulk SiP was also synthesized by collaborators in Germany using red phosphorous and silicon as starting materials (Appendix D.1) and is pictured in Figure 6.12A. A standard sample of SiP was produced using the same method as for SnP_3 in Section 6.1 above. A standard sample dispersion can be seen in Figure 6.12B and was characterized by both EDX and TEM (Figures 6.12C and 6.12D respectively). EDX measurements on individual nanosheets confirmed the Si:P ratio of approximately 1:1. There was also some oxidation present, higher than that observed in SnP_3. The copper peak appears due to the copper grids used as substrates for TEM/EDX measurements. It may be a case that SiP is less stable and more prone to oxidation effects than SnP_3. Another explanation may be that an oxide layer in formed on the surface of SiP, whereas complete dissolution is favoured for SnP_3 which would result in a lower measured oxide content. TEM images (Figure 6.12D) of the standard sample show large nanosheets, some more than 2-3 μm in length with a typically broad size distribution from the large centrifugation range used.

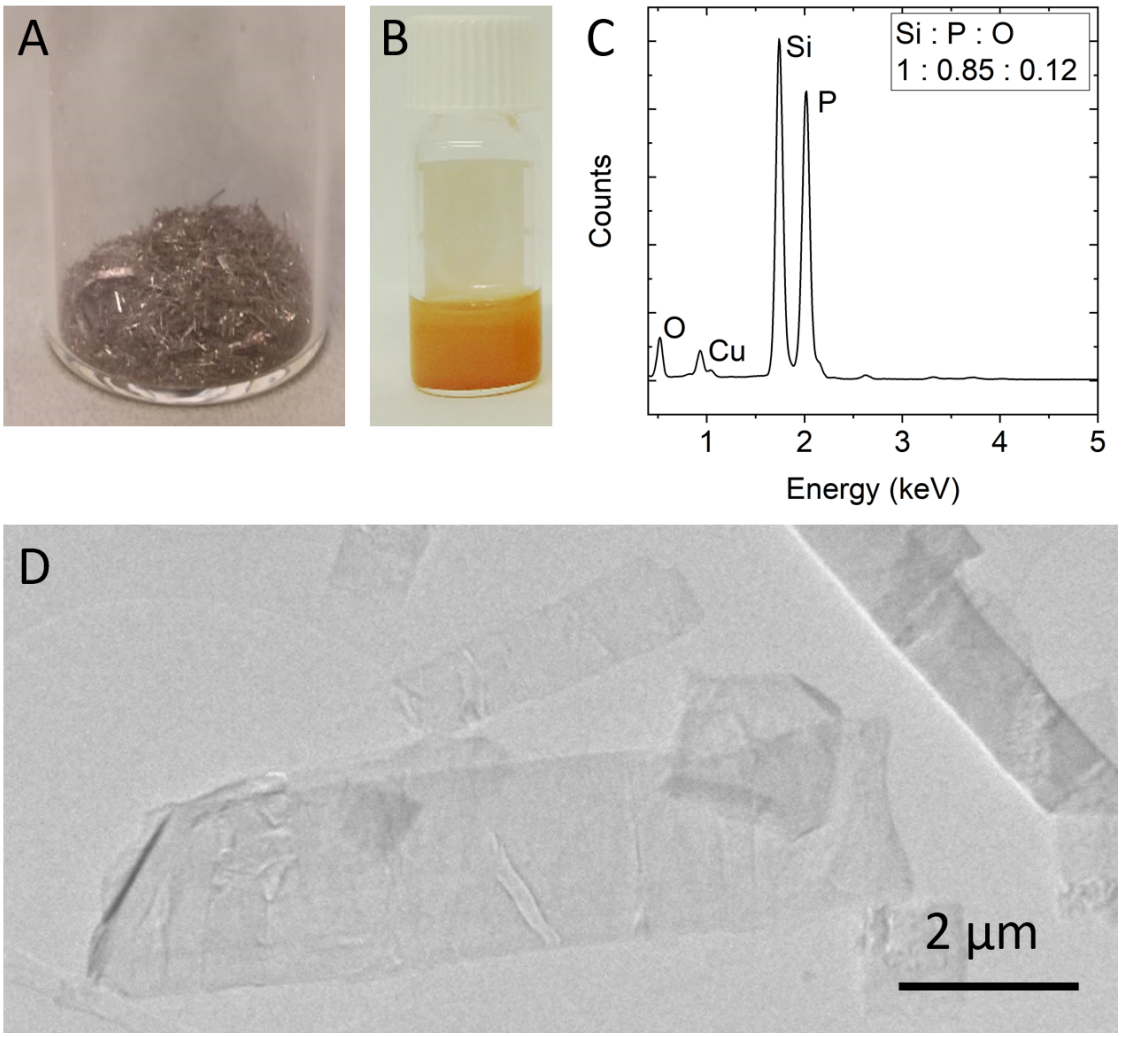

Figure 6.12: (A) Starting material as synthesised by collaborators at Universität Leipzig. (B) Image of size-selected SiP nanosheets dispersed in NMP increasing in centrifugation speed (decreasing size) from left to right. (C) Example of an EDX spectrum measured from an SiP nanosheet in the TEM, confirming the ratio of Si to P while giving an approximate measure for the amount of oxidation in the sample. (D) Representative TEM image of liquid exfoliated SiP nanosheets (standard sample).

Optical spectroscopy of the standard sample shows clear excitonic features in the visible region (Figure 6.13A). The extinction spectra is dominated by scattering until the point at which the absorbance increases from 0 at approximately 600 nm (2.06 eV). This adsorption band edge is expected given the bright orange dispersions. SiP monolayers are predicted to have a direct band gap at 1.9 eV with excitonic features in optical absorption spectra beginning at 2 eV.[399] This not clearly observed in the spectra of the standard sample, but will be discussed again in context of size-selected dispersions below. The absorbance measured of 400 hours and shows a decrease in intensity over time in Figure

6.13B to approximately 80 % of the initial value. This suggests that SiP dispersions are more stable in liquid than SnP_3 but with the drop of intensity by more than 10 %, immediate film formation is still advised. In conjunction with the EDX analysis, it is suggested that formation of a stable oxide layer is favoured for SiP in particular due to the observed saturation of the absorbance for $>$ 300h

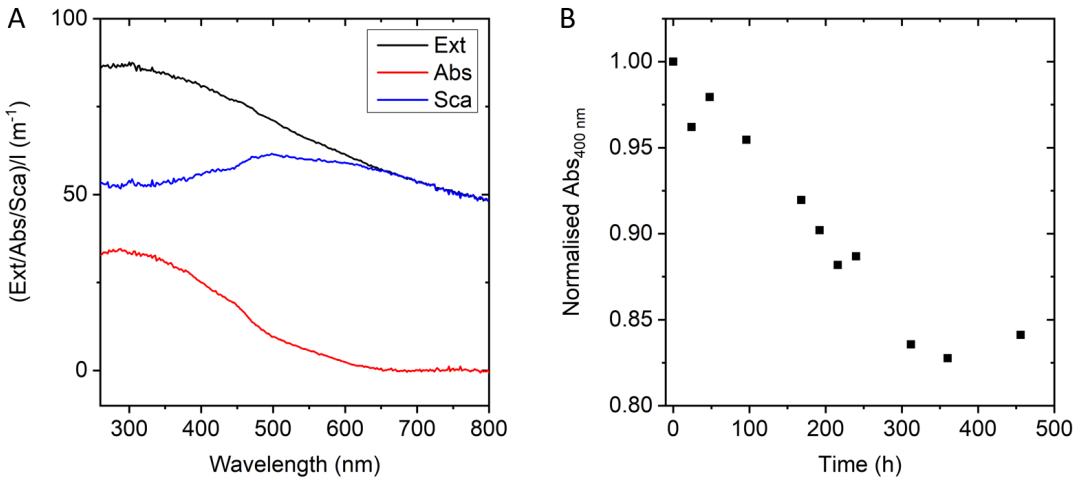

Figure 6.13: (A) Optical extinction, absorption and scattering spectra of an SiP standard sample trapped from 0.03-2.6 k g. (B) Time dependence study of a standard SiP sample. A plot of absorbance at 400 nm normalised to Abs_{400nm} at 0 h (fresh sample) shows a decrease in intensity over time to approximately 85% of the initial value.

Further characterization was completed on the standard sample using Raman spectroscopy. The standard sample prepared through liquid phase exfoliation is compared with the synthesized bulk powder in Figure 6.14 below. DFT calculations from Li et al.[413] suggest that the experimental spectra below contain many characteristic peaks of o-SiP, in agreement with theory, most notably the resonant $A_1{}^6$ peak at 261 cm^{-1} and the $A_1{}^7$ peak 305 cm^{-1}.

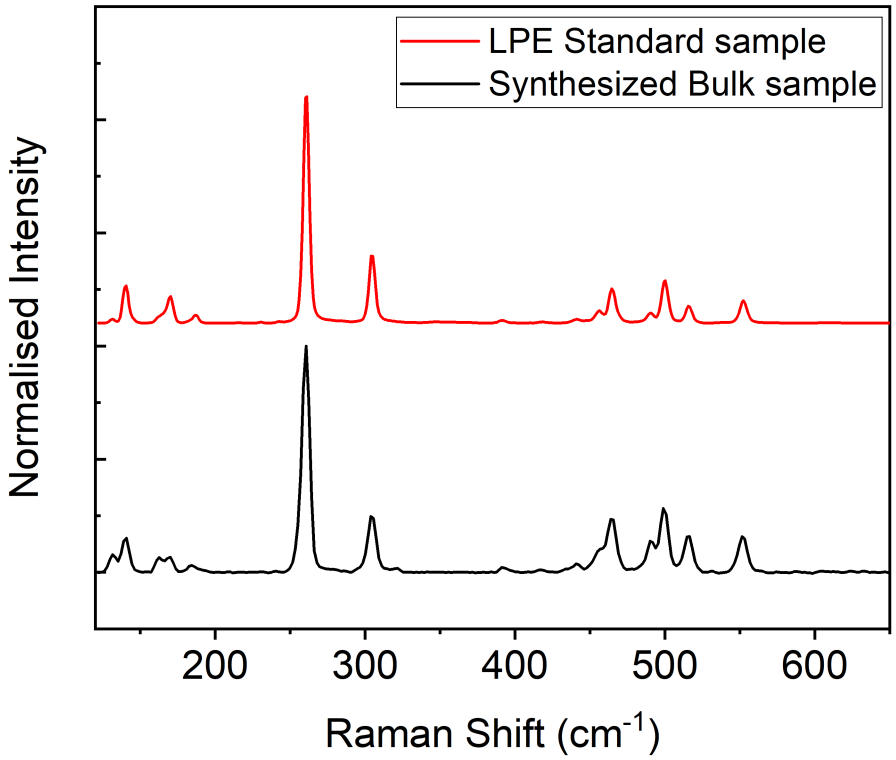

Figure 6.14: Raman spectra for synthesized bulk material (black) and liquid exfoliated standard sample (red) normalized to their maximum. The bulk and exfoliated samples are very similar, indicating that the exfoliation process was not very destructive.

6.2.5 Size-selection of SiP

Size-selection and further characterisation was carried out at Heidelberg University by the author of this thesis. Liquid phase exfoliation yields polydisperse samples and so to observe spectral changes with nanosheet dimension, the dispersion was subject to liquid cascade centrifugation (LCC),[20] similar to previous work (Section 6.2.2 and Chapter 4). The concentration decreased with increasing centrifugation speed with the colour changing from orange to yellow.

AFM microscopy was performed to investigate the size of nanosheets in each size fraction. Representative images for 3 of these fractions are displayed in Figure 6.15 below. In line with previous work, the length, width and height of roughly 200 nanosheets were measured for each sample, applying established corrections to account for tip broadening and pixelation effects. Step height analysis using the same method as both BN and

SnP_3 was applied to convert the apparent nanosheet thickness to number of monolayers or layer number, N. The step height was found to be 2 nm. Histograms of both nanosheet layer number and length are shown in Figure 6.15. There is a typical narrowing of the log-normal distribution of both parameters with increasing centrifugation speed (left to right).

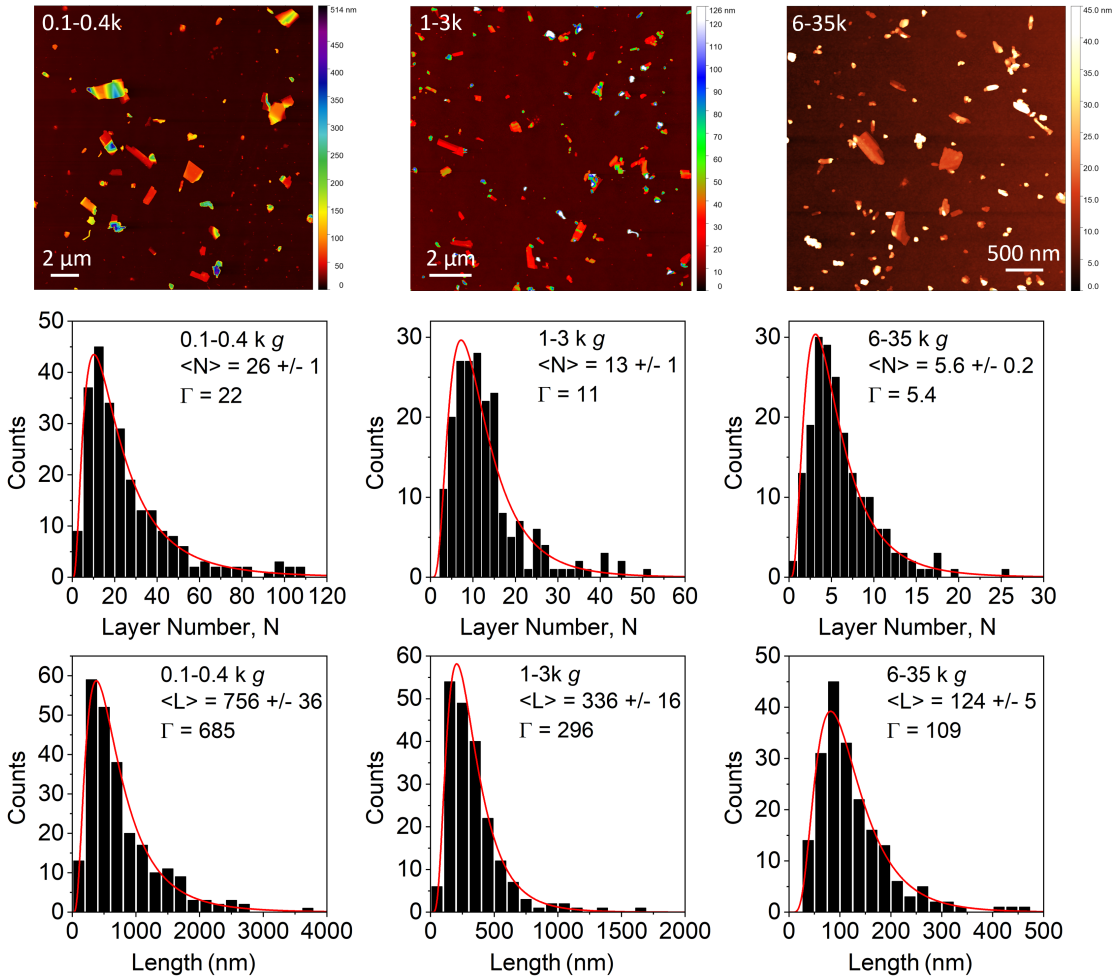

Figure 6.15: Representative AFM images (top row), layer number (middle row) and length (bottom row) distribution histograms on three trappings produced from the standard size selection cascade. From left to right: 0.1-0.4k *g*, 1-3k *g*, 6-35k *g*.

The mean nanosheet length and thickness, <L> and <N>, were estimated through statistical analysis of the microscopy data. Mean nanosheet length <L> scales with centrifugal forces with a power law of -0.51, in line with previous 2D materials[20,202,264,310] (Figure 6.16A). This scaling also agrees with centrifugation theory by Peukert et al.[311] (Section 3.1.2). Mean nanosheet layer number <N> also scales with centrifugal force as $g^{-0.34}$

(Figure 6.16B).

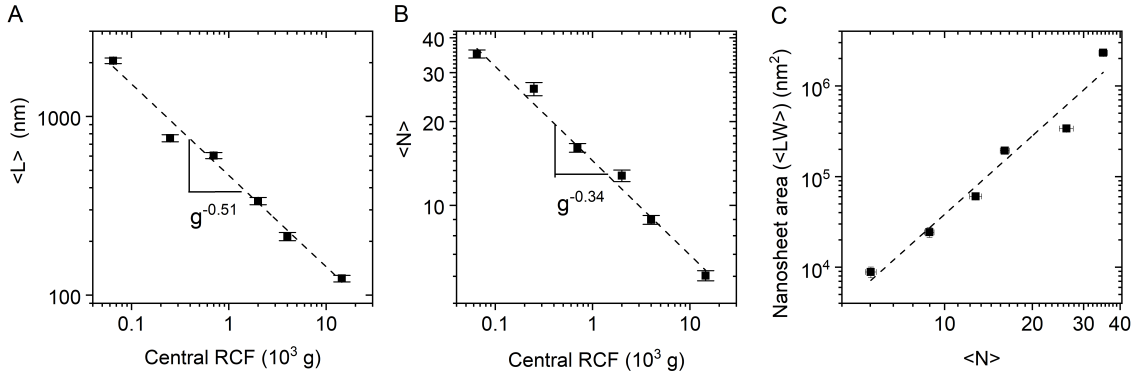

Figure 6.16: (A) Mean nanosheet length, <L> as a function of central centrifugal force g. The dashed line is a linear fit to the data with $g^{-0.51}$ scaling. (B) Mean layer number <N> as a function of central centrifugal force g. The dashed line is a linear fit to the data with $g^{-0.34}$ scaling. (C) Mean nanosheet area (approximated as length $\times$ width) plotted versus layer number for each size. The dashed line is a linear fit of the data (Area= $54<N>^{2.87}$). Extrapolating the fit to <N>=1 gives the characteristic monolayer area and length.

From the extrapolation from the line (dashed line, Figure 6.16C), the characteristic monolayer area is approximately 54 nm^2 giving a characteristic monolayer length D_{ML} of 7.35 nm. The theoretical monolayer height, h_0, of SiP is 0.72 nm.[399] This allows for the in-plane to out-of plane Young's modulus ratio to be calculated through equation 6.1 above giving a value of $Y_{In-plane}/Y_{Out-of-plane}$= 5.10. The value is similar to those reported for selenide and sulphide TMDs; MoS_2, WS_2, WSe_2 and $PtSe_2$[202] and very close to the black phosphorous ratio of 4.93 reported by Ji et al.[201] Both SiP and SnP_3 materials examined in this chapter are compared to other LPE materials in literature in Figure 6.17 below, suggesting that these materials are in agreement with equipartition theory with values close to previously studied TMDs.

Similarly, the aspect ratio can be found using equation 6.2 above. The aspect ratio for SiP nanosheets was calculated to be 60 for the largest 30-100 *g* sample and 23 for the smallest 6-35 k *g* sample. All other sizes were estimated to have aspect ratios in this range. These ratios are slightly larger than those observed for SnP_3 nanosheets, indicating larger, thinner sheets in agreement with both TEM and AFM statistical analysis.

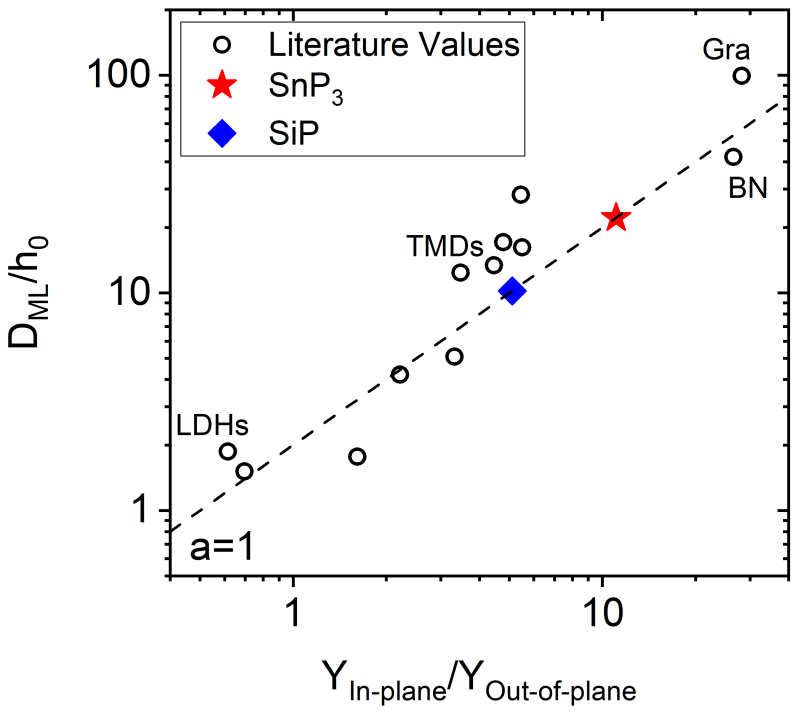

Figure 6.17: Characteristic monolayer length D_{ML} to monolayer thickness ratio versus the Young's modulus in-plane to out of plane ratio for a range of 2D materials (empty circles) as reported by Backes et al.[202] and for SnP_3 (red star) and SiP (blue diamond) examined in this chapter. The dashed line is a fit to Equation 6.1.

Optical spectroscopy of size selected samples shows spectral changes with nanosheet dimension, typical of many 2D materials.[19,26,191,312] Normalised extinction spectra show a decrease in intensity at higher wavelength with decreasing nanosheet size as seen in Figure 6.18A. Similar to BN, there is a broad scattering background in the extinction spectra that increases with size. Once the absorbance is separated from the extinction in Figure 6.18B, a peak appears at 270 nm. Moreover, a peak at approximately 650 nm starts to appear as nanosheets decrease in size. The scattering is plotted in Figure 6.18C, increasingly prominent for larger nanosheets in agreement with other 2D materials and scattering theory which predicts that scattering coefficient increases with increasing <L>.[264]

The scattering clearly features to a lesser extent in smaller sizes. The absorbance is non-zero at 650 nm for the largest size while for the smallest size, other than a slight peak at this wavelength it remains at approximately zero until 500 nm. The peak only starts to appear from the 0.1-0.4 k *g* sample and smaller. The absorbance band edge shows a clear blueshift with for increasing centrifugation speed in Figure 6.18B. The absorbance band

edge for each size was estimated by locating the position in energy that the normalised intensity was 0.025. This absorbance band energy (in eV, extracted from Figure 6.18B) is plotted as a function of layer number, indicating a decrease in energy with increasing nanosheet thickness (Figure 6.18D). There does appear to be a levelling off position when nanosheet thickness approaches bulk values ($>$ 10 layers), suggesting that the position is in fact dependent on confinement and dielectric screening effects from a decrease in nanosheet thickness.[19,192]

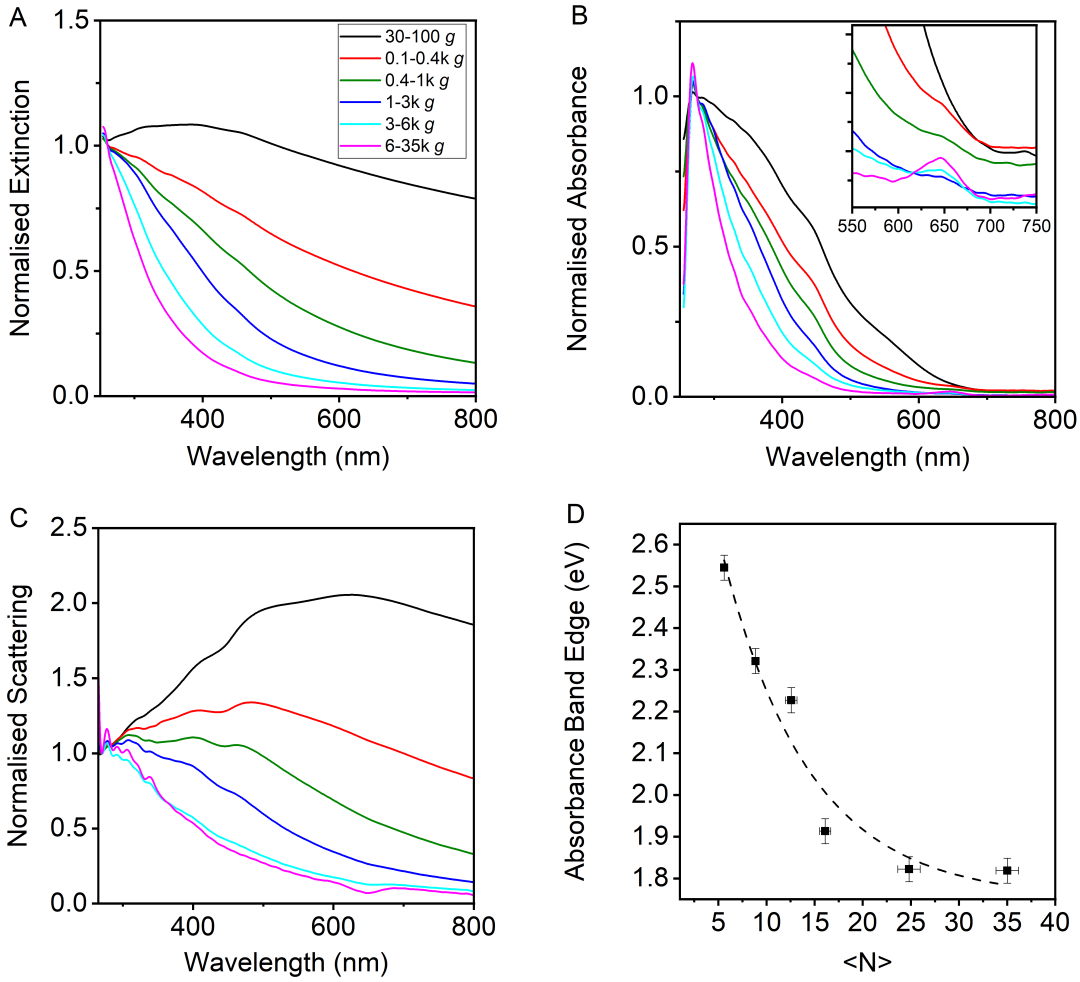

Figure 6.18: (A) Optical extinction spectra normalized to the extinction at 260 nm showing change in spectral shape with nanosheet size. Normalising to the extinction at 260 nm shows higher intensity between 300 and 800 nm for increasing nanosheet size (B) Optical absorption spectra normalized to the absorption at 275 nm showing dependence the adsorbance band edge dependence on nanosheet size, Inset: Zoom of the region 550-750 nm. (C) Optical scattering spectra, calculated from subtracting the extinction from the absorption spectra normalized to the scattering at 260 nm showing a change in spectral shape with nanosheet size. (D) The position of the absorbance band edge (in eV) versus nanosheet thickness shows an increase in peak intensity with increasing thickness. Dashed line is an empirical fit of the data (Equation 6.4).

The relationship between <N> and the absorbance band edge (in eV) is fit from the data in Figure 6.18D to get the following empirical formula:

$$\langle N \rangle = 3.6791 - 9.0594 \ln(Abs_{Edge} - 1.7522) \tag{6.4}$$

By carefully measuring the absorbance band edge, the number of SiP layers can be estimated, providing a useful metric for this new material.

Spectral shifts with nanosheet size can also be examined with Raman spectroscopy. Raman spectra for all sizes normalized to the peak at 263 cm^{-1} are displayed in Figure 6.19 below. Similar to the standard sample, characteristic SiP Raman active modes[413] are found at 163, 172, 263, 306, 466, 500 and 555 cm^{-1}. There is also a mode predicted at 516 cm^{-1}.[413] This mode however may be masked by the intense SiO_2 substrate peak at 520 cm^{-1}. Efforts were made to subtract the silicon peak from each spectrum due to its increased contribution for lower nanosheet concentration (smaller sized) samples, this was not completely effective so the data is presented without subtraction below. The substrate peaks are indicated by *.

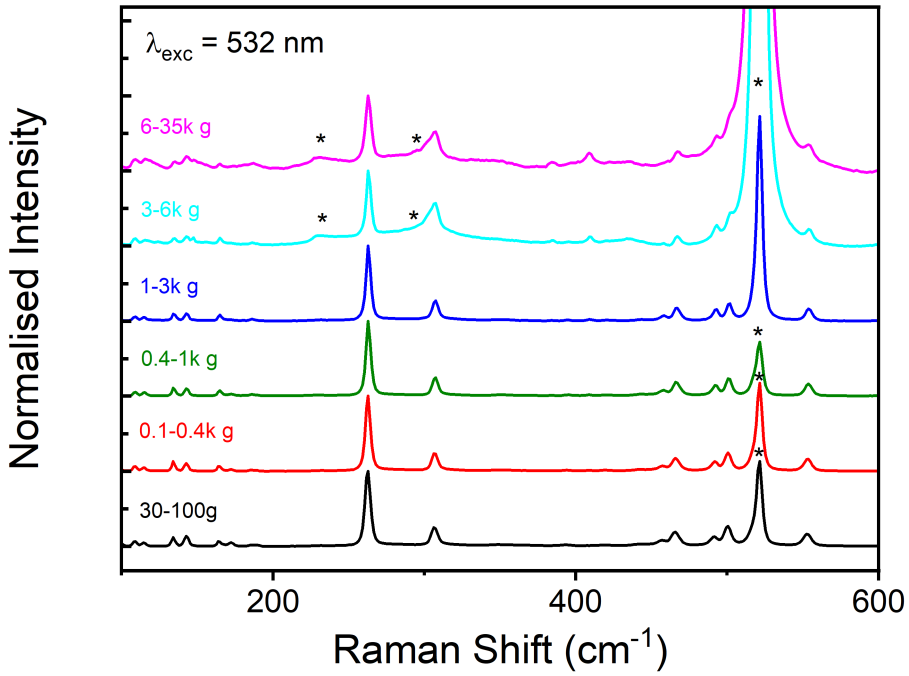

Figure 6.19: Raman spectra of size-selected SiP nanosheets (excitation wavelength,λ_{ex} = 532 nm) dispersions, each normalized to the peak at 263 cm^{-1} (A_1^6 mode[413]). The SiO_2 substrate peaks are indicated by *.

New peaks appear to evolve in fractions containing smaller nanosheets at around 400 cm^{-1}, not previously observed experimentally or predicted theoretically, possibly due to an increased level of oxidation in smaller size samples. This idea is supported by AFM images of the smaller sizes which show many non-2D material start to appear. A sample was prepared in the centrifugation range 35-270 k *g* showing a high level of potentially oxidized impurities. Due to the large amount of aggregation of any possible nanosheets, it was deemed uncountable and disregarded from size-dependent results (Figure 6.20). However, it does give insights into the type of material isolated at high centrifugal accelerations and may be the reason for this peak signature at 409 cm^{-1} in the Raman spectra.

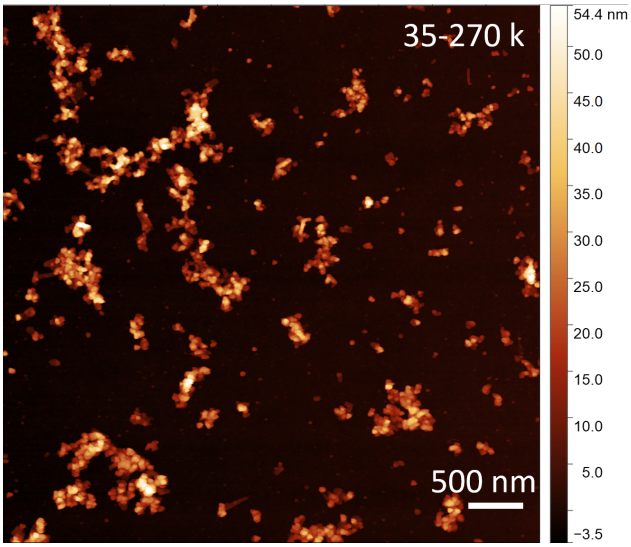

Figure 6.20: Representative image of the additional 35-270 k *g* sample prepared showing a large amount of aggregation and degradation in the sample, a possible explanation for the Raman peak at 409 cm^{-1} observed in other small size fractions.

Zooming in on the region between 395 and 420 cm^{-1}, there is clearly an evolving peak with decreasing size (Figure 6.21A). The relative intensity of this peak (intensity ratio 409/263 cm^{-1}) versus relative centrifugal force is plotted in Figure 6.21B. Similar to absorbance measurements, there appears to be an increase in intensity with increasing centrifugation speed. The intensity begins to level off at low speeds. This may be due to confinement effects associated with thin nanosheets however it could also arise from lateral size or degradation and so it is plotted as a function relative centrifugal force. The author of this thesis exfoliated material, performed the AFM, UV-Vis and Raman spectroscopy measurements and analysed resulting data.

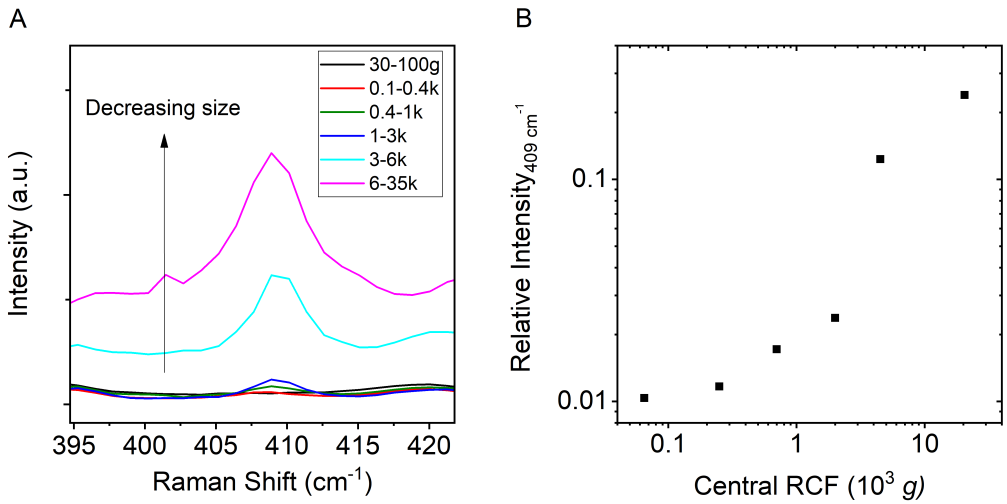

Figure 6.21: Raman spectra of size-selected SiP nanosheets (excitation wavelength, λ_{ex} = 532 nm) dispersions shows an increasing peak at 409 cm^{-1} with increasing centrifugation speed (B) Relative intensity of the Raman peak at 409 cm^{-1} (intensity ratio 409/263 cm^{-1}) as a function of relative centrifugal force (RCF, 10^3 *g*) shows a increase in intensity with decreasing size.

6.2.6 Lithium storage of SiP

The electrochemical studies were carried out by Dr Ruiyuan Tian and Mark McCrystall. SiP-CNT composites were made using the same method as SnP_3 in order to test the material's Li storage capabilities. Representative scanning electron microscopy (SEM) images of the SiP/SWCNT composites taken by Cian Gabbett can be seen in Figure 6.22A,B. The films are mostly uniform with nanotubes dispersed evenly throughout, possibly with less aggregation than the SnP_3 films.

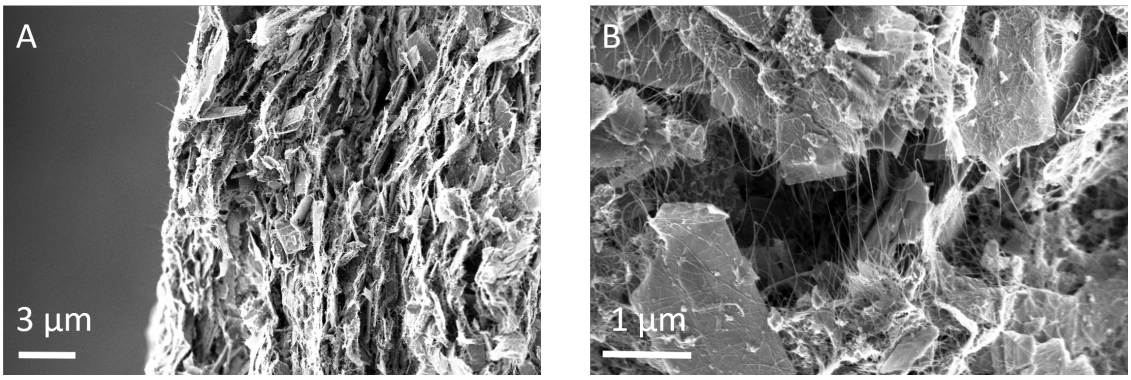

Figure 6.22: (A,B) SEM images at two magnifications of SiP/nanotube composite films used for battery tests (mass fraction of nanotubes M_f = 25%, electrode mass per area: M_T/A = 2.3 mg cm^{-2}).

Once again, although a detailed electrochemical study is beyond the scope of this thesis, the first results can be seen in Figure 6.23 below. SiP is a material with a theoretical capacitance of 3060 mAh g^{-1},[408] the highest known 2D material to date. This is nearly twice as high as SnP_3 and second only to Si (3580 mAh g^{-1}).[430] The specific capacity normalised to the total electrode mass (Q/M) is plotted versus the current density (I/M). To improve the capacity, cells were prepared using a fluoroethylene carbonate (FEC)-based electrolyte as opposed to the more standard ethylene carbonate (EC). FEC-based electrodes have been reported to form a stable solid electrolyte interphase (SEI), increasing the cycling performance of Si based electrodes.[431,432] The specific capacity comes close to theoretical capacity for FEC-based electrodes at low current densities in Figure 6.23. Specific capacities of over 1000 mAh g^{-1} are measured with relatively high current densities of over 3000 mA g^{-1}. Battery testing is ongoing with SiP-CNT based electrodes to complete a study similar to that shown for SnP_3.

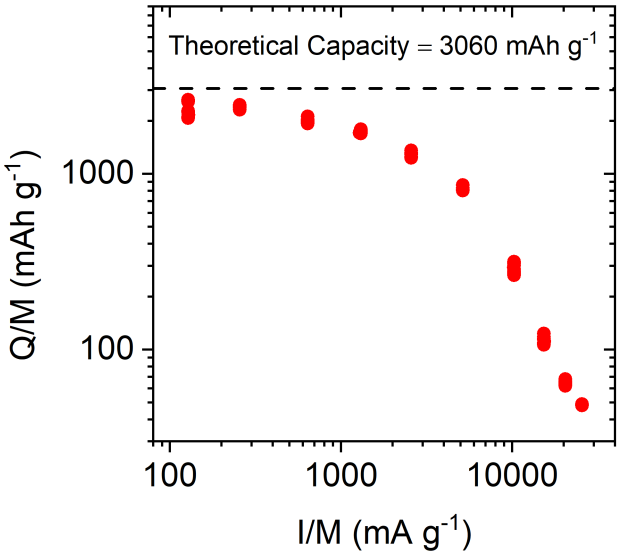

Figure 6.23: Specific charging capacity plotted versus current density for composite anodes. Data is shown for both standard cells and those fabricated with fluoroethylene carbonate (FEC) electrolyte additive. The dashed line represents the theoretical capacity of SiP

6.3 Conclusions

In this chapter two novel materials, SnP_3 and SiP were successfully exfoliated and characterised. EDX spectra of SnP_3 showed relatively low levels of oxidation (5%) indicating that the LPE process was non-destructive, confirmed by very similar bulk and exfoliated Raman

spectra. Examining the UV-Vis extinction spectrum over time, The intensity dropped to approximately 65$\%$ of its initial value suggesting that the dispersions should be processed relatively quickly to avoid sample degradation. AFM on size selected samples revealed the nanosheets exfoliated are relatively thick for low speed speed centrifugation (<N> =106) but once dispersions are trapped at higher speeds thin nanosheets can be isolated of less than 20 layers. The in-plane to out-plane Young's modulus ratio was found to be 11, similar to TMDs and indicative of a decent exfoliation efficiency. Relatively low aspect ratios of 10-30 was suggested to give better performance in battery electrodes, shortening diffusion times. SnP_3-CNT composites formed high performance lithium storage anodes, displaying record capacity for a 2D-based anode when normalised to total electrode mass. With the help of CNTs, very thick electrodes (>300 μm) leading to the highest reported (stable) areal capacity for a 2D-based electrode.

EDX of liquid exfoliated SiP indicated a higher level of oxidation (12$\%$) than SnP_3, suggesting that exfoliated SiP may be more prone to oxidation. A time dependence study of a standard SiP sample however revealed that a drop of intensity of approximately 18$\%$ indicating that liquid exfoliated SiP may in fact be more stable in dispersion than SnP_3. AFM on size selected samples showed relatively thin nanosheets with the two smallest fractions producing mean layer numbers of less than 10. The in-plane to out-plane Young's modulus ratio was found to be 5.1, indicative of a good exfoliation efficiency, though not as high as SnP_3. Spectral changes with size due to edge and confinement effects were observed through both UV-Vis and Raman spectroscopy. Cells prepared using FEC-based electrolyte came close to the theoretical capacity (3060 mAh g^{-1}) at low current densities. A more thorough electrochemical study is required but SiP batteries could be the highest areal and specific capacity 2D lithium-storing electrode reported to date.

7

We had a kettle; we let it leak: Our not repairing made it worse. We haven't had any tea for a week... The bottom is out of the Universe.

–Rudyard Kipling

Exfoliation of Graphite in a Kitchen Kettle

***

ULTRASONICATION HAS BEEN SHOWN TO SUCCESSFULLY exfoliate 2D materials in Chapters 4, 5 and 6. In LPE, as ultrasonic energy propagates through the liquid medium bubbles are created, a phenomenon known as acoustic cavitation. The violent collapse of these bubbles produces extremely high local temperatures (5000 °C) and pressure (500 atm)[433] causing scission and tearing of the parent crystallite (see Section 3.1.1). Ultrasonication is relatively new to the field of acoustics, Langevin first conceiving the ultrasonic quartz-steel transducer for submarine detection in 1916.[434,435] The acoustics of bubble collapse however was of interest to the scientific community prior to this due to the humble kitchen kettle. The earliest reports of bubble formation in a boiling kettle were produced by Reynolds in 1894,[436] a study which was expanded in succeeding years[437] and later commented on by Sir William Bragg[438] who noted

> The sounds of the kettle are very interesting... The little bubbles of steam... collapse, and do so with great suddenness, so that the sides strike against each other with a sharp smack. The blow is as hard and unyielding as when steel meets steel, and so there arises a noise from the kettle as if blows were rained upon it by innumerable tiny hammers.

Lord Rayleigh while studying the noise of a hissing kettle, developed the first mathematical model for the collapse of cavities in liquids predicting very high localised temperatures and pressures not unlike ultrasonication.[439] The collapsing bubbles led to the idea that 2D materials could be possibly produced by boiling rather than acoustic cavitation from an ultrasonic probe.

The difference between boiling and cavitation is defined among physicists but cavitation is used universally in the engineering field to describe the collapse of bubbles, regardless of their origin. The mechanism for bubble formation is different when comparing boiling and cavitation, best represented by a pressure-temperature phase diagram in Figure 7.1A. Bubbles induced by cavitation (e.g. ultrasonication) is the vertical transition occurring when the pressure drops below the vapour pressure.[440] Boiling is the horizontal phase transition at constant pressure by increasing the bulk liquid temperature, T (Figure 7.1A). In a rolling boil, the vapour pressure matches the ambient pressure where vapour-filled cavities (bubbles) rise and collapse.[441]

Boiling of water in a kettle takes place in a number of stages, represented by a typical boiling curve in Figure 7.1B. The curve shows the relationship between two important parameters: the heater surface heat flux (flow of energy through the element) and the excess temperature. The excess temperature is the temperature in excess of the normal saturation temperature, $\Delta T_E = T_{surface} - T_{saturation}$ (i.e. amount the surface temperature is higher than the saturation temperature).[442] The saturation temperature is the temperature at which vaporisation takes place (water = 100 °C at 1 atm). At a critical superheat, ΔT_c (point B), a vapour film forms around the element resisting heat transfer and decreasing the heat flux and overall efficiency.[440,443] A kettle runs below this point in the nucleate boiling regime where the excess temperature stays between 10-30 °C.

Initially, heat is transferred from the element in the bottom of the kettle to the bulk liquid by convection currents, when the surface temperature is only a few degrees higher than the surrounding saturated liquid.[443] Once the water temperature (measured at the sensor) reaches approximately 70 °C ($\Delta T_E \approx 10$°C), nucleate boiling is initiated in which vapour bubbles form at various sites on the heater surface.[443,444] As the element temperature increases further, the bubbles break away and rise to the cooler temperature at

the top of the kettle, reaching the free surface and collapsing.[441,443] The hissing noise a kettle makes in the early stages of the nucleate boiling regime is attributed to bubbles rising and annihilating. Close to the boiling point, vapour bubbles coalesce and form jets and columns that contain large vapour bubbles, stretching from the bottom of the kettle. The explosive cracking sounds heard just before a kettle boils are as a result of these large vapour bubbles collapsing at the top surface.[444]

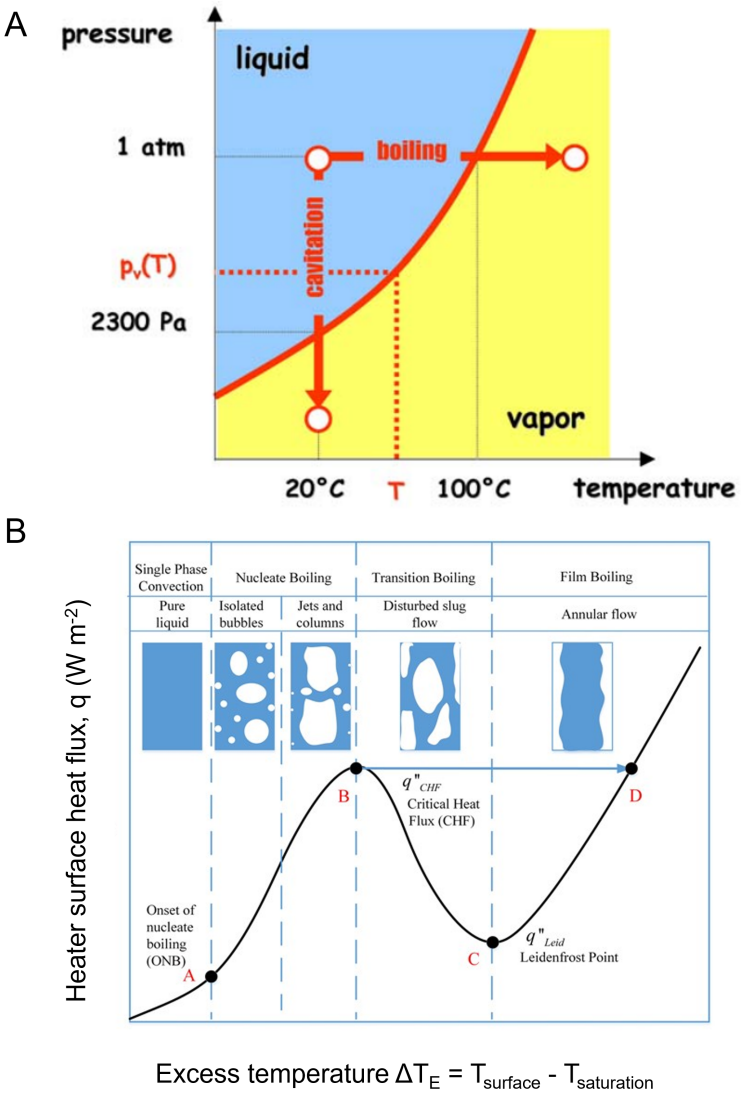

Figure 7.1: (A) Phase diagram for water shows cavitation as vertical path at constant temperature and boiling corresponding to a horizontal path at constant pressure. Image from Franc et al.[445] (B) A typical boiling curve showing the different stages of water boiling in a kettle up to point B. The element heat flux as a function of excess temperature (i.e. the temperature difference between the heater surface and the saturation temperature) is plotted. Initially water is heated through convection currents. As the temperature increases bubbles form on the element, rising to the surface and collapsing causing localised high temperatures and pressures. Image adapted from Hu et al.[442]

Exfoliation is expected to take place in the nucleate boiling regime where bubbles form and collapse. The larger vapour bubbles collapsing close to boiling point may release a greater amount of energy increasing the exfoliation efficiency compared to the earlier stages.

In this chapter, a kitchen kettle is used in place of an ultrasonic probe to create the same bubble collapse effect that leads to exfoliation, an idea conceived by Dr. Andrew Harvey. Aqueous surfactant solution was naturally chosen as a suitable liquid medium as opposed to a low boiling point solvent stabilisers. The aims of this work were to see if a common household machine like the kettle could in fact exfoliate any material at all and if so characterise nanosheets produced through microscopy and spectroscopy. Two kettle techniques are demonstrated, the first a standard kitchen kettle producing very low yields after multiple iterations of a full boil and the second a modification of the kettle in which a cooling coil allows for a rolling boil to be maintained for long periods of time, increasing the amount of bubble formation and collapse. Few layer graphene in non-negligible quantities is produced with the modified setup however through spectroscopic and microscopic characterisation appears far more defective than ultrasonicated graphene.

7.1 Experimental Methods

7.1.1 Sample Preparation

The initial condition and standard sample preparation, UV-Vis spectroscopy, TEM and EDX were performed by Dr Andrew Harvey. For initial testing with the standard setup, 40 g L^{-1} Haydale small flake graphite (GNP-E1) was added to the kettle (Igenix Cordless Jug Kettle, IG7270 1.7L) along with 1 L of aqueous sodium dodecyl sulfate (SDS, Sigma Aldrich BioXtra, $\geq$ 99.0%) solution (2.5 g L^{-1}). The kettle was switched on and allowed to run until 5 seconds before boiling over. An indicator that this point was reached was when the liquid could be seen rising up the measurement window at which point it was removed from the base. The dispersion was placed in a metal beaker in an ice bath to cool back to room temperature. This is labelled as 1 cycle in the kettle. For cycling tests, this process was repeated numerous times (1-8 cycles), cooling the dispersion in a metal beaker after each iteration and then placing back in the kettle for boiling. A fixed

volume of 1 L and 140 second heating time was used. A range of heating times were examined. A stopwatch was used for this time study, the kettle was removed from the base, essentially stopping any further power to the kettle after a time in the range 5-140 s, at a fixed volume of 1 L and 6 cycles. Similarly, the volume of liquid was tested in the range of 0.5-1.6 L, using a fixed time of 140 seconds and 6 cycles. The concentration of starting graphite was also varied in the range 5-80 g L^{-1}, using a fixed time of 140 s, volume of 1 L and 6 cycles (1 cycle is described above). For each study, except the cycling, the top 200 mL of each dispersion was centrifuged due to volume limitations of the machine. The centrifugation was performed at 100 *g* for 1 h in a Thermo Scientific Heraeus Megafuge 16 Centrifuge using a TX-400 swinging bucket rotor . For the cycling study, 20 mL of dispersion was removed after each cycle and centrifuged in a similar manner. The sediment was discarded and supernatant subject to a further centrifugation at 3000 g for 1 h to remove small impurities. The sediment was collected and redispersed in 5 mL of aqueous surfactant solution, used for characterisation. A standard sample was prepared using 80 g L^{-1} starting material, 6 cycles, 1 L and heating time of 140 s, trapped from 0.1-3k *g*. Size-selected sample using liquid cascade centrifugation (Section 3.1.2) with the following centrifugation speeds; 0.1k *g*, 0.4k *g*, 0.9k *g*, 1.6k *g* and 3k *g* were prepared using the same conditions as the standard sample.

The optimised kettle setup was designed and created by Dr. Andrew Harvey and David O'Mahony. A cooling coil was connected to a pump that allowed ice water to circulate through. The coil was placed approximately 5 cm from the bottom of the kettle with the lid remaining open. Similar parameters to the standard kettle were tested with time study ranging from 5-60 min and volume study of 0.5-1 L with the same centrifugation trapping of 0.1-3k *g* as above. A standard sample for the optimised kettle was made using a volume of 700 mL, heating time of 45 minutes, starting material concentration of 80 g L^{-1} and trapped from 0.1-3k *g*. Size selected samples were made using the same centrifugation parameters as the standard kettle and experimental conditions of the optimised standard sample (45 mins, 700 mL, 80 g L^{-1} graphite concentration).

The Haydale graphite was also tip sonicated for comparison. Graphite powder was probe sonicated (VibraCell CVX, 750W) at a concentration of 80 g L^{-1} powder dispersed in a 2.5 g L^{-1} aqueous SDS solution for 5 h with 60% amplitude and pulse of 6 s on and

2 off. The volume used was 80 mL. The dispersion was then centrifuged using the same cascade as described above.

7.1.2 Characterisation

Atomic force microscopy was completed using a Bruker Multimode 8 Atomic Force microscope in ScanAsyst mode with Bruker OLTESPA-R3 cantilevers. Each liquid sample was diluted until the sample was transparent (optical density of approx. 0.2). 10 μL of each sample was drop cast onto a pre-heated (180 °C) Si/SiO_2 (300 nm oxide layer) wafer. The wafer was then washed with water to remove excess surfactant on the surface. Individually deposited nanosheets were analysed through measurement with the AFM. Previously established length corrections[20] were applied to correct nanosheet length from tip broadening effects. Raman spectroscopy was using an Horiba Jobin Yvon LabRAM HR800 with a 532 nm excitation laser in air under ambient conditions. The Raman emission was collected by a 100×, long working distance objective lens, 1800 cm^{-1} grating with 10 $\%$ of the laser power ($\sim$ 1.4 mW). Sample were prepared by vacuum filtration of each sample onto a nitrocellulose membrane. A minimum of 10 spectra at different positions on the membrane were recorded and averaged. Optical spectra were measured using a Perkin Elmer Lambda 1050 UV-Visible spectrometer with a quartz cuvette (path length 4 mm). The spectrometer was equipped with an integrating sphere for measuring the absorption where scattering effects are removed.

In preparation for TEM imaging, each dispersion was diluted to optical transparency and manually drop-cast one drop at a time onto a holey carbon TEM grid with the aim of dropping approximately 0.1 mg of material. The grids were left to dry in air and then placed overnight in a vacuum oven at 70 °C to dry completely before measuring. Bright field TEM imaging was performed using a JEOL 2100 microscope. Energy-dispersive X-ray (EDX) spectroscopy was performed in situ with TEM imaging using an 80 mm^2 XMAX EDX detector. XPS measurements were taken (by Conor Cullen) using a VG Scientific ESCAlab Mk II system with a non-monochromatic Al K(α) X-ray source. Core-level spectra were acquired at a pass energy of 20 eV. Spectra were fitted with a Shirley-type background, component peaks were fitted with a combination of Gaussian-Lorentzian and Doniach-Sunjic line shapes using the software CasaXPS.

7.2 Results and Discussion

7.2.1 Initial exfoliation in a standard kitchen kettle

For preliminary testing, nanographite powder (40 g L^{-1}) was added to a standard kitchen kettle along with a standard 2.5 g L^{-1} sodium dodecyl sulfate (SDS) aqueous solution (Figure 7.2A). The kettle was switched on and let come to a near boil. The addition of surfactant naturally creates more bubbles in the liquid and so when heated, the volume expanded more than traditional water in a kettle. If the kettle was allowed to reach boiling point, the standard 1L volume would expand to such an extent as to overflow and flood the electronics in the removable base. The kettle was therefore powered off as the liquid began to rise, about 3-5 seconds before boiling point.

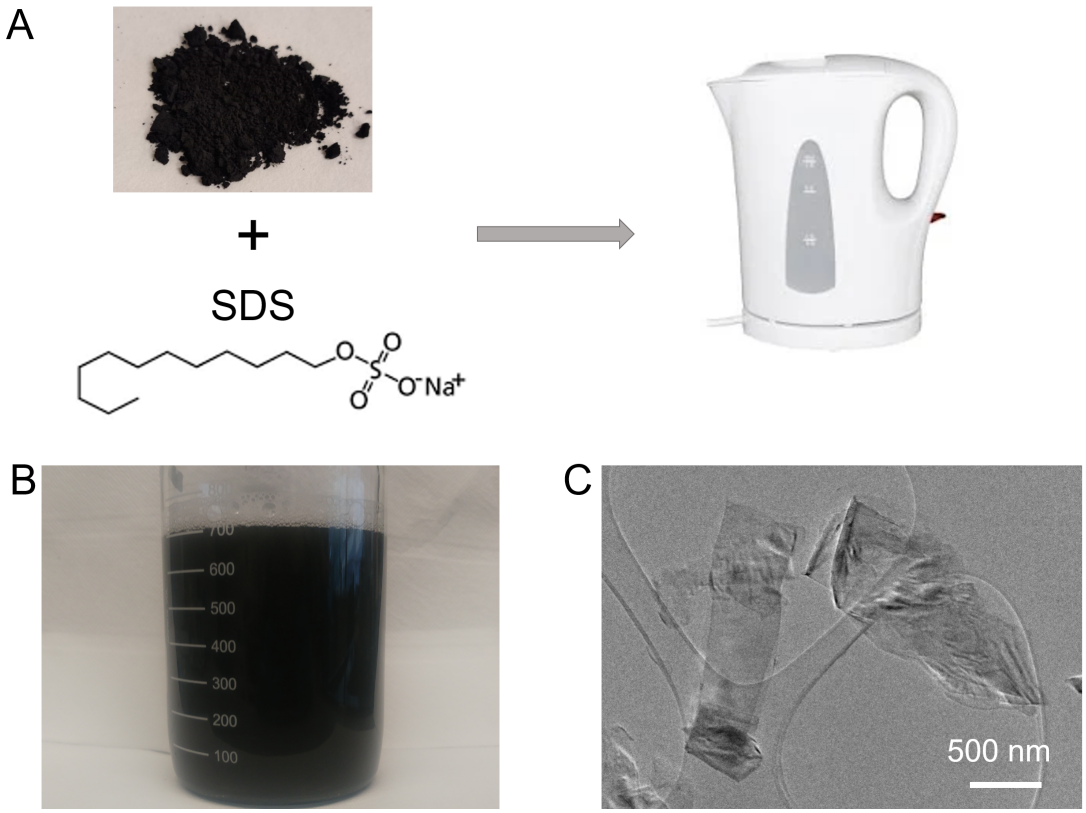

Figure 7.2: (A) Starting materials, graphite and aqueous sodium dodecyl sulfate (SDS) solution put in a standard kitchen kettle and set to boil. The kettle was switched off just before boiling point to ensure there was no overflow and subsequent damage to the fuse. (B) A picture of the resulting dispersion poured straight from the kettle. (C) Representative TEM images of initial dispersions made using the standard kettle shows thin graphene like material, with sheets a few microns in length.

The dispersion when removed from the kettle is typically black in colour, shown in Figure 7.2B. To remove unexfoliated material, the dispersion was centrifuged with a trapping of 0.1-3k g. The sample was imaged with TEM, showing relatively thin, graphene-like nanosheets microns in length (Figure 7.2C).

Four key experimental variables were identified as being important on the yield of nanosheets in the final dispersion namely initial graphite concentration ($Conc_i$), number of cycles the dispersion was boiled, heating time in the kettle and the volume of liquid used. One cycle was allowing the kettle to come to a near boil (heating time of 140 s) and cooling the dispersion back to room temperature for any subsequent cycles. Each parameter was varied while keeping the others constant. All samples were analysed with UV-Vis spectroscopy. Using the Beer-Lambert law (Section 3.2.1) and the size independent extinction coefficient at 750 nm (ε_{750nm} = 5450 L g^{-1} m^{-1}),[67] the nanosheet concentration of each sample was calculated. The starting concentration of graphite was varied from 5-80 g L^{-1} and shows an intuitive increase in nanosheet concentration with increasing initial concentration (Figure 7.3A). The slope of the linear fit gives the yield to be $3.58\times10^{-2}\%$, much lower than typical LPE yields of around 10%.[67,336]

Similarly, the nanosheet concentration increases with the number of heating cycles the dispersion undergoes (Figure 7.3B). Each sample was cooled back to 20 °C in an ice bath between cycles to ensure the same conditions were used for each repetition. It is probable that the increase in bubble collapse over many cycles leads to more scission of the graphite crystal, increasing the number of nanosheets. The same logic applies for the increase in nanosheet concentration with heating time, ranging from 5 to 140 seconds in Figure 7.3C. The heating time is limited to a maximum of 150 seconds for a standard volume of 1 L at which point the kettle comes to a boil and switches off. In standard LPE samples the concentration has been found to scale with time$^{1/2}$,[25,190] represented by the dashed line in Figure 7.3C. Although the kettle samples do not follow this trend exactly, it is not far from this behaviour.

Finally there is an increase in nanosheet concentration with increasing volume up to a maximum volume 1.6 L, the size of the kettle determining the 0.5-1.6 L range (Figure 7.3D). This is in contrast to shear mixed graphene shown by Paton et al.[215] where

increased volume decreased the nanosheet concentration. The larger the volume also means that it is more difficult to remove the kettle from the power base before it overflows. With these results in mind, a standard sample protocol was created using a volume of 1 L, 6 cycles, 80 g L^{-1} and 140 seconds of heating (the maximum possible).

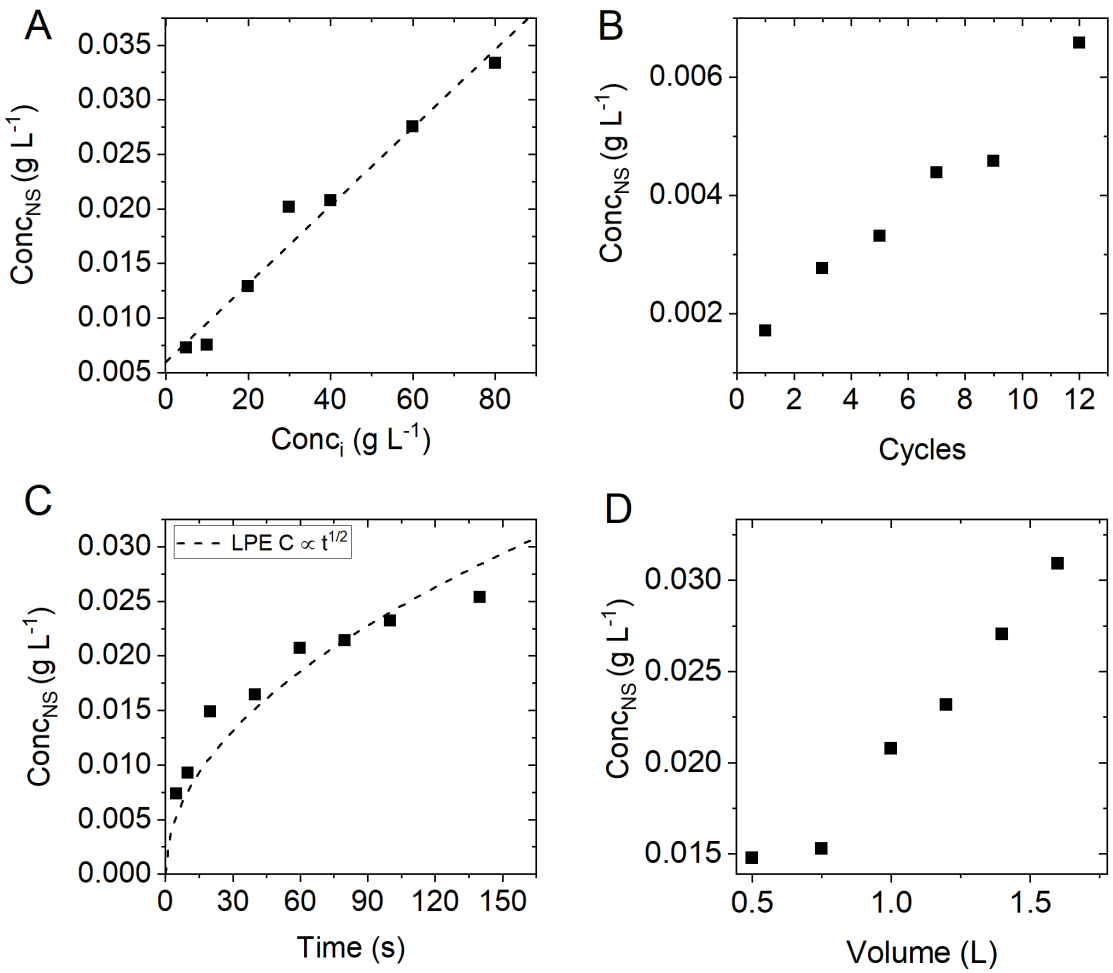

Figure 7.3: Initial conditions study of kettle exfoliated material. The nanosheet concentration was calculated from UV-Vis spectra using Beer-Lambert Law and the size-independent extinction coefficient at 750 nm,[67] ε_{750}= 5450 L g^{-1} m^{-1} (A) Final nanosheet concentration versus initial graphite concentration. The slope of the linear fit gives a yield of $3.58\times10^{-2}\%$ (B) Nanosheet concentration as a function of the number of cycles in the kettle. One cycle was bringing the kettle to just short of boiling point, as the liquid began to rise upwards. (C) Nanosheet concentration versus time the kettle was powered on. The dashed line is guideline for Conc $\propto$ time$^{1/2}$ behaviour observed in LPE samples.[24,26] (D) Nanosheet concentration versus starting volume of liquid.

The standard sample using the above parameters was characterised both microscopically and spectroscopically to probe the type of material produced. TEM statistical length analysis of hundreds of nanosheets gives a broad log-normal distribution and mean nanosheet length of 1258 nm (Figure 7.4A). This is comparable with LPE graphene and other materials suggesting the kettle exfoliates with a similar scission and tearing mechanism, creating analogous length scales. However, it is also possible that the centrifuge is just selecting a similar length distribution. The optical extinction (ε), absorption (α) and scattering (σ) spectra are shown in Figure 7.4B. The extinction spectra is similar to graphene, mainly broad and featureless with an increased contribution from scattering for decreasing wavelengths. The polydisperse nature of the sample broadens the well-defined peak of a theoretical spectrum. Spectroscopic metrics[67] for nanosheet thickness (used in Chapter 5) estimate the number of layers to be between 10-16, above the limit for reliable metrics, and so AFM is used below for a more accurate quantitative analysis.

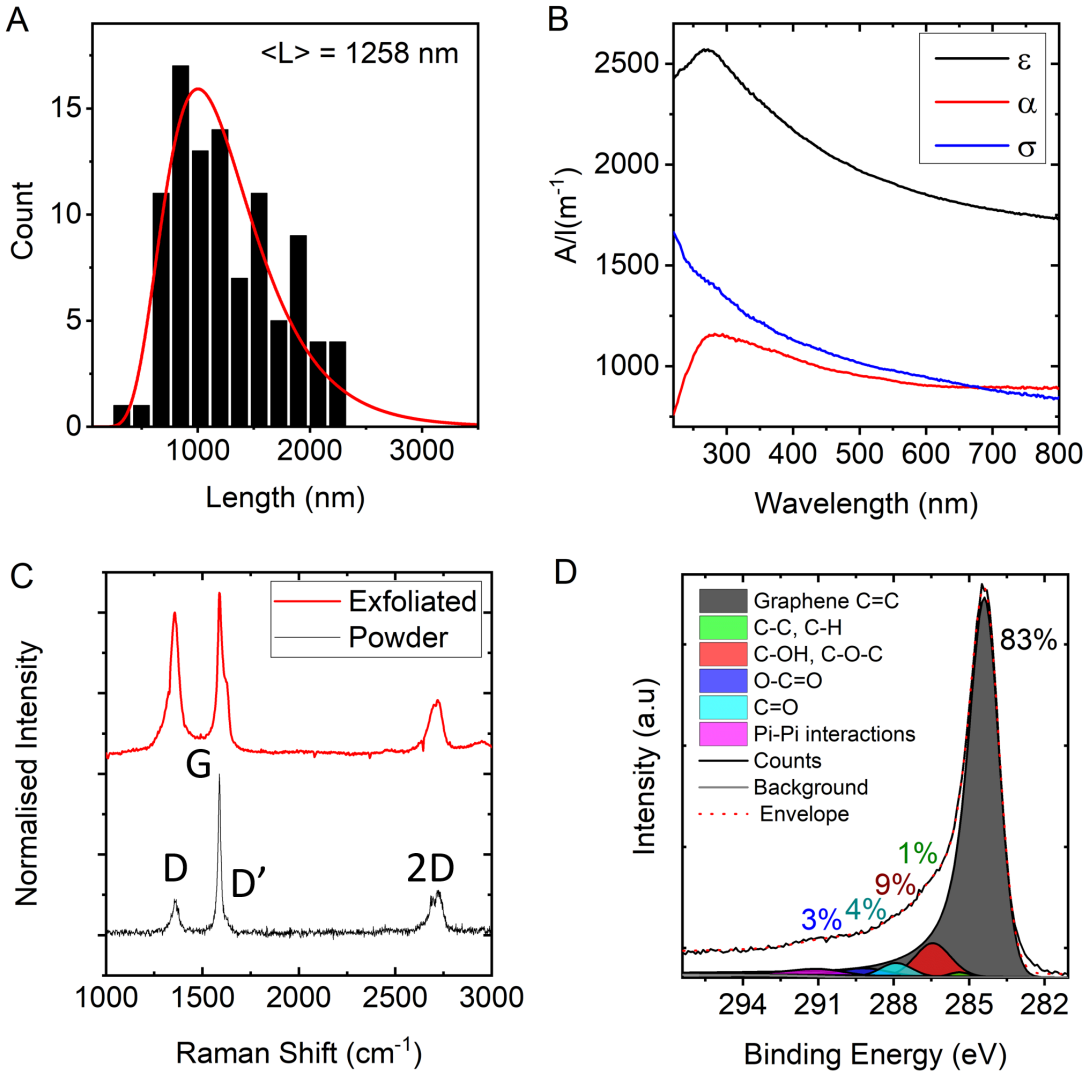

Figure 7.4: (A) TEM length histogram from a standard sample made using the standard kettle set up shows a broad log-normal distribution with the mean nanosheet length <L>=1285 nm. (B) UV-Vis extinction (black), absorbance (red) and scattering (blue) spectra of a standard sample made using the standard kettle. (C) Raman spectra of both a standard kettle sample (red) and the starting powder (black). There is a clear increase in D ($\sim$ 1350 cm^{-1}) and D' ($\sim$1620 cm^{-1}) peaks suggesting the nanomaterial produced contains a large amount of defects. (D) X-ray photoelectron spectroscopy (XPS) analysis of the carbon 1s core-level region reveals the characteristic asymmetric lineshape associated with graphene. Deconvolution of the lineshape reveals a small number of oxidation components present.

Raman spectroscopy was performed to compare the exfoliated product to the starting material. For all dispersions studied by Raman, thin films were formed by vacuum filtration. Raman spectra at a number of points on the film were measured for each sample and averaged. The starting material is a typical graphite spectrum with small D ($\sim$ 1350 cm^{-1}) and 2D ($\sim$ 2700 cm^{-1}) bands compared to the G band ($\sim$ 1580 cm^{-1}), indicating a rela-

tively low defect content before exfoliation (Figure 7.4C). The exfoliated material on the other hand has a significantly larger D peak, suggesting that the process induces defects or that it selects defective material. The 2D band is only slightly larger compared to the bulk, a possible indication that the amount of few layer graphene produced is low. In general, edge defects are unavoidable in the LPE process due to the fact that sonication induces scission which cut parent graphite crystallites into small flakes.[199,336] Smaller nanosheets were reported to have a greater edge to basal plane ratio than larger ones, increasing the edge defect population.[199,336]

X-ray photoelectron spectroscopy (XPS) also detects the presence of defects in carbon materials that can lead to new peaks and alter the peak position and line width of the carbon 1s core level.[45,446] XPS analysis of this carbon 1s core-level region of the kettle sample reveals the characteristic asymmetric lineshape associated with graphene (Figure 7.4D). Deconvolution of the lineshape reveals a number of minor components accounting for flake edges, oxides, and defects in the material, while the majority (83%) of carbon atoms are found to be in the sp^2 hybridised, C=C configuration of graphene. This analysis is in agreement with the Raman spectra indicating that defects are present in the exfoliated sample, the type of defects are discussed in more detail below. A comparison of this XPS data with LPE graphene is displayed in Figure E.1. The kettle sample appears to have greater contributions from defects and oxides compared to the liquid exfoliated sample.

To more accurately probe nanosheet thickness, AFM was performed on three size selected trappings of a sample made in the kettle, representative images of which are shown in Figure 7.5 (top row). As in Chapters 4, 5 and 6, pixelation and tip broadening effects result in an overestimation of nanosheet length and width. To adjust for these effects, a correction formula was applied in line with previous work for LPE nanosheets.[19,20,67] The apparent height of a single graphene layer was reported previously for graphene to be 0.9 nm[67,215] allowing for the calculation of layer number. In principle the step height could be different for kettle exfoliation material however this was not accounted for in this study. Any deviation from the 0.9 nm step height it most likely very small. Statistical analysis of nanosheet length for each size shows a narrowing of a broad log-normal distribution, typical of LPE 2D materials. The number of layers however is very large, the mean number of layers ranging from 95 for the 0.1-0.4 k *g* sample to 48 for the 0.9-1.6 k *g* sample, far

thicker than standard LPE graphene that produces samples with <N> <20 layers even for low centrifugation speeds.[202] The kettle only produces the bubbles that collapse and exfoliate material for approximately 10-15 seconds prior to boiling and so even with a number of cycles, this short window for the more explosive later stages of boiling resulted in partial exfoliation of graphite. The degree of exfoliation could be increased by increasing the time that bubbles were continuously formed in the kettle, the design and implementation of which is discussed below.

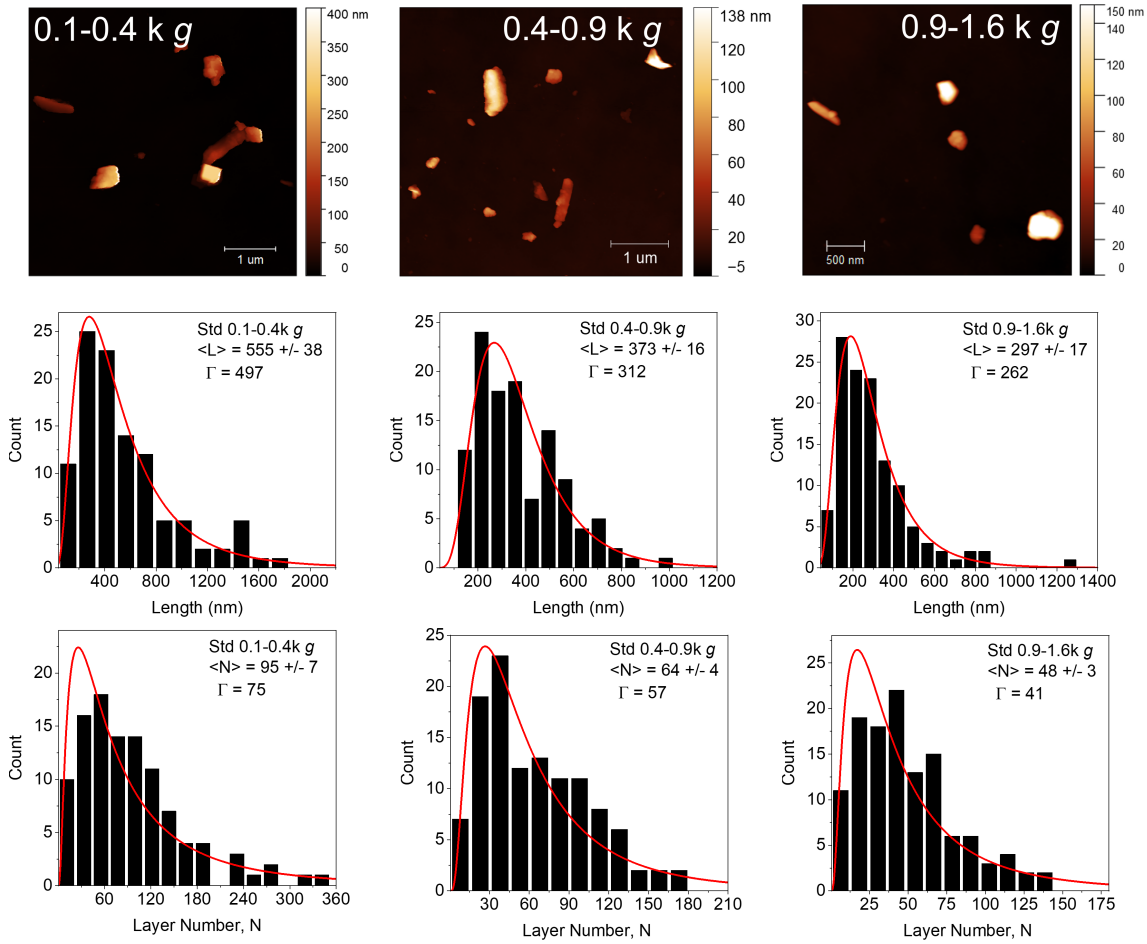

Figure 7.5: Representative AFM images (top row), layer number (middle row) and length (bottom row) distribution histograms on three trappings produced from the standard size selection cascade. Γ is the width of the log-normal distribution. From left to right: 0.1-0.4k *g*, 0.4-0.9k *g*, 0.9-1.6k *g*.

7.2.2 Optimising the kettle design for exfoliation

A new experimental setup was designed by Dr. Andrew Harvey and created by David O'Mahony in which a stainless steel coil pumped with circulating ice water is lowered in the kettle (Figure 7.6A). The temperature gradient provided by the cooling coil allows for continuous bubble formation without the kettle switching off. The kettle has a thermostat that breaks the electrical connection to the element when the boiling point is reached, switching it off. Simply leaving the lid open with no cooling coil would cause too much evaporation of the liquid. A combination of the cooling coil and open lid means thermal energy can escape in the form of steam so the dispersion never reaches boiling point that triggers the thermostat, allowing the kettle to bubble continuously. The sound of the bubbles violently collapsing would suggest that the power supplied is enough to maintain the liquid in the nucleate boiling regime. Temperature probes a few centimetres below the top of the liquid and above the element show a 50°C gradient i.e. 90 °C just above the element and 40°C just below the surface of the liquid.

The ice water is circulated from a cold water supply through the coil and into warm water output bath (Figure 7.6B). A typical black graphene dispersion produced by the optimised kettle can be seen in Figure 7.6C. A kitchen kettle is not designed to run for more than a couple of minutes at a time and so it switches off after approximately 45 mins with the cooling coil. This may be due to overheating of the element and electronics in the power base. Once the kettle is left to cool for a couple of hours, it is operational again. The same initial graphite concentration, surfactant concentration, volume of 1 L and centrifugation parameters were used along with a running time of 45 mins to make a standard sample with the optimised kettle setup.

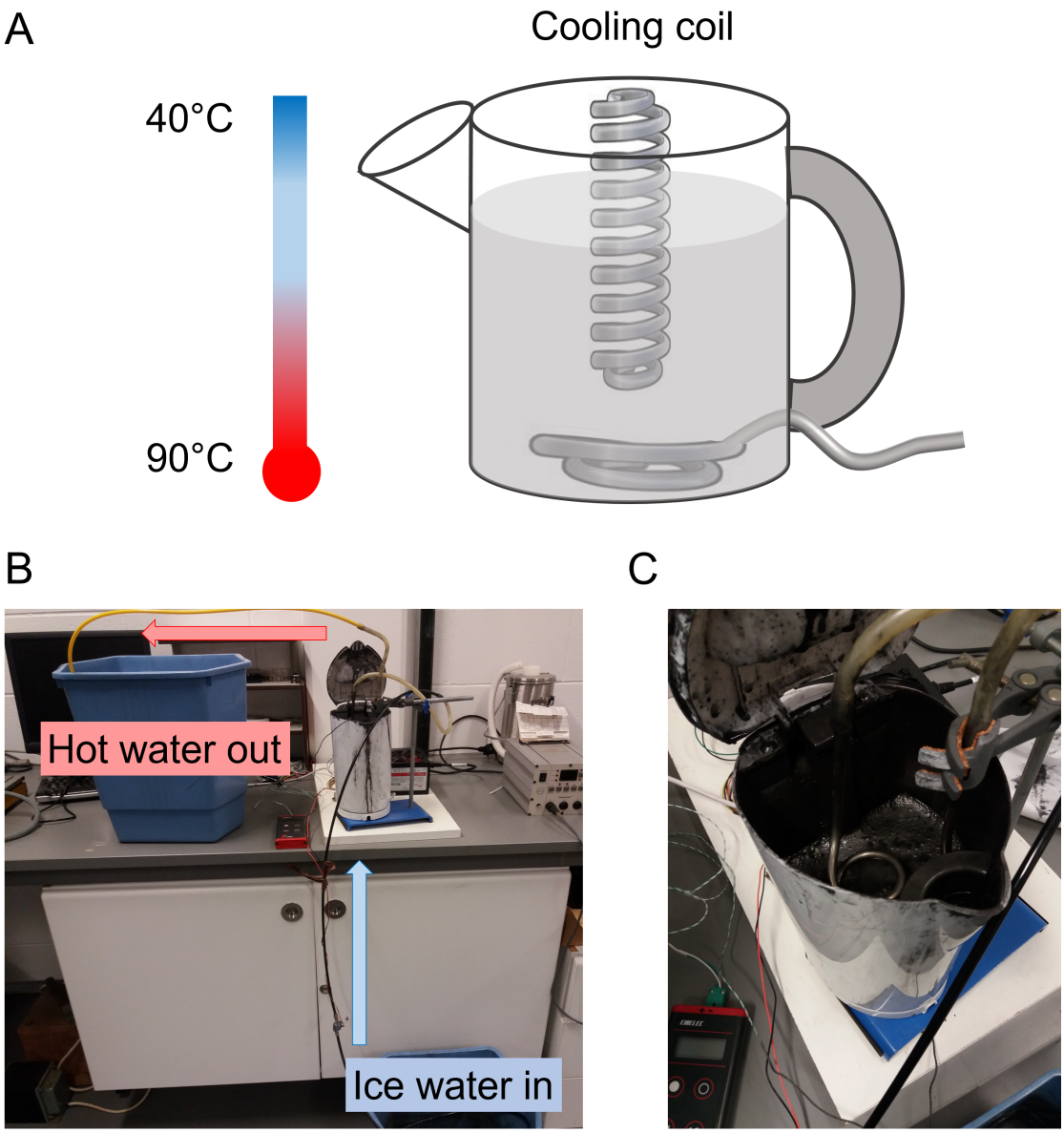

Figure 7.6: (A) Schematic representation of the design to optimise exfoliation conditions in the kettle. A cooling coil circulating ice cold water would increase the temperature gradient between the bottom of the kettle and top. (B), (C) Images of the experimental setup.

Size selection using the same centrifugation speeds as the standard kettle provided three comparable samples for AFM imaging and statistical analysis. Representative images are shown in Figure 7.7 (top row). The nanosheet length distributions are comparable to the standard kettle samples with mean nanosheet lengths within 50 nm of the standard means across all sizes, suggesting the new setup does not change the scission of the material during exfoliation. There is however a narrowing of the layer number distribution across all sizes for the optimised (opt) samples (Figure 7.7, bottom row) indicating that the

interlayer bonds between parent crystals are broken to a much greater extent using the new experimental design. This behaviour does not agree with equipartition in energy hypothesis mentioned previously (Section 2.3) so other factors, such as defect content, must play a role as discussed below. The higher exfoliation efficacy is most likely due to the creation of more bubbles for a sustained period of time. The 0.9-1.6k *g* smallest trapping has a very large number of nanosheets 5 layers or less compared to the other counts. Although this trend is preferable, indicating better exfoliation of the starting material, it does not follow the standard log-normal distribution seen in Chapter 4 and for other 2D materials.[24, 133, 192, 202]

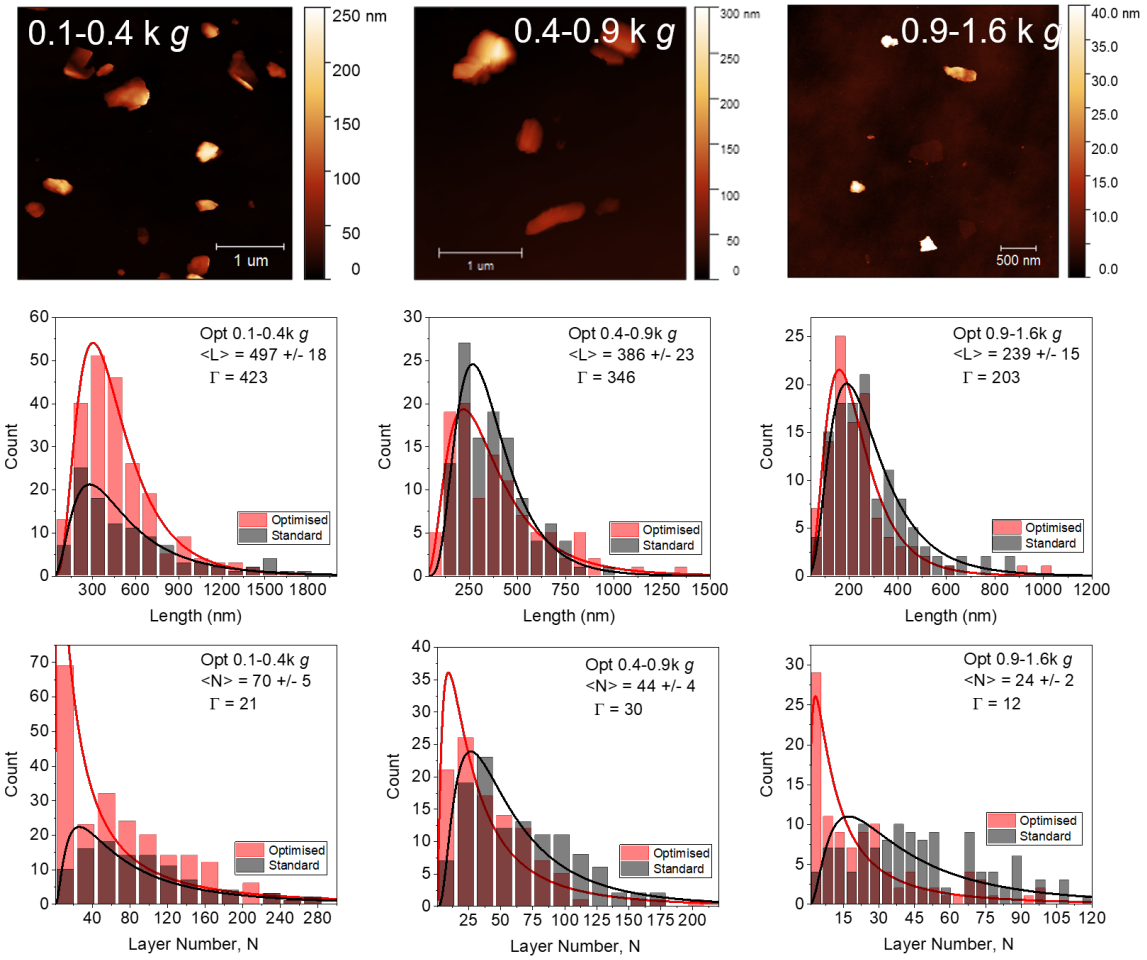

Figure 7.7: Representative AFM images (top row), layer number (middle row) and length (bottom row) distribution histograms on three trappings produced from the optimised kettle size selection cascade (red) overlayed with the standard kettle data (black). Γ is the width of the log normal distribution for each optimised sample. From left to right: 0.1-0.4k *g*, 0.4-0.9k *g*, 0.9-1.6k *g*.

7.2.3 Comparison between standard and optimised kettles

To test whether the new design was in fact optimising the exfoliation yield of graphite, the experimental variables of heating time and volume were analysed this time using the new setup. Since the kettle was run continuously, the number of cycles is not applicable. The heating times for the optimised kettle were longer than the standard kettle but also show a ten-fold increase in nanosheet yield (Figure 7.8A). The longest possible heating time gave the highest nanosheet concentration. The volume study was limited due to the displacement of liquid caused by inserting the cooling coil and so the maximum volume was 1 L. Furthermore, a minimum volume of 0.5L was required to sustain near-boiling for 45 minutes while also being the minimum safe volume designated by the manufacturer. Once again, there is a factor of 10 increase in nanosheet concentration in comparison to the standard kettle but nanosheet concentration for the optimised kettle varies weakly with volume (Figure 7.8B). The production rate P_r (nanosheet mass/time) can also be calculated by using the concentration (C) and volume (V) where $P_r = VC/t$. The highest production rate for the 1 L sample was found to be 0.19 g h^{-1}. This can be compared to the production rate of shear-exfoliated graphene of 1.44 g h^{-1} by Paton et al.[215] and shows the kettle needs vast improvements for any future scale-up.

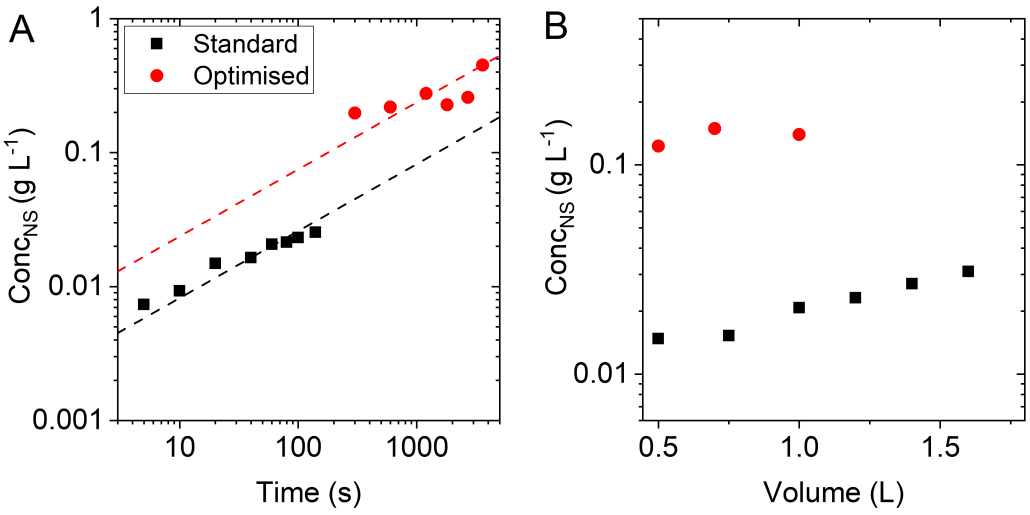

Figure 7.8: Comparison of experimental variables between standard (black data) and optimised (red data) kettles all show an order of magnitude increase in nanosheet concentration using the optimised setup. The optimised setup was run continuously for 45 mins and so number of cycle is not comparable. (A) Nanosheet concentration versus time the kettle was powered on. The dashed lines are guidelines for Conc $\propto$ time$^{1/2}$ behaviour observed in LPE samples.[24,26] (B) Nanosheet concentration versus starting volume of liquid.

Using the AFM data from the standard and optimised setups, Figures 7.5 and 7.7, the nanosheet area versus layer number can be plotted, each data point representing an individual nanosheet (Figure 7.9). Reflecting the previous histograms, there are more few layer graphene sheets produced in the optimised kettle. For LPE 2D materials the nanosheet area has been shown to increase with layer number with roughly quadratic scaling.[202] The power law trend (Area $\propto N^2$, represented by dashed line) can be seen for nanosheets above 10 layers in Figure 7.9 but appears to be shifted to thicker N compared to LPE graphene[202] and more similar to the SnP_3 data cloud shown in Chapter 6. One would expect this power law to extend below 10 layers i.e. nanosheet area would be smaller for thinner nanosheets, however this do not appear to be the case. As seen in Figure 7.9, nanosheet area is scattered for sheets of less than 10 layers, ranging from 0.002- 0.5 μm^2.

It is possible that two regimes exist. In the first regime neighbouring layers both contain basal plane defects that face one another, reducing the out-of-plane modulus. This functionalization in the basal plane leads to a widening of the interlayer spacing at this point and weakens the π-π interactions. The chance that two stacks with basal plane defects on the outer surface face one another however is relatively low and will happen in the minority of cases but produces large FLG sheets as seen in the first regime (blue region) in Figure 7.9. It is likely that the bubble collapse from boiling is less violent than collapsing bubbles in sonication which can result in inertial cavitation, identified as a primary source of exfoliation/scission.[204] On the other hand, the kettle does not appear to be as efficient a process as ultrasonication and so in the majority of cases the basal plane defective graphene is not efficiently exfoliated, producing partially exfoliated material (red region, Figure 7.9). The increased bubble formation and collapse using the optimised setup increases the energy available for peeling these defective sites and so the FLG population is larger for this dataset.

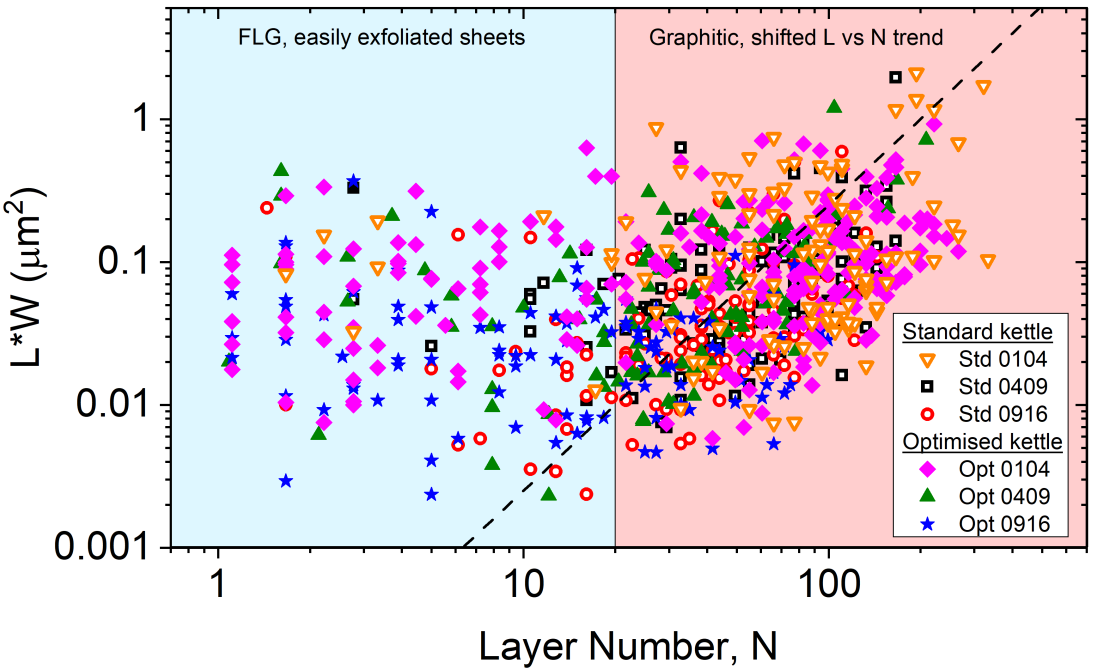

Figure 7.9: Nanosheet area (approximated as L $\times$W) versus layer number data clouds for size selected samples using both the standard and optimised kettles suggest that in general, the trend is shifted to thicker N compared to ultrasonicated 2D materials[133] but there is some few layer graphene (FLG, $<$ 10 layers) present. The dashed line is a power law guideline observed in for many 2D materials[202] with equation Area = $2.5\times10^{-5}N^2$. There is an increase in the number of FLG sheets in the optimised setup compared to standard kettle which is also reflected in the statistical analysis in Figures 7.5 and 7.7.

To further analyse the defect content of the exfoliated material, Raman spectroscopy was performed, comparing standard and optimised samples. The two spectra are very similar with a near identical 2D peak, attributed to the observation that the majority of the graphene/graphite volume is still in the form of thick sheets which dominate the spectroscopic response. The I_D/I_G ratio for the standard kettle is 0.54 while the optimised kettle is 0.68 indicative of a higher defect content, in agreement with the proposed regimes in the AFM data clouds. Raman probes the volume of nanosheets rather than the number so the high D band would suggest that the more graphitic material (red regime, Figure 7.9) is also defective, not just the FLG. More FLG is exfoliated for the optimised setup but these sheets appear defective to a greater extent. Due to the high D band in both spectra, multiple peak fitting is required to accurately measure peak intensity which will then be used for further defect analysis. The D, G and D' bands are fit to a triple Lorentzian, an example fitting shown in Figure 7.10B with full table available in Appendix E.2. The R

squared of the fitting is 0.99 confirming that Lorentzian peaks are the correct choice.

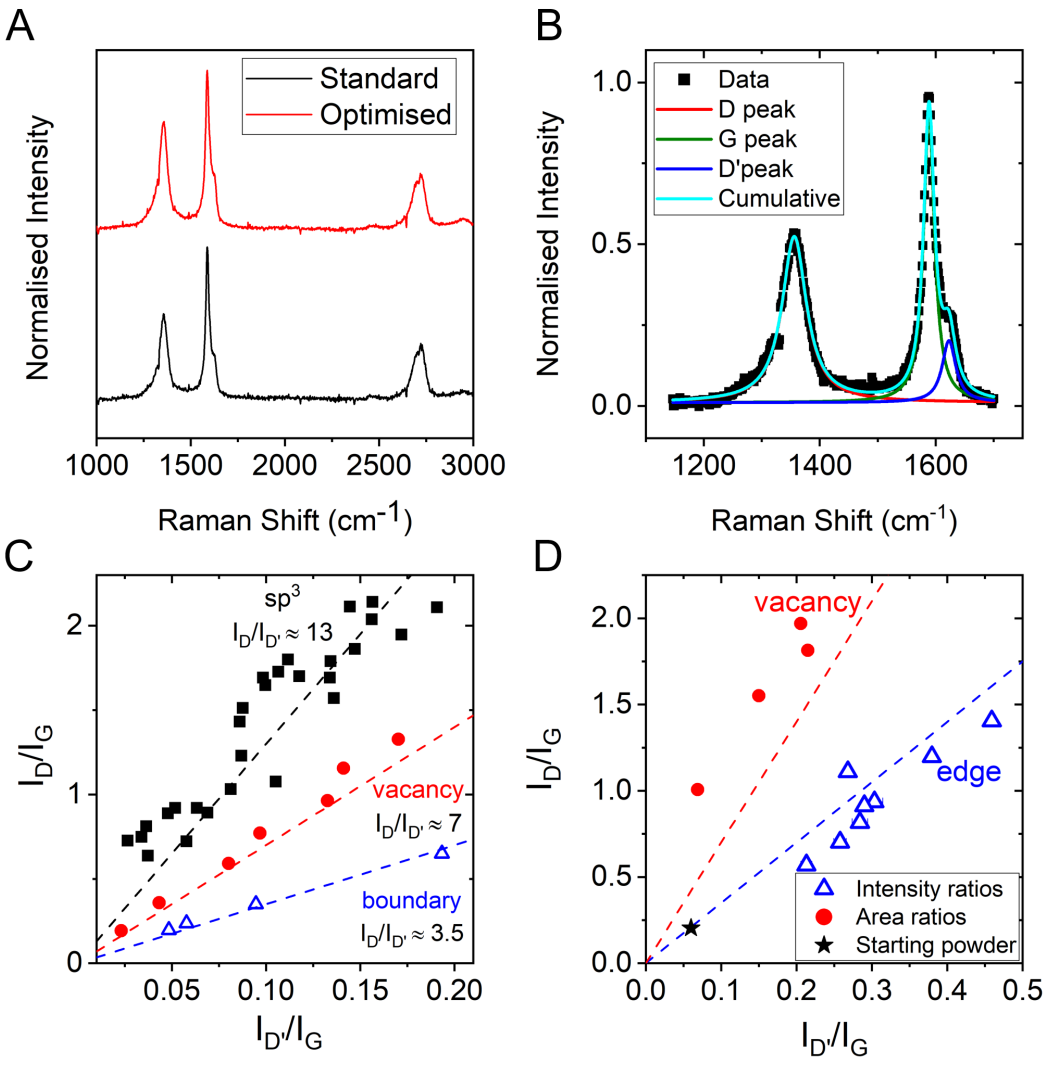

Figure 7.10: (A) Raman spectra (excitation wavelength, λ_{ex} = 532 nm) of two films made from a standard sample of both methods (standard and optimised kettles), normalized to the G band at 1580 cm^{-1}. Both spectra show very similar peak G, D' and 2D peaks. The D band intensity is higher for the optimised kettle, suggesting that more defective material is produced. (B) Due to the high D band, a triple Lorentzian peak fitting is required for estimated of the ID/IG and ID'/IG ratios used to analyse the quality of samples produced. A full table of the fitting can be found in Appendix E.2. (C) Data extracted from Eckmann et al.[44] shows the linear dependence of the I_D/I_G and $I_{D'}/I_G$ ratios for different types of defects. (D) Films from both standard and optimised kettle were analysed and the ID/IG versus ID'/IG ratios were plotted, suggesting that the defects present in the samples are mostly edges. However, this theory is contradicted when the area ratios are taken instead, indicating that more basal plane defects are present. It is likely that the nanosheets contain a combination of both edge and vacancy defects.

The nature of defects in graphene samples has been studied for micro-mechanically exfo-

liated flakes by Eckmann et al.[44] The slope of I_D/I_G versus $I_{D'}/I_G$ (i.e. the $I_{D'}/I_D$ intensity ratio) was reported to increase for different types of graphene defects; boundary ($\sim$ 3), vacancy ($\sim$ 7) and sp^3 hybridisation ($\sim$ 13), the data was extracted[44] and represented in Figure 7.10C. Peaks from Raman spectra for numerous samples using both standard and optimised kettles were analysed as described above and I_D/I_G versus $I_{D'}/I_G$ ratio plotted for each in Figure 7.10D. The starting material is also included. The intensity ratios are consistent with edge-type defects (blue dashed line) for all samples both standard and optimised. Other authors[67,207,447] have also observed an edge-defect intensity ratio for LPE graphene. Backes et al.[67] suggested that edge defects are invariably detected due to the nature of the Raman measurement. Here, the dispersions were vacuum filtrated onto nitrocellulose membranes and so the graphene naturally restacks itself. The laser is estimated to probe 25,000 nanosheets per measurements and so edges will always be detected giving rise to edge defect-induced Raman scattering.[67]

In addition to peak intensity ratios the integrated area ratios for a number of samples are plotted in Figure 7.10D (red circles). Using the integrated area from the Lorentzian peak fitting, the ratios follow the vacancy defect regime. Basal plane defects may explain the abundance of large, thin nanosheets produced from the kettle sample (Figure 7.9) where crystallites that are defective across the plane, rather than just on the edges, aid the exfoliation. It may be the case that for nanosheets probed, edge defects outweigh vacancy defects causing the edge-induced Raman scattering to mask signatures from vacancies. In contrast Bracamonte et al.,[448] suggest that the bulk defects measured by Raman are not vacancies or other basal-plane defects but topological in nature, likely formed as a result of the cavitation process. In a study by Jorio et al.,[449] measuring the disorder of graphene via Raman spectroscopy, they note that peak intensity ratio is a more suitable measure of defect density compared to integrated area, suggesting that the area is very much dependent on the FWHM which in turn depends on the fitting procedure. Eckmann et al.[44] reported that for low disorder, the use of integrated area and peak intensity is equivalent however this trend diverges for higher defect concentrations where a decrease in intensity is balanced by an increase in the peak FWHM. The high D band present in all Raman spectra would suggest that there are a large number of defects in the exfoliated material. From the intensity and area ratios data (Figure 7.10), it is likely that the nanosheets contain both edge and vacancy defects.

7.2.4 Comparison between kettle and tip sonicated exfoliation

The starting material was exfoliated using the standard LPE method to compare with the kettle exfoliated material. Three sized samples were prepared using the same centrifugation parameters as the kettle samples above. Representative AFM images of the three sizes are shown in Figure 7.11 (top row), decreasing in size with increasing centrifugation speed as expected.

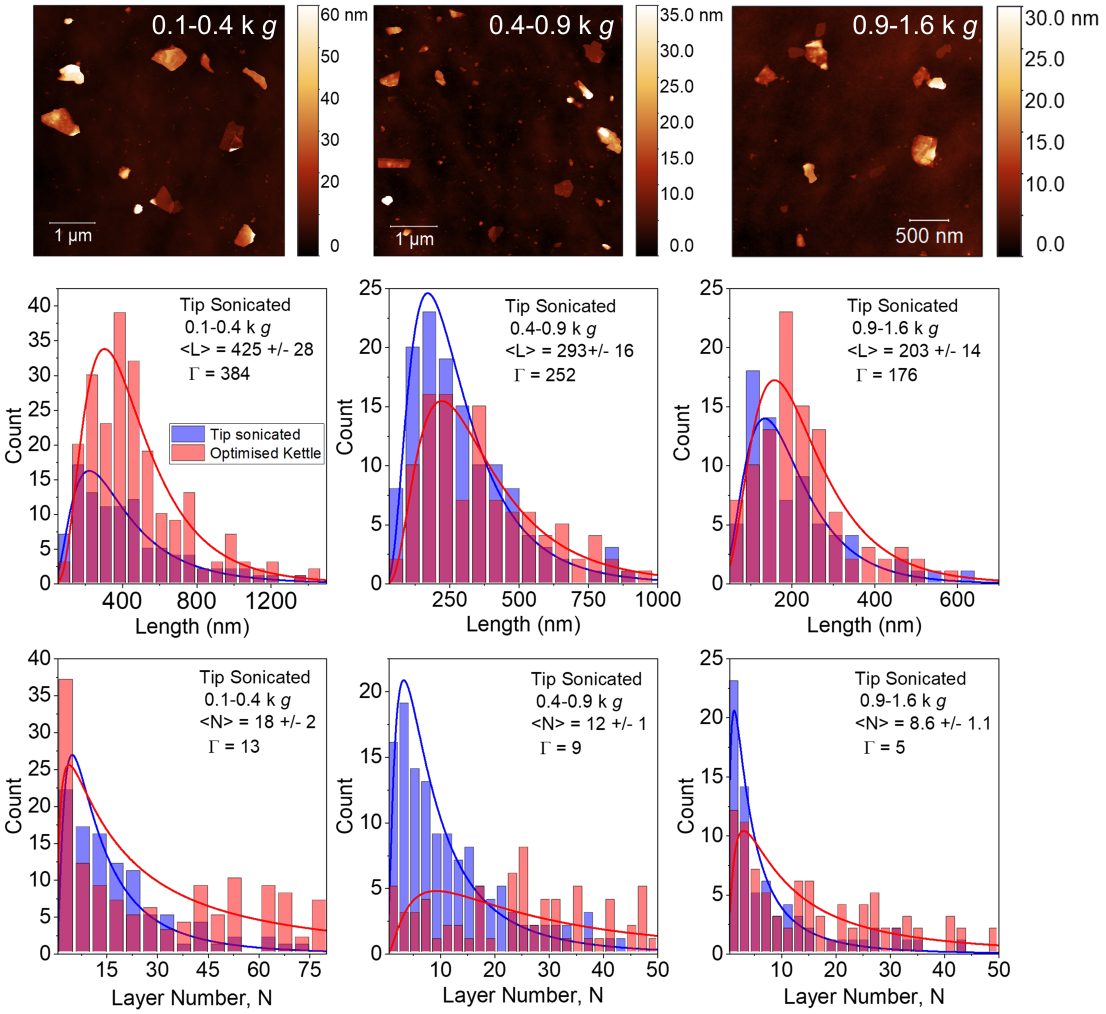

Figure 7.11: Representative AFM images (top row), layer number (middle row) and length (bottom row) distribution histograms on three trappings produced by tip sonication of the starting Haydale graphite (blue) overlaid with the optimised kettle data (red). Γ is the width of the log normal distribution for each tip sonicated sample. From left to right: 0.1-0.4k *g*, 0.4-0.9k *g*, 0.9-1.6k *g*.

The height scales are considerably lower than kettle exfoliation, indicating much thinner nanosheets are produced. Log-normal distributions of both nanosheet length and layer

number confirm that nanosheets are slightly smaller in length, though not significantly, and much thinner (Figure 7.11). The nanosheet length and layer number have a $g^{-0.48}$ and $g^{-0.49}$ power-law scaling in agreement with other LPE 2D materials, shown in Appendix E.3. The nanosheet area versus layer number data cloud is also shifted down in number of layers, indicating more thorough exfoliation compared to the kettle (Appendix E.3).

The mean nanosheet area as a function of mean layer number is plotted for standard LPE graphene (Sigma Aldrich graphite with sodium cholate, extracted from Backes et al.), the tip-sonicated Haydale graphite and the standard and optimised kettle methods in Figure 7.12. Three data points is quite a minimal dataset for these fits. Further measurements are planned to add more but for now preliminary conclusions are drawn based on the data available. As discussed in Chapter 6, the nanosheet area increases as a power law with thickness. This power law was shown to be material dependent by Backes et al.[202]

The tip sonicated material clearly produces thinner and slightly smaller sheets than the kettle with similar centrifugation trappings. The Sigma Aldrich (LPE Gra SC data points) starting material appears to produce thinner nanosheets than the Haydale graphite, indicative of a different in-plane and out-of-plane binding strength in the two graphite sources. Li et al.[199] reported that the degree of graphite exfoliation is dependent on the defect density of the starting material since parent crystallites are said to fragment initially along naturally existing vacancy defects. One would expect other starting graphites to sit on slightly different lines but ultrasonication generally produces mean layer numbers of <10 layers regardless of the starting material. When the Haydale graphite is tip-sonicated, crystallites undergo extremely efficient scission along existing basal plane defects, producing less defective, thinner graphene. On the other hand, with the kettle, the data is shifted significantly upwards in layer number. The optimised kettle setup gives lower mean layer numbers than the standard kettle as discussed in the previous section.

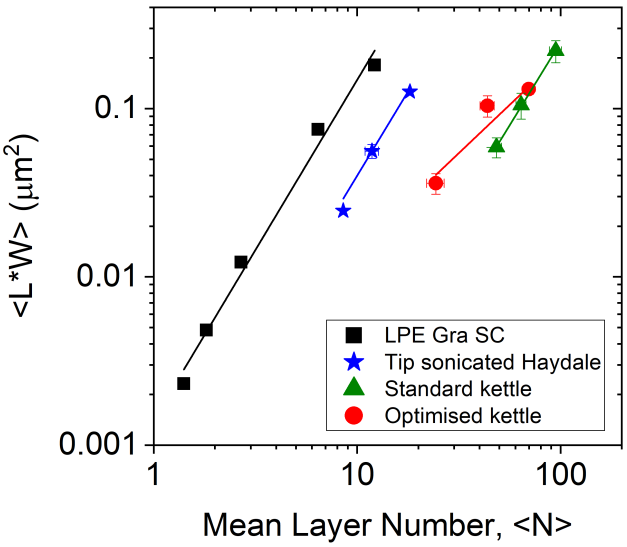

Figure 7.12: Plot of mean nanosheet area as function of mean layer number. The nanosheet area increases as a power-law with thickness as shown by the linear fits. The LPE graphene data was extracted from Backes et al.[202] There is a clear shift in thickness both with starting material and kettle exfoliated material. While the optimised process is shifted downwards from the standard kettle, the plot indicates the kettle is perhaps a low-energy technique and does not exfoliate to the same extent as tip sonication.

It is useful at this point to briefly address the power consumption in both systems. The ultrasonicator displays the wattage and total energy imparted to a liquid while powered on to give a rough estimation of the amount of power that the 750 W machine contributes to shearing material in the liquid. The sonic tip displays 50 W while running at a standard amplitude with 80 mL of graphite and surfactant solution. In contrast, the kettle manufacturer states that the wattage of the kettle is 2.2 kW, a higher power piece of equipment compared to the sonic tip. A rough calculation of the power imparted to the liquid in the kettle can be completed using a standard heat transfer equation:

$$P = \frac{Q}{t} = \frac{mC\Delta T}{t} \tag{7.1}$$

where P is power, Q is heat energy (in Joules), m is the mass of the liquid, C is specific heat capacity of the liquid, ΔT is the change in temperature and t is time. Approximating the liquid to have the same specific capacity as water (4180 J kg^{-1} K^{-1}) and measuring the time taken for the temperature to change by 20 K gives a predicted power of 1.1 kW. Not all of this energy however will go into fragmentation and exfoliation of the material, with

a large percentage being lost to the heat of vaporisation at higher temperatures (water changing to steam near boiling) and the sound of the bubbles.

A further comparison can be made by calculating the intensity (power per area) imparted by each equipment. A sonic probe has a circular area of approximately 1.33 cm^2 (diameter = 12.7 mm) giving an intensity of 50/1.33 = 38 W cm^{-2}. Conversely, the element of the kettle is approximated to be a rectangular area of 30 cm x 1 cm (formed into a U shape in the kettle). This gives a heat flux or intensity of 1100/30 = 36 W cm^{-2}. Although these are very crude estimations, the intensity is approximately the same despite the kettle being a higher power device. The sonic tip however is imparting this power to a volume of liquid approximately 10 times smaller than the kettle, 80 mL for the sonic tip compared to 700 mL in the kettle. The intensity per volume is therefore larger in the sonic tip which may be crucial in the exfoliation and fragmentation processes resulting in smaller, thinner nanosheets. A power consumption socket would give an estimation on the amount of power being drawn from the mains by both pieces of equipment and is planned for the near future.

Multiple authors[202,450] have shown that decreasing the sonication energy by bath sonicating instead of tip sonication leads to a decrease in graphene yield. Moreover, more large monolayers have been produced at relatively low centrifugal acceleration with bath sonication compared to tip sonication, in agreement with the idea that the energy used for exfoliation in a kettle may be lower, producing larger monolayers.[202] The kettle may only exfoliate a certain amount of material, most likely preferentially exfoliating defective material first. The defective material is in the form of large, thin sheets as seen with bath sonication, however the population is low. This may explain the thicker LW versus N relationship given that more boiling is required to further exfoliate nanosheets. Unfortunately, the kettle exfoliation is labour intensive and limited to 45 minutes even with the optimised setup, limiting the rate at which nanosheets are produced. In contrast, sonication times are typically in the range of 5-12 hours. It is possible that longer exfoliation times or more cycles in both kettle setups could lead to thinner and smaller sheets, more in keeping with ultrasonication and shifting the mean layer number downwards. Further investigations using alternative exfoliation methods in combination with a more elaborate Raman analysis are required for a comprehensive understanding. The author of this thesis performed

some of the sample preparation and UV-Vis spectroscopy measurements and all AFM and Raman spectroscopy measurements and analysis.

7.2.5 Applying kettle exfoliated nanomaterial to strain sensors

Exfoliated material from the standard kettle was embedded in a polysilicone matrix producing G-putty, a highly sensitive viscoelastic polymer.[68] Sample production and testing was performed by Daniel O'Driscoll. The final product is pictured in Figure 7.13A. To test the electromechanical properties of the G-putty, the fractional resistance increase was measured and plotted as a function of strain for four test runs (Figure 7.13B). After each test the sample was reformed before testing again. The solid lines are a guideline for the eye to illustrate linearity. This behaviour is in line with that predicted for conductive nanocomposites where the electrical properties can change on application of an applied strain, ϵ, as seen by O'Driscoll et al.[451]

There is however, a variation between runs that is more clearly observed in a plot of the zero-strain conductivity (measured before tensile tests where the sample was under strain) versus test number (Figure 7.13C). The addition of the kettle material makes the composite electrically conductive, however the conductivity is different from test to test. It may be as a result of water loss overtime from handling and reforming causing changes in conductivity. The slope of the fractional resistance increase versus strain linear fit is a parameter known as the Gauge factor, a commonly used sensitivity metric indicating the sensing response of a nanocomposite. The Gauge factor across four tests was measured to be in the range of 200-500 as shown in Figure 7.13D. Once again, there was variation from test to test for possible reasons described above. These values, although not as high as those measured by Boland et al.[68] of up to 1000, exceed those compared to the majority of graphene-polymer strain sensors where G is reported to be less than 100.[452,453]

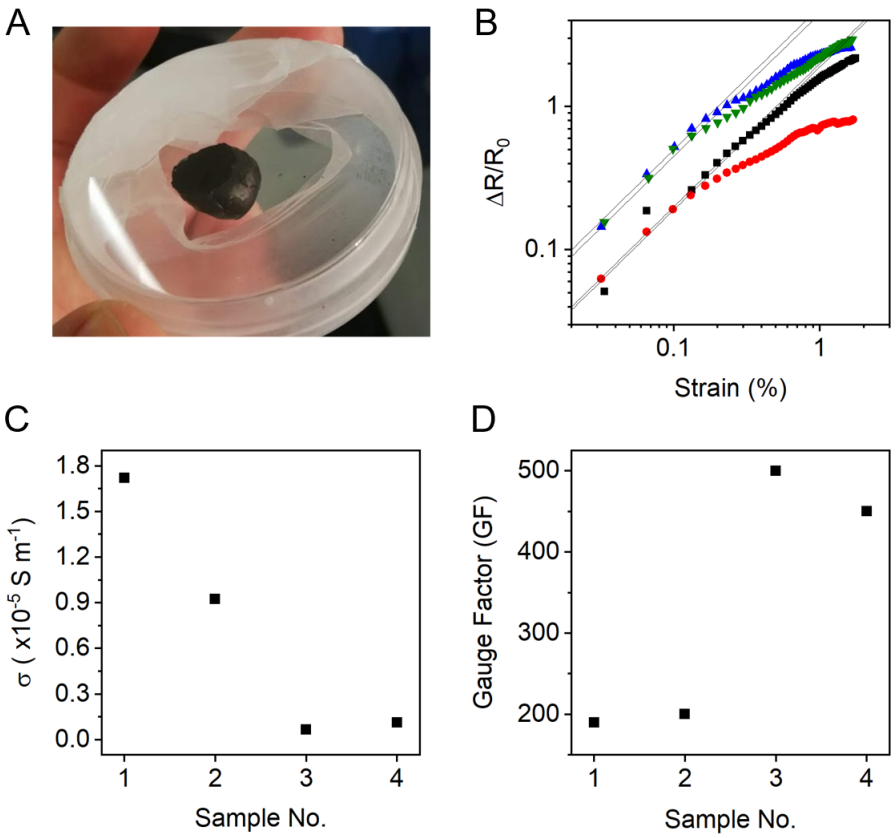

Figure 7.13: Applying kettle exfoliated material to strain sensors. (A) G-putty made by embedding kettle exfoliated graphene in viscoelastic polysilicone, similar to those shown by Boland et al.[68] (B) Fractional resistance increase plotted as a function of strain for 4 different G-putty samples. The solid lines illustrate linearity. (C) Zero-strain conductivity of G-putty plotted versus sample number shows varying performance across samples (D) G-putty strain-sensing sensitivity factor, Gauge Factor (ratio of fractional resistance to strain) versus sample number shows very high values, >100 for every sample.

7.3 Conclusion

This chapter has shown that the collapse of bubbles as a result of boiling rather than the widely used ultrasonication for LPE does in fact exfoliate graphite but perhaps only partially. A standard kettle showed an increase in nanosheet concentration with increased number of cycles and heating time, indicating that further energy input resulting in greater bubble collapse would lead to more exfoliation. An optimised kettle was designed allowing for a near-boiling temperature to be maintained through the use of a cooling coil. The increased heating time of 45 minutes using the optimised set up gave a 10-fold increase in nanosheet concentration in comparison to the standard kettle. EDX and XPS mea-

surements indicated that the kettle exfoliated material revealed characteristic graphene signatures but also those from oxygen suggesting the presence of defects. Similarly Raman spectra highlighted a large D band indicative of defect graphene with higher intensity peak for the optimised kettle in comparison to the standard.

AFM on size-selected samples from both standard and optimised method showed an increase in FLG with the optimised kettle. The energy output from the standard kettle was found to only partially exfoliate the material, producing a graphitic-like L-N relationship with few nanosheets below 10 layers. The higher energy optimised kettle exfoliated with greater efficiency, producing a much higher population of few layer sheets. It was suggested that two regimes exists in exfoliation with the optimised kettle, the first similar to the standard kettle in which partial exfoliation of graphite results in a thicker L-N relationship. In the second regime large, thin nanosheets were exfoliated as a result of neighbouring basal-plane defective sheets being easily peeled from one another with the optimised energy input. The kettle samples were revealed to produce thicker nanosheets when compared to tip-sonicated nanosheets with the same starting material. The starting material however was found to be more defective than the commonly used Sigma Aldrich graphite, a possible explanation as to why any graphene could be exfoliated in a kitchen kettle.

Graphene produced with the standard kettle was used to make G-putty, a viscoelastic sensor demonstrating Gauge factors of up to 500. This value is relatively high in the strain-sensor field, providing a possible application route for kettle-exfoliated material. This proof-of-concept study has shown that boiling successfully exfoliates graphite in a similar manner but to a lesser extent than ultrasonication. There is certainly scope to further optimise the energy output of the kettle which would most likely result in a higher exfoliation efficiency. Experiments that may give further insights to the kettle exfoliation process are outlined in the future work section of Chapter 8.

8

Conclusions and Future Work

***

This work aimed to further characterise commonly used 2D materials, investigate the stabilisation of nanosheets in aqueous surfactant solutions, exfoliate new materials with potential battery electrode applications and propose a new method of exfoliation. Overall, the LPE method was examined in more detail and expanded to new layered materials. The fundamental physics underlying the exfoliation process was also used to create a new production method for graphene.

The spectroscopy of h-BN, previously thought to contain very little information, revealed features that changed systematically with nanosheet size, allowing for nanosheet thickness metrics to be established through UV-Vis and Raman spectroscopy. BN was liquid exfoliated in surfactant and size selected. Using atomic force microscopy the nanosheets in each size fraction were statistically analysed, producing the mean nanosheet length and volume fraction weighted mean layer number for each sample. A well-defined absorbance peak was observed at approximately 6 eV in the UV-Vis spectrometer, with a zero absorbance at energies of less than 3.5 eV consistent with wide bandgap semiconductor. By relating the nanosheet thickness to the position of peak maximum, a thickness-dependent metric was generated suggested to arise from excitonic confinement effects. The exci-

tonic peak for LPE BN was Stokes-shifted upwards by 0.4 eV when compared to previously reported values[315–317] which were attributed to the different sample environments.

Raman spectroscopy measurements showed a single G band mode of h-BN at approximately 1366 cm^{-1}. A SC surfactant peak was found to contribute at this position and subtracted using double Lorentzian fitting to accurately determine the position and width of the h-BN G band. A linear fit of peak width as a function of inverse nanosheet thickness suggested that broadening is due to solvatochromic effects. A model was designed based on the change in peak width with the outer monolayer-liquid interface and related to the nanosheet thickness. The model can be used as a metric for an estimation of nanosheet thickness from the width of the G band. This metric could be altered for other systems where the air-substrate interface is well-defined such as CVD grown BN. Two metrics, from two different spectroscopic techniques provide a quantification of layer number for a commonly used 2D material. While the UV-Vis metric will primarily be used for liquid exfoliated h-BN, the Raman spectroscopy metric, whilst providing insights into the G-band Raman mode, could in fact be useful to many researchers producing 2D h-BN with other methods.

While various surfactants had been used as stabilizers during liquid phase exfoliation, the effect of surfactant choice and concentration on nanosheet yield and dimensions had yet to be explored comprehensively. A broad range of commercially available standard surfactants were chosen to investigate the role of surfactants in liquid phase exfoliation using WS_2 as a model system. Through both UV-Vis and Raman spectroscopy as well as zeta potential measurements, the effect of each surfactant on the concentration, lateral size and thickness of nanosheets was investigated. In general, all ionic surfactants studied behaved in a similar manner: when exfoliated, all nanosheets were found to become laterally smaller and thinner at surfactant concentrations above $\sim$10 mM. The average number of layers fells as low as 2 with lengths as low as 50 nm for very high surfactant concentrations (70 mM). Nanosheet concentration also decreased at the same surfactant concentration threshold of 10 mM.

Therefore, it was suggested that surfactant choice might be less critical a factor in LPE than one might expected. Other factors such as cost and environmental effects could

prove more important when choosing a suitable surfactant for liquid phase exfoliation, an important result for large-scale producers of graphene for example. Ionic conductivity measurements revealed that all surfactants fall on the same curve for nanosheet dimensions, increasing in ionic conductivity with increasing surfactant concentration. A threshold ionic conductivity value of 0.5 mS cm^{-1} was noted to be the point at which electrostatic screening takes effect resulting in destabilization of nanosheets in dispersion - an interesting results indicating that the surfactant concentration has a vital role to play in the stabilisation of LPE nanosheets.

In addition to examining the LPE technique with commonly used materials such as h-BN and WS_2, two novel 2D materials SnP_3 and SiP were liquid exfoliated for the first time. Layered 2D materials have both high surface areas compared to bulk and the potential to store large amounts of lithium in lithium ion batteries. The improvement of LIBs would help the increasingly important development of electric vehicles and energy storage. Two materials were selected from 2D crystal databases,[379–382] on account of their elemental composition containing silicon and phosphorous both with high theoretical capacities. Indeed both of these compounds, SnP_3 and SiP, were predicted to have extremely high specific capacities of 1670 and 3060 mAh g^{-1} respectively. SnP_3 was liquid exfoliated and fully characterised using a range of spectroscopy and microscopy. Examining the UV-Vis extinction spectrum over time, the intensity dropped to approximately 65% of its initial value indicating that the dispersions should be processed relatively quickly to avoid sample degradation. AFM on size selected samples revealed the nanosheets exfoliated and trapped at higher speeds are relatively thin ($<$20 layers) but low speeds produce very thick nanosheets with low aspect ratios for all sizes of 10-30. These low ratios however were suggested to give better performance in battery electrodes, as larger aspect ratios can lead to long diffusion times. SnP_3-CNT composites formed high performance lithium storage anodes, displaying record capacity for a 2D-based anode when normalised to total electrode mass and reaching near-theoretical capacity when normalised to the active mass. With the addition of CNTs, very thick electrodes ($>$300 μm) were fabricated, leading to the highest reported (stable) areal capacity for a 2D-based electrode.

A time dependence study of a standard SiP sample revealed that a drop of intensity of approximately 18% indicating that liquid exfoliated SiP may in fact be more stable in

dispersion than SnP_3. However, EDX showed higher levels of oxidation at approximately 12%. AFM on size selected samples showed thinner nanosheets than SnP_3, with the two smallest fractions producing mean layer numbers of less than 10, albeit isolated at higher relative centrifugal force. Spectral changes with size due to edge and confinement effects were observed through both UV-Vis and Raman spectroscopy. The absorbance band edge was found to downshift with increasing layer number. Similarly, the normalised Raman intensity at 409 cm^{-1} was observed to decrease in intensity with increasing nanosheet size. Cells prepared using FEC-based electrolyte came close to theoretical capacity (3060 mAh g^{-1}) at low current densities. More electrochemical testing is still needed but SiP batteries could be the highest areal and specific capacity 2D lithium-storing electrode ever reported. There is potential for both of these novel 2D materials for use in LIBs, however the laboratory synthesis of both materials is tedious and time consuming. This could be overcome by the use of large-scale ball milling combined with automated pelletising. Wet-jet milling[454] may also help in the upscaling of liquid-exfoliation to produce large quantities of these high-performing 2D materials.

Ultrasonication, the method used to produce these 2D battery materials as well as the h-BN and WS_2 in other chapters works on the basis of bubble collapse. Another way bubbles are formed and collapse is in a kitchen kettle, a technique which was examined and optimised using graphite as a starting material. Two kettle techniques were demonstrated, the first a standard kitchen kettle producing very low yields of graphene after multiple cycles and the second a modification of the kettle in which a cooling coil allows for a rolling boiling to be maintained for long periods of time, increasing the number of bubbles. The increased heating time using the optimised set up gave a 10-fold increase in nanosheet concentration. EDX and XPS measurements revealed characteristic graphene signatures but also oxygen peaks suggesting the presence of defects. Similarly, a large D band was observed in Raman spectra, indicative of defective graphene.

AFM on size-selected samples confirmed the improved exfoliation efficiency of the optimised method through an increase in FLG. It was suggested that the energy output from the standard kettle only partially exfoliates, producing graphitic-like material with few nanosheets below 10 layers. The optimised kettle exfoliated the material for longer times and in turn with greater efficiency. Two regimes were proposed to exist in exfoliation

with the optimised kettle. The first regime was similar to the standard kettle in which only partial exfoliation of graphite occurred. In the second regime large, thin nanosheets were exfoliated by neighbouring basal-plane defective sheets being easily cleaved from one another with the optimised energy input. The kettle samples were revealed to produce thicker nanosheets when compared to tip-sonicated nanosheets with the same starting material.

Graphene produced with the standard kettle was used to make G-putty, a viscoelastic sensor demonstrating Gauge factors of up to 500. The exfoliation in a kitchen kettle is in its infancy and what was presented was a proof-of-concept study. The work demonstrated that boiling successfully exfoliates graphite in a similar manner but to a lesser extent than ultrasonication. There is scope to further optimise the energy output and heating time of the kettle which would lead to greater efficiency. Upscaling this process to industrial levels may be achievable, given the relatively simplicity of the setup.

The results presented in this thesis advance our current understanding of nanosheet dimensions and their interaction with light in a variety of aqueous surfactant solutions. The two novel materials exfoliated suggest there are potentially many more 2D materials yet to be explored with promising battery applications. A new method of nanosheet production confirms that bubble collapse is at the heart of the liquid-exfoliation process whether it be ultrasonication or boiling.

Future Work

Two new materials were synthesised and exfoliated in Chapter 6, inspired by a wave of 2D databases in recent years predicting over a thousand possible two-dimensional layered materials.[379–382] Other unexplored materials containing Si, Ge and P may be exfoliated and integrated into composite electrodes with high capacities. The theoretical capacities of these materials can be calculated prior to any synthesis and exfoliation. An ideal material would be one with a high theoretical capacity that is easily synthesised or commercially available but perhaps more crucially be chemically stable with a high degree of lithium reversibility. Potential materials of interest from the database by Cheon et al.[382] include $In_2(PSe_3)_3$, $Ni(P_3)_2$, $Sb(PO_3)_5$ and Si_2CuP_3 all containing large amounts of phosphorous

or silicon. Of course these databases are not only a useful resource for new battery materials. There is a tremendous amount of potential in these lists to find novel materials that could be liquid-phase exfoliated for a range of other applications including electronic devices and catalysts.

The work in Chapter 7 showed that the partial exfoliation of graphite in a kettle is possible with increased FLG produced when a rolling boil is maintained for a long period of time. The data cloud in Figure 7.9 showed two distinct L-N relationships for the kettle exfoliated material leading to the proposal of two exfoliation regimes, the FLG thought to be produced through easy peeling of neighbouring defective stacks. It would be interesting to test whether the relative population in each regime changes when the same dispersion is subject to two subsequent exfoliation runs. The sample would be prepared in the kettle as standard, centrifuged to remove unexfoliated material and then exfoliated a second time. By doing so, the idea would be that the sample would be enriched in defective material. Defective layers that were perhaps in the middle of a stack in the first exfoliation, having been peeled through the boiling process might now be on the surface at the solid-liquid interface and so may be even more easily cleaved in subsequent exfoliation. Moreover, for every cleaved surface, two new defective surfaces are created where a similar process can occur. A sample would be made with two repeated exfoliation runs and then subject to the same size selection parameters and compared to both the standard and optimised kettle data in the cloud.

When comparing the tip-sonicated Haydale graphite, the graphite used in the kettle exfoliation, to Sigma Aldrich graphite, commonly used in LPE, the Haydale graphite was upshifted to thicker layer numbers for low speed trappings. This suggests that the Haydale graphite may in fact be more defective than Sigma Aldrich, confirmed by the higher Raman I_D/I_G ratio of 0.2 compared to 0.08 for Sigma Aldrich.[67] As a way of supporting the proposal that the kettle exfoliates primarily defective material, a low defect starting graphite e.g. from Henglide Qingdao Graphite Company could be tested. By comparing the yields and dimension of graphene produced by low and high defect starting materials, the exfoliation mechanism described above could be confirmed.

More data points in the plot of mean nanosheet area versus layer number (Figure 7.12)

for the tip-sonicated Haydale graphite i.e. smaller sizes, would also give insights into the exfoliation mechanism of this particular starting material. The yield from ultrasonication is large enough that many more sizes can be trapped at higher centrifugation speeds. It may be the case that smaller sizes are in line with the Sigma Aldrich data, changing the slope of the Haydale tip-sonicated fitted line, related to the characteristic monolayer length, D_{ML}, and in-plane out-of-plane ratio. This result could give a higher D_{ML} than initially thought, indicative of larger, thin sheets produced but most likely more defective. Raman spectroscopy on size-selected, tip-sonicated Haydale graphite would help in the analysis of the defect content and is planned for the near future.

The role of the surfactant in the boiling process could also been examined in more detailed. Previous studies have shown that additives have a vital part to play in bubble formation as a result of nucleated boiling.[455,456] The addition of surfactants to water increases the surface tension of the solution and at low concentrations is found to enhance the nucleate boiling process by increasing the number of active nucleation sites from which bubbles are formed. Sonochemical studies have reported similar behaviour where bubble population is increased but size reduced when surfactants are added.[457] In higher concentration surfactant solutions however more bubbles are observed that may in fact suppress any coalescence, causing considerable foaming.[455] Foaming of course would be potentially problematic in the kettle set up and so high surfactant concentrations may be avoided. A study varying the surfactant concentration at low concentrations on the other hand could tune the amount of bubble collapse while boiling, increasing the yield of exfoliated material.

Appendices

***

A Methods

A.1 Photographs of experimental setups

Figure A.1: Hettich Mikro 220R Centrifuge with fixed angle rotor 1016 used for size-selecting LPE samples.

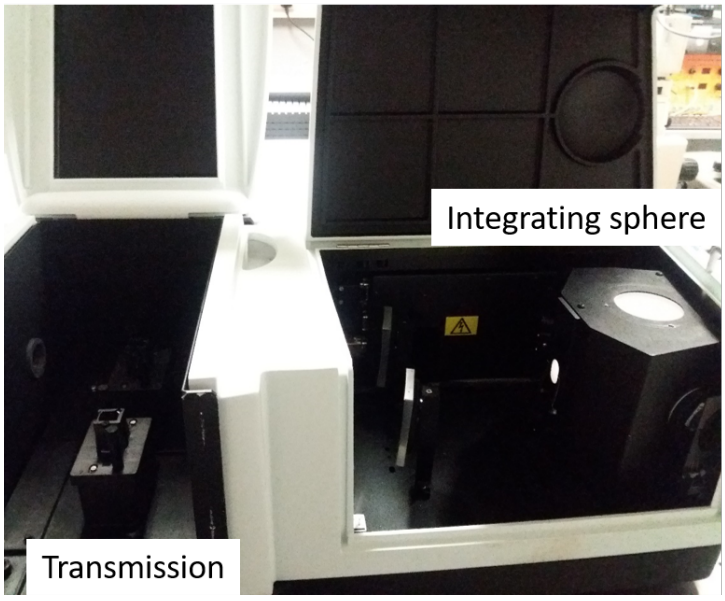

Figure A.2: Perkin Elmer Lambda 1050 UV-Visible Spectrometer with built-in integrating sphere to measure the true absorbance of samples.

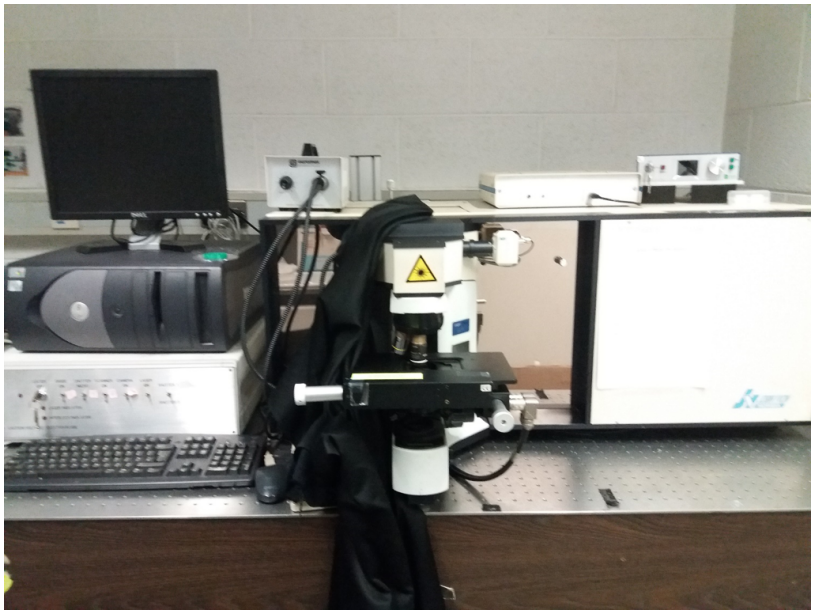

Figure A.3: Horiba Jobin-Yvon LabRAM HR80 Raman Spectrometer with 614 nm and 532 nm lasers used in this work.

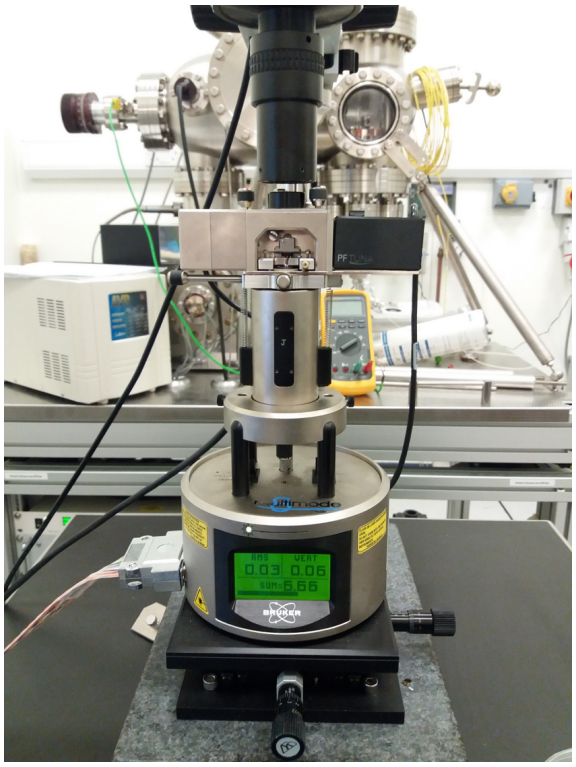

Figure A.4: Bruker Multimode 8 atomic force microscope used in ScanAsyst^{TM}mode with OLTESPA-R3 probes.

Figure A.5: Left: Folded capillary cell and right: Malvern Zetasizer used to measure the zeta potential of LPE samples.

A.2 Sonication time dependence on nanosheet dimension and concentration

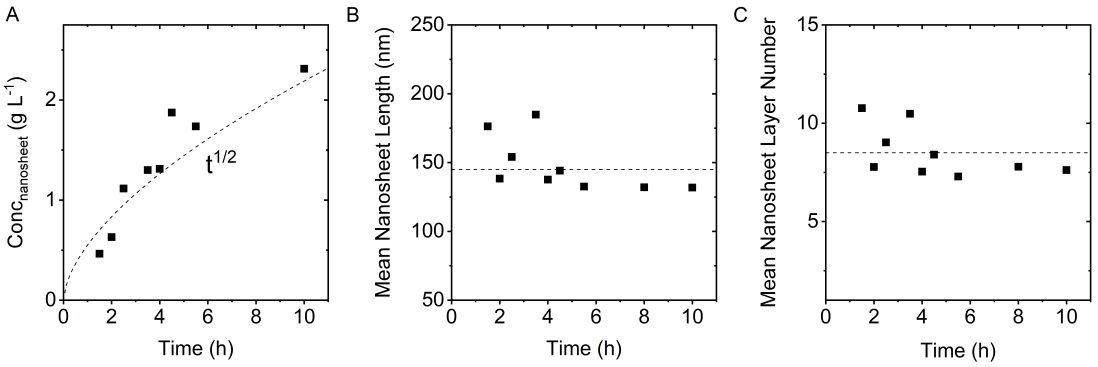

Figure A.6: Sonication time dependence using WS_2 showing (A) Concentration, (B) Mean nanosheet length and (C) mean nanosheet thickness as a function of sonication time. Concentration scales with time$^{1/2}$ as reported previously.[25,191] Nanosheet dimension does not vary considerably with sonication time. All parameters were estimated using established metrics with the same methods as the WS_2 nanosheets in Chapter 5.

A.3 Uncertainties in AFM analysis

Mean arithmetic values are extracted from 100-250 nanosheet counts for each sample with the standard error of the mean used as a measure of uncertainty for each mean <N> and <L>. Size-selected LPE graphene data is shown in Figure A.7 below as a sample data set to analyse uncertainties.

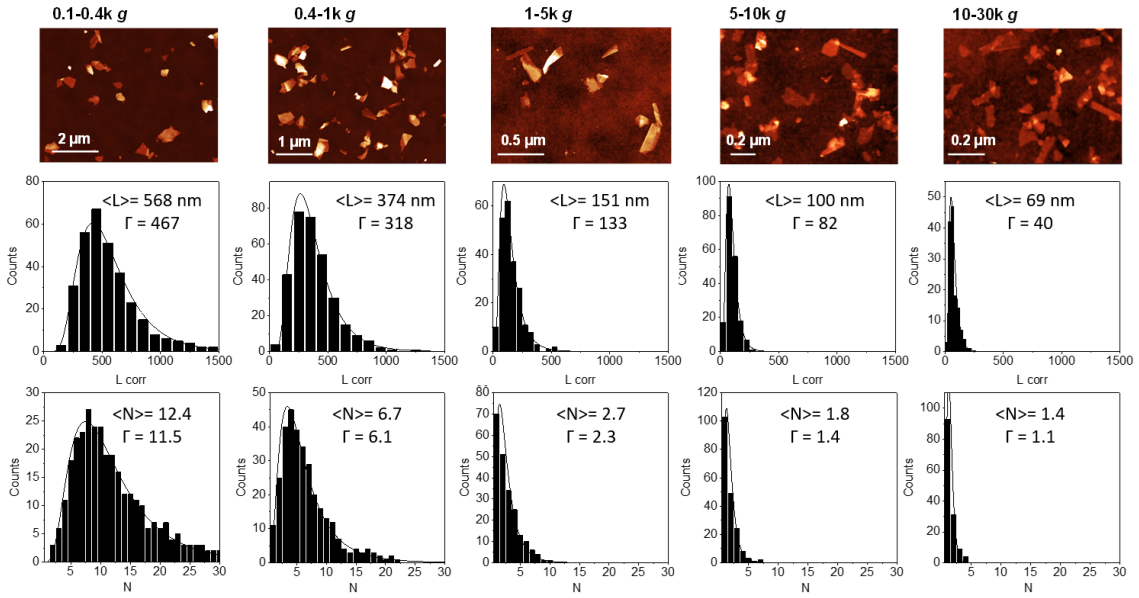

Figure A.7: Representative AFM images (top row), length (middle row) and layer number (bottom row) distribution histograms on five graphene trappings produced from a standard size selection cascade. The width of each log-normal distribution, Γ , is given. From left to right: 0.1-0.4k *g*, 0.4-1k *g*, 1-5k *g*, 5-10k *g* and 10-30k *g*,. Data from Backes et al.[202]

The mean nanosheet length (nm) and layer number is extracted from the log-normal distributions of each sample. From the histograms above, the population distribution width narrows as the centrifugation speed increases and nanosheet dimension decreases. The standard deviation of each data set is related to the distribution width while the standard error of the mean gives the error associated with each mean. The more polydisperse a sample is, the larger the standard deviation and width. For the lower centrifugation speeds, the distribution is wider resulting in a larger standard deviation as shown in Figure A.8 below. As the centrifugation speed is increased and the nanosheet dimension decreases both the width and standard deviation decrease relative to the standard error of the mean due a decrease in sample polydispersity.

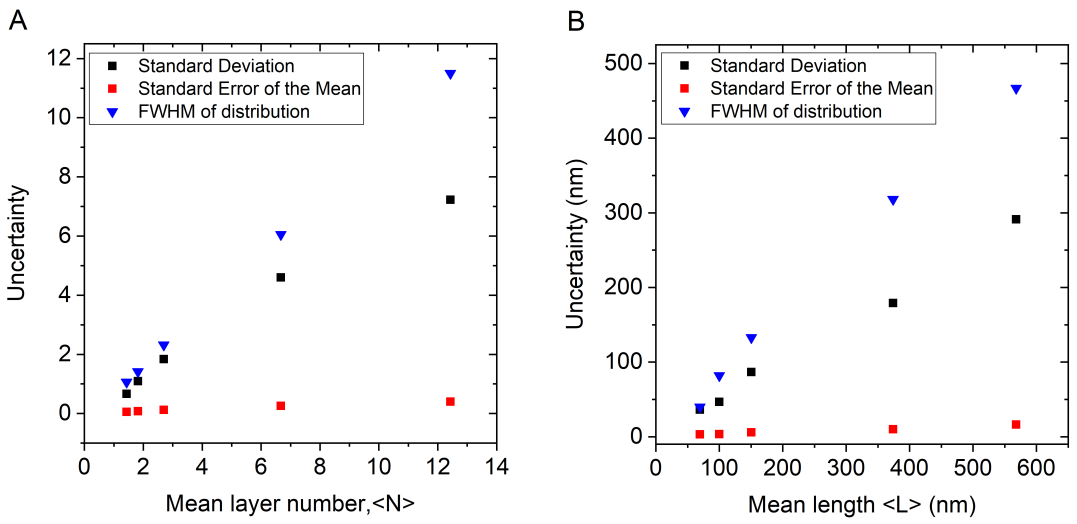

Figure A.8: Standard deviation (black), standard error of the mean (red) and full width at half maximum (blue) versus (A) mean layer number and (B) mean nanosheet length (nm) for size-selected LPE graphene data extracted from Figure A.7 above.

The distribution width gives information on how broad the dimension distribution is but has less of an impact on the nanosheet average size. For example, if a peak shifts with <N>, the distribution width will have an impact on the peak width, whereas the average will change the position. This is seen more clearly in Figure A.8 where the standard error of the mean varies weakly with nanosheet size compared to the standard deviation and FWHM. Research thus far (and in this thesis) is focused on analysing the average properties of each trapping and so the uncertainty in mean nanosheet dimensions are represented by the standard error of the mean. The width of the distribution is represented throughout the thesis however, as an indication of the range of nanosheets present in a trapping.

B Spectroscopic metrics of h-BN

B.1 Additional AFM data

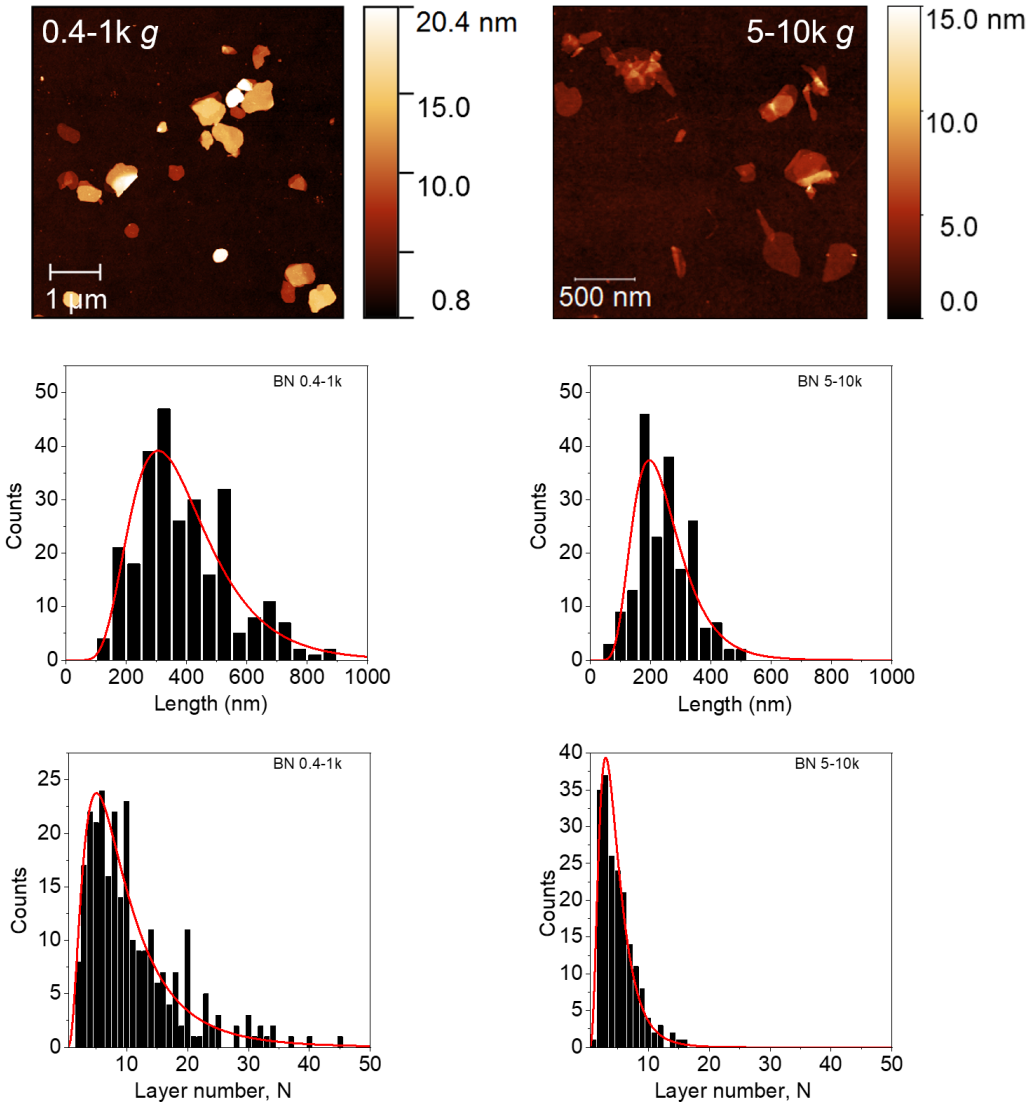

Figure B.1: Representative AFM images (top row), layer number (middle row) and length (bottom row) distribution histograms on two trappings produced from the standard size selection cascade. From left to right: 0.4-1k *g*, 5-10k *g*.

B.2 Weighted <N> comparison

The arithmetic versus volume fraction mean layer number are compared in Figure B.2 below where $<N>_{Vf}$ is shown to be directly proportional to <N> with a ratio of ~ 1.5. The volume fraction mean layer number is an alternative measure of nanosheet thickness which reflects the fact that mass tends to be concentrated in thicker nanosheets. The volume fraction weighted mean nanosheet thickness is analogous to the weight-average-molecular-weight in polymer physics[309] as opposed to arithmetic <N> comparable to the number-average-molecular-weight. Weighting by volume fractions will give a different quantitative relationship when comparing to spectroscopic values than if one used number means, however the trend will remain the same.

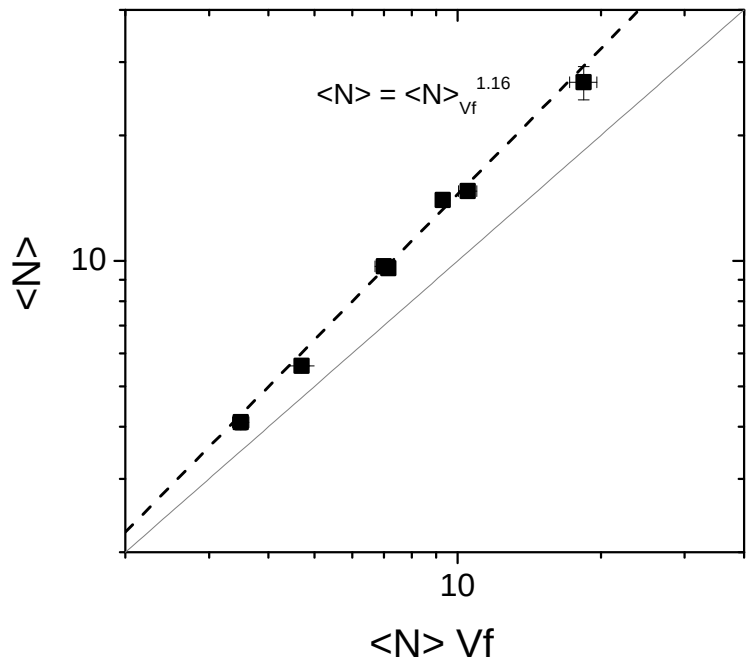

Figure B.2: Relationship between the arithmetic mean layer number, <N> and the volume fraction weighted mean layer number, $<N>_{Vf}$

B.3 Overnight Centrifugation Decoupling

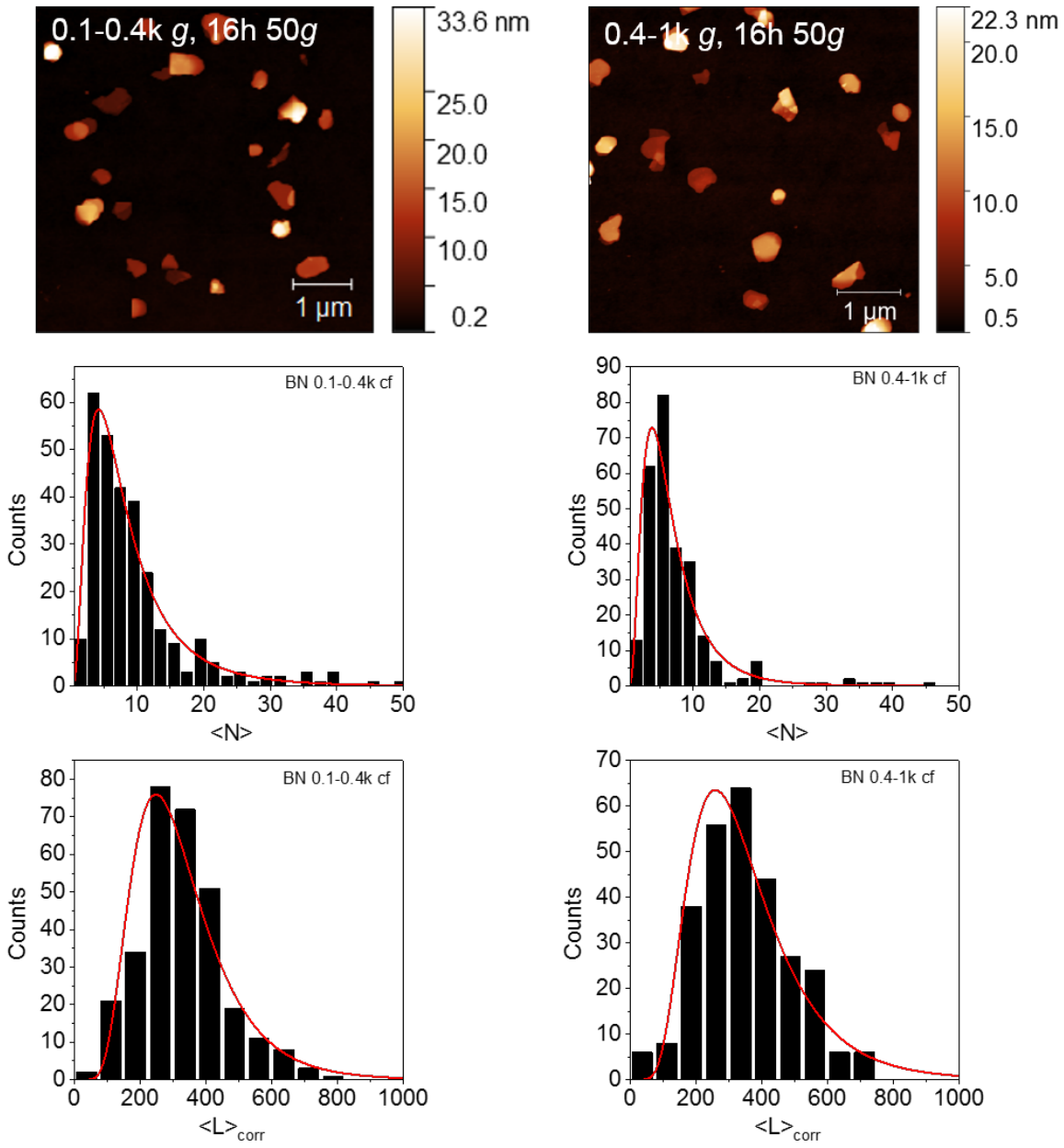

Figure B.3: Representative AFM images, layer number $\langle N \rangle$ and length $\langle L \rangle$ distribution histograms on two fractions after LCC that were subjected to a 16 h centrifugation at 50 g to obtain a different length-thickness relationship. Left: from the initial 0.1-0.4k *g*, right: from the initial 0.4-1k *g* sample. The lateral size distribution is very similar in both trappings, but the nanosheets in the 0.4-1k *g* sample are significantly thinner after the overnight centrifugation.

B.4 Scattering dependence on nanosheet size and thickness

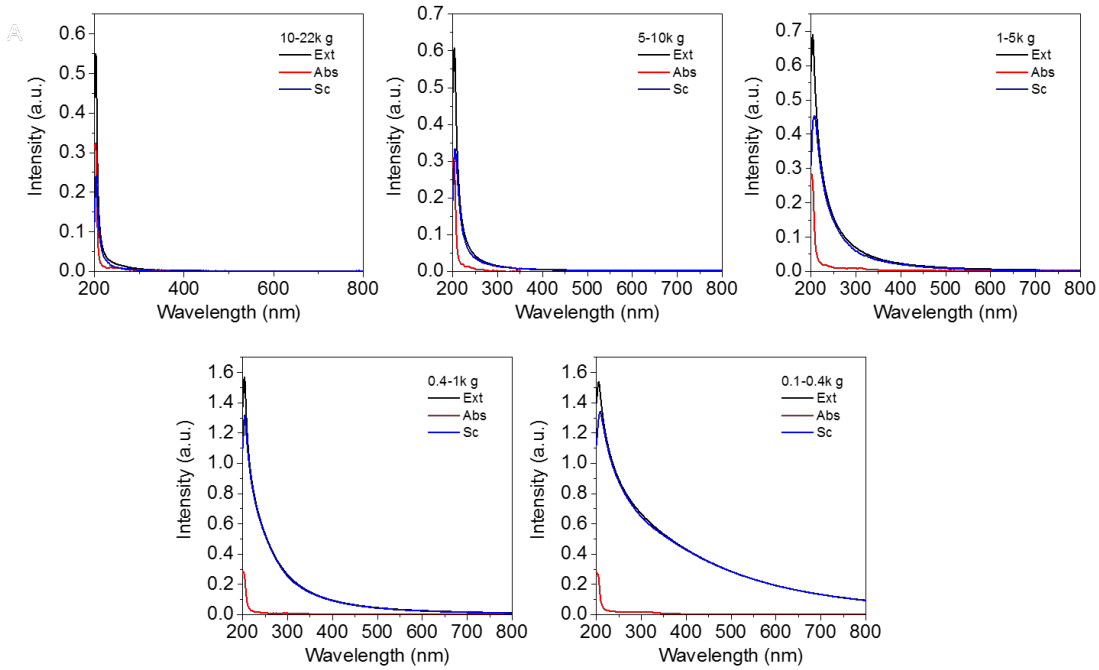

Figure B.4: Absorbance/Extinction/Scattering spectra of the BN standard samples.

B.5 Raman Laser Power

The following Raman laser power experiments were carried out by Dr. Claudia Backes at Heidelberg University.

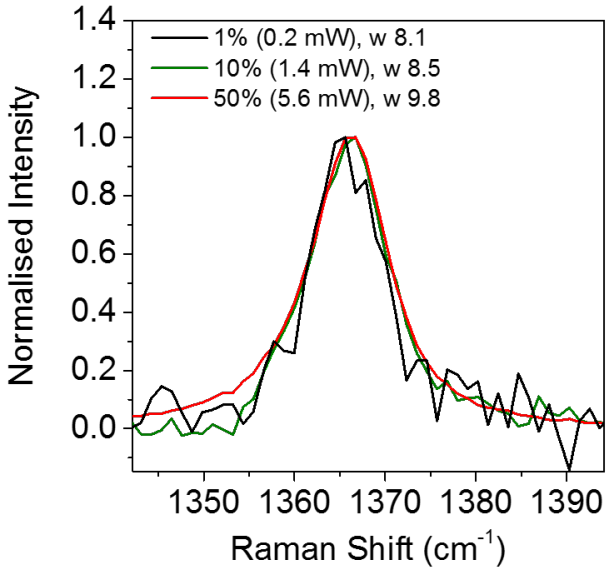

Figure B.5: Raman spectra of bulk h-BN measured at different laser power as indicated in the figure legend. At higher laser power ($>$ 5mW), noticeable broadening is observed due to sample heating. The laser power was thus fixed to 1.4 mW as a compromise between signal intensity and heating induced broadening.

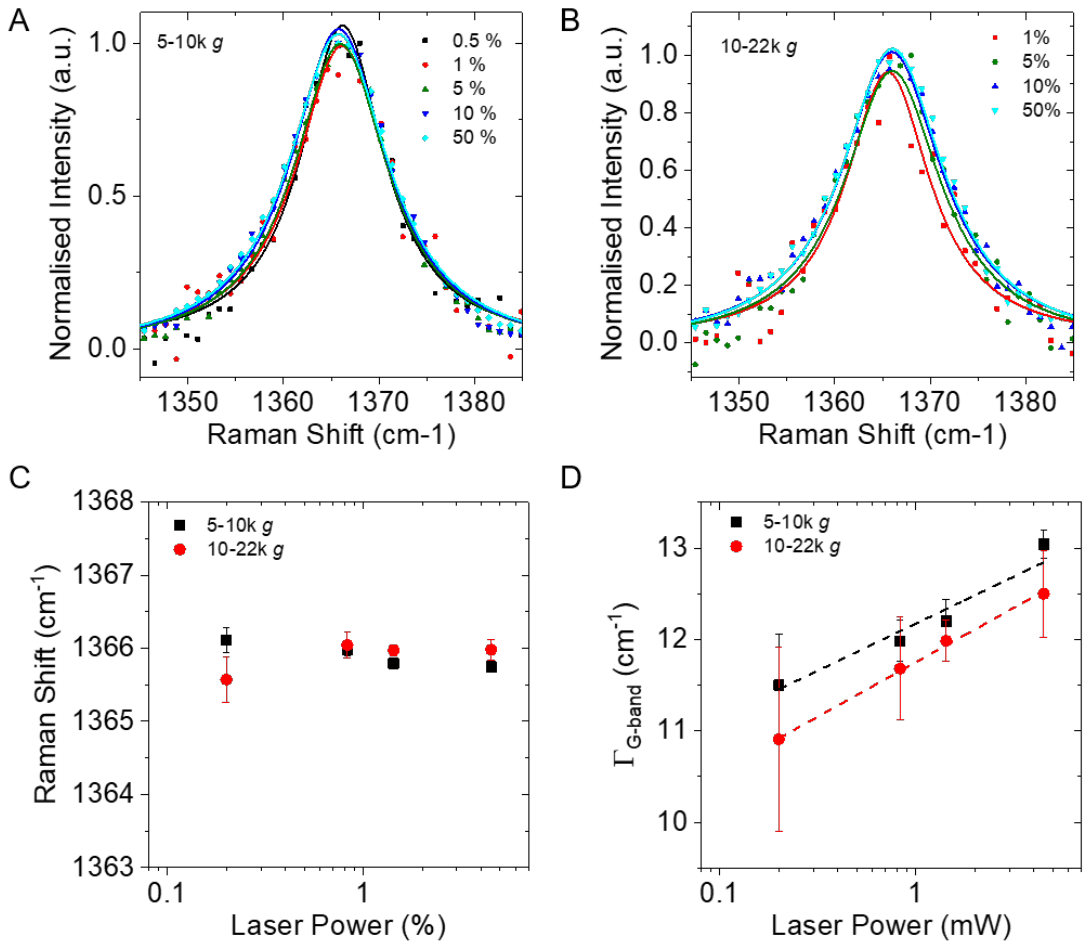

Figure B.6: Impact of laser power.(A-B) Fitted Raman spectra of the thinnest samples 5-10k *g* (A) and 10-22k *g* (B) measured at different laser power. To reduce the error in the fit, the samples were transferred to H_2O by centrifugation prior to deposition to reduce potential contribution from SC to the spectra. (C) Plot of G-band position as function of laser power. (D) Plot of G-band width as function of laser power. A logarithmic increase in width with laser power is found in both cases, as shown in the panel. We found Γ_0 to increase with increasing central-g value (decreasing thickness). However, for both samples, Γ'=1.19. The laser power of 1.4 mW was chosen as compromise between good signal to noise ratio and broadening induced by heating. Note that measurements below a laser power of 0.2 mW gave a very poor signal to noise ratio even for $>$ 100 accumulations and extensive integration times ($>$ 10 s per spectrum).

This power dependent data implies the linewidth to be the sum of an intrinsic and a power dependent contribution. With reference to the fits, this then implies that

$$\Gamma_{\mathrm{G-band}} = \Gamma^{\mathrm{Bulk}}_{\mathrm{G-band},0} + \Gamma' \log P + \frac{2\Delta\Gamma_{\mathrm{M-B}}}{\langle N\rangle_{Vf}+1} \approx 8.5 + 1.19 \log P + \frac{17}{\langle N\rangle_{Vf}+1} \qquad \text{(B.1)}$$

and so the volume weighted mean layer number <N>$_{Vf}$ is

$$\langle N \rangle_{Vf} = \frac{17.2}{\left(\Gamma_{\mathrm{G-band}} - 8.5 - 1.19 \log P\right)} - 1 \tag{B.2}$$

where Γ_{G-band} is in cm^{-1} and P is in mW.

B.6 G-band Comparison with Mean Nanosheet Length

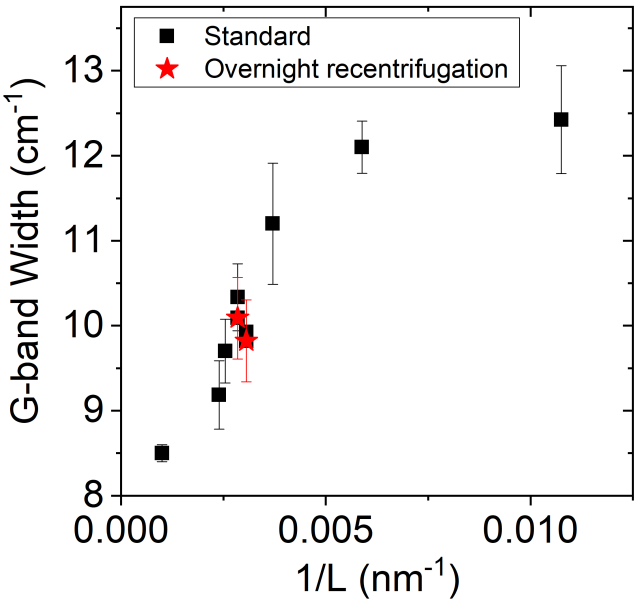

Figure B.7: Plot of the BN G-band width (FWHM) as function of 1/<L>. The data is more scattered compared to the plot of the FWHM as function of 1/<N> shown in Figure 4.8D suggesting that the broadening is an effect related to the nanosheet thickness rather than lateral size.

C Effects of Surfactant Choice and Concentration on Nanosheet Dimension

C.1 Experimental Design

A two step sonication process was performed in this study as a way of removing impurities present in the starting material. The first sonication was done in deionised water and impurities were removed in the discarded supernatant after high speed centrifugation. On first look, it may seem that this extra step is unnecessary and time-consuming. However, a set of reference experiments were completed (by Dr. Claudia Backes) where no purification step was done. MoS_2 was exfoliated via tip sonication for both 1 h and 8 h in sodium cholate aqueous surfactant solution (1.5 g L^{-1}) without any pretreatments. The samples were immediately filtered without centrifugation such that the nanomaterial remained on the filter membrane. The filtered liquid was then analysed. As a further comparison, MoS_2 was also bath-sonicated in pure water.

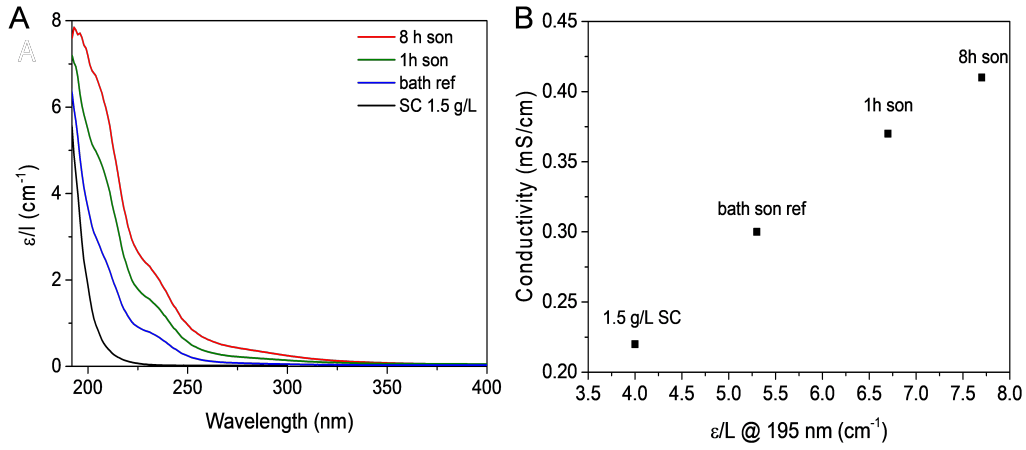

Figure C.1: Reference experiment to illustrate the importance of the pre-cleaning sonication step. (A) Extinction spectra of the filtered liquid from MoS_2 tip-sonicated in aqueous SC (1.5 g L^{-1}) compared to bath sonication in pure water and the aqueous SC solution. (B) Plot of ionic conductivity of these samples as function of extinction at 195 nm.

In Figure C.1 above, there is some absorbance detected in the UV-Vis region. As mentioned in Chapter 5, oxidation can occur in the UV region of the absorbance spectra, skewing the <L> metric. Therefore peak intensity ratios across the visible region were chosen in efforts to mitigate this factor (Details C.2). The absorbance of the filtered liquids has a dif-

ferent spectroscopic fingerprint than pure SC which can be attributed to soluble impurities that are released on sonication. These features are similar in the bath and tip sonicated samples. Longer sonication times lead to more pronounced features in the spectra. This suggests that an initial sonication in water can remove a large amount of impurities, although tip sonication in surfactant might be even more efficient. Unfortunately, this would add an additional uncertainty to the final surfactant concentration so a compromise was made and pre-sonication was completed in water.

The need for removal of impurities is demonstrated in Figure C.1B. A plot of the ionic conductivity (measured in situ with Zeta potential) versus the extinction at 195 nm gives well-defined scaling. High conductivity values for tip sonication show that impurities are indeed predominantly ionic in nature. In Chapter 5, it was noted that the observed drop in nanosheet concentration, <L> and <N> is due to electrostatic screening resulting in destabilization. It is therefore important to rule out effects on ionic conductivities due to impurities. This can be done to a large extent by performing the two-step sonication.

As well as the two-step sonication, a two-step centrifugation was also completed. Each sample was centrifuged at low speed to remove large, unexfoliated material and then to centrifuge at high speed to remove very small nanomaterial, potentially remaining impurities and most importantly, to increase the nanosheet concentration in all samples to facilitate the PL/Raman measurements. After the high speed step, the sediment was redispersed in the nominal surfactant concentration i.e. the same surfactant concentration in which it was exfoliated. To investigate whether there was a considerable change in samples pre and post high speed trapping, two samples were prepared in which the supernatant after low speed centrifugation was analyzed. By doing this, no additional surfactant was added after exfoliation but very small residues and nanoparticles remained in dispersions. The samples were characterized with the same methods and trapped (0.1-21 k *g*) and non-trapped (0.1 k *g* supernatant) samples and compared in Figure 5.4, Chapter 5.

C.2 Metric Comparison: UV and Visible Range

The <N> metric shown in Chapter 5 is only strictly accurate for <N> <10 layers above which point the material becomes bulk like. However, nanosheets produced via LPE have intrinsically linked length and thickness i.e. as nanosheets become laterally larger they

are also thicker. Larger, thicker nanosheets will have a greater scattering contribution to the thickness. The scattering is red-shifted to the absorbance in the resonant regime and so the A-exciton peak shift above 10 layers is in fact due to the overall increase in dimension. This can be seen for nanosheets with lengths >150 nm and layer number >10. The increased scattering contribution for <L> >150 nm changes the scaling of the peak intensity ratio in the visible range, reducing the reliability of the metric. The <L> metric using spectral positions in the UV region is still expected to hold and since larger nanosheets were found in lower surfactant concentrations (Section 5.2.4 Chapter 5)), the UV region is not expected to skewed by surfactant absorbance.

As a test of the size/thickness determination accuracy, <L> was determined from two different metrics in Figure C.2B. The metric with the ratio of the A exciton to the extinction at the local minimum of 290 nm is used for L > 150 nm because it allows for greater sensitivity for larger nanosheets, while Ext_{465}/Ext_{365} was used for L < 150 nm. L versus N in Figure C.2A bends at larger N values due to the fact that this visible range metrics are less accurate for larger nanosheets. L vs N in Figure C.2B follows a linear fit on log-log of L-N as reported previously.[19,133,202] This is probably a more realistic picture of the size-thickness relation. Having said that, the average nanosheet length versus surfactant concentration (Figure C.3) becomes more scattered. Importantly, the overall trend is not influenced by varying between metrics. Metric for all L values in Figure C.2A (and Chapter 5) and for L <150 nm in C.2B for WS_2:[361]

$$< \mathrm{L} >= \frac{3.698238Ext_{465nm} - Ext_{365nm}}{0.01164Ext_{365nm} + 0.00111Ext_{465nm}} \tag{C.3}$$

Metric for L >150 nm in Figure C.2B for WS_2:[20]

$$< \mathrm{L} >= \frac{1000\frac{Ext_{A-exciton}}{Ext_{290nm}} - 7.6}{2.8} \tag{C.4}$$

Metric for L in Figure C.2A and B for MoS_2:[363]

$$< \mathrm{L} >= \frac{0.48182Ext_{400nm} - Ext_{443nm}}{0.01774Ext_{443nm} - 0.02125Ext_{400nm}} \tag{C.5}$$

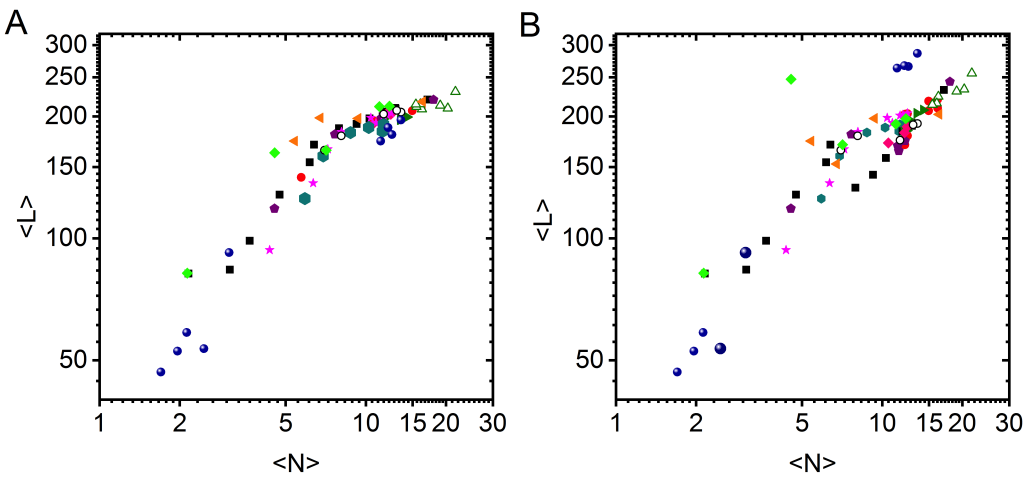

Figure C.2: (A) Mean nanosheet length versus mean nanosheet layer number using Equation C.3 as in Chapter 5 and Biccai et al.[361] (B) Nanosheet length versus mean nanosheet layer number using Equation C.3 from Biccai et al.[361] for L <150 nm and Equation C.4 for L >150 nm from Backes et al.[20] In both (A) and (B) the metric for MoS_2 used is from Djamil et al.[363] as in Equation C.5 and Chapter 5.

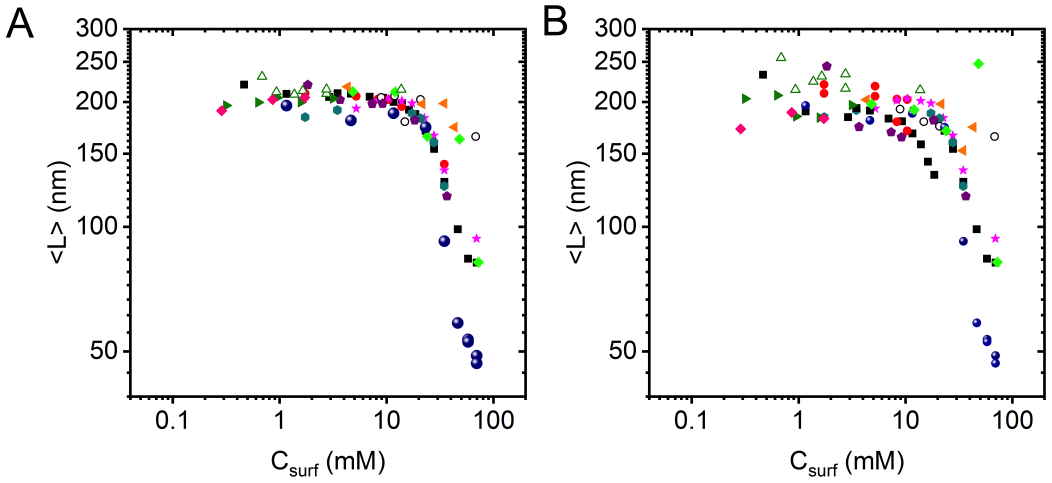

Figure C.3: (A) Mean nanosheet length as a function of surfactant concentration using Equation C.3 as in Chapter 5 and Biccai et al.[361] (B) Nanosheet length as a function of surfactant concentration using Equation C.3 from Biccai et al.[361] for L <150 nm and Equation C.4 for L >150 nm from Backes et al.[20] In both (A) and (B) the metric for MoS_2 used is from Djamil et al.[363] as in Equation C.5 and Chapter 5.

C.3 Error Analysis

In order to test the reproducibility of the experiments, the 2 g L^{-1} SC sample was made 3 times and a mean value was calculated from UV Vis spectrometry. The standard error of

the mean (SE) was also estimated and tabulated below. This demonstrates that the reproducibility errors are generally low (3% for <N>, 1% for <L> and 9% for concentration).

Sample	UV-Vis <L> (nm)	UV-Vis <N>	$Conc_{NS}$ (g L^{-1})
1	209	12.6	2.57
2	212	13.3	2.04
3	207	12	1.87
Mean ± SE	209.7 ± 1.3	12.6 ± 0.4	2.16 ± 0.21

Figure C.4: Table of values of a 2 g L^{-1} SC sample produced 3 times and measured via UV-Vis spectroscopy and mean and SE calculated

To further assess the error in determining nanosheet dimensions and concentrations from the UV-Vis based metrics, the published correlation (see Figure C.5) was re-analyzed to estimate the overall standard error of the regression used to establish the metrics. This can be considered as a combined error from AFM uncertainty to determine the standard error of the mean size, uncertainty in determining the metric values from UV-Vis (extinction ratio and peak position, respectively), as well as batch to batch variations. For each data point, the distance of the data point to the fit curve was measured and divided by the respective <L> and <N> values of the fit line. The overall error of the regression was then determined as the average of these values. This gives an overall error of 6% for <L> and 13% for <N>. In the case of concentration, another 5% error was added to the 6% error used from determining <L> to account for pipetting errors and uncertainties in measuring the sample volume. The error in number of nanosheets per volume is the combined error of <L>, <N> and concentration which was determined as follows with all errors as percentages.

The uncertainty in the volume of 1 nanosheet was estimated as:

$$\Delta V_{1NS} = \sqrt{(2\Delta L)^2 + (\Delta N)^2} \tag{C.6}$$

The mass of nanosheets was estimated from the error in concentration and volume of liquid (as 5% pipette error) as:

$$\Delta Mass = \sqrt{(\Delta Conc_{NS})^2 + (\Delta Vol_{Liquid})^2} \tag{C.7}$$

The total volume of nanosheets was estimated using the ΔMass, the density (WS_2 : 7.5g cm^{-3}) , and the volume of 1 nanosheet:

$$\Delta V_{TotalNS} = \sqrt{(\Delta Mass)^2 + (\Delta V_{1NS})^2} \tag{C.8}$$

Finally the nanosheets/vol was estimated through the total number of nanosheets as a ratio of liquid volume. Again we include a 5% pipette error to factor in the volume uncertainty:

$$\Delta(Nanosheets/Vol) = \sqrt{(\Delta V_{TotalNS})^2 + (\Delta V_{Liquid})^2} \tag{C.9}$$

Giving a total error for the nanosheets per volume to be 22% as seen in the error bars of Figures 5.5, 5.7 and 5.8 in Chapter 5.

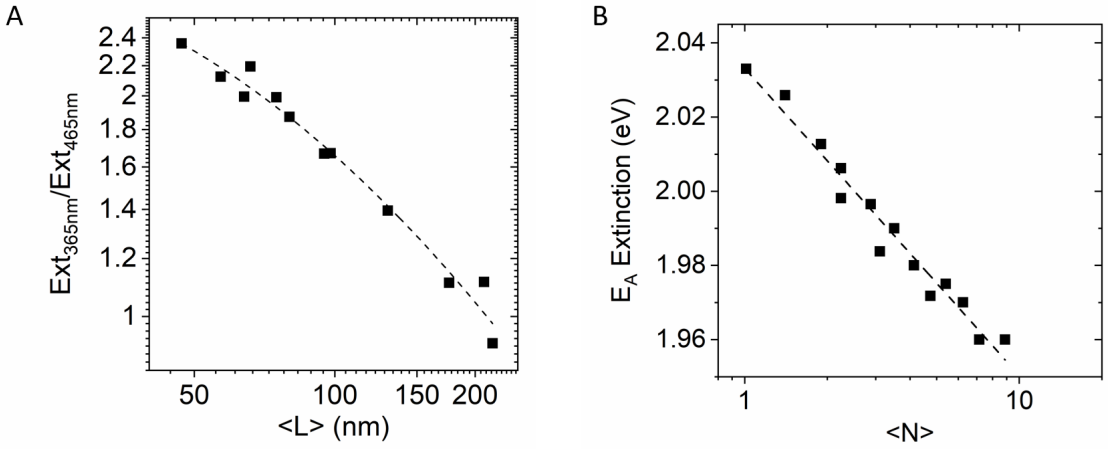

Figure C.5: (A) Data and metric (dashed line) from Biccai et al.[361] used to establish the L metric error of 6% above (B) Data and metric (dashed line) from Synnatschke et al.[133] used to establish the N metric error of 13% above.

C.4 Robustness of Metrics

Given the number of samples in this study (>80), it was not feasible to do statistical microscopy with each sample requiring at least 100 nanosheet counts. Metrics allowed us to quickly and efficiently estimate L, N and concentration for each sample. After initial reports on spectroscopic metrics for LPE TMDs,[19,20] subsequent work has further verified their robustness.[202,289,370,423] To even further validate the metrics however, statistical microscopy was completed on 0.1, 2 and 40 g L^{-1} SC samples as well as the 0.1 and 40 g L^{-1} SC used in the re-stabilization test as represented in the Figures C.6, C.7 and C.8 below.

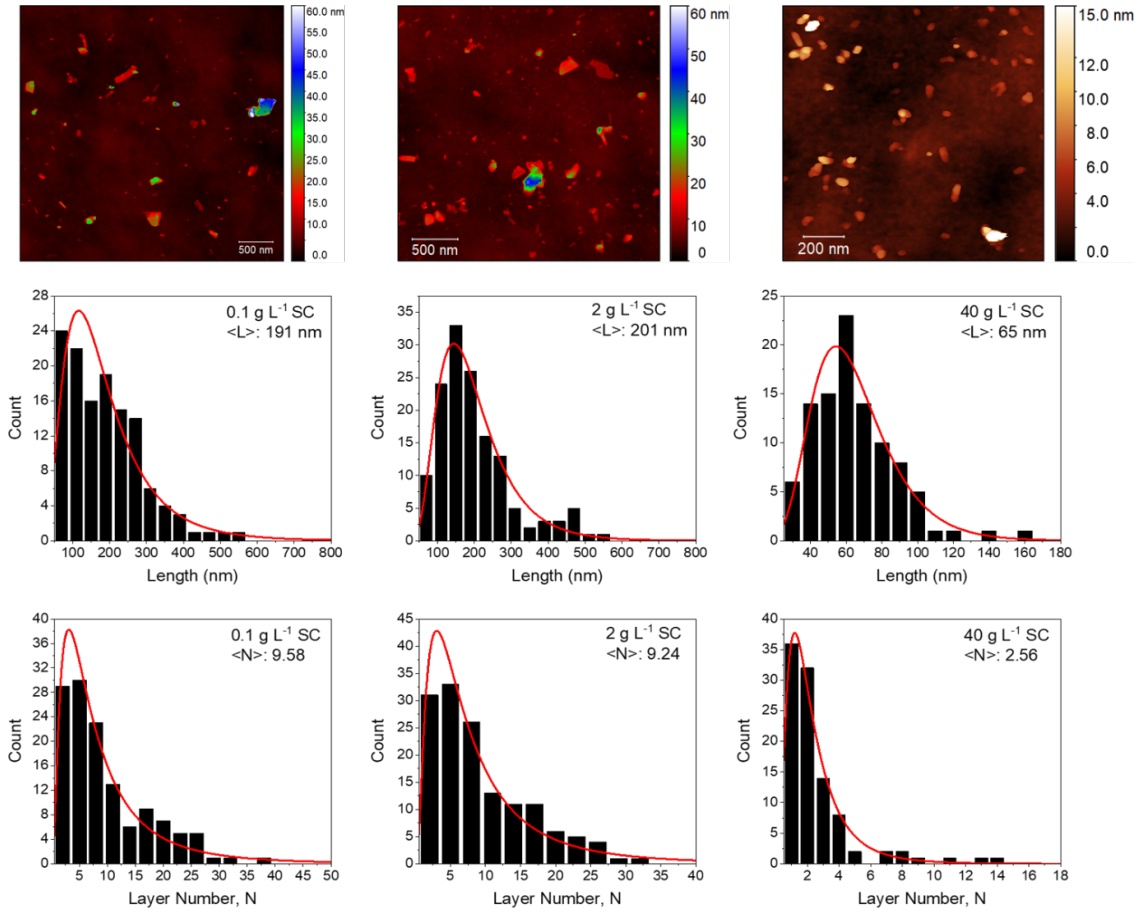

Figure C.6: Top Row: Representative AFM sample images for 0.1, 2 and 40 g L^{-1} SC samples respectively (from left to right). Middle Row: Length histograms for 0.1, 2 and 40 g L^{-1} SC samples respectively (from left to right). Bottom Row: Layer number histograms for 0.1, 2 and 40 g L^{-1} SC samples (from left to right) showing characteristic log-normal distribution for LPE materials.

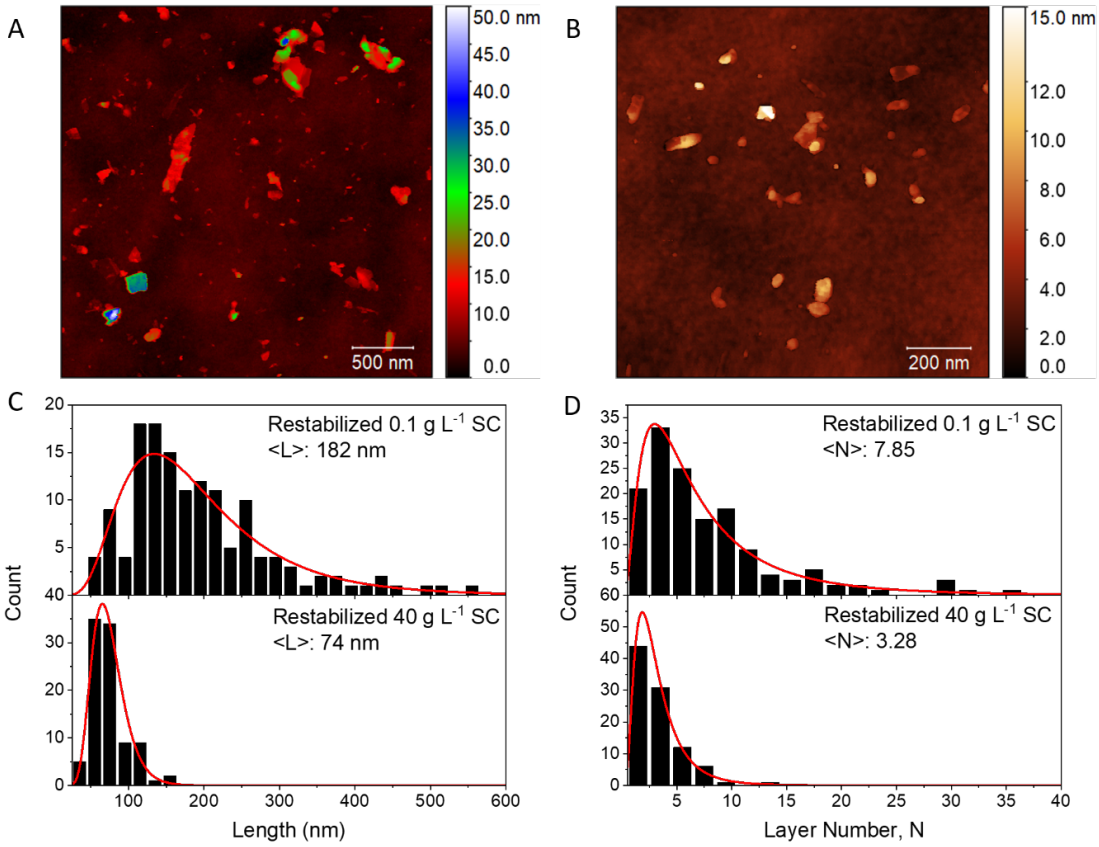

Figure C.7: (A) Representative AFM sample image for 0.1 g L^{-1} re-stabilized sample. (B) Representative AFM sample image for 40 g L^{-1} re-stabilized sample (C,D) Comparison of the population distribution between low and high concentration restabilized dispersions for (C) Nanosheet Length, L and (D) Layer number, N.

Sample	AFM <L> (nm)	UV-Vis <L> (nm)	AFM <N>	UV-Vis <N>
2 g L^{-1} SC	201 ± 9	210	9.3 ± 0.6	12.6
0.1 g L^{-1} SC	191 ± 11	199	9.6 ± 0.7	11.6
40 g L^{-1} SC	65 ± 3	75	2.6 ± 0.3	2.0
Restabilized 0.1 g L^{-1} SC	196 ± 9	182	7.9 ± 0.6	8.7
Restabilized 40 g L^{-1} SC	74 ± 3	78	3.3 ± 0.2	3.2

Figure C.8: A comparison of <L> and <N> values from both UV-Vis spectroscopy and AFM.

C.5 Surfactant type, starting concentration and material comparisons

Sodium Deoxycholate versus Sodium Cholate

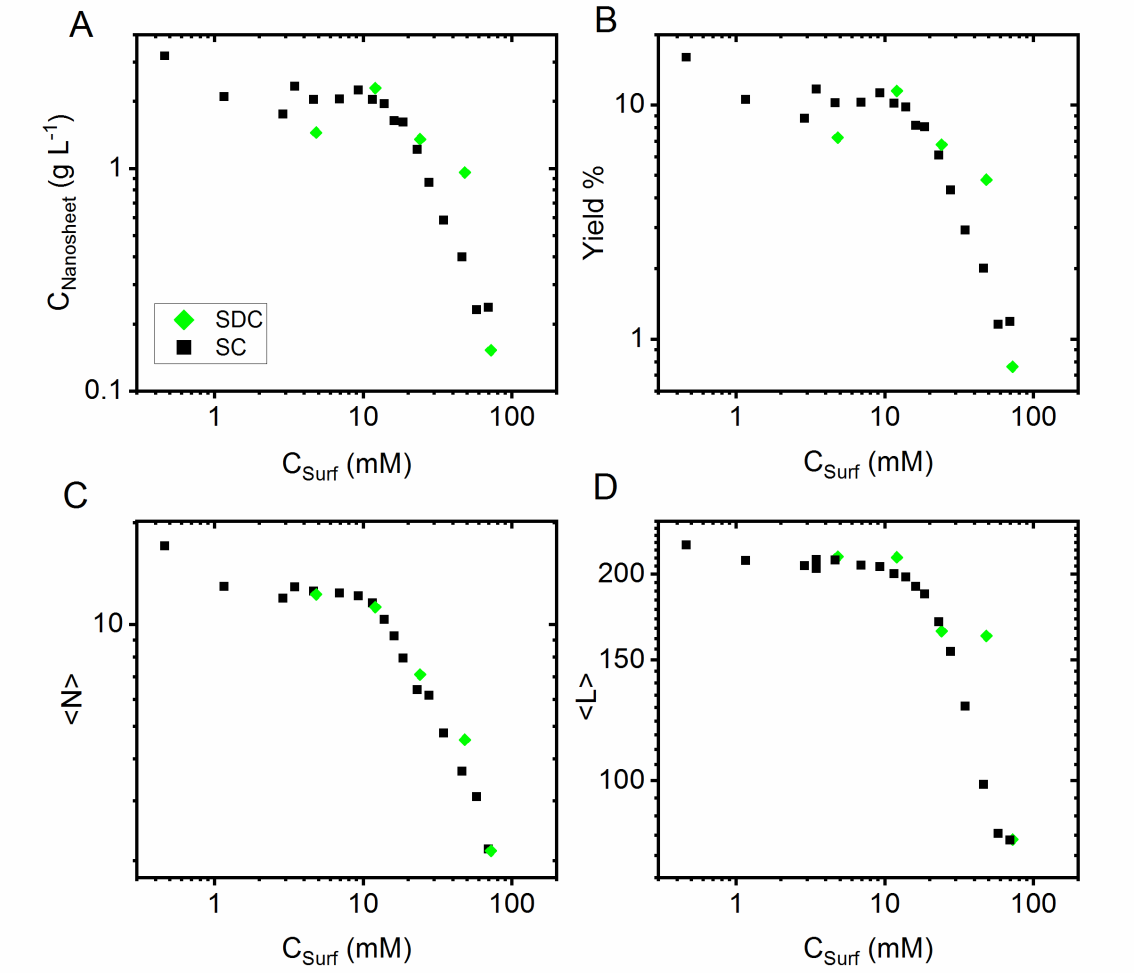

Figure C.9: Concentration, yield% and nanosheet dimensions for both sodium cholate (black) and sodium deoxycholate (green) surfactants (A) Nanosheet concentration as a function of surfactant concentration with nanosheet concentration (B) Yield% plotted versus surfactant concentration (C) Mean layer number <N> as a function of surfactant concentration (D) Mean nanosheet length <L> as a function of surfactant concentration.

Starting WS_2 concentration comparison

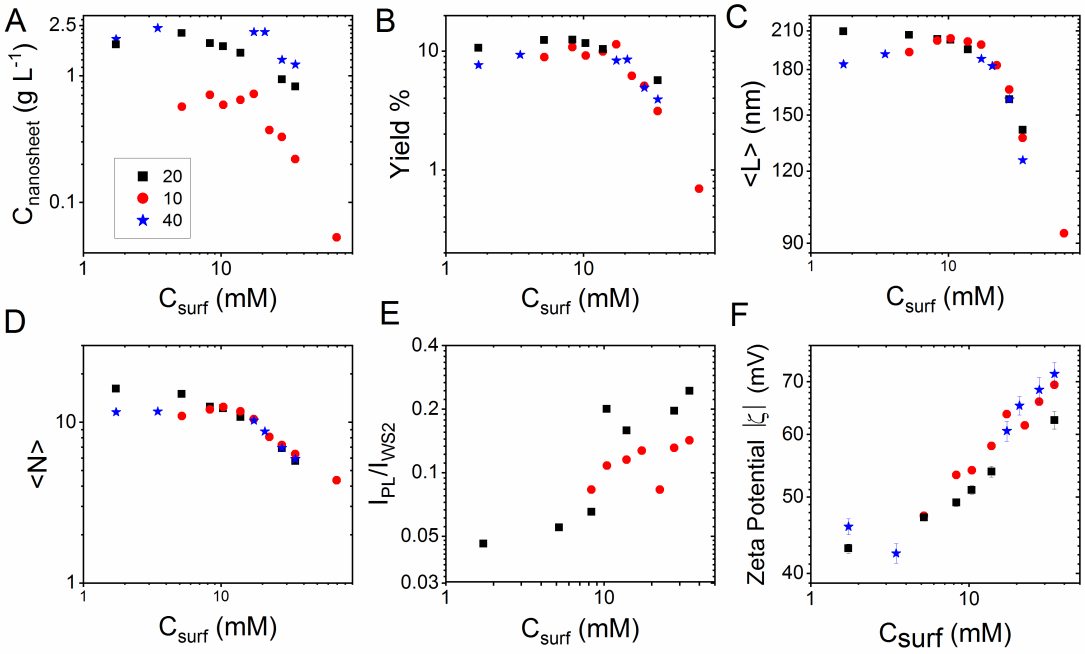

Figure C.10: Concentration, yield%, nanosheet dimensions, absolute zeta potential and Raman/PL ratio for three different starting concentrations of WS_2 (10, 20 and 40 g L^{-1}) versus surfactant concentration.Other than an increase (decrease) in nanosheet concentration for an increased (decreased) amount of starting material, starting concentration does not affect the outcome (A)Nanosheet concentration as a function of surfactant concentration with nanosheet concentration expressed in molarity for better comparison across materials (B) Yield% plotted versus surfactant concentration (C) Mean nanosheet length <L> as a function of surfactant concentration (D) Average layer number <N> as a function of surfactant concentration (E) Intensity PL/Intensity WS_2 Raman mode as a function of surfactant concentration (F) Absolute zeta potential plotted versus surfactant concentration.

Material dependence, a comparison of WS_2, MoS_2 and Graphene

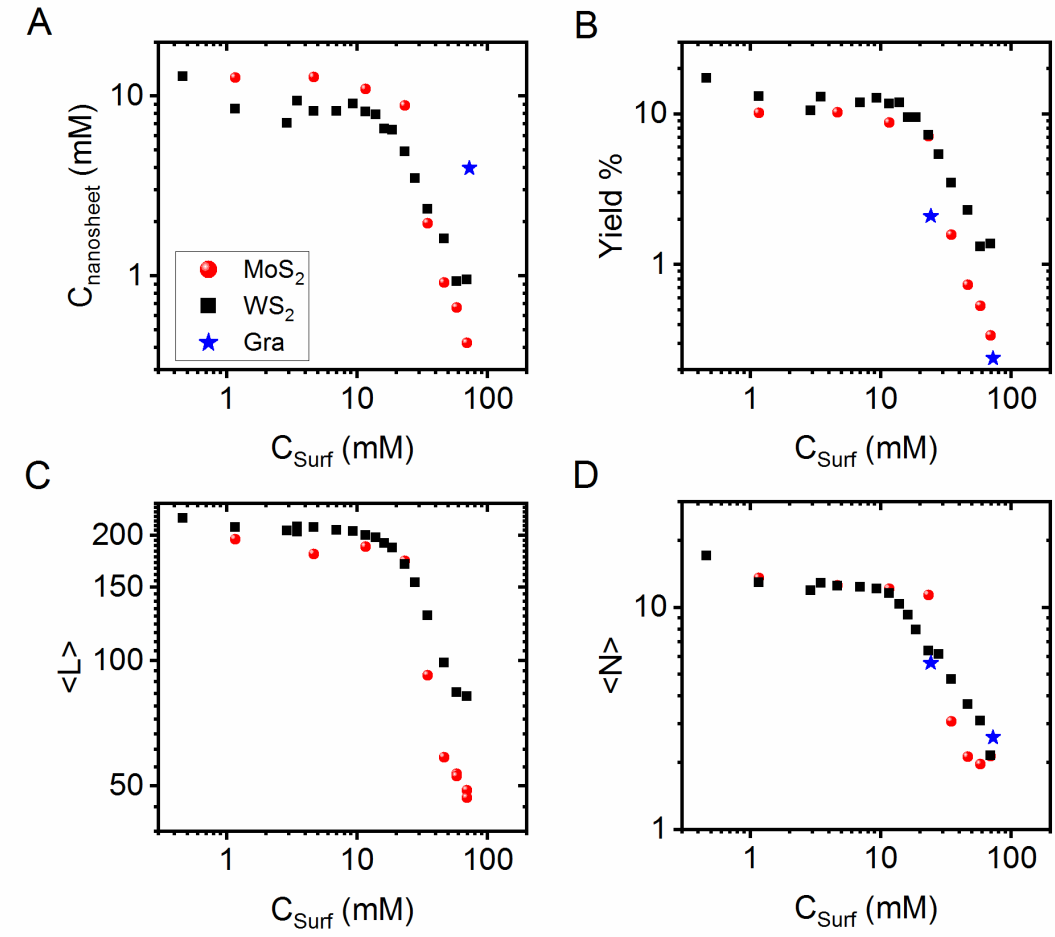

Figure C.11: Concentration, yield% and nanosheet dimensions for three different nanomaterials: WS_2, MoS_2 and graphene in SC (A) Nanosheet concentration as a function of surfactant concentration with nanosheet concentration expressed in molarity for better comparison across materials (B) Yield% plotted versus surfactant concentration (C) Mean nanosheet length <L> as a function of surfactant concentration (D) Mean layer number <N> as a function of surfactant concentration.

Changing the surfactant head group: LDS vs. SDS

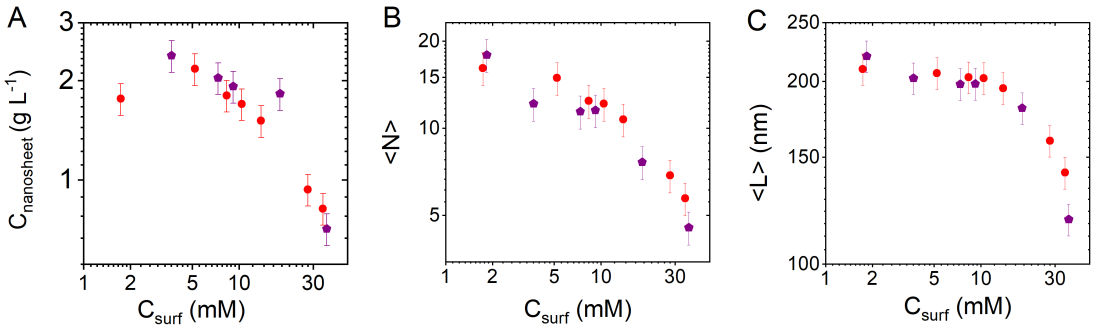

Figure C.12: Concentration and nanosheet dimensions for both lithium dodecyl sulfate (LDS) and sodium dodecyl sulfate (SDS) surfactant (A) Nanosheet concentration as a function of surfactant concentration (B) Mean layer number <N> as a function of surfactant concentration (C) Mean nanosheet length <L> as a function of surfactant concentration.

C.6 Non-ionic Surfactants

Concentration, thickness and length remain relatively constant for non-ionic surfactants compared to their ionic counterparts (Figure C.13). Non-ionic surfactants such as those used in this work stabilize nanosheets by creating a bulky, physical barrier between the nanosheets preventing any reaggregation. It appears that this steric hindrance alone from bulky molecules such as Tween20/80® and Brij® leads to thicker and bigger nanosheets than ionic surfactants. It may be possible that electrostatic interactions between ionic surfactants and their dissociated ions with the material enable further exfoliation towards smaller and thinner nanosheets. It is likely that Tween® and Brij® have weaker attractive interactions between their tail groups and the nanosheet surface compared to ionics. Similarly for the head group, ionics have a charged head group that creates strong repulsive interactions with water ions while the head group of non-ionics has no charge and thus only create short-range repulsive interactions in the environment.

In terms of stability there is a decreasing zeta potential for increasing non-ionic surfactant concentration. The effective surface charge present at low surfactant concentration may be due to adsorption of charged impurities as predicted for graphene stabilized in non-ionic surfactant.[246] An increase in surfactant concentration could decrease the effective concentration of impurities and lower the zeta potential as seen in Figure C.13. WS_2 nanosheets coated with non-ionic surfactants may be partially stabilized by smaller electrostatic interactions which is why there is a small rather than negligible zeta potential, even at high surfactant concentration.

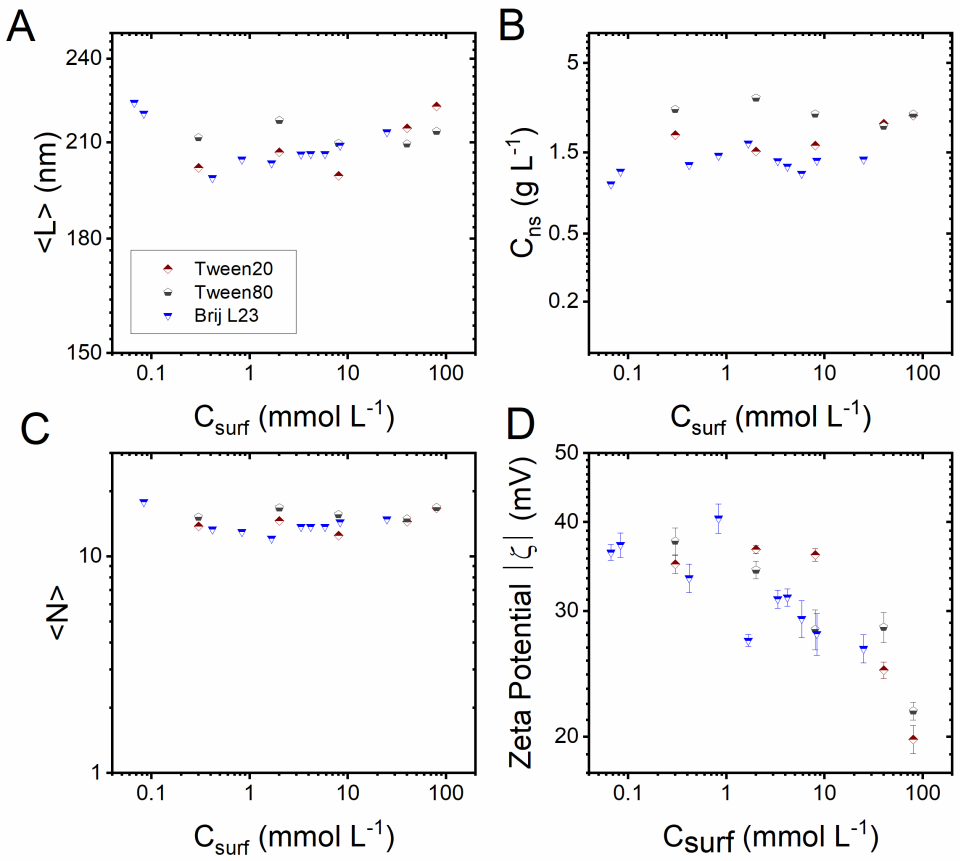

Figure C.13: Non-ionic surfactant nanosheet dimensions, concentration and zeta potential (A) Average nanosheet length <L> as a function of surfactant concentration obtained via metrics discussed in C.2 (B) Nanosheet concentration as a function of surfactant concentration (C) Average layer number <N> as a function of surfactant concentration obtained via metrics discussed in C.2 (D) Absolute zeta potential plotted versus surfactant concentration.

C.7 Comparison of Surfactant Type

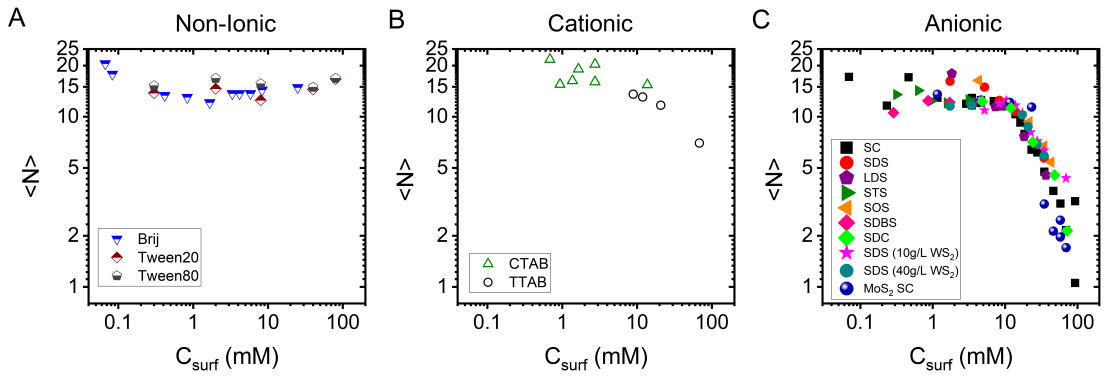

Figure C.14: Mean number of layers plotted versus surfactant concentration for (A) Nonionic (B) Cationic and (C) Anionic surfactants.

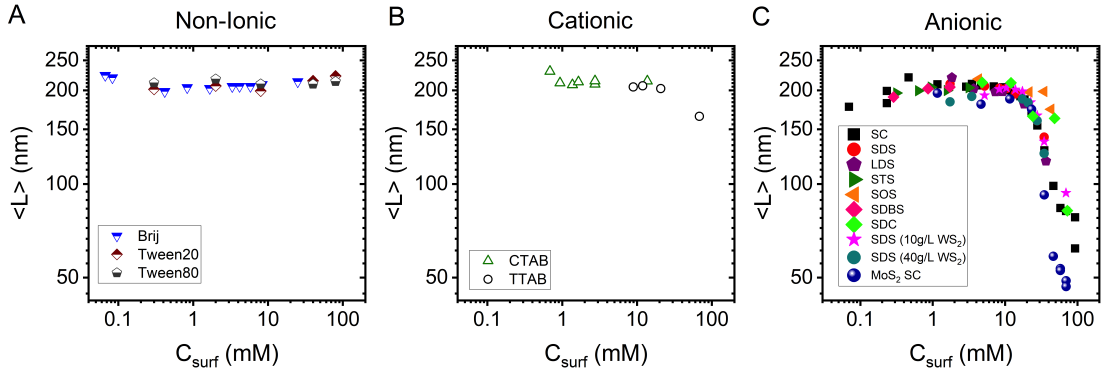

Figure C.15: Mean number of layers plotted versus surfactant concentration for (A) Nonionic (B) Cationic and (C) Anionic surfactants.

C.8 Raman Peak Intensity versus Peak Area

Each Raman spectrum was background subtracted and normalized to the WS_2 2LA(M) and E^1_2g (Γ) modes are present at approximately 356 cm^{-1}. Both the intensity ratio using the height of the PL peak in the normalized spectra as well as the fitted area were extracted. The PL/Raman intensity was found to scale linearly with PL area (Lorentzian fitted) in line with previously investigated Raman spectra of LPE WS_2 nanosheets,[370] in Figure C.16 below.

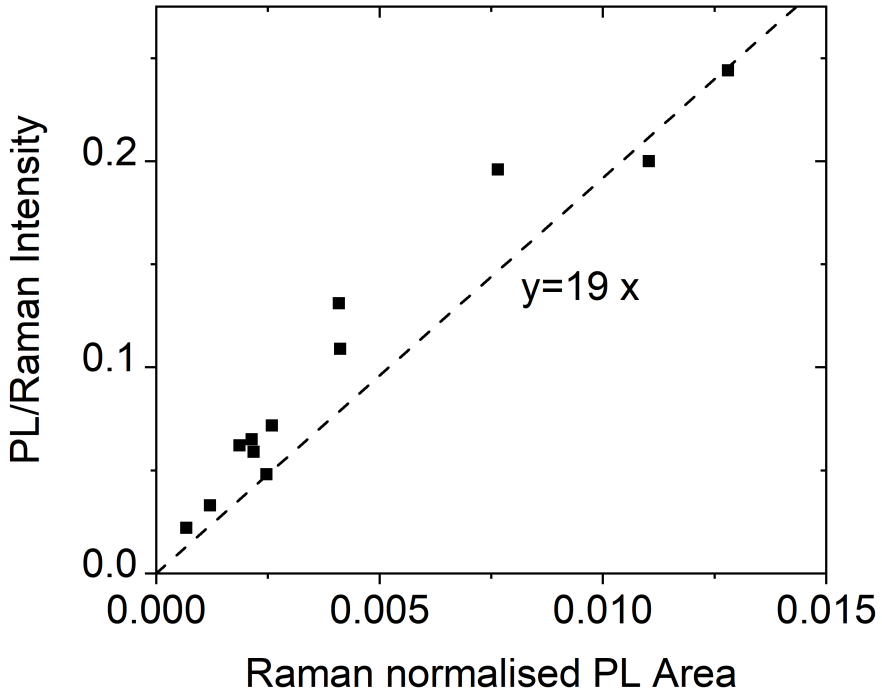

Figure C.16: Raman Intensity ratio (Photoluminescence to Raman signal) plotted versus Area of the PL peak at approximately 2460 cm^{-1}, for a random selection of points across a range of surfactants.

D Novel 2D materials for battery applications: SnP_3 and SiP

D.1 Synthesis methods for SnP_3 and SiP

SnP_3

SnP_3 was synthesised by Dr. Christopher Benndorf and Prof. Oliver Oeckler at Universität Leipzig. Powdered red phosphorus (98.9%, ABCR, Karlsruhe, Germany) and tin (99.999%, Fémipari Kútató Intézet, Budapest, Hungary) were used as starting materials. Before synthesis, phosphorus was treated with boiling aqueous NaOH solution ($\sim$ 25%) and washed several times with demineralized water and acetone. The powder was dried in vacuum and stored under a dry argon atmosphere. The tin was cleaned with concentrated hydrochloric acid, demineralized water and acetone. The tin and phosphorous were subsequently mixed in the atomic ratio of Sn:P = 0.3:1 totalling a mass of 500 mg, and sealed in a silica glass ampule under argon atmosphere (dried over P_4O_{10}, silica gel and titanium sponge at 873 K). The sample was heated slowly to a temperature of 673 K for 7 d and cooled to room temperature by switching off the furnace. The substance was then ground to a fine powder and cold-pressed into a pellet of 6 mm diameter. This pellet was placed into a small corundum crucible and again sealed in a silica ampule under argon. The sample was then annealed at 673 K for 7 d. This procedure was repeated (heating for 11 d) after intermediate grinding and pelletizing steps to produce the final material. Its purity was checked by powder X-ray diffraction, the sample contained $\sim$ 3 wt % Sn_3P_4.

SiP

SiP was synthesised by Dr. Christopher Benndorf and Prof. Oliver Oeckler at Universität Leipzig. Silicon phosphide SiP was synthesized by using Si pieces (99.9999%, VEB Spurenmetalle, Freiberg, GDR), powdered red phosphorus (98.9%, ABCR, Karlsruhe, Germany) and tin rod (2 cm diameter, 99.999%, Fémipari Kútató Intézet, Budapest, Hungary). The Si was ground to a fine powder in cyclohexane to reduce impurities due to surface oxidation before use. The phosphorus was treated with boiling aqueous NaOH solution (w $\sim$ 25%) and washed several times with demineralized water and acetone. The powder was dried in vacuum and stored under a dry argon atmosphere. The tin rod was cleaned with hydrochloric acid (w $\sim$ 3%) and demineralized water and cut into pieces of approximately

500 mg. Mixtures of 500 mg Si and P in the atomic ratio of Si : P = 1 : 1 and approximately 6 g of tin pieces were then sealed in evacuated silica ampoules. The samples were heated slowly (heating rate 2 K min^{-1}) to 673 K and kept at this temperature for 24 h to prevent the strongly exothermic reaction of phosphorus and tin. The temperature was then increased to 1223 K within 12 h and kept for 7 d. Finally the samples were cooled to room temperature by switching off the furnace. The resulting ingots were cleaned with demineralized water and treated with boiling hydrochloric acid (400 mL, w $\sim$ 35%) to remove the tin flux. The remaining SiP was vacuum-filtrated and washed six times with boiling hydrochloric acid (w $\sim$ 35%), boiling demineralized water and acetone. The substance appeared in form of transparent dark reddish-brownish plate-like crystals with a yield of circa 75%. Other than the SiP crystals, a small amount of an opaque colourless side-product was observed using a light microscope which could not be dissolved in H_2O, hydrochloric acid or common organic solvents (EtOH, acetone, ethyl acetate).

D.2 UV-Vis spectra of size-selected SiP

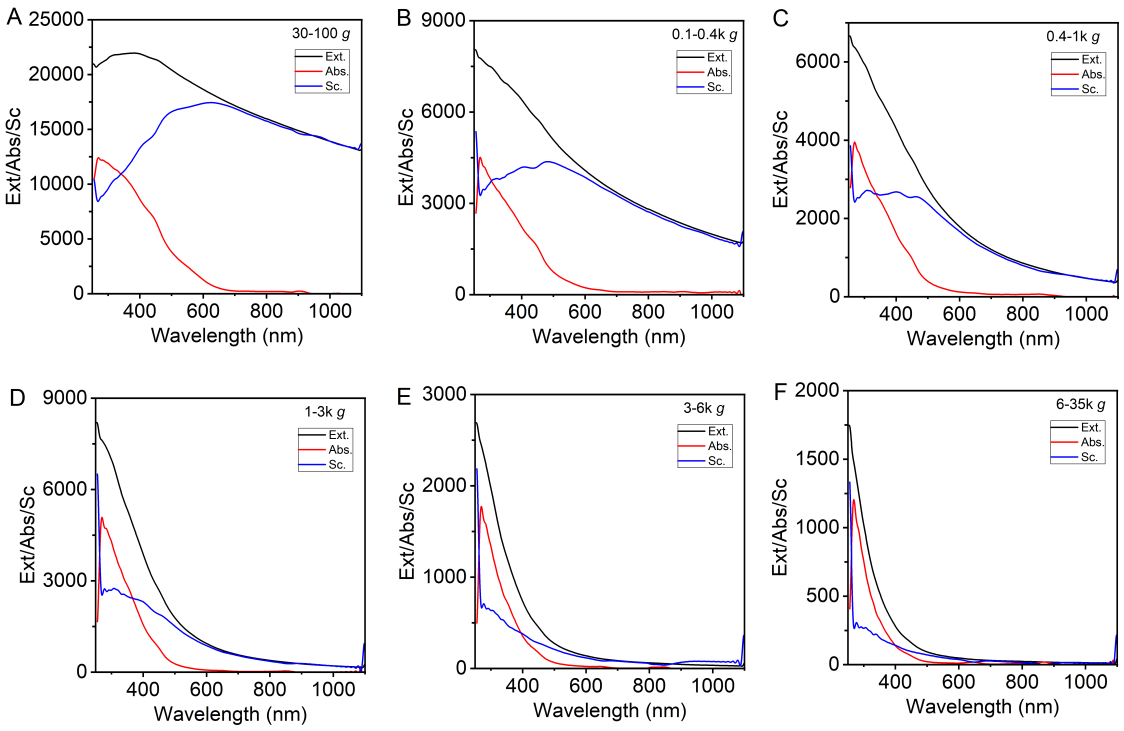

Figure D.1: (A-F) Optical extinction, absorption and scattering spectra for each size fraction in the cascade.

D.3 Non-resonant Raman (785 nm) of SiP

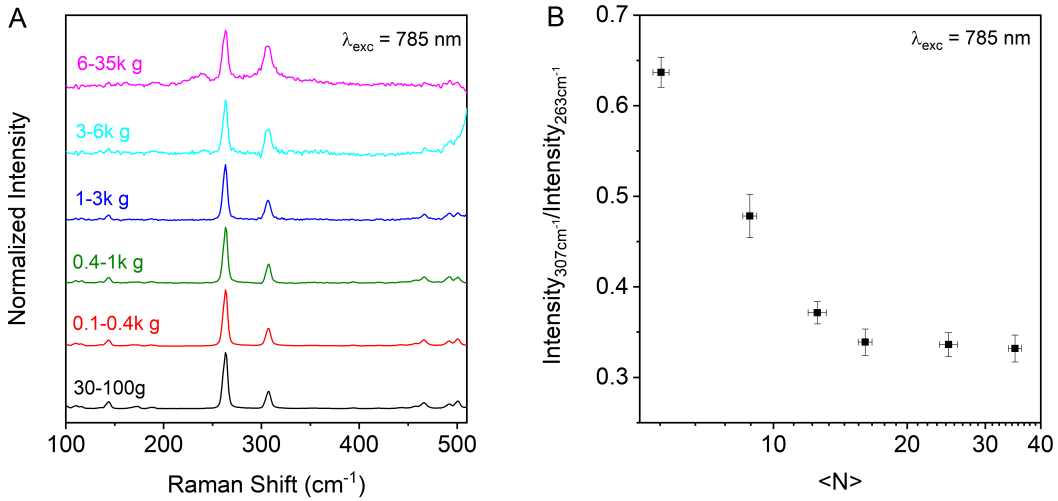

Figure D.2: Raman spectra of size-selected SiP nanosheets (excitation wavelength, λ_{ex} = 785 nm) dispersions, each normalized to the peak at 263 cm^{-1} (A_1^6 mode.[413]) (B) Ratio of the intensity of the Raman peak at 307 cm^{-1} to 263 cm^{-1} as a function of nanosheet thickness shows a decrease in intensity ratio with increasing size, levelling out as nanosheets reach bulk values ($>$ 10 layers)

E Exfoliation of Graphite in a Kitchen Kettle

E.1 XPS Comparison with LPE Graphene

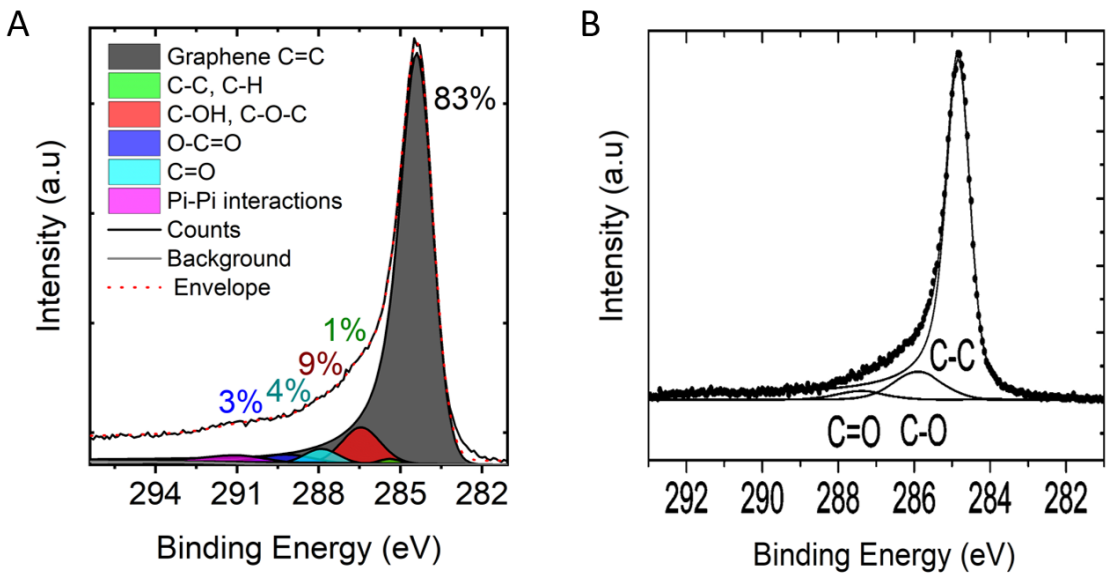

Figure E.1: X-ray photoelectron spectroscopy (XPS) comparison of kettle graphene with LPE graphene (A) XPS analysis of the carbon 1s core-level region of the kettle exfoliated graphite reveals the characteristic asymmetric lineshape associated with graphene. Deconvolution of the lineshape reveals a small number of oxidation components present. (B) XPS analysis of the carbon 1s core-level region of liquid phase exfoliated graphite with contributions from C-C, C-O and C=O bonds. There appears to be slightly less contributions from the oxide species, indicative of a less defective product. Image adapted from Lotya et al.[190]

E.2 Lorentzian peak fitting of the Raman spectra

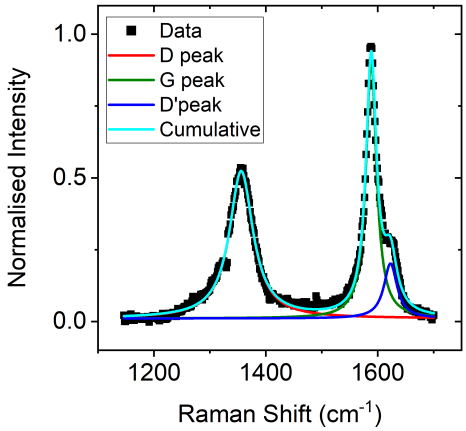

Model	Lorentz		
Equation	y = y0 + (2*A/pi)*(w/(4*(x-xc)^2 + w^2))		
--	D peak	G peak	D' peak
y0	0.01 ± 0.00	0.01 ± 0.00	0.01 ± 0.00
xc	1356.05 ± 0.22	1588.46 ± 0.10	1622.91 ± 0.53
w	51.13 ± 0.77	22.71 ± 0.32	28.51 ± 1.76
A	41.02 ± 0.53	32.00 ± 0.42	8.56 ± 0.48
Adj. R-Square	0.99		

Figure E.2: Example Raman spectrum of a graphene sample made in a standard kettle (excitation wavelength, λ_{ex} = 532 nm) normalized to the G band at 1580 cm^{-1}. The D, G and D' bands were fitted with a triple Lorentzian to extract the true peak intensities and area. The output of the fitting, used to calculate the ratios is shown in the table (right)

E.3 Additional AFM analysis of tip-sonicated graphite

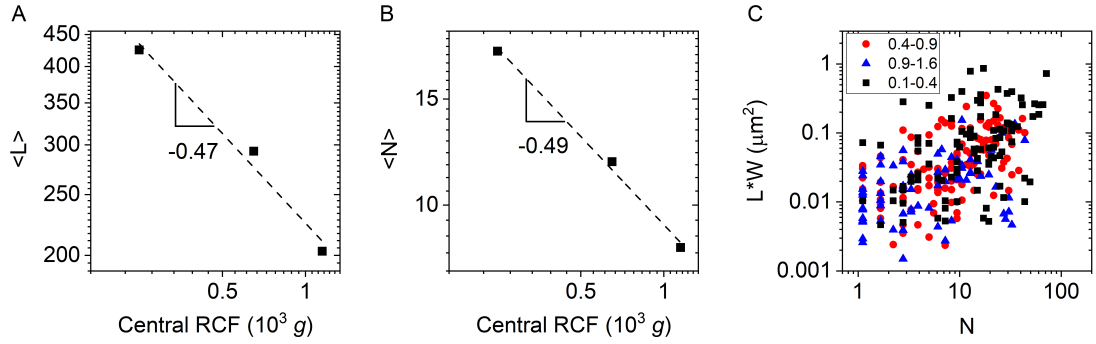

Figure E.3: (A) Mean nanosheet length, <L> as a function of central centrifugal force g. The dashed line is a linear fit to the data with g$^{-0.47}$ scaling, in agreement with the g$^{-0.5}$ of other 2D materials.[20,202,264,310] (B) Mean layer number <N> as a function of central centrifugal force g. The dashed line is a linear fit to the data with g$^{-0.49}$ scaling (C) Nanosheet area (approximated as length × width) plotted versus layer number for three different sizes. Each point represents an individual nanosheet measured by AFM.

Bibliography

***

[1] G. E. Moore, "Cramming more components onto integrated circuits," *IEEE Solid-state Circuits Society Newsletter*, vol. 11, no. 3, pp. 33–35, 2006.

[2] R. P. Feynman, "There's plenty of room at the bottom," *California Institute of Technology, Engineering and Science Magazine*, vol. 23.

[3] I. Freestone, N. Meeks, M. Sax, and C. Higgitt, "The Lycurgus cup—a Roman nanotechnology," *Gold Bulletin*, vol. 40, no. 4, pp. 270–277, 2007.

[4] M. Reibold, P. Paufler, A. Levin, W. Kochmann, N. Pätzke, and D. Meyer, "Carbon nanotubes in an ancient Damascus sabre," *Nature*, vol. 444, no. 7117, pp. 286–286, 2006.

[5] G. Binnig, H. Rohrer, C. Gerber, and E. Weibel, "Surface studies by scanning tunneling microscopy," *Physical Review Letters*, vol. 49, no. 1, p. 57, 1982.

[6] G. Binnig, C. F. Quate, and C. Gerber, "Atomic Force Microscope," *Physical Review Letters*, vol. 56, no. 9, p. 930, 1986.

[7] H. W. Kroto, J. R. Heath, S. C. O'Brien, R. F. Curl, and R. E. Smalley, "C60: Buckminsterfullerene," *Nature*, vol. 318, no. 6042, pp. 162–163, 1985.

[8] S. Iijima, "Helical microtubules of graphitic carbon," *Nature*, vol. 354, no. 6348, pp. 56–58, 1991.

[9] K. S. Novoselov, A. K. Geim, S. V. Morozov, D. Jiang, Y. Zhang, S. V. Dubonos, I. V. Grigorieva, and A. A. Firsov, "Electric field effect in atomically thin carbon films," *Science*, vol. 306, no. 5696, pp. 666–669, 2004.

[10] S. Das, H.-Y. Chen, A. V. Penumatcha, and J. Appenzeller, "High performance multilayer MoS2 transistors with scandium contacts," *Nano Letters*, vol. 13, no. 1, pp. 100–105, 2013.

[11] K. I. Bolotin, K. J. Sikes, Z. Jiang, M. Klima, G. Fudenberg, J. Hone, P. Kim, and H. Stormer, "Ultrahigh electron mobility in suspended graphene," *Solid State Communications*, vol. 146, no. 9-10, pp. 351–355, 2008.

[12] Z. Yin, H. Li, H. Li, L. Jiang, Y. Shi, Y. Sun, G. Lu, Q. Zhang, X. Chen, and H. Zhang, "Single-layer MoS2 phototransistors," *ACS Nano*, vol. 6, no. 1, pp. 74–80, 2012.

[13] L. Qu, Y. Liu, J.-B. Baek, and L. Dai, "Nitrogen-doped graphene as efficient metal-free electrocatalyst for oxygen reduction in fuel cells," *ACS Nano*, vol. 4, no. 3, pp. 1321–1326, 2010.

[14] J. Kibsgaard, Z. Chen, B. N. Reinecke, and T. F. Jaramillo, "Engineering the surface structure of MoS 2 to preferentially expose active edge sites for electrocatalysis," *Nature Materials*, vol. 11, no. 11, pp. 963–969, 2012.

[15] Y. Liu and X. Peng, "Recent advances of supercapacitors based on two-dimensional materials," *Applied Materials Today*, vol. 8, pp. 104–115, 2017.

[16] X. Zhang, L. Hou, A. Ciesielski, and P. Samorì, "2D materials beyond graphene for high-performance energy storage applications," *Advanced Energy Materials*, vol. 6, no. 23, p. 1600671, 2016.

[17] Y. Hernandez, V. Nicolosi, M. Lotya, F. M. Blighe, Z. Sun, S. De, I. McGovern, B. Holland, M. Byrne, Y. K. Gun'Ko, *et al.*, "High-yield production of graphene by liquid-phase exfoliation of graphite," *Nature Nanotechnology*, vol. 3, no. 9, p. 563, 2008.

[18] J. N. Coleman, M. Lotya, A. O'Neill, S. D. Bergin, P. J. King, U. Khan, K. Young, A. Gaucher, S. De, R. J. Smith, *et al.*, "Two-dimensional nanosheets produced by liquid exfoliation of layered materials," *Science*, vol. 331, no. 6017, pp. 568–571, 2011.

[19] C. Backes, R. J. Smith, N. McEvoy, N. C. Berner, D. McCloskey, H. C. Nerl, A. O'Neill, P. J. King, T. Higgins, D. Hanlon, *et al.*, "Edge and confinement effects allow in situ measurement of size and thickness of liquid-exfoliated nanosheets," *Nature Communications*, vol. 5, p. ncomms5576, 2014.

[20] C. Backes, B. M. Szydłowska, A. Harvey, S. Yuan, V. Vega-Mayoral, B. R. Davies, P.-l. Zhao, D. Hanlon, E. J. Santos, M. I. Katsnelson, *et al.*, "Production of highly monolayer enriched dispersions of liquid-exfoliated nanosheets by liquid cascade centrifugation," *ACS Nano*, vol. 10, no. 1, pp. 1589–1601, 2016.

[21] D. Gerchman and A. K. Alves, "Solution-processable exfoliation and suspension of atomically thin WSe2," *Journal of Colloid and Interface Science*, vol. 468, pp. 247–252, 2016.

[22] A. Harvey, X. He, I. J. Godwin, C. Backes, D. McAteer, N. C. Berner, N. McEvoy, A. Ferguson, A. Shmeliov, M. E. Lyons, *et al.*, "Production of Ni(OH)2 nanosheets by liquid phase exfoliation: from optical properties to electrochemical applications," *Journal of Materials Chemistry A*, vol. 4, no. 28, pp. 11046–11059, 2016.

[23] D. McAteer, I. J. Godwin, Z. Ling, A. Harvey, L. He, C. S. Boland, V. Vega-Mayoral, B. Szydłowska, A. A. Rovetta, C. Backes, *et al.*, "Liquid Exfoliated Co(OH)2 Nanosheets as Low-Cost, Yet High-Performance, Catalysts for the Oxygen Evolution Reaction," *Advanced Energy Materials*, 2018.

[24] J. B. Boland, A. Harvey, R. Tian, D. Hanlon, V. Vega-Mayoral, B. Szydlowska, A. Griffin, T. Stimpel-Lindner, S. Jaskaniec, V. Nicolosi, *et al.*, "Liquid phase exfoliation of MoO 2 nanosheets for lithium ion battery applications," *Nanoscale Advances*, vol. 1, no. 4, pp. 1560–1570, 2019.

[25] D. Hanlon, C. Backes, T. M. Higgins, M. Hughes, A. O'Neill, P. King, N. McEvoy, G. S. Duesberg, B. Mendoza Sanchez, H. Pettersson, *et al.*, "Production of molybdenum trioxide nanosheets by liquid exfoliation and their application in high-performance supercapacitors," *Chemistry of Materials*, vol. 26, no. 4, pp. 1751–1763, 2014.

[26] D. Hanlon, C. Backes, E. Doherty, C. S. Cucinotta, N. C. Berner, C. Boland, K. Lee, A. Harvey, P. Lynch, Z. Gholamvand, *et al.*, "Liquid exfoliation of solvent-stabilized few-layer black phosphorus for applications beyond electronics," *Nature Communications*, vol. 6, 2015.

[27] N. Nitta, F. Wu, J. T. Lee, and G. Yushin, "Li-ion battery materials: present and future," *Materials Today*, vol. 18, no. 5, pp. 252–264, 2015.

[28] A. K. Geim and I. V. Grigorieva, "Van der Waals heterostructures," *Nature*, vol. 499, no. 7459, p. 419, 2013.

[29] D. Jariwala, V. K. Sangwan, L. J. Lauhon, T. J. Marks, and M. C. Hersam, "Emerging device applications for semiconducting two-dimensional transition metal dichalcogenides," *ACS Nano*, vol. 8, no. 2, pp. 1102–1120, 2014.

[30] X. Li, Y. Zhu, W. Cai, M. Borysiak, B. Han, D. Chen, R. D. Piner, L. Colombo, and R. S. Ruoff, "Transfer of large-area graphene films for high-performance transparent conductive electrodes," *Nano Letters*, vol. 9, no. 12, pp. 4359–4363, 2009.

[31] Y. Chen, C. Tan, H. Zhang, and L. Wang, "Two-dimensional graphene analogues for biomedical applications," *Chemical Society Reviews*, vol. 44, no. 9, pp. 2681–2701, 2015.

[32] Z. Li, G. Zhu, R. Yang, A. C. Wang, and Z. L. Wang, "Muscle-driven in vivo nanogenerator," *Advanced materials*, vol. 22, no. 23, pp. 2534–2537, 2010.

[33] P. R. Wallace, "The band theory of graphite," *Physical Review*, vol. 71, no. 9, p. 622, 1947.

[34] G. W. Semenoff, "Condensed-matter simulation of a three-dimensional anomaly," *Physical Review Letters*, vol. 53, no. 26, p. 2449, 1984.

[35] E. Fradkin, "Critical behavior of disordered degenerate semiconductors. I. Models, symmetries, and formalism," *Physical Review B*, vol. 33, no. 5, p. 3257, 1986.

[36] F. D. M. Haldane, "Model for a quantum Hall effect without Landau levels: Condensed-matter realization of the" parity anomaly"," *Physical Review Letters*, vol. 61, no. 18, p. 2015, 1988.

[37] P. W. Atkins, J. De Paula, and J. Keeler, *Atkins' Physical Chemistry*. 9 ed., 2018.

[38] A. C. Neto, F. Guinea, N. M. Peres, K. S. Novoselov, and A. K. Geim, "The electronic properties of graphene," *Reviews of Modern Physics*, vol. 81, no. 1, p. 109, 2009.

[39] R. Peierls, "Quelques propriétés typiques des corps solides," in *Annales de l'institut Henri Poincaré*, vol. 5, pp. 177–222, 1935.

[40] L. D. Landau, "Zur Theorie der phasenumwandlungen II," *Phys. Z. Sowjetunion*, vol. 11, no. 545, pp. 26–35, 1937.

[41] J. C. Meyer, A. K. Geim, M. I. Katsnelson, K. S. Novoselov, T. J. Booth, and S. Roth, "The structure of suspended graphene sheets," *Nature*, vol. 446, no. 7131, pp. 60–63, 2007.

[42] A. Fasolino, J. Los, and M. I. Katsnelson, "Intrinsic ripples in graphene," *Nature Materials*, vol. 6, no. 11, pp. 858–861, 2007.

[43] M. H. Gass, U. Bangert, A. L. Bleloch, P. Wang, R. R. Nair, and A. Geim, "Free-standing graphene at atomic resolution," *Nature Nanotechnology*, vol. 3, no. 11, pp. 676–681, 2008.

[44] A. Eckmann, A. Felten, A. Mishchenko, L. Britnell, R. Krupke, K. S. Novoselov, and C. Casiraghi, "Probing the nature of defects in graphene by Raman spectroscopy," *Nano Letters*, vol. 12, no. 8, pp. 3925–3930, 2012.

[45] F. Banhart, J. Kotakoski, and A. V. Krasheninnikov, "Structural defects in graphene," *ACS Nano*, vol. 5, no. 1, pp. 26–41, 2011.

[46] A. Hashimoto, K. Suenaga, A. Gloter, K. Urita, and S. Iijima, "Direct evidence for atomic defects in graphene layers," *Nature*, vol. 430, no. 7002, pp. 870–873, 2004.

[47] P. T. Araujo, M. Terrones, and M. S. Dresselhaus, "Defects and impurities in graphene-like materials," *Materials Today*, vol. 15, no. 3, pp. 98–109, 2012.

[48] W. D. Callister and D. G. Rethwisch, *Materials science and engineering*, vol. 5. John Wiley & Sons NY, 2011.

[49] Z. Ni, L. Ponomarenko, R. Nair, R. Yang, S. Anissimova, I. Grigorieva, F. Schedin, P. Blake, Z. Shen, E. Hill, *et al.*, "On resonant scatterers as a factor limiting carrier mobility in graphene," *Nano Letters*, vol. 10, no. 10, pp. 3868–3872, 2010.

[50] D. Boukhvalov and M. Katsnelson, "Chemical functionalization of graphene with defects," *Nano Letters*, vol. 8, no. 12, pp. 4373–4379, 2008.

[51] M. Dresselhaus, A. Jorio, A. Souza Filho, and R. Saito, "Defect characterization in graphene and carbon nanotubes using Raman spectroscopy," *Philosophical Transactions of the Royal Society A: Mathematical, Physical and Engineering Sciences*, vol. 368, no. 1932, pp. 5355–5377, 2010.

[52] L. G. Cançado, A. Jorio, E. M. Ferreira, F. Stavale, C. A. Achete, R. B. Capaz, M. V. d. O. Moutinho, A. Lombardo, T. Kulmala, and A. C. Ferrari, "Quantifying defects in graphene via Raman spectroscopy at different excitation energies," *Nano Letters*, vol. 11, no. 8, pp. 3190–3196, 2011.

[53] C. Beenakker, "Colloquium: Andreev reflection and Klein tunneling in graphene," *Reviews of Modern Physics*, vol. 80, no. 4, p. 1337, 2008.

[54] A. C. Ferrari and D. M. Basko, "Raman spectroscopy as a versatile tool for studying the properties of graphene," *Nature Nanotechnology*, vol. 8, no. 4, pp. 235–246, 2013.

[55] F. Schedin, A. K. Geim, S. V. Morozov, E. Hill, P. Blake, M. Katsnelson, and K. S. Novoselov, "Detection of individual gas molecules adsorbed on graphene," *Nature Materials*, vol. 6, no. 9, pp. 652–655, 2007.

[56] T. Ohta, A. Bostwick, T. Seyller, K. Horn, and E. Rotenberg, "Controlling the electronic structure of bilayer graphene," *Science*, vol. 313, no. 5789, pp. 951–954, 2006.

[57] A. K. Geim and K. S. Novoselov, "The rise of graphene," in *Nanoscience and technology: a collection of reviews from Nature journals*, pp. 11–19, World Scientific, 2010.

[58] Y. Zhang, Y.-W. Tan, H. L. Stormer, and P. Kim, "Experimental observation of the quantum Hall effect and Berry's phase in graphene," *nature*, vol. 438, no. 7065, pp. 201–204, 2005.

[59] Y. Zhang, T.-T. Tang, C. Girit, Z. Hao, M. C. Martin, A. Zettl, M. F. Crommie, Y. R. Shen, and F. Wang, "Direct observation of a widely tunable bandgap in bilayer graphene," *Nature*, vol. 459, no. 7248, pp. 820–823, 2009.

[60] K. F. Mak, C. H. Lui, J. Shan, and T. F. Heinz, "Observation of an electric-field-induced band gap in bilayer graphene by infrared spectroscopy," *Physical Review Letters*, vol. 102, no. 25, p. 256405, 2009.

[61] S. Morozov, K. Novoselov, F. Schedin, D. Jiang, A. Firsov, and A. Geim, "Two-dimensional electron and hole gases at the surface of graphite," *Physical Review B*, vol. 72, no. 20, p. 201401, 2005.

[62] R. Saito, M. Hofmann, G. Dresselhaus, A. Jorio, and M. Dresselhaus, "Raman spectroscopy of graphene and carbon nanotubes," *Advances in Physics*, vol. 60, no. 3, pp. 413–550, 2011.

[63] L. Malard, M. A. Pimenta, G. Dresselhaus, and M. Dresselhaus, "Raman spectroscopy in graphene," *Physics Reports*, vol. 473, no. 5-6, pp. 51–87, 2009.

[64] A. C. Ferrari, J. Meyer, V. Scardaci, C. Casiraghi, M. Lazzeri, F. Mauri, S. Piscanec, D. Jiang, K. Novoselov, S. Roth, *et al.*, "Raman spectrum of graphene and graphene layers," *Physical Review Letters*, vol. 97, no. 18, p. 187401, 2006.

[65] Y. Hao, Y. Wang, L. Wang, Z. Ni, Z. Wang, R. Wang, C. K. Koo, Z. Shen, and J. T. Thong, "Probing layer number and stacking order of few-layer graphene by Raman spectroscopy," *Small*, vol. 6, no. 2, pp. 195–200, 2010.

[66] D. Graf, F. Molitor, K. Ensslin, C. Stampfer, A. Jungen, C. Hierold, and L. Wirtz, "Spatially resolved Raman spectroscopy of single-and few-layer graphene," *Nano Letters*, vol. 7, no. 2, pp. 238–242, 2007.

[67] C. Backes, K. R. Paton, D. Hanlon, S. Yuan, M. I. Katsnelson, J. Houston, R. J. Smith, D. McCloskey, J. F. Donegan, and J. N. Coleman, "Spectroscopic metrics allow in situ measurement of mean size and thickness of liquid-exfoliated few-layer graphene nanosheets," *Nanoscale*, vol. 8, no. 7, pp. 4311–4323, 2016.

[68] C. S. Boland, U. Khan, G. Ryan, S. Barwich, R. Charifou, A. Harvey, C. Backes, Z. Li, M. S. Ferreira, M. E. Möbius, *et al.*, "Sensitive electromechanical sensors using viscoelastic graphene-polymer nanocomposites," *Science*, vol. 354, no. 6317, pp. 1257–1260, 2016.

[69] S. Chatterjee, J. Wang, W. Kuo, N. Tai, C. Salzmann, W. Li, R. Hollertz, F. Nüesch, and B. Chu, "Mechanical reinforcement and thermal conductivity in expanded graphene nanoplatelets reinforced epoxy composites," *Chemical Physics Letters*, vol. 531, pp. 6–10, 2012.

[70] J. Liang, Y. Huang, L. Zhang, Y. Wang, Y. Ma, T. Guo, and Y. Chen, "Molecular-level dispersion of graphene into poly (vinyl alcohol) and effective reinforcement of their nanocomposites," *Advanced Functional Materials*, vol. 19, no. 14, pp. 2297–2302, 2009.

[71] A. Capasso, A. D. R. Castillo, H. Sun, A. Ansaldo, V. Pellegrini, and F. Bonaccorso, "Ink-jet printing of graphene for flexible electronics: an environmentally-friendly approach," *Solid State Communications*, vol. 224, pp. 53–63, 2015.

[72] A. G. Kelly, T. Hallam, C. Backes, A. Harvey, A. S. Esmaeily, I. Godwin, J. Coelho, V. Nicolosi, J. Lauth, A. Kulkarni, *et al.*, "All-printed thin-film transistors from networks of liquid-exfoliated nanosheets," *Science*, vol. 356, no. 6333, pp. 69–73, 2017.

[73] A. G. Kelly, D. Finn, A. Harvey, T. Hallam, and J. N. Coleman, "All-printed capacitors from graphene-BN-graphene nanosheet heterostructures," *Applied Physics Letters*, vol. 109, no. 2, p. 023107, 2016.

[74] T. Kobayashi, M. Bando, N. Kimura, K. Shimizu, K. Kadono, N. Umezu, K. Miyahara, S. Hayazaki, S. Nagai, Y. Mizuguchi, *et al.*, "Production of a 100-m-long high-quality graphene transparent conductive film by roll-to-roll chemical vapor deposition and transfer process," *Applied Physics Letters*, vol. 102, no. 2, p. 023112, 2013.

[75] X. Wang, L. Zhi, and K. Müllen, "Transparent, conductive graphene electrodes for dye-sensitized solar cells," *Nano Letters*, vol. 8, no. 1, pp. 323–327, 2008.

[76] C. Huang, C. Li, and G. Shi, "Graphene based catalysts," *Energy & Environmental Science*, vol. 5, no. 10, pp. 8848–8868, 2012.

[77] Y. Wang, Z. Shi, Y. Huang, Y. Ma, C. Wang, M. Chen, and Y. Chen, "Supercapacitor devices based on graphene materials," *The Journal of Physical Chemistry C*, vol. 113, no. 30, pp. 13103–13107, 2009.

[78] C. Liu, Z. Yu, D. Neff, A. Zhamu, and B. Z. Jang, "Graphene-based supercapacitor with an ultrahigh energy density," *Nano Letters*, vol. 10, no. 12, pp. 4863–4868, 2010.

[79] G. K. Dimitrakakis, E. Tylianakis, and G. E. Froudakis, "Pillared graphene: a new 3D network nanostructure for enhanced hydrogen storage," *Nano Letters*, vol. 8, no. 10, pp. 3166–3170, 2008.

[80] C. Ataca, E. Aktürk, S. Ciraci, and H. Ustunel, "High-capacity hydrogen storage by metallized graphene," *Applied Physics Letters*, vol. 93, no. 4, p. 043123, 2008.

[81] T. Kuila, S. Bose, P. Khanra, A. K. Mishra, N. H. Kim, and J. H. Lee, "Recent advances in graphene-based biosensors," *Biosensors and Bioelectronics*, vol. 26, no. 12, pp. 4637–4648, 2011.

[82] S. D. McCullen, D. R. Stevens, W. A. Roberts, L. I. Clarke, S. H. Bernacki, R. E. Gorga, and E. G. Loboa, "Characterization of electrospun nanocomposite scaffolds and biocompatibility with adipose-derived human mesenchymal stem cells," *International Journal of Nanomedicine*, vol. 2, no. 2, p. 253, 2007.

[83] N. Li, X. Zhang, Q. Song, R. Su, Q. Zhang, T. Kong, L. Liu, G. Jin, M. Tang, and G. Cheng, "The promotion of neurite sprouting and outgrowth of mouse hippocampal cells in culture by graphene substrates," *Biomaterials*, vol. 32, no. 35, pp. 9374–9382, 2011.

[84] A. J. Ryan, C. J. Kearney, N. Shen, U. Khan, A. G. Kelly, C. Probst, E. Brauchle, S. Biccai, C. D. Garciarena, V. Vega-Mayoral, *et al.*, "Electroconductive biohybrid collagen/pristine graphene composite biomaterials with enhanced biological activity," *Advanced Materials*, vol. 30, no. 15, p. 1706442, 2018.

[85] S. Iijima and T. Ichihashi, "Single-shell carbon nanotubes of 1-nm diameter," *Nature*, vol. 363, no. 6430, pp. 603–605, 1993.

[86] E. G. Gamaly and T. W. Ebbesen, "Mechanism of carbon nanotube formation in the arc discharge," *Physical Review B*, vol. 52, no. 3, p. 2083, 1995.

[87] A. M. Cassell, J. A. Raymakers, J. Kong, and H. Dai, "Large scale CVD synthesis of single-walled carbon nanotubes," *The Journal of Physical Chemistry B*, vol. 103, no. 31, pp. 6484–6492, 1999.

[88] Y.-L. Li, I. A. Kinloch, and A. H. Windle, "Direct spinning of carbon nanotube fibers from chemical vapor deposition synthesis," *Science*, vol. 304, no. 5668, pp. 276–278, 2004.

[89] A. Hirsch and O. Vostrowsky, "Functionalization of carbon nanotubes," in *Functional Molecular Nanostructures*, pp. 193–237, Springer, 2005.

[90] G. Dresselhaus, S. Riichiro, *et al.*, *Physical properties of carbon nanotubes*. World scientific, 1998.

[91] P. J. Harris, "Carbon nanotubes and related structures: new materials for the twenty-first century," *American Journal of Physics*, vol. 72, no. 3, pp. 415–415, 2004.

[92] A. Graf, Y. Zakharko, S. P. Schießl, C. Backes, M. Pfohl, B. S. Flavel, and J. Zaumseil, "Large scale, selective dispersion of long single-walled carbon nanotubes with high photoluminescence quantum yield by shear force mixing," *Carbon*, vol. 105, pp. 593–599, 2016.

[93] J. Zaumseil, "Semiconducting Single-Walled Carbon Nanotubes or Very Rigid Conjugated Polymers: A Comparison," *Advanced Electronic Materials*, vol. 5, no. 2, p. 1800514, 2019.

[94] W. Liang, M. Bockrath, D. Bozovic, J. H. Hafner, M. Tinkham, and H. Park, "Fabry-Perot interference in a nanotube electron waveguide," *Nature*, vol. 411, no. 6838, pp. 665–669, 2001.

[95] R. H. Baughman, A. A. Zakhidov, and W. A. De Heer, "Carbon nanotubes–the route toward applications," *Science*, vol. 297, no. 5582, pp. 787–792, 2002.

[96] A. Javey, J. Guo, Q. Wang, M. Lundstrom, and H. Dai, "Ballistic carbon nanotube field-effect transistors," *Nature*, vol. 424, no. 6949, pp. 654–657, 2003.

[97] P. G. Collins, A. Zettl, H. Bando, A. Thess, and R. Smalley, "Nanotube nanodevice," *Science*, vol. 278, no. 5335, pp. 100–102, 1997.

[98] R. Martel, T. Schmidt, H. Shea, T. Hertel, and P. Avouris, "Single-and multi-wall carbon nanotube field-effect transistors," *Applied Physics Letters*, vol. 73, no. 17, pp. 2447–2449, 1998.

[99] S. J. Kang, C. Kocabas, T. Ozel, M. Shim, N. Pimparkar, M. A. Alam, S. V. Rotkin, and J. A. Rogers, "High-performance electronics using dense, perfectly aligned arrays of single-walled carbon nanotubes," *Nature Nanotechnology*, vol. 2, no. 4, pp. 230–236, 2007.

[100] V. Derycke, R. Martel, J. Appenzeller, and P. Avouris, "Carbon nanotube inter-and intramolecular logic gates," *Nano Letters*, vol. 1, no. 9, pp. 453–456, 2001.

[101] Y. Wu, X. Zhang, A. Leung, and W. Zhong, "An energy-equivalent model on studying the mechanical properties of single-walled carbon nanotubes," *Thin-Walled Structures*, vol. 44, no. 6, pp. 667–676, 2006.

[102] K. I. Tserpes and P. Papanikos, "Finite element modeling of the tensile behavior of carbon nanotubes, graphene and their composites," in *Modeling of carbon nanotubes, graphene and their composites*, pp. 303–329, Springer, 2014.

[103] M.-F. Yu, O. Lourie, M. J. Dyer, K. Moloni, T. F. Kelly, and R. S. Ruoff, "Strength and breaking mechanism of multiwalled carbon nanotubes under tensile load," *Science*, vol. 287, no. 5453, pp. 637–640, 2000.

[104] E. W. Wong, P. E. Sheehan, and C. M. Lieber, "Nanobeam mechanics: elasticity, strength, and toughness of nanorods and nanotubes," *Science*, vol. 277, no. 5334, pp. 1971–1975, 1997.

[105] A. S. Claye, J. E. Fischer, C. B. Huffman, A. G. Rinzler, and R. E. Smalley, "Solid-state electrochemistry of the Li single wall carbon nanotube system," *Journal of the Electrochemical Society*, vol. 147, no. 8, p. 2845, 2000.

[106] K. S. Novoselov, D. Jiang, F. Schedin, T. Booth, V. Khotkevich, S. Morozov, and A. K. Geim, "Two-dimensional atomic crystals," *Proceedings of the National Academy of Sciences*, vol. 102, no. 30, pp. 10451–10453, 2005.

[107] R. G. Dickinson and L. Pauling, "The crystal structure of molybdenite," *Journal of the American Chemical Society*, vol. 45, no. 6, pp. 1466–1471, 1923.

[108] R. Frindt, "Optical Absorption of a Few Unit-Cell Layers of MoS2," *Physical Review*, vol. 140, no. 2A, p. A536, 1965.

[109] J. A. Wilson and A. Yoffe, "The transition metal dichalcogenides discussion and interpretation of the observed optical, electrical and structural properties," *Advances in Physics*, vol. 18, no. 73, pp. 193–335, 1969.

[110] P. Joensen, R. Frindt, and S. R. Morrison, "Single-layer MoS2," *Materials Research Bulletin*, vol. 21, no. 4, pp. 457–461, 1986.

[111] M. Chhowalla, H. S. Shin, G. Eda, L.-J. Li, K. P. Loh, and H. Zhang, "The chemistry of two-dimensional layered transition metal dichalcogenide nanosheets," *Nature Chemistry*, vol. 5, no. 4, p. 263, 2013.

[112] R. Lv, J. A. Robinson, R. E. Schaak, D. Sun, Y. Sun, T. E. Mallouk, and M. Terrones, "Transition metal dichalcogenides and beyond: synthesis, properties, and applications of single- and few-layer nanosheets," *Accounts of Chemical Research*, vol. 48, no. 1, pp. 56–64, 2015.

[113] Q. H. Wang, K. Kalantar-Zadeh, A. Kis, J. N. Coleman, and M. S. Strano, "Electronics and optoelectronics of two-dimensional transition metal dichalcogenides," *Nature Nanotechnology*, vol. 7, no. 11, pp. 699–712, 2012.

[114] B. Schönfeld, J. Huang, and S. Moss, "Anisotropic mean-square displacements (MSD) in single-crystals of 2H-and 3R-MoS2," *Acta Crystallographica Section B: Structural Science*, vol. 39, no. 4, pp. 404–407, 1983.

[115] Z. Zeng, X. Sun, D. Zhang, W. Zheng, X. Fan, M. He, T. Xu, L. Sun, X. Wang, and A. Pan, "Controlled vapor growth and nonlinear optical applications of large-area 3R phase WS2 and WSe2 atomic layers," *Advanced Functional Materials*, vol. 29, no. 11, p. 1806874, 2019.

[116] R. J. Toh, Z. Sofer, J. Luxa, D. Sedmidubskỳ, and M. Pumera, "3R phase of MoS2 and WS2 outperforms the corresponding 2H phase for hydrogen evolution," *Chemical Communications*, vol. 53, no. 21, pp. 3054–3057, 2017.

[117] M. Py and R. Haering, "Structural destabilization induced by lithium intercalation in MoS2 and related compounds," *Canadian Journal of Physics*, vol. 61, no. 1, pp. 76–84, 1983.

[118] K. Chang, X. Hai, H. Pang, H. Zhang, L. Shi, G. Liu, H. Liu, G. Zhao, M. Li, and J. Ye, "Targeted synthesis of 2H-and 1T-phase MoS2 monolayers for catalytic hydrogen evolution," *Advanced Materials*, vol. 28, no. 45, pp. 10033–10041, 2016.

[119] S. Manzeli, D. Ovchinnikov, D. Pasquier, O. V. Yazyev, and A. Kis, "2D transition metal dichalcogenides," *Nature Reviews Materials*, vol. 2, no. 8, p. 17033, 2017.

[120] Y. Ding, Y. Wang, J. Ni, L. Shi, S. Shi, and W. Tang, "First principles study of structural, vibrational and electronic properties of graphene-like MX2 (M= Mo, Nb, W, Ta; X= S, Se, Te) monolayers," *Physica B: Condensed Matter*, vol. 406, no. 11, pp. 2254–2260, 2011.

[121] K. F. Mak, C. Lee, J. Hone, J. Shan, and T. F. Heinz, "Atomically thin MoS2: a new direct-gap semiconductor," *Physical Review Letters*, vol. 105, no. 13, p. 136805, 2010.

[122] T. Li and G. Galli, "Electronic properties of MoS2 nanoparticles," *The Journal of Physical Chemistry C*, vol. 111, no. 44, pp. 16192–16196, 2007.

[123] A. Splendiani, L. Sun, Y. Zhang, T. Li, J. Kim, C.-Y. Chim, G. Galli, and F. Wang, "Emerging photoluminescence in monolayer MoS2," *Nano Letters*, vol. 10, no. 4, pp. 1271–1275, 2010.

[124] A. Berkdemir, H. R. Gutiérrez, A. R. Botello-Méndez, N. Perea-López, A. L. Elías, C.-I. Chia, B. Wang, V. H. Crespi, F. López-Urías, J.-C. Charlier, *et al.*, "Identification of individual and few layers of WS 2 using Raman spectroscopy," *Scientific Reports*, vol. 3, p. 1755, 2013.

[125] E. Del Corro, H. Terrones, A. Elias, C. Fantini, S. Feng, M. A. Nguyen, T. E. Mallouk, M. Terrones, and M. A. Pimenta, "Excited excitonic states in 1L, 2L, 3L, and bulk WSe2 observed by resonant Raman spectroscopy," *ACS Nano*, vol. 8, no. 9, pp. 9629–9635, 2014.

[126] P. Hajiyev, C. Cong, C. Qiu, and T. Yu, "Contrast and Raman spectroscopy study of single- and few-layered charge density wave material: 2H-TaSe2," *Scientific Reports*, vol. 3, no. 1, pp. 1–6, 2013.

[127] H. Zeng and X. Cui, "An optical spectroscopic study on two-dimensional group-VI transition metal dichalcogenides," *Chemical Society Reviews*, vol. 44, no. 9, pp. 2629–2642, 2015.

[128] S. Mouri, Y. Miyauchi, and K. Matsuda, "Tunable photoluminescence of monolayer MoS2 via chemical doping," *Nano Letters*, vol. 13, no. 12, pp. 5944–5948, 2013.

[129] K. M. McCreary, A. T. Hanbicki, G. G. Jernigan, J. C. Culbertson, and B. T. Jonker, "Synthesis of large-area WS 2 monolayers with exceptional photoluminescence," *Scientific Reports*, vol. 6, p. 19159, 2016.

[130] Y. Li, Y. Rao, K. F. Mak, Y. You, S. Wang, C. R. Dean, and T. F. Heinz, "Probing symmetry properties of few-layer MoS2 and h-BN by optical second-harmonic generation," *Nano Letters*, vol. 13, no. 7, pp. 3329–3333, 2013.

[131] H.-P. Komsa and A. V. Krasheninnikov, "Effects of confinement and environment on the electronic structure and exciton binding energy of MoS2 from first principles," *Physical Review B*, vol. 86, no. 24, p. 241201, 2012.

[132] G. D. Scholes and G. Rumbles, "Excitons in nanoscale systems," in *Materials For Sustainable Energy: A Collection of Peer-Reviewed Research and Review Articles from Nature Publishing Group*, pp. 12–25, World Scientific, 2011.

[133] K. Synnatschke, P. A. Cieslik, A. Harvey, A. Castellanos-Gomez, T. Tian, C.-J. Shih, A. Chernikov, E. J. Santos, J. N. Coleman, and C. Backes, "Length-and Thickness-Dependent Optical Response of Liquid-Exfoliated Transition Metal Dichalcogenides," *Chemistry of Materials*, vol. 31, no. 24, pp. 10049–10062, 2019.

[134] T. Mueller and E. Malic, "Exciton physics and device application of two-dimensional transition metal dichalcogenide semiconductors," *npj 2D Materials and Applications*, vol. 2, no. 1, pp. 1–12, 2018.

[135] A. Chernikov, T. C. Berkelbach, H. M. Hill, A. Rigosi, Y. Li, O. B. Aslan, D. R. Reichman, M. S. Hybertsen, and T. F. Heinz, "Exciton binding energy and nonhydrogenic Rydberg series in monolayer WS2," *Physical Review Letters*, vol. 113, no. 7, p. 076802, 2014.

[136] T. Cheiwchanchamnangij and W. R. Lambrecht, "Quasiparticle band structure calculation of monolayer, bilayer, and bulk MoS2," *Physical Review B*, vol. 85, no. 20, p. 205302, 2012.

[137] R. Miller and D. Kleinman, "Excitons in GaAs quantum wells," *Journal of Luminescence*, vol. 30, no. 1-4, pp. 520–540, 1985.

[138] G. Wang, A. Chernikov, M. M. Glazov, T. F. Heinz, X. Marie, T. Amand, and B. Urbaszek, "Colloquium: Excitons in atomically thin transition metal dichalcogenides," *Reviews of Modern Physics*, vol. 90, no. 2, p. 021001, 2018.

[139] M. M. Ugeda, A. J. Bradley, S.-F. Shi, H. Felipe, Y. Zhang, D. Y. Qiu, W. Ruan, S.-K. Mo, Z. Hussain, Z.-X. Shen, *et al.*, "Giant bandgap renormalization and excitonic effects in a monolayer transition metal dichalcogenide semiconductor," *Nature Materials*, vol. 13, no. 12, pp. 1091–1095, 2014.

[140] M. R. Molas, K. Nogajewski, A. O. Slobodeniuk, J. Binder, M. Bartos, and M. Potemski, "The optical response of monolayer, few-layer and bulk tungsten disulfide," *Nanoscale*, vol. 9, no. 35, pp. 13128–13141, 2017.

[141] R. Frisenda, Y. Niu, P. Gant, A. J. Molina-Mendoza, R. Schmidt, R. Bratschitsch, J. Liu, L. Fu, D. Dumcenco, A. Kis, *et al.*, "Micro-reflectance and transmittance spectroscopy: a versatile and powerful tool to characterize 2D materials," *Journal of Physics D: Applied Physics*, vol. 50, no. 7, p. 074002, 2017.

[142] A. Arora, M. Koperski, K. Nogajewski, J. Marcus, C. Faugeras, and M. Potemski, "Excitonic resonances in thin films of WSe2: from monolayer to bulk material," *Nanoscale*, vol. 7, no. 23, pp. 10421–10429, 2015.

[143] Y. Niu, S. Gonzalez-Abad, R. Frisenda, P. Marauhn, M. Drüppel, P. Gant, R. Schmidt, N. S. Taghavi, D. Barcons, A. J. Molina-Mendoza, *et al.*, "Thickness-dependent differential reflectance spectra of monolayer and few-layer MoS2, MoSe2, WS2 and WSe2," *Nanomaterials*, vol. 8, no. 9, p. 725, 2018.

[144] C. Ruppert, O. B. Aslan, and T. F. Heinz, "Optical properties and band gap of single-and few-layer MoTe2 crystals," *Nano Letters*, vol. 14, no. 11, pp. 6231–6236, 2014.

[145] B. Radisavljevic, A. Radenovic, J. Brivio, V. Giacometti, and A. Kis, "Single-layer MoS2 transistors," *Nature Nanotechnology*, vol. 6, no. 3, pp. 147–150, 2011.

[146] T. F. Jaramillo, K. P. Jørgensen, J. Bonde, J. H. Nielsen, S. Horch, and I. Chorkendorff, "Identification of active edge sites for electrochemical H2 evolution from MoS2 nanocatalysts," *Science*, vol. 317, no. 5834, pp. 100–102, 2007.

[147] E. Gourmelon, O. Lignier, H. Hadouda, G. Couturier, J. Bernède, J. Tedd, J. Pouzet, and J. Salardenne, "MS2 (M= W, Mo) photosensitive thin films for solar cells," *Solar Energy Materials and Solar Cells*, vol. 46, no. 2, pp. 115–121, 1997.

[148] M. Bernardi, M. Palummo, and J. C. Grossman, "Extraordinary sunlight absorption and one nanometer thick photovoltaics using two-dimensional monolayer materials," *Nano Letters*, vol. 13, no. 8, pp. 3664–3670, 2013.

[149] L. Britnell, R. Ribeiro, A. Eckmann, R. Jalil, B. Belle, A. Mishchenko, Y.-J. Kim, R. Gorbachev, T. Georgiou, S. Morozov, *et al.*, "Strong light-matter interactions in heterostructures of atomically thin films," *Science*, vol. 340, no. 6138, pp. 1311–1314, 2013.

[150] J. Wong, D. Jariwala, G. Tagliabue, K. Tat, A. R. Davoyan, M. C. Sherrott, and H. A. Atwater, "High photovoltaic quantum efficiency in ultrathin van der Waals heterostructures," *ACS Nano*, vol. 11, no. 7, pp. 7230–7240, 2017.

[151] K. Chang and W. Chen, "In situ synthesis of MoS2/graphene nanosheet composites with extraordinarily high electrochemical performance for lithium ion batteries," *Chemical Communications*, vol. 47, no. 14, pp. 4252–4254, 2011.

[152] K. Chang and W. Chen, "L-cysteine-assisted synthesis of layered MoS2/graphene composites with excellent electrochemical performances for lithium ion batteries," *ACS Nano*, vol. 5, no. 6, pp. 4720–4728, 2011.

[153] Y. Liu, X. He, D. Hanlon, A. Harvey, U. Khan, Y. Li, and J. N. Coleman, "Electrical, mechanical, and capacity percolation leads to high-performance MoS2/nanotube composite lithium ion battery electrodes," *ACS Nano*, vol. 10, no. 6, pp. 5980–5990, 2016.

[154] J. Williams, L. DiCarlo, and C. Marcus, "Quantum Hall effect in a gate-controlled pn junction of graphene," *Science*, vol. 317, no. 5838, pp. 638–641, 2007.

[155] J.-U. Lee, D. Yoon, H. Kim, S. W. Lee, and H. Cheong, "Thermal conductivity of suspended pristine graphene measured by Raman spectroscopy," *Physical Review B*, vol. 83, no. 8, p. 081419, 2011.

[156] M. Fontana, T. Deppe, A. K. Boyd, M. Rinzan, A. Y. Liu, M. Paranjape, and P. Barbara, "Electron-hole transport and photovoltaic effect in gated MoS2 Schottky junctions," *Scientific Reports*, vol. 3, p. 1634, 2013.

[157] D. MacNeill, G. Stiehl, M. Guimaraes, R. Buhrman, J. Park, and D. Ralph, "Control of spin–orbit torques through crystal symmetry in WTe2/ferromagnet bilayers," *Nature Physics*, vol. 13, no. 3, pp. 300–305, 2017.

[158] A. C. Jones and M. L. Hitchman, *Chemical vapour deposition: precursors, processes and applications*. London: Royal Society of Chemistry, 2009.

[159] Q. Yu, J. Lian, S. Siriponglert, H. Li, Y. P. Chen, and S.-S. Pei, "Graphene segregated on Ni surfaces and transferred to insulators," *Applied Physics Letters*, vol. 93, no. 11, p. 113103, 2008.

[160] L. G. De Arco, Y. Zhang, A. Kumar, and C. Zhou, "Synthesis, transfer, and devices of single- and few-layer graphene by chemical vapor deposition," *IEEE Transactions on Nanotechnology*, vol. 8, no. 2, pp. 135–138, 2009.

[161] A. Reina, X. Jia, J. Ho, D. Nezich, H. Son, V. Bulovic, M. S. Dresselhaus, and J. Kong, "Large area, few-layer graphene films on arbitrary substrates by chemical vapor deposition," *Nano Letters*, vol. 9, no. 1, pp. 30–35, 2009.

[162] X. Li, C. W. Magnuson, A. Venugopal, J. An, J. W. Suk, B. Han, M. Borysiak, W. Cai, A. Velamakanni, Y. Zhu, *et al.*, "Graphene films with large domain size by a two-step chemical vapor deposition process," *Nano Letters*, vol. 10, no. 11, pp. 4328–4334, 2010.

[163] Y. Zhan, Z. Liu, S. Najmaei, P. M. Ajayan, and J. Lou, "Large-area vapor-phase growth and characterization of MoS2 atomic layers on a SiO2 substrate," *Small*, vol. 8, no. 7, pp. 966–971, 2012.

[164] J.-H. Lee, E. K. Lee, W.-J. Joo, Y. Jang, B.-S. Kim, J. Y. Lim, S.-H. Choi, S. J. Ahn, J. R. Ahn, M.-H. Park, *et al.*, "Wafer-scale growth of single-crystal monolayer graphene on reusable hydrogen-terminated germanium," *Science*, vol. 344, no. 6181, pp. 286–289, 2014.

[165] K. Kang, S. Xie, L. Huang, Y. Han, P. Y. Huang, K. F. Mak, C.-J. Kim, D. Muller, and J. Park, "High-mobility three-atom-thick semiconducting films with wafer-scale homogeneity," *Nature*, vol. 520, no. 7549, pp. 656–660, 2015.

[166] S. Tongay, W. Fan, J. Kang, J. Park, U. Koldemir, J. Suh, D. S. Narang, K. Liu, J. Ji, J. Li, *et al.*, "Tuning interlayer coupling in large-area heterostructures with CVD-grown MoS2 and WS2 monolayers," *Nano Letters*, vol. 14, no. 6, pp. 3185–3190, 2014.

[167] J. W. Suk, A. Kitt, C. W. Magnuson, Y. Hao, S. Ahmed, J. An, A. K. Swan, B. B. Goldberg, and R. S. Ruoff, "Transfer of CVD-grown monolayer graphene onto arbitrary substrates," *ACS Nano*, vol. 5, no. 9, pp. 6916–6924, 2011.

[168] G. Bacon, "The reduction of the crystalline perfection of graphite by grinding," *Acta Crystallographica*, vol. 5, no. 3, pp. 392–392, 1952.

[169] H. Gasparoux and B. Lambert, "Etude de la cinetique de guerison des defauts crees dans un graphite par broyage," *Carbon*, vol. 8, no. 5, pp. 573–586, 1970.

[170] D. Chaira and S. K. Karak, "Fabrication of nanostructured materials by mechanical milling," *Handbook of Mechanical Nanostructuring*, pp. 379–416, 2015.

[171] H. Zhang, L. B. Kong, H. L.-W. Chan, C.-L. Mak, X. Yao, Y. Wang, and Z. Chen, "Hybrid Processing of Electroceramic Composites Involving High-Energy Ball Milling," *Handbook of Mechanical Nanostructuring*, pp. 577–611, 2015.

[172] L. H. Li, Y. Chen, G. Behan, H. Zhang, M. Petravic, and A. M. Glushenkov, "Large-scale mechanical peeling of boron nitride nanosheets by low-energy ball milling," *Journal of Materials Chemistry*, vol. 21, no. 32, pp. 11862–11866, 2011.

[173] H. Wu, W. Zhao, H. Hu, and G. Chen, "One-step in situ ball milling synthesis of polymer-functionalized graphene nanocomposites," *Journal of Materials Chemistry*, vol. 21, no. 24, pp. 8626–8632, 2011.

[174] Z. Wu, B. Fang, A. Bonakdarpour, A. Sun, D. P. Wilkinson, and D. Wang, "WS2 nanosheets as a highly efficient electrocatalyst for hydrogen evolution reaction," *Applied Catalysis B: Environmental*, vol. 125, pp. 59–66, 2012.

[175] A. Ambrosi, X. Chia, Z. Sofer, and M. Pumera, "Enhancement of electrochemical and catalytic properties of MoS2 through ball-milling," *Electrochemistry Communications*, vol. 54, pp. 36–40, 2015.

[176] V. Nicolosi, M. Chhowalla, M. G. Kanatzidis, M. S. Strano, and J. N. Coleman, "Liquid exfoliation of layered materials," *Science*, vol. 340, no. 6139, p. 1226419, 2013.

[177] G. Eda, H. Yamaguchi, D. Voiry, T. Fujita, M. Chen, and M. Chhowalla, "Photoluminescence from chemically exfoliated MoS2," *Nano Letters*, vol. 11, no. 12, pp. 5111–5116, 2011.

[178] K. C. Knirsch, N. C. Berner, H. C. Nerl, C. S. Cucinotta, Z. Gholamvand, N. McEvoy, Z. Wang, I. Abramovic, P. Vecera, M. Halik, *et al.*, "Basal-plane functionalization of chemically exfoliated molybdenum disulfide by diazonium salts," *ACS Nano*, vol. 9, no. 6, pp. 6018–6030, 2015.

[179] E. Benavente, M. A. Santa Ana, F. Mendizábal, and G. González, "Intercalation chemistry of molybdenum disulfide," *Coordination Chemistry Reviews*, vol. 224, no. 1-2, pp. 87–109, 2002.

[180] J. M. Englert, C. Dotzer, G. Yang, M. Schmid, C. Papp, J. M. Gottfried, H.-P. Steinrück, E. Spiecker, F. Hauke, and A. Hirsch, "Covalent bulk functionalization of graphene," *Nature Chemistry*, vol. 3, no. 4, p. 279, 2011.

[181] X. Fan, P. Xu, D. Zhou, Y. Sun, Y. C. Li, M. A. T. Nguyen, M. Terrones, and T. E. Mallouk, "Fast and efficient preparation of exfoliated 2H MoS2 nanosheets by sonication-assisted lithium intercalation and infrared laser-induced 1T to 2H phase reversion," *Nano Letters*, vol. 15, no. 9, pp. 5956–5960, 2015.

[182] S. Kajiyama, L. Szabova, K. Sodeyama, H. Iinuma, R. Morita, K. Gotoh, Y. Tateyama, M. Okubo, and A. Yamada, "Sodium-ion intercalation mechanism in MXene nanosheets," *ACS Nano*, vol. 10, no. 3, pp. 3334–3341, 2016.

[183] A. Y. S. Eng, A. Ambrosi, Z. Sofer, P. Simek, and M. Pumera, "Electrochemistry of transition metal dichalcogenides: strong dependence on the metal-to-chalcogen composition and exfoliation method," *ACS Nano*, vol. 8, no. 12, pp. 12185–12198, 2014.

[184] S. Ida, D. Shiga, M. Koinuma, and Y. Matsumoto, "Synthesis of hexagonal nickel hydroxide nanosheets by exfoliation of layered nickel hydroxide intercalated with dodecyl sulfate ions," *Journal of the American Chemical Society*, vol. 130, no. 43, pp. 14038–14039, 2008.

[185] C. R. Ryder, J. D. Wood, S. A. Wells, Y. Yang, D. Jariwala, T. J. Marks, G. C. Schatz, and M. C. Hersam, "Covalent functionalization and passivation of exfoliated black phosphorus via aryl diazonium chemistry," *Nature Chemistry*, vol. 8, no. 6, pp. 597–602, 2016.

[186] Z. Ding, S. K. Bux, D. J. King, F. L. Chang, T.-H. Chen, S.-C. Huang, and R. B. Kaner, "Lithium intercalation and exfoliation of layered bismuth selenide and bismuth telluride," *Journal of Materials Chemistry*, vol. 19, no. 17, pp. 2588–2592, 2009.

[187] A. Kumar, A. L. M. Reddy, A. Mukherjee, M. Dubey, X. Zhan, N. Singh, L. Ci, W. E. Billups, J. Nagurny, G. Mital, *et al.*, "Direct synthesis of lithium-intercalated graphene for electrochemical energy storage application," *ACS Nano*, vol. 5, no. 6, pp. 4345–4349, 2011.

[188] R. Ma and T. Sasaki, "Nanosheets of oxides and hydroxides: Ultimate 2D charge-bearing functional crystallites," *Advanced materials*, vol. 22, no. 45, pp. 5082–5104, 2010.

[189] G. Walker and W. Garrett, "Chemical exfoliation of vermiculite and the production of colloidal dispersions," *Science*, vol. 156, no. 3773, pp. 385–387, 1967.

[190] M. Lotya, Y. Hernandez, P. J. King, R. J. Smith, V. Nicolosi, L. S. Karlsson, F. M. Blighe, S. De, Z. Wang, I. McGovern, *et al.*, "Liquid phase production of graphene by exfoliation of graphite in surfactant/water solutions," *Journal of the American Chemical Society*, vol. 131, no. 10, pp. 3611–3620, 2009.

[191] A. Harvey, C. Backes, Z. Gholamvand, D. Hanlon, D. McAteer, H. C. Nerl, E. McGuire, A. Seral-Ascaso, Q. M. Ramasse, N. McEvoy, *et al.*, "Preparation of gallium sulfide nanosheets by liquid exfoliation and their application as hydrogen evolution catalysts," *Chemistry of Materials*, vol. 27, no. 9, pp. 3483–3493, 2015.

[192] A. Griffin, A. Harvey, B. Cunningham, D. Scullion, T. Tian, C.-J. Shih, M. Gruening, J. F. Donegan, E. J. Santos, C. Backes, *et al.*, "Spectroscopic size and thickness metrics for liquid-exfoliated h-BN," *Chemistry of Materials*, vol. 30, no. 6, pp. 1998–2005, 2018.

[193] J. B. Boland, R. Tian, A. Harvey, V. Vega-Mayoral, A. Griffin, D. V. Horvath, C. Gabbett, M. Breshears, J. Pepper, Y. Li, *et al.*, "Liquid phase exfoliation of GeS nanosheets in ambient conditions for lithium ion battery applications," *2D Materials*, vol. 7, no. 3, p. 035015, 2020.

[194] L. van Wijngaarden, "Mechanics of collapsing cavitation bubbles," *Ultrasonics sonochemistry*, vol. 29, pp. 524–527, 2016.

[195] S.-W. Ohl, E. Klaseboer, and B. C. Khoo, "Bubbles with shock waves and ultrasound: a review," *Interface focus*, vol. 5, no. 5, p. 20150019, 2015.

[196] J. N. Coleman, "Liquid exfoliation of defect-free graphene," *Accounts of Chemical Research*, vol. 46, no. 1, pp. 14–22, 2013.

[197] F. Bonaccorso and Z. Sun, "Solution processing of graphene, topological insulators and other 2d crystals for ultrafast photonics," *Optical Materials Express*, vol. 4, no. 1, pp. 63–78, 2014.

[198] C. Backes, T. M. Higgins, A. Kelly, C. Boland, A. Harvey, D. Hanlon, and J. N. Coleman, "Guidelines for exfoliation, characterization and processing of layered materials produced by liquid exfoliation," *Chemistry of Materials*, vol. 29, no. 1, pp. 243–255, 2017.

[199] Z. Li, R. J. Young, C. Backes, W. Zhao, X. Zhang, A. A. Zhukov, E. Tillotson, A. P. Conlan, F. Ding, S. J. Haigh, *et al.*, "Mechanisms of liquid-phase exfoliation for the production of graphene," *ACS nano*, vol. 14, no. 9, pp. 10976–10985, 2020.

[200] M. Yi and Z. Shen, "A review on mechanical exfoliation for the scalable production of graphene," *Journal of Materials Chemistry A*, vol. 3, no. 22, pp. 11700–11715, 2015.

[201] L.-J. Ji, Y. Qin, D. Gui, W. Li, Y. Li, X. Li, and P. Lu, "Quantifying the Exfoliation Ease Level of 2D Materials via Mechanical Anisotropy," *Chemistry of Materials*, vol. 30, no. 24, pp. 8732–8738, 2018.

[202] C. Backes, D. Campi, B. M. Szydłowska, K. Synnatschke, E. Ojala, F. Rashvand, A. Harvey, A. Griffin, Z. Sofer, N. Marzari, *et al.*, "Equipartition of Energy Defines the Size-Thickness Relationship in Liquid-Exfoliated Nanosheets," *ACS Nano*, 2019.

[203] K. Kouroupis-Agalou, A. Liscio, E. Treossi, L. Ortolani, V. Morandi, N. M. Pugno, and V. Palermo, "Fragmentation and exfoliation of 2-dimensional materials: a statistical approach," *Nanoscale*, vol. 6, no. 11, pp. 5926–5933, 2014.

[204] P. Turner, M. Hodnett, R. Dorey, and J. D. Carey, "Controlled sonication as a route to in-situ graphene flake size control," *Scientific Reports*, vol. 9, no. 1, pp. 1–8, 2019.

[205] Z. Y. Xia, S. Pezzini, E. Treossi, G. Giambastiani, F. Corticelli, V. Morandi, A. Zanelli, V. Bellani, and V. Palermo, "The exfoliation of graphene in liquids by electrochemical, chemical, and sonication-assisted techniques: A nanoscale study," *Advanced Functional Materials*, vol. 23, no. 37, pp. 4684–4693, 2013.

[206] A. Liscio, K. Kouroupis-Agalou, X. D. Betriu, A. Kovtun, E. Treossi, N. M. Pugno, G. De Luca, L. Giorgini, and V. Palermo, "Evolution of the size and shape of 2D nanosheets during ultrasonic fragmentation," *2D Materials*, vol. 4, no. 2, p. 025017, 2017.

[207] C. E. Halbig, T. J. Nacken, J. Walter, C. Damm, S. Eigler, and W. Peukert, "Quantitative investigation of the fragmentation process and defect density evolution of oxo-functionalized graphene due to ultrasonication and milling," *Carbon*, vol. 96, pp. 897–903, 2016.

[208] A. Alaferdov, A. Gholamipour-Shirazi, M. Canesqui, Y. A. Danilov, and S. Moshkalev, "Size-controlled synthesis of graphite nanoflakes and multi-layer graphene by liquid phase exfoliation of natural graphite," *Carbon*, vol. 69, pp. 525–535, 2014.

[209] S. Barwich, U. Khan, and J. N. Coleman, "A technique to pretreat graphite which allows the rapid dispersion of defect-free graphene in solvents at high concentration," *The Journal of Physical Chemistry C*, vol. 117, no. 37, pp. 19212–19218, 2013.

[210] X. Zhang, Z. Sui, B. Xu, S. Yue, Y. Luo, W. Zhan, and B. Liu, "Mechanically strong and highly conductive graphene aerogel and its use as electrodes for electrochemical power sources," *Journal of Materials Chemistry*, vol. 21, no. 18, pp. 6494–6497, 2011.

[211] F. Torrisi, T. Hasan, W. Wu, Z. Sun, A. Lombardo, T. S. Kulmala, G.-W. Hsieh, S. Jung, F. Bonaccorso, P. J. Paul, *et al.*, "Inkjet-printed graphene electronics," *ACS Nano*, vol. 6, no. 4, pp. 2992–3006, 2012.

[212] D. J. Finn, M. Lotya, G. Cunningham, R. J. Smith, D. McCloskey, J. F. Donegan, and J. N. Coleman, "Inkjet deposition of liquid-exfoliated graphene and MoS 2 nanosheets for printed device applications," *Journal of Materials Chemistry C*, vol. 2, no. 5, pp. 925–932, 2014.

[213] B. Mendoza-Sánchez, J. Coelho, A. Pokle, and V. Nicolosi, "A 2D graphene-manganese oxide nanosheet hybrid synthesized by a single step liquid-phase co-exfoliation method for supercapacitor applications," *Electrochimica Acta*, vol. 174, pp. 696–705, 2015.

[214] Q. He, Z. Zeng, Z. Yin, H. Li, S. Wu, X. Huang, and H. Zhang, "Fabrication of flexible MoS2 thin-film transistor arrays for practical gas-sensing applications," *Small*, vol. 8, no. 19, pp. 2994–2999, 2012.

[215] K. R. Paton, E. Varrla, C. Backes, R. J. Smith, U. Khan, A. O'Neill, C. Boland, M. Lotya, O. M. Istrate, P. King, *et al.*, "Scalable production of large quantities of defect-free few-layer graphene by shear exfoliation in liquids," *Nature Materials*, vol. 13, no. 6, pp. 624–630, 2014.

[216] H. Li, L. Jing, W. Liu, J. Lin, R. Y. Tay, S. H. Tsang, and E. H. T. Teo, "Scalable production of few-layer boron sheets by liquid-phase exfoliation and their superior supercapacitive performance," *ACS Nano*, vol. 12, no. 2, pp. 1262–1272, 2018.

[217] G. Cunningham, D. Hanlon, N. McEvoy, G. S. Duesberg, and J. N. Coleman, "Large variations in both dark-and photoconductivity in nanosheet networks as nanomaterial is varied from MoS2 to WTe2," *Nanoscale*, vol. 7, no. 1, pp. 198–208, 2015.

[218] C. Wu, F. Li, W. Wu, W. Chen, and T. Guo, "Liquid-phase exfoliation of chemical vapor deposition-grown single layer graphene and its application in solution-processed transparent electrodes for flexible organic light-emitting devices," *Applied Physics Letters*, vol. 105, no. 24, p. 243509, 2014.

[219] S. Xie, O. M. Istrate, P. May, S. Barwich, A. P. Bell, U. Khan, and J. N. Coleman, "Boron nitride nanosheets as barrier enhancing fillers in melt processed composites," *Nanoscale*, vol. 7, no. 10, pp. 4443–4450, 2015.

[220] J. Biscarat, M. Bechelany, C. Pochat-Bohatier, and P. Miele, "Graphene-like BN/gelatin nanobiocomposites for gas barrier applications," *Nanoscale*, vol. 7, no. 2, pp. 613–618, 2015.

[221] S. Biccai, C. S. Boland, D. P. O'Driscoll, A. Harvey, C. Gabbett, D. R. O'Suilleabhain, A. J. Griffin, Z. Li, R. J. Young, and J. N. Coleman, "Negative gauge factor piezoresistive composites based on polymers filled with MoS2 nanosheets," *ACS Nano*, vol. 13, no. 6, pp. 6845–6855, 2019.

[222] J. Sun, H.-W. Lee, M. Pasta, H. Yuan, G. Zheng, Y. Sun, Y. Li, and Y. Cui, "A phosphorene–graphene hybrid material as a high-capacity anode for sodium-ion batteries," *Nature Nanotechnology*, vol. 10, no. 11, p. 980, 2015.

[223] J. M. Hughes, D. Aherne, and J. N. Coleman, "Generalizing solubility parameter theory to apply to one-and two-dimensional solutes and to incorporate dipolar interactions," *Journal of Applied Polymer Science*, vol. 127, no. 6, pp. 4483–4491, 2013.

[224] W. Cao, J. Wang, and M. Ma, "Exfoliation of two-dimensional materials: the role of entropy," *The Journal of Physical Chemistry Letters*, vol. 10, no. 5, pp. 981–986, 2019.

[225] M. L. Huggins, "Solutions of long chain compounds," *The Journal of Chemical Physics*, vol. 9, no. 5, pp. 440–440, 1941.

[226] P. J. Flory, "Thermodynamics of high polymer solutions," *The Journal of Chemical Physics*, vol. 10, no. 1, pp. 51–61, 1942.

[227] J. N. Coleman, "Liquid-phase exfoliation of nanotubes and graphene," *Advanced Functional Materials*, vol. 19, no. 23, pp. 3680–3695, 2009.

[228] J. H. Hildebrand and R. Scott, "Solubility of Non-electrolytes," 1950.

[229] C. M. Hansen, *Hansen solubility parameters: A user's handbook*. CRC Press, 2 ed., 2007.

[230] J. L. Gardon, "Critical review of concepts common to cohesive energy density, surface tension, tensile strength, heat of mixing, interfacial tension, and butt joint strength," *Journal of Colloid and Interface Science*, vol. 59, no. 3, pp. 582–596, 1977.

[231] D. Mathieu, "Pencil and Paper Estimation of Hansen Solubility Parameters," *ACS omega*, vol. 3, no. 12, pp. 17049–17056, 2018.

[232] M. J. Rosen and J. T. Kunjappu, *Surfactants and interfacial phenomena*. Hoboken, New Jersey: John Wiley & Sons, 3 ed., 2004.

[233] J. N. Israelachvili, *Intermolecular and surface forces*. San Diego: Academic press, 3 ed., 2011.

[234] E. Ruckenstein and R. Nagarajan, "Critical micelle concentration. Transition point for micellar size distribution," *The Journal of Physical Chemistry*, vol. 79, no. 24, pp. 2622–2626, 1975.

[235] H. V. Helmholtz, "Studien über electrische Grenzschichten," *Annalen der Physik*, vol. 243, no. 7, pp. 337–382, 1879.

[236] M. Gouy, "Sur la constitution de la charge électrique à la surface d'un électrolyte," *Journal of Theoretical and Applied Physics*, vol. 9, no. 1, pp. 457–468, 1910.

[237] G. Gouy, "Sur la fonction électrocapillaire," in *Annales de physique*, vol. 9, pp. 129–184, 1917.

[238] D. L. Chapman, "LI. A contribution to the theory of electrocapillarity," *The London, Edinburgh, and Dublin Philosophical Magazine and Journal of Science*, vol. 25, no. 148, pp. 475–481, 1913.

[239] O. Stern, "Zur theorie der elektrolytischen doppelschicht," *Zeitschrift für Elektrochemie und angewandte physikalische Chemie*, vol. 30, no. 21-22, pp. 508–516, 1924.

[240] B. Derjaguin and L. Landau, "The theory of stability of highly charged lyophobic sols and coalescence of highly charged particles in electrolyte solutions," *Acta Physicochim. URSS*, vol. 14, no. 633-52, p. 58, 1941.

[241] J. T. G. Overbeek and E. Verwey, *Theory of the Stability of Lyophobic Colloids: The interaction of Sol Particles Having an Electric Double Layer*. Amsterdam: Elsevier, 1 ed., 1948.

[242] H. Hamaker, "The London—van der Waals attraction between spherical particles," *Physica*, vol. 4, no. 10, pp. 1058–1072, 1937.

[243] C.-R. Hsing, C. Cheng, J.-P. Chou, C.-M. Chang, and C.-M. Wei, "Van der Waals interaction in a boron nitride bilayer," *New Journal of Physics*, vol. 16, no. 11, p. 113015, 2014.

[244] N. Rathod and S. G. Hatzikiriakos, "The effect of surface energy of boron nitride on polymer processability," *Polymer Engineering & Science*, vol. 44, no. 8, pp. 1543–1550, 2004.

[245] P. Debye, "The theory of electrolytes I. The lowering of the freezing point and related occurrences," *Physikalische Zeitschrift*, vol. 24, pp. 185–206, 1923.

[246] R. J. Smith, M. Lotya, and J. N. Coleman, "The importance of repulsive potential barriers for the dispersion of graphene using surfactants," *New Journal of Physics*, vol. 12, no. 12, p. 125008, 2010.

[247] F. P. Capote and M. L. De Castro, *Analytical applications of ultrasound*. Amsterdam: Elsevier, 2007.

[248] T. J. Mason and J. P. Lorimer, *Applied Sonochemistry: the Uses of Power Ultrasound in Chemistry and Processing*. Weinheim: Wiley-VCH, 2002.

[249] J.-L. Capelo-Martínez, *Ultrasound in chemistry: analytical applications*. Weinheim: Wiley-VCH, 2009.

[250] G. Yang, J.-J. Zhu, K. Okitsu, Y. Mizukoshi, B. M. Teo, N. Enomoto, S. G. Babu, B. Neppolian, M. Ashokkumar, S. Shaik, *et al.*, *Handbook of ultrasonics and sonochemistry*. Singapore: Springer Nature, 2016.

[251] K. S. Suslick and G. J. Price, "Applications of ultrasound to materials chemistry," *Annual Review of Materials Science*, vol. 29, no. 1, pp. 295–326, 1999.

[252] H. Briggs, J. Johnson, and W. Mason, "Properties of liquids at high sound pressure," *The Journal of the Acoustical Society of America*, vol. 19, no. 4, pp. 664–677, 1947.

[253] Sonics and Materials Inc., "Vcx 500 / vcx 750, ultrasonic processors for small and medium volume applications." https://www.sonics.com/liquid-processing/products/vibra-cell-processors/vcx-500-vcx-750/, 2020. [Online; accessed 2-June-2020].

[254] G. J. Kynch, "A theory of sedimentation," *Transactions of the Faraday society*, vol. 48, pp. 166–176, 1952.

[255] J. M. Graham *et al.*, *Biological centrifugation*. Oxford: Bios, 2001.

[256] O. Akbulut, C. R. Mace, R. V. Martinez, A. A. Kumar, Z. Nie, M. R. Patton, and G. M. Whitesides, "Separation of nanoparticles in aqueous multiphase systems through centrifugation," *Nano Letters*, vol. 12, no. 8, pp. 4060–4064, 2012.

[257] W. Mächtle and L. Börger, *Analytical ultracentrifugation of polymers and nanoparticles*. Berlin: Springer Science & Business Media, 2006.

[258] J. B. Hubbard and J. F. Douglas, "Hydrodynamic friction of arbitrarily shaped Brownian particles," *Physical Review E*, vol. 47, no. 5, p. R2983, 1993.

[259] B. Clark, T. Frost, and M. Russellm, *UV spectroscopy Techniques, instrumentation, data handling, 1993*. 1993.

[260] T. Owen, *Fundamentals of modern UV-visible spectroscopy: A Primer*. Berlin: Agilent Technologies, 2000.

[261] D. F. Swinehart, "The Beer-Lambert law," *Journal of Chemical Education*, vol. 39, no. 7, p. 333, 1962.

[262] K. Suzuki, A. Kobayashi, S. Kaneko, K. Takehira, T. Yoshihara, H. Ishida, Y. Shiina, S. Oishi, and S. Tobita, "Reevaluation of absolute luminescence quantum yields of standard solutions using a spectrometer with an integrating sphere and a back-thinned CCD detector," *Physical Chemistry Chemical Physics*, vol. 11, no. 42, pp. 9850–9860, 2009.

[263] S. Leyre, E. Coutino-Gonzalez, J. Joos, J. Ryckaert, Y. Meuret, D. Poelman, P. Smet, G. Durinck, J. Hofkens, G. Deconinck, *et al.*, "Absolute determination of photoluminescence quantum efficiency using an integrating sphere setup," *Review of Scientific Instruments*, vol. 85, no. 12, p. 123115, 2014.

[264] A. Harvey, C. Backes, J. B. Boland, X. He, A. Griffin, B. Szydlowska, C. Gabbett, J. F. Donegan, and J. N. Coleman, "Non-resonant light scattering in dispersions of 2D nanosheets," *Nature Communications*, vol. 9, no. 1, pp. 1–11, 2018.

[265] J. W. Strutt, "LVIII. On the scattering of light by small particles," *The London, Edinburgh, and Dublin Philosophical Magazine and Journal of Science*, vol. 41, no. 275, pp. 447–454, 1871.

[266] G. Mie, "Beiträge zur Optik trüber Medien, speziell kolloidaler Metallösungen," *Annalen der physik*, vol. 330, no. 3, pp. 377–445, 1908.

[267] M. Born and E. Wolf, *Principles of optics: Electromagnetic theory of propagation, interference and diffraction of light*. Cambridge: Cambridge University Press, 7 ed., 1999.

[268] H. C. Hulst and H. C. van de Hulst, *Light scattering by small particles*. New York: Dover Publications, 1981.

[269] R. L. McCreery, *Raman spectroscopy for chemical analysis*, vol. 225. New York: John Wiley & Sons, 2005.

[270] P. Larkin, *Infrared and Raman spectroscopy: principles and spectral interpretation*. San Diego: Elsevier, 2 ed., 2017.

[271] G. Herzberg, *Molecular Spectra and Molecular Structure: Infrared and Raman spectra of polyatomic molecules*, vol. 2. New York: Van Nostrand Company, 1 ed., 1945.

[272] G. Haugstad, *Atomic force microscopy: Understanding basic modes and advanced applications*. Hoboken, New Jersey: John Wiley & Sons, 2012.

[273] B. Voigtländer, *Scanning probe microscopy: Atomic force microscopy and scanning tunneling microscopy*. 2015.

[274] P. Eaton and P. West, *Atomic Force Microscopy*. Oxford: Oxford University Press, 2010.

[275] P. Nemes-Incze, Z. Osváth, K. Kamarás, and L. Biró, "Anomalies in thickness measurements of graphene and few layer graphite crystals by tapping mode atomic force microscopy," *Carbon*, vol. 46, no. 11, pp. 1435–1442, 2008.

[276] P. Hu, L. Wang, M. Yoon, J. Zhang, W. Feng, X. Wang, Z. Wen, J. C. Idrobo, Y. Miyamoto, D. B. Geohegan, *et al.*, "Highly responsive ultrathin GaS nanosheet photodetectors on rigid and flexible substrates," *Nano Letters*, vol. 13, no. 4, pp. 1649–1654, 2013.

[277]

[278] L. Rayleigh, "XV. On the theory of optical images, with special reference to the microscope," *The London, Edinburgh, and Dublin Philosophical Magazine and Journal of Science*, vol. 42, no. 255, pp. 167–195, 1896.

[279] D. B. Murphy, *Fundamentals of light microscopy and electronic imaging*. New York: John Wiley & Sons, 2002.

[280] D. B. Williams and C. B. Carter, "The transmission electron microscope," in *Transmission electron microscopy*, pp. 3–17, New York: Springer, 1996.

[281] B. Fultz and J. M. Howe, *Transmission electron microscopy and diffractometry of materials*. Berlin: Springer, 3 ed., 2012.

[282] C. Hetherington, "Aberration correction for TEM," *Materials Today*, vol. 7, no. 12, pp. 50–55, 2004.

[283] D. Shindo and T. Oikawa, *Analytical electron microscopy for materials science*. 2002.

[284] J. C. Russ, *Fundamentals of Energy Dispersive X-Ray Analysis: Butterworths Monographs in Materials*. London: Butterworth-Heinemann, 2013.

[285] J. I. Goldstein, D. E. Newbury, J. R. Michael, N. W. Ritchie, J. H. J. Scott, and D. C. Joy, *Scanning electron microscopy and X-ray microanalysis*. New York: Springer, 4 ed., 2018.

[286] W. Zhou and Z. L. Wang, *Scanning microscopy for nanotechnology: Techniques and applications*. New York: Springer, 2007.

[287] M. Kaszuba, J. Corbett, F. M. Watson, and A. Jones, "High-concentration zeta potential measurements using light-scattering techniques," *Philosophical Transactions of the Royal Society A: Mathematical, Physical and Engineering Sciences*, vol. 368, no. 1927, pp. 4439–4451, 2010.

[288] R. J. Hunter, *Zeta potential in colloid science: principles and applications*. London: Academic Press, 3 ed., 1988.

[289] E. Varrla, C. Backes, K. R. Paton, A. Harvey, Z. Gholamvand, J. McCauley, and J. N. Coleman, "Large-scale production of size-controlled MoS2 nanosheets by shear exfoliation," *Chemistry of Materials*, vol. 27, no. 3, pp. 1129–1139, 2015.

[290] I. Tucker, J. Corbett, J. Fatkin, R. Jack, M. Kaszuba, B. MacCreath, and F. McNeil-Watson, "Laser Doppler Electrophoresis applied to colloids and surfaces," *Current Opinion in Colloid & Interface Science*, vol. 20, no. 4, pp. 215–226, 2015.

[291] D. Henry, "The cataphoresis of suspended particles. Part I.—The equation of cataphoresis," *Proceedings of the Royal Society of London. Series A, Containing Papers of a Mathematical and Physical Character*, vol. 133, no. 821, pp. 106–129, 1931.

[292] M. v. Smoluchowski, "Handbuch der Elektrizität und des Magnetismus," *Band II, Barth-Verlag, Leipzig*, pp. 366–427, 1921.

[293] C. Lee, H. Yan, L. E. Brus, T. F. Heinz, J. Hone, and S. Ryu, "Anomalous lattice vibrations of single-and few-layer MoS2," *ACS Nano*, vol. 4, no. 5, pp. 2695–2700, 2010.

[294] D. Golberg, Y. Bando, Y. Huang, T. Terao, M. Mitome, C. Tang, and C. Zhi, "Boron nitride nanotubes and nanosheets," *ACS Nano*, vol. 4, no. 6, pp. 2979–2993, 2010.

[295] L. Schué, B. Berini, A. C. Betz, B. Plaçais, F. Ducastelle, J. Barjon, and A. Loiseau, "Dimensionality effects on the luminescence properties of hBN," *Nanoscale*, vol. 8, no. 13, pp. 6986–6993, 2016.

[296] S. Yamamura, M. Takata, and M. Sakata, "Charge density of hexagonal boron nitride using synchrotron radiation powder data by maximum entropy method," *Journal of Physics and Chemistry of Solids*, vol. 58, no. 2, pp. 177–183, 1997.

[297] N. Ooi, A. Rairkar, L. Lindsley, and J. Adams, "Electronic structure and bonding in hexagonal boron nitride," *Journal of Physics: Condensed Matter*, vol. 18, no. 1, p. 97, 2005.

[298] Y. K. Yap, *BCN nanotubes and related nanostructures*, vol. 6. New York: Springer, 2009.

[299] K. Watanabe, T. Taniguchi, and H. Kanda, "Direct-bandgap properties and evidence for ultraviolet lasing of hexagonal boron nitride single crystal," *Nature Materials*, vol. 3, no. 6, p. 404, 2004.

[300] X. Cui, G.-H. Lee, Y. D. Kim, G. Arefe, P. Y. Huang, C.-H. Lee, D. A. Chenet, X. Zhang, L. Wang, F. Ye, *et al.*, "Multi-terminal transport measurements of MoS2 using a van der Waals heterostructure device platform," *Nature Nanotechnology*, vol. 10, no. 6, pp. 534–540, 2015.

[301] C. R. Dean, A. F. Young, I. Meric, C. Lee, L. Wang, S. Sorgenfrei, K. Watanabe, T. Taniguchi, P. Kim, K. L. Shepard, *et al.*, "Boron nitride substrates for high-quality graphene electronics," *Nature Nanotechnology*, vol. 5, no. 10, pp. 722–726, 2010.

[302] S. Roth, F. Matsui, T. Greber, and J. Osterwalder, "Chemical vapor deposition and characterization of aligned and incommensurate graphene/hexagonal boron nitride heterostack on Cu (111)," *Nano Letters*, vol. 13, no. 6, pp. 2668–2675, 2013.

[303] C. Palacios-Berraquero, M. Barbone, D. M. Kara, X. Chen, I. Goykhman, D. Yoon, A. K. Ott, J. Beitner, K. Watanabe, T. Taniguchi, *et al.*, "Atomically thin quantum light-emitting diodes," *Nature Communications*, vol. 7, p. 12978, 2016.

[304] C. Zhi, Y. Bando, C. Tang, H. Kuwahara, and D. Golberg, "Large-scale fabrication of boron nitride nanosheets and their utilization in polymeric composites with improved thermal and mechanical properties," *Advanced Materials*, vol. 21, no. 28, pp. 2889–2893, 2009.

[305] J. Taha-Tijerina, T. N. Narayanan, G. Gao, M. Rohde, D. A. Tsentalovich, M. Pasquali, and P. M. Ajayan, "Electrically insulating thermal nano-oils using 2D fillers," *ACS Nano*, vol. 6, no. 2, pp. 1214–1220, 2012.

[306] D. Nečas and P. Klapetek, "Gwyddion: an open-source software for SPM data analysis," *Open Physics*, vol. 10, no. 1, pp. 181–188, 2012.

[307] M. Xu, D. Fujita, H. Chen, and N. Hanagata, "Formation of monolayer and few-layer hexagonal boron nitride nanosheets via surface segregation," *Nanoscale*, vol. 3, no. 7, pp. 2854–2858, 2011.

[308] Y. Wang, C. Zhou, W. Wang, and Y. Zhao, "Preparation of two dimensional atomic crystals BN, WS2, and MoS2 by supercritical CO2 assisted with ultrasound," *Industrial & Engineering Chemistry Research*, vol. 52, no. 11, pp. 4379–4382, 2013.

[309] M. Rubinstein and R. H. Colby, *Polymer physics*, vol. 23. Oxford University Press New York, 2003.

[310] J. Walter, T. J. Nacken, C. Damm, T. Thajudeen, S. Eigler, and W. Peukert, "Determination of the lateral dimension of graphene oxide nanosheets using analytical ultracentrifugation," *Small*, vol. 11, no. 7, pp. 814–825, 2015.

[311] T. Nacken, C. Damm, J. Walter, A. Rüger, and W. Peukert, "Delamination of graphite in a high pressure homogenizer," *RSC Advances*, vol. 5, no. 71, pp. 57328–57338, 2015.

[312] M. Singh, E. Della Gaspera, T. Ahmed, S. Walia, R. Ramanathan, J. van Embden, E. Mayes, and V. Bansal, "Soft Exfoliation of 2D SnO with size-dependent optical properties," *2D Materials*, 2017.

[313] L. Yadgarov, C. L. Choi, A. Sedova, A. Cohen, R. Rosentsveig, O. Bar-Elli, D. Oron, H. Dai, and R. Tenne, "Dependence of the absorption and optical surface plasmon scattering of MoS2 nanoparticles on aspect ratio, size, and media," *ACS Nano*, vol. 8, no. 4, pp. 3575–3583, 2014.

[314] S. O'Brien, A. Harvey, A. Griffin, T. Donnelly, D. Mulcahy, J. Coleman, J. Donegan, and D. McCloskey, "Light scattering and random lasing in aqueous suspensions of hexagonal boron nitride nanoflakes," *Nanotechnology*, vol. 28, no. 47, p. 47LT02, 2017.

[315] X. Du, J. Li, J. Lin, and H. Jiang, "The origins of near band-edge transitions in hexagonal boron nitride epilayers," *Applied Physics Letters*, vol. 108, no. 5, p. 052106, 2016.

[316] T. Doan, J. Li, J. Lin, and H. Jiang, "Bandgap and exciton binding energies of hexagonal boron nitride probed by photocurrent excitation spectroscopy," *Applied Physics Letters*, vol. 109, no. 12, p. 122101, 2016.

[317] L. Museur and A. Kanaev, "Near band-gap photoluminescence properties of hexagonal boron nitride," *Journal of Applied Physics*, vol. 103, no. 10, p. 103520, 2008.

[318] A. Raja, L. Waldecker, J. Zipfel, Y. Cho, S. Brem, J. D. Ziegler, M. Kulig, T. Taniguchi, K. Watanabe, E. Malic, *et al.*, "Dielectric disorder in two-dimensional materials," *Nature Nanotechnology*, vol. 14, no. 9, pp. 832–837, 2019.

[319] J. Serrano, A. Bosak, R. Arenal, M. Krisch, K. Watanabe, T. Taniguchi, H. Kanda, A. Rubio, and L. Wirtz, "Vibrational properties of hexagonal boron nitride: inelastic X-Ray scattering and ab initio calculations," *Physical Review Letters*, vol. 98, no. 9, p. 095503, 2007.

[320] J. Wu, W.-Q. Han, W. Walukiewicz, J. W. Ager, W. Shan, E. Haller, and A. Zettl, "Raman spectroscopy and time-resolved photoluminescence of BN and B x C y N z nanotubes," *Nano Letters*, vol. 4, no. 4, pp. 647–650, 2004.

[321] M. Silly, P. Jaffrennou, J. Barjon, J.-S. Lauret, F. Ducastelle, A. Loiseau, E. Obraztsova, B. Attal-Tretout, and E. Rosencher, "Luminescence properties of hexagonal boron nitride: Cathodoluminescence and photoluminescence spectroscopy measurements," *Physical Review B*, vol. 75, no. 8, p. 085205, 2007.

[322] M. A. Pimenta, E. del Corro, B. R. Carvalho, C. Fantini, and L. M. Malard, "Comparative study of Raman spectroscopy in graphene and MoS2-type transition metal dichalcogenides," *Accounts of Chemical Research*, vol. 48, no. 1, pp. 41–47, 2014.

[323] S. Reich, A. Ferrari, R. Arenal, A. Loiseau, I. Bello, and J. Robertson, "Resonant Raman scattering in cubic and hexagonal boron nitride," *Physical Review B*, vol. 71, no. 20, p. 205201, 2005.

[324] Q. Cai, D. Scullion, A. Falin, K. Watanabe, T. Taniguchi, Y. Chen, E. J. Santos, and L. H. Li, "Raman signature and phonon dispersion of atomically thin boron nitride," *Nanoscale*, vol. 9, no. 9, pp. 3059–3067, 2017.

[325] R. V. Gorbachev, I. Riaz, R. R. Nair, R. Jalil, L. Britnell, B. D. Belle, E. W. Hill, K. S. Novoselov, K. Watanabe, T. Taniguchi, *et al.*, "Hunting for monolayer boron nitride: optical and Raman signatures," *Small*, vol. 7, no. 4, pp. 465–468, 2011.

[326] L. Schué, I. Stenger, F. Fossard, A. Loiseau, and J. Barjon, "Characterization methods dedicated to nanometer-thick hBN layers," *2D Materials*, vol. 4, no. 1, p. 015028, 2016.

[327] I. Stenger, L. Schue, M. Boukhicha, B. Bérini, B. Placais, A. Loiseau, and J. Barjon, "Low frequency Raman spectroscopy of few-atomic-layer thick hBN crystals," *2D Materials*, 2017.

[328] L.-H. Liu, G. Zorn, D. G. Castner, R. Solanki, M. M. Lerner, and M. Yan, "A simple and scalable route to wafer-size patterned graphene," *Journal of Materials Chemistry*, vol. 20, no. 24, pp. 5041–5046, 2010.

[329] W. Du, X. Jiang, and L. Zhu, "From graphite to graphene: direct liquid-phase exfoliation of graphite to produce single-and few-layered pristine graphene," *Journal of Materials Chemistry A*, vol. 1, no. 36, pp. 10592–10606, 2013.

[330] M. Naguib, O. Mashtalir, J. Carle, M. Kurtoglu, V. Presser, J. Lu, L. Hultman, Y. Gogotsi, and M. W. Barsoum, "MXenes: A new family of 2D early transition metal carbides produced by exfoliation of the MAX phases," in *Abstracts of Papers of the American Chemical Society*, vol. 244, ACS, 2012.

[331] N. R. Tummala and A. Striolo, "Role of counterion condensation in the self-assembly of sds surfactants at the water- graphite interface," *The Journal of Physical Chemistry B*, vol. 112, no. 7, pp. 1987–2000, 2008.

[332] M. Buzaglo, M. Shtein, S. Kober, R. Lovrinčić, A. Vilan, and O. Regev, "Critical parameters in exfoliating graphite into graphene," *Physical Chemistry Chemical Physics*, vol. 15, no. 12, pp. 4428–4435, 2013.

[333] Y. J. Lee, L. Huang, H. Wang, M. L. Sushko, B. Schwenzer, I. A. Aksay, and J. Liu, "Structural rearrangement and dispersion of functionalized graphene sheets in aqueous solutions," *Colloids and Interface Science Communications*, vol. 8, pp. 1–5, 2015.

[334] M. Poorsargol, B. Sohrabi, and M. Dehestani, "Study of the Gemini Surfactants' Self-Assembly on Graphene Nanosheets: Insights from Molecular Dynamic Simulation," *The Journal of Physical Chemistry A*, vol. 122, no. 15, pp. 3873–3885, 2018.

[335] S. Wang, M. Yi, and Z. Shen, "The effect of surfactants and their concentration on the liquid exfoliation of graphene," *RSC advances*, vol. 6, no. 61, pp. 56705–56710, 2016.

[336] M. Lotya, P. J. King, U. Khan, S. De, and J. N. Coleman, "High-concentration, surfactant-stabilized graphene dispersions," *ACS Nano*, vol. 4, no. 6, pp. 3155–3162, 2010.

[337] A. Gupta, V. Arunachalam, and S. Vasudevan, "Water dispersible, positively and negatively charged MoS2 nanosheets: surface chemistry and the role of surfactant binding," *The Journal of Physical Chemistry Letters*, vol. 6, no. 4, pp. 739–744, 2015.

[338] S. Lin, C.-J. Shih, M. S. Strano, and D. Blankschtein, "Molecular insights into the surface morphology, layering structure, and aggregation kinetics of surfactant-stabilized graphene dispersions," *Journal of the American Chemical Society*, vol. 133, no. 32, pp. 12810–12823, 2011.

[339] A. Gupta and S. Vasudevan, "Understanding Surfactant Stabilization of MoS2 Nanosheets in Aqueous Dispersions from Zeta Potential Measurements and Molecular Dynamics Simulations," *The Journal of Physical Chemistry C*, vol. 122, no. 33, pp. 19243–19250, 2018.

[340] P. Ramalingam, S. T. Pusuluri, S. Periasamy, R. Veerabahu, and J. Kulandaivel, "Role of deoxy group on the high concentration of graphene in surfactant/water media," *RSC Advances*, vol. 3, no. 7, pp. 2369–2378, 2013.

[341] S. Vera-López, P. Martínez, M. San Andrés, A. Díez-Pascual, and M. Valiente, "Study of graphene dispersions in sodium dodecylsulfate by steady-state fluorescence of pyrene," *Journal of Colloid and Interface Science*, vol. 514, pp. 415–424, 2018.

[342] L. B. Pártay, P. Jedlovszky, and M. Sega, "Molecular aggregates in aqueous solutions of bile acid salts. Molecular dynamics simulation study," *The Journal of Physical Chemistry B*, vol. 111, no. 33, pp. 9886–9896, 2007.

[343] J. Texter, "Graphene dispersions," *Current Opinion in Colloid & Interface Science*, vol. 19, no. 2, pp. 163–174, 2014.

[344] B. White, S. Banerjee, S. O'Brien, N. J. Turro, and I. P. Herman, "Zeta-potential measurements of surfactant-wrapped individual single-walled carbon nanotubes," *The Journal of Physical Chemistry C*, vol. 111, no. 37, pp. 13684–13690, 2007.

[345] M. D. Clark, S. Subramanian, and R. Krishnamoorti, "Understanding surfactant aided aqueous dispersion of multi-walled carbon nanotubes," *Journal of Colloid and Interface Science*, vol. 354, no. 1, pp. 144–151, 2011.

[346] A. J. Blanch, C. E. Lenehan, and J. S. Quinton, "Optimizing surfactant concentrations for dispersion of single-walled carbon nanotubes in aqueous solution," *The Journal of Physical Chemistry B*, vol. 114, no. 30, pp. 9805–9811, 2010.

[347] Z. Xu, X. Yang, and Z. Yang, "A molecular simulation probing of structure and interaction for supramolecular sodium dodecyl sulfate/single-wall carbon nanotube assemblies," *Nano Letters*, vol. 10, no. 3, pp. 985–991, 2010.

[348] M. Islam, E. Rojas, D. Bergey, A. Johnson, and A. Yodh, "High weight fraction surfactant solubilization of single-wall carbon nanotubes in water," *Nano Letters*, vol. 3, no. 2, pp. 269–273, 2003.

[349] P. Angelikopoulos and H. Bock, "The science of dispersing carbon nanotubes with surfactants," *Physical Chemistry Chemical Physics*, vol. 14, no. 27, pp. 9546–9557, 2012.

[350] M. S. Strano, V. C. Moore, M. K. Miller, M. J. Allen, E. H. Haroz, C. Kittrell, R. H. Hauge, and R. Smalley, "The role of surfactant adsorption during ultrasonication in the dispersion of single-walled carbon nanotubes," *Journal of nanoscience and Nanotechnology*, vol. 3, no. 1-2, pp. 81–86, 2003.

[351] H. Wang, "Dispersing carbon nanotubes using surfactants," *Current Opinion in Colloid & Interface Science*, vol. 14, no. 5, pp. 364–371, 2009.

[352] S. Utsumi, M. Kanamaru, H. Honda, H. Kanoh, H. Tanaka, T. Ohkubo, H. Sakai, M. Abe, and K. Kaneko, "RBM band shift-evidenced dispersion mechanism of single-wall carbon nanotube bundles with NaDDBS," *Journal of Colloid and Interface Science*, vol. 308, no. 1, pp. 276–284, 2007.

[353] R. M. Fernandes, B. Abreu, B. Claro, M. Buzaglo, O. Regev, I. Furo, and E. F. Marques, "Dispersing carbon nanotubes with ionic surfactants under controlled conditions: comparisons and insight," *Langmuir*, vol. 31, no. 40, pp. 10955–10965, 2015.

[354] H. Wang, W. Zhou, D. L. Ho, K. I. Winey, J. E. Fischer, C. J. Glinka, and E. K. Hobbie, "Dispersing single-walled carbon nanotubes with surfactants: a small angle neutron scattering study," *Nano Letters*, vol. 4, no. 9, pp. 1789–1793, 2004.

[355] L. Vaisman, H. D. Wagner, and G. Marom, "The role of surfactants in dispersion of carbon nanotubes," *Advances in Colloid and Interface Science*, vol. 128, pp. 37–46, 2006.

[356] B. Vigolo, A. Penicaud, C. Coulon, C. Sauder, R. Pailler, C. Journet, P. Bernier, and P. Poulin, "Macroscopic fibers and ribbons of oriented carbon nanotubes," *Science*, vol. 290, no. 5495, pp. 1331–1334, 2000.

[357] J.-M. Bonard, T. Stora, J.-P. Salvetat, F. Maier, T. Stöckli, C. Duschl, L. Forró, W. A. de Heer, and A. Châtelain, "Purification and size-selection of carbon nanotubes," *Advanced Materials*, vol. 9, no. 10, pp. 827–831, 1997.

[358] A. Schlierf, H. Yang, E. Gebremedhn, E. Treossi, L. Ortolani, L. Chen, A. Minoia, V. Morandi, P. Samorì, C. Casiraghi, *et al.*, "Nanoscale insight into the exfoliation mechanism of graphene with organic dyes: effect of charge, dipole and molecular structure," *Nanoscale*, vol. 5, no. 10, pp. 4205–4216, 2013.

[359] D. Parviz, S. Das, H. T. Ahmed, F. Irin, S. Bhattacharia, and M. J. Green, "Dispersions of non-covalently functionalized graphene with minimal stabilizer," *ACS Nano*, vol. 6, no. 10, pp. 8857–8867, 2012.

[360] X. Just-Baringo, Y. Shin, A. Panigrahi, M. Zarattini, V. Nagyte, L. Zhao, K. Kostarelos, C. Casiraghi, and I. Larrosa, "Palladium catalysed C–H arylation of pyrenes: access to a new class of exfoliating agents for water-based graphene dispersions," *Chemical Science*, vol. 11, no. 9, pp. 2472–2478, 2020.

[361] S. Biccai, S. Barwich, D. Boland, A. Harvey, D. Hanlon, N. McEvoy, and J. N. Coleman, "Exfoliation of 2D materials by high shear mixing," *2D Materials*, vol. 6, no. 1, p. 015008, 2018.

[362] W. Zhao, Z. Ghorannevis, L. Chu, M. Toh, C. Kloc, P.-H. Tan, and G. Eda, "Evolution of electronic structure in atomically thin sheets of WS2 and WSe2," *ACS Nano*, vol. 7, no. 1, pp. 791–797, 2013.

[363] J. Djamil, A.-L. Hansen, C. Backes, W. Bensch, U. Schürmann, L. Kienle, A. Düvel, and P. Heitjans, "Using light, X-rays and electrons for evaluation of the nanostructure of layered materials," *Nanoscale*, vol. 10, no. 45, pp. 21142–21150, 2018.

[364] T. Nakato, J. Kawamata, and S. Takagi, *Inorganic Nanosheets and Nanosheet-Based Materials*. Tokyo: Springer Japan, 2017.

[365] K. Park, H. Koerner, and R. A. Vaia, "Depletion-induced shape and size selection of gold nanoparticles," *Nano Letters*, vol. 10, no. 4, pp. 1433–1439, 2010.

[366] H. Evans, "117. Alkyl sulphates. Part I. Critical micelle concentrations of the sodium salts," *Journal of the Chemical Society (Resumed)*, pp. 579–586, 1956.

[367] L. Sepulveda and J. Cortés, "Ionization degrees and critical micelle concentrations of hexadecyltrimethylammonium and tetradecyltrimethylammonium micelles with different counterions," *The Journal of Physical Chemistry*, vol. 89, no. 24, pp. 5322–5324, 1985.

[368] M. Poorsargol, M. Alimohammadian, B. Sohrabi, and M. Dehestani, "Dispersion of graphene using surfactant mixtures: Experimental and molecular dynamics simulation studies," *Applied Surface Science*, vol. 464, pp. 440–450, 2019.

[369] T. W. Davey, W. A. Ducker, A. R. Hayman, and J. Simpson, "Krafft temperature depression in quaternary ammonium bromide surfactants," *Langmuir*, vol. 14, no. 12, pp. 3210–3213, 1998.

[370] L. Ueberricke, J. N. Coleman, and C. Backes, "Robustness of Size Selection and Spectroscopic Size, Thickness and Monolayer Metrics of Liquid-Exfoliated WS2," *Physica Status Solidi (B)*, vol. 254, no. 11, p. 1700443, 2017.

[371] S. Grieger, B. M. Szydłowska, V. Rao, E. Steinmann, M. Dodds, Z. Gholamvand, G. S. Duesberg, J. Zaumseil, and C. Backes, "Site-selective oxidation of monolayered liquid-exfoliated WS2 by shielding the basal plane through adsorption of a facial amphiphile," *Angewandte Chemie International Edition*, 2020.

[372] X. Zang, T. Wang, Z. Han, L. Li, and X. Wu, "Recent advances of 2D nanomaterials in the electrode materials of lithium-ion batteries," *Nano*, vol. 14, no. 02, p. 1930001, 2019.

[373] R. Tian, M. Breshears, D. V. Horvath, and J. N. Coleman, "The rate performance of two-dimensional material-based battery electrodes may not be as good as commonly believed," *ACS nano*, vol. 14, no. 3, pp. 3129–3140, 2020.

[374] P. Xiong, L. Peng, D. Chen, Y. Zhao, X. Wang, and G. Yu, "Two-dimensional nanosheets based Li-ion full batteries with high rate capability and flexibility," *Nano Energy*, vol. 12, pp. 816–823, 2015.

[375] G. Du, Z. Guo, S. Wang, R. Zeng, Z. Chen, and H. Liu, "Superior stability and high capacity of restacked molybdenum disulfide as anode material for lithium ion batteries," *Chemical Communications*, vol. 46, no. 7, pp. 1106–1108, 2010.

[376] Y. Liu, L. Ren, X. Qi, L. Yang, J. Li, Y. Wang, and J. Zhong, "Hydrothermal exfoliated molybdenum disulfide nanosheets as anode material for lithium ion batteries," *Journal of Energy Chemistry*, vol. 23, no. 2, pp. 207–212, 2014.

[377] H. Sun, A. E. D. R. Castillo, S. Monaco, A. Capasso, A. Ansaldo, M. Prato, D. A. Dinh, V. Pellegrini, B. Scrosati, L. Manna, *et al.*, "Binder-free graphene as an advanced anode for lithium batteries," *Journal of Materials Chemistry A*, vol. 4, no. 18, pp. 6886–6895, 2016.

[378] R. Wang, C. Xu, J. Sun, Y. Liu, L. Gao, H. Yao, and C. Lin, "Heat-induced formation of porous and free-standing MoS2/GS hybrid electrodes for binder-free and ultralong-life lithium ion batteries," *Nano Energy*, vol. 8, pp. 183–195, 2014.

[379] J. Zhou, L. Shen, M. D. Costa, K. A. Persson, S. P. Ong, P. Huck, Y. Lu, X. Ma, Y. Chen, H. Tang, *et al.*, "2DMatPedia, an open computational database of two-dimensional materials from top-down and bottom-up approaches," *Scientific Data*, vol. 6, no. 1, pp. 1–10, 2019.

[380] S. Haastrup, M. Strange, M. Pandey, T. Deilmann, P. S. Schmidt, N. F. Hinsche, M. N. Gjerding, D. Torelli, P. M. Larsen, A. C. Riis-Jensen, *et al.*, "The Computational 2D Materials Database: high-throughput modeling and discovery of atomically thin crystals," *2D Materials*, vol. 5, no. 4, p. 042002, 2018.

[381] N. Mounet, M. Gibertini, P. Schwaller, D. Campi, A. Merkys, A. Marrazzo, T. Sohier, I. E. Castelli, A. Cepellotti, G. Pizzi, *et al.*, "Two-dimensional materials from high-throughput computational exfoliation of experimentally known compounds," *Nature Nanotechnology*, vol. 13, no. 3, pp. 246–252, 2018.

[382] G. Cheon, K.-A. N. Duerloo, A. D. Sendek, C. Porter, Y. Chen, and E. J. Reed, "Data mining for new two-and one-dimensional weakly bonded solids and lattice-commensurate heterostructures," *Nano Letters*, vol. 17, no. 3, pp. 1915–1923, 2017.

[383] J.-W. Park and C.-M. Park, "Electrochemical Li Topotactic Reaction in Layered SnP3 for Superior Li-Ion Batteries," *Scientific Reports*, vol. 6, no. 1, pp. 1–8, 2016.

[384] J. Gullman and O. Olofsson, "The crystal structure of SnP3 and a note on the crystal structure of GeP3," *Journal of Solid State Chemistry*, vol. 5, no. 3, pp. 441–445, 1972.

[385] B. Ghosh, S. Puri, A. Agarwal, and S. Bhowmick, "SnP3: a previously unexplored two-dimensional material," *The Journal of Physical Chemistry C*, vol. 122, no. 31, pp. 18185–18191, 2018.

[386] S. Sun, F. Meng, H. Wang, H. Wang, and Y. Ni, "Novel two-dimensional semiconductor SnP 3: high stability, tunable bandgaps and high carrier mobility explored using first-principles calculations," *Journal of Materials Chemistry A*, vol. 6, no. 25, pp. 11890–11897, 2018.

[387] P.-L. Gong, F. Zhang, L.-F. Huang, H. Zhang, L. Li, R.-C. Xiao, B. Deng, H. Pan, and X.-Q. Shi, "Multifunctional two-dimensional semiconductors SnP3: universal mechanism of layer-dependent electronic phase transition," *Journal of Physics: Condensed Matter*, vol. 30, no. 47, p. 475702, 2018.

[388] O. Hod, "Graphite and hexagonal boron-nitride have the same interlayer distance. Why?," *Journal of Chemical Theory and Computation*, vol. 8, no. 4, pp. 1360–1369, 2012.

[389] D. Su, S. Dou, and G. Wang, "Ultrathin MoS2 nanosheets as anode materials for sodium-ion batteries with superior performance," *Advanced Energy Materials*, vol. 5, no. 6, p. 1401205, 2015.

[390] M. S. Ramzan, V. Bacic, Y. Jing, and A. Kuc, "Electronic Properties of a New Family of Layered Materials from Groups 14 and 15: First-Principles Simulations," *The Journal of Physical Chemistry C*, vol. 123, no. 41, pp. 25470–25476, 2019.

[391] L.-P. Feng, A. Li, P.-C. Wang, and Z.-T. Liu, "Novel two-dimensional semiconductor SnP3 with high carrier mobility, good light absorption, and strong interlayer quantum confinement," *The Journal of Physical Chemistry C*, vol. 122, no. 42, pp. 24359–24367, 2018.

[392] Y. Jing, Y. Ma, Y. Li, and T. Heine, "GeP3: A small indirect band gap 2D crystal with high carrier mobility and strong interlayer quantum confinement," *Nano Letters*, vol. 17, no. 3, pp. 1833–1838, 2017.

[393] C.-S. Liu, X.-L. Yang, J. Liu, and X.-J. Ye, "Theoretical prediction of two-dimensional SnP3 as a promising anode material for Na-ion batteries," *ACS Applied Energy Materials*, vol. 1, no. 8, pp. 3850–3859, 2018.

[394] S. Zhang, Z. Yan, Y. Li, Z. Chen, and H. Zeng, "Atomically thin arsenene and antimonene: semimetal–semiconductor and indirect–direct band-gap transitions," *Angewandte Chemie International Edition*, vol. 54, no. 10, pp. 3112–3115, 2015.

[395] M. Shirayama, H. Kadowaki, T. Miyadera, T. Sugita, M. Tamakoshi, M. Kato, T. Fujiseki, D. Murata, S. Hara, T. N. Murakami, *et al.*, "Optical transitions in hybrid perovskite solar cells: ellipsometry, density functional theory, and quantum efficiency analyses for CH3NH3PbI3," *Physical Review Applied*, vol. 5, no. 1, p. 014012, 2016.

[396] N. J. Jeon, J. H. Noh, Y. C. Kim, W. S. Yang, S. Ryu, and S. I. Seok, "Solvent engineering for high-performance inorganic–organic hybrid perovskite solar cells," *Nature Materials*, vol. 13, no. 9, pp. 897–903, 2014.

[397] F. Niu, M. Cai, J. Pang, X. Li, D. Yang, and G. Zhang, "Gas molecular adsorption effects on the electronic and optical properties of monolayer SnP3," *Vacuum*, vol. 168, p. 108823, 2019.

[398] X.-L. Zhu, P.-F. Liu, J. Zhang, P. Zhang, W.-X. Zhou, G. Xie, and B.-T. Wang, "Monolayer SnP 3: an excellent p-type thermoelectric material," *Nanoscale*, vol. 11, no. 42, pp. 19923–19932, 2019.

[399] H. Shu, "Electronic, transport, and optical properties of atomically thin silicon phosphide: first-principles calculations," *Materials Research Express*, vol. 6, no. 2, p. 026428, 2018.

[400] P. Schmidt and R. Stickler, "Silicon phosphide precipitates in diffused silicon," *Journal of the Electrochemical Society*, vol. 111, no. 10, p. 1188, 1964.

[401] C. Beck and R. Stickler, "Crystallography of SiP and SiAs single crystals and of SiP precipitates in Si," *Journal of Applied Physics*, vol. 37, no. 13, pp. 4683–4687, 1966.

[402] M. Servidori and A. Armigliato, "Electron microscopy of silicon monophosphide precipitates in P-diffused silicon," *Journal of Materials Science*, vol. 10, no. 2, pp. 306–313, 1975.

[403] A. Armigliato, M. Servidori, S. Solmi, and I. Vecchi, "On the growth of stacking faults and dislocations induced in silicon by phosphorus predeposition," *Journal of Applied Physics*, vol. 48, no. 5, pp. 1806–1812, 1977.

[404] D. Nobili, A. Armigliato, M. Finnetti, and S. Solmi, "Precipitation as the phenomenon responsible for the electrically inactive phosphorus in silicon," *Journal of Applied Physics*, vol. 53, no. 3, pp. 1484–1491, 1982.

[405] C. Barreteau, B. Michon, C. Besnard, and E. Giannini, "High-pressure melt growth and transport properties of SiP, SiAs, GeP, and GeAs 2D layered semiconductors," *Journal of Crystal Growth*, vol. 443, pp. 75–80, 2016.

[406] C. Li, S. Wang, X. Zhang, N. Jia, T. Yu, M. Zhu, D. Liu, and X. Tao, "Controllable seeded flux growth and optoelectronic properties of bulk o-SiP crystals," *CrystEngComm*, vol. 19, no. 46, pp. 6986–6991, 2017.

[407] Z. Wen, Y. Wang, Z. Chen, and J. Shi, "Chemical Vapor Growth of Silicon Phosphide Nanostructures," *MRS Advances*, pp. 1–8.

[408] R. Reinhold, D. Mikhailova, T. Gemming, A. Missyul, C. Nowka, S. Kaskel, and L. Giebeler, "Silicon monophosphide as a possible lithium battery anode material," *Journal of Materials Chemistry A*, vol. 6, no. 41, pp. 19974–19978, 2018.

[409] M. Ashton, S. B. Sinnott, and R. G. Hennig, "Computational discovery and characterization of polymorphic two-dimensional IV–V materials," *Applied Physics Letters*, vol. 109, no. 19, p. 192103, 2016.

[410] A.-Q. Cheng, Z. He, J. Zhao, H. Zeng, and R.-S. Chen, "Monolayered silicon and germanium monopnictide semiconductors: excellent stability, high absorbance, and strain engineering of electronic properties," *ACS applied materials & interfaces*, vol. 10, no. 6, pp. 5133–5139, 2018.

[411] B. Huang, H. L. Zhuang, M. Yoon, B. G. Sumpter, and S.-H. Wei, "Highly stable two-dimensional silicon phosphides: Different stoichiometries and exotic electronic properties," *Physical Review B*, vol. 91, no. 12, p. 121401, 2015.

[412] S. Kansara, P. D. Bhuyan, Y. Sonvane, and S. K. Gupta, "Two-dimensional silicon phosphide: low effective mass and direct band gap for future devices applications," *Journal of Materials Science*, vol. 54, no. 18, pp. 11878–11888, 2019.

[413] C. Li, S. Wang, C. Li, T. Yu, N. Jia, J. Qiao, M. Zhu, D. Liu, and X. Tao, "Highly sensitive detection of polarized light using a new group IV–V 2D orthorhombic SiP," *Journal of Materials Chemistry C*, vol. 6, no. 27, pp. 7219–7225, 2018.

[414] Z. Ma, J. Zhuang, X. Zhang, and Z. Zhou, "SiP monolayers: New 2D structures of group IV–V compounds for visible-light photohydrolytic catalysts," *Frontiers of Physics*, vol. 13, no. 3, p. 138104, 2018.

[415] B. Mortazavi and T. Rabczuk, "Anisotropic mechanical properties and strain tuneable band-gap in single-layer SiP, SiAs, GeP and GeAs," *Physica E: Low-dimensional Systems and Nanostructures*, vol. 103, pp. 273–278, 2018.

[416] B. Mortazavi, M. Shahrokhi, G. Cuniberti, and X. Zhuang, "Two-Dimensional SiP, SiAs, GeP and GeAs as Promising Candidates for Photocatalytic Applications," *Coatings*, vol. 9, no. 8, p. 522, 2019.

[417] R. N. Somaiya, Y. A. Sonvane, and S. K. Gupta, "Exploration of the strain and thermoelectric properties of hexagonal SiX (X= N, P, As, Sb, and Bi) monolayers," *Physical Chemistry Chemical Physics*, vol. 22, no. 7, pp. 3990–3998, 2020.

[418] S. Zhang, S. Guo, Y. Huang, Z. Zhu, B. Cai, M. Xie, W. Zhou, and H. Zeng, "Two-dimensional SiP: an unexplored direct band-gap semiconductor," *2D Materials*, vol. 4, no. 1, p. 015030, 2016.

[419] E. Kroumova, M. Aroyo, J. Perez-Mato, A. Kirov, C. Capillas, S. Ivantchev, and H. Wondratschek, "Bilbao crystallographic server: useful databases and tools for phase-transition studies," *Phase Transitions: A Multinational Journal*, vol. 76, no. 1-2, pp. 155–170, 2003.

[420] K. D. Rasamani, F. Alimohammadi, and Y. Sun, "Interlayer-expanded MoS2," *Materials Today*, vol. 20, no. 2, pp. 83–91, 2017.

[421] W. Wang, S. Dai, X. Li, J. Yang, D. J. Srolovitz, and Q. Zheng, "Measurement of the cleavage energy of graphite," *Nature Communications*, vol. 6, no. 1, pp. 1–7, 2015.

[422] L. Li, J. Kim, C. Jin, G. J. Ye, D. Y. Qiu, H. Felipe, Z. Shi, L. Chen, Z. Zhang, F. Yang, *et al.*, "Direct observation of the layer-dependent electronic structure in phosphorene," *Nature Nanotechnology*, vol. 12, no. 1, p. 21, 2017.

[423] C. Backes, D. Hanlon, B. M. Szydlowska, A. Harvey, R. J. Smith, T. M. Higgins, and J. N. Coleman, "Preparation of liquid-exfoliated transition metal dichalcogenide nanosheets with controlled size and thickness: a state of the art protocol," *JoVE (Journal of Visualized Experiments)*, no. 118, p. e54806, 2016.

[424] B. Eifert, M. Becker, C. T. Reindl, M. Giar, L. Zheng, A. Polity, Y. He, C. Heiliger, and P. J. Klar, "Raman studies of the intermediate tin-oxide phase," *Physical Review Materials*, vol. 1, no. 1, p. 014602, 2017.

[425] H. Zheng, J. Li, X. Song, G. Liu, and V. S. Battaglia, "A comprehensive understanding of electrode thickness effects on the electrochemical performances of Li-ion battery cathodes," *Electrochimica Acta*, vol. 71, pp. 258–265, 2012.

[426] D. McAteer, Z. Gholamvand, N. McEvoy, A. Harvey, E. O'Malley, G. S. Duesberg, and J. N. Coleman, "Thickness dependence and percolation scaling of hydrogen production rate in MoS2 nanosheet and nanosheet–carbon nanotube composite catalytic electrodes," *ACS Nano*, vol. 10, no. 1, pp. 672–683, 2016.

[427] R. Tian, A. Griffin, M. McCrystall, M. Breshears, A. Harvey, C. Gabbett, D. V. Horváth, C. Backes, Y. Jing, T. Heine, *et al.*, "Liquid Exfoliated SnP3 Nanosheets for Very High Areal Capacity Lithium-Ion Batteries," *Advanced Energy Materials*, p. 2002364, 2020.

[428] S.-H. Park, P. J. King, R. Tian, C. S. Boland, J. Coelho, C. J. Zhang, P. McBean, N. McEvoy, M. P. Kremer, D. Daly, *et al.*, "High areal capacity battery electrodes enabled by segregated nanotube networks," *Nature Energy*, vol. 4, no. 7, pp. 560–567, 2019.

[429] X. Wang, Y. Fan, R. A. Susantyoko, Q. Xiao, L. Sun, D. He, and Q. Zhang, "High areal capacity Li ion battery anode based on thick mesoporous Co3O4 nanosheet networks," *Nano Energy*, vol. 5, pp. 91–96, 2014.

[430] M. Obrovac and L. Christensen, "Structural changes in silicon anodes during lithium insertion/extraction," *Electrochemical and Solid State Letters*, vol. 7, no. 5, p. A93, 2004.

[431] H. Nakai, T. Kubota, A. Kita, and A. Kawashima, "Investigation of the solid electrolyte interphase formed by fluoroethylene carbonate on Si electrodes," *Journal of The Electrochemical Society*, vol. 158, no. 7, p. A798, 2011.

[432] N.-S. Choi, K. H. Yew, K. Y. Lee, M. Sung, H. Kim, and S.-S. Kim, "Effect of fluoroethylene carbonate additive on interfacial properties of silicon thin-film electrode," *Journal of Power Sources*, vol. 161, no. 2, pp. 1254–1259, 2006.

[433] K. S. Suslick, "Sonochemistry," *Science*, vol. 247, no. 4949, pp. 1439–1445, 1990.

[434] E. Klein, "Some background history of ultrasonics," *The Journal of the Acoustical Society of America*, vol. 20, no. 5, pp. 601–604, 1948.

[435] C. Chilowsky and P. Langevin, "Procédés et appareils pour la production de signaux sous-marins dirigés et pour la localisation à distance d'obstacles sous-marins," *French patent*, vol. 502913, 1916.

[436] O. Reynolds, "Experiments showing the boiling of water in an open tube at ordinary temperatures," *Scientific Papers on Mechanical and Physical Subject*, vol. 2, pp. 1900–1903, 1894.

[437] O. Reynolds, A. W. Brightmore, and W. H. Moorby, *Papers on Mechanical and Physical Subjects*, vol. 2. Cambridge University Press, 1901.

[438] W. H. Bragg, *The World of Sound: Six lectures delivered before a juvenile auditory at the Royal institution, Christmas, 1919*. London: G. Bell and Sons, 1 ed., 1920.

[439] L. R. O. F.R.S., "VIII. On the pressure developed in a liquid during the collapse of a spherical cavity," *The London, Edinburgh, and Dublin Philosophical Magazine and Journal of Science*, vol. 34, no. 200, pp. 94–98, 1917.

[440] C. E. Brennen, *Cavitation and bubble dynamics*. Cambridge: Cambridge University Press, 2014.

[441] C. Xiao and D. Heyes, "Cavitation in stretched liquids," *Proceedings of the Royal Society of London. Series A: Mathematical, Physical and Engineering Sciences*, vol. 458, no. 2020, pp. 889–910, 2002.

[442] H. Hu, C. Xu, Y. Zhao, K. J. Ziegler, and J. Chung, "Boiling and quenching heat transfer advancement by nanoscale surface modification," *Scientific Reports*, vol. 7, no. 1, pp. 1–16, 2017.

[443] J. Welty, G. L. Rorrer, and D. G. Foster, *Fundamentals of momentum, heat, and mass transfer*. New York: John Wiley & Sons, 5 ed., 2008.

[444] S. Aljishi and J. Tatarkiewicz, "Why does heating water in a kettle produce sound?," *American Journal of Physics*, vol. 59, no. 7, pp. 628–632, 1991.

[445] J.-P. Franc, "Physics and control of cavitation," in *Von Karman Institute, RTO Lecture Series, Design and analysis of high speed pumps*, 2006.

[446] H. Estrade-Szwarckopf, "XPS photoemission in carbonaceous materials: A "defect" peak beside the graphitic asymmetric peak," *Carbon*, vol. 42, no. 8-9, pp. 1713–1721, 2004.

[447] U. Khan, A. O'Neill, M. Lotya, S. De, and J. N. Coleman, "High-concentration solvent exfoliation of graphene," *Small*, vol. 6, no. 7, pp. 864–871, 2010.

[448] M. V. Bracamonte, G. I. Lacconi, S. E. Urreta, and L. E. F. Foa Torres, "On the nature of defects in liquid-phase exfoliated graphene," *The Journal of Physical Chemistry C*, vol. 118, no. 28, pp. 15455–15459, 2014.

[449] A. Jorio, E. H. M. Ferreira, M. V. Moutinho, F. Stavale, C. A. Achete, and R. B. Capaz, "Measuring disorder in graphene with the G and D bands," *Physica Status Solidi (B)*, vol. 247, no. 11-12, pp. 2980–2982, 2010.

[450] R. Durge, R. Kshirsagar, and P. Tambe, "Effect of sonication energy on the yield of graphene nanosheets by liquid-phase exfoliation of graphite," *Procedia Engineering*, vol. 97, pp. 1457–1465, 2014.

[451] D. P. O'Driscoll, V. Vega-Mayoral, I. Harley, C. S. Boland, and J. N. Coleman, "Optimising composite viscosity leads to high sensitivity electromechancial sensors," *2D Materials*, vol. 5, no. 3, p. 035042, 2018.

[452] H. Liu, Y. Li, K. Dai, G. Zheng, C. Liu, C. Shen, X. Yan, J. Guo, and Z. Guo, "Electrically conductive thermoplastic elastomer nanocomposites at ultralow graphene loading levels for strain sensor applications," *Journal of Materials Chemistry C*, vol. 4, no. 1, pp. 157–166, 2016.

[453] Z. Jing, Z. Guang-Yu, and S. Dong-Xia, "Review of graphene-based strain sensors," *Chinese Physics B*, vol. 22, no. 5, p. 057701, 2013.

[454] A. D. R. Castillo, V. Pellegrini, A. Ansaldo, F. Ricciardella, H. Sun, L. Marasco, J. Buha, Z. Dang, L. Gagliani, E. Lago, *et al.*, "High-yield production of 2D crystals by wet-jet milling," *Materials Horizons*, vol. 5, no. 5, pp. 890–904, 2018.

[455] V. M. Wasekar and R. M. Manglik, "A review of enhanced heat transfer in nucleate pool boiling of aqueous surfactant and polymeric solutions," *Journal of Enhanced Heat Transfer*, vol. 6, no. 2-4, 1999.

[456] L. Cheng, D. Mewes, and A. Luke, "Boiling phenomena with surfactants and polymeric additives: a state-of-the-art review," *International Journal of Heat and Mass Transfer*, vol. 50, no. 13-14, pp. 2744–2771, 2007.

[457] Y. Iida, M. Ashokkumar, T. Tuziuti, T. Kozuka, K. Yasui, A. Towata, and J. Lee, "Bubble population phenomena in sonochemical reactor: II. Estimation of bubble size distribution and its number density by simple coalescence model calculation," *Ultrasonics Sonochemistry*, vol. 17, no. 2, pp. 480–486, 2010.